UNIVERSITY OF CALIFORNIA
Los Angeles

Data-Driven Modeling and Control of Extreme Aerodynamic Flows: Super Resolution, Manifold Identification, and Phase-Amplitude Reduction

A dissertation submitted in partial satisfaction
of the requirements for the degree
Doctor of Philosophy in Mechanical Engineering

by

Kai Fukami

2024

ABSTRACT OF THE DISSERTATION

Data-Driven Modeling and Control of Extreme Aerodynamic Flows:
Super Resolution, Manifold Identification, and Phase-Amplitude Reduction

by

Kai Fukami
Doctor of Philosophy in Mechanical Engineering
University of California, Los Angeles, 2024
Professor Kunihiko Taira, Chair

In this thesis, we develop data-driven techniques to analyze unsteady aerodynamic flows under extremely gusty conditions for global field reconstruction, low-order modeling, and control. We first consider global field reconstruction from sparse sensors through the lens of generalized super-resolution analysis. This thesis offers a survey with comprehensive case studies of machine-learning-based super resolution for turbulent flows. Supervised machine-learning-based sparse reconstruction is then performed with vortical flows in a pump sump, an example of industrial turbulence. In addition, we establish a robust sparse reconstruction technique for situations in which the numbers and positions of sensors are changing over time, referred to as a Voronoi-tessellation-assisted convolutional neural network. We demonstrate its performance and robustness against noisy sensor measurements with a range of fluid flow examples. Defining interpolation and extrapolation conditions of machine-learning-based studies in unsteady flows is challenging due to their high-dimensionality and scale-invariant nature. For this reason, we consider nonlinear data-driven scaling of turbulent flows to reveal scale-invariant vortical structures across Reynolds numbers. This nonlinear scaling provides insights for supporting machine-learning-based studies

of turbulent flows.

To perform flow control leveraging the reconstructed fields from sparse sensors, we then consider constructing a control strategy of flows in a low-order subspace identified by nonlinear machine-learning-based data compression. We develop a nonlinear observable-augmented autoencoder that can incorporate physical observables in identifying a low-dimensional latent manifold. This thesis considers extreme vortex-gust airfoil interactions occurring when modern small aircraft fly in severe atmospheric conditions. Under such extreme aerodynamic situations, wings experience massive separation while exhibiting sharp and highly unsteady aerodynamic force responses. Although it is challenging to analyze the nonlinear, transient nature of extreme aerodynamics with conventional linear techniques, we reveal that the underlying physics of a collection of time-varying vortical flows in a high-dimensional space can be expressed on a low-rank manifold leveraging the present data-driven compression. It is also demonstrated that efficient control strategies can be derived at a minimal cost with the assistance of phase-amplitude reduction on the discovered manifold. These developed data-driven strategies offer a new perspective on reconstructing, modeling, and controlling a range of extremely unsteady flows.

The dissertation of Kai Fukami is approved.

Jeffrey D. Eldredge

Mitchell Spearrin

Jacob Bortnik

Steven L. Brunton

Kunihiko Taira, Committee Chair

University of California, Los Angeles

2024

TABLE OF CONTENTS

LIST OF FIGURES

ACKNOWLEDGMENTS

Here, let me leave my acknowledgments to those who have supported me during my Ph.D. study at UCLA.

I first thank my Ph.D. supervisor, Professor Kunihiko (Sam) Taira (hereafter called Sam) for his kind and enthusiastic supervision over my Ph.D. journey. While my Ph.D. course at UCLA has taken approximately 3.5 years, my research studies over the past 6 years have been mostly supported by him including the term when I was in his group as a visiting research scholar at Florida State University and UCLA. All of the research activities with Sam are unforgettable (including when we crafted pixelized turbulence figures with scissors and glue in his office). Sam is always serving as a role model for me in pursuing academic activities as an aerodynamicist. His passion for tackling challenging aerodynamic problems is remarkable, which triggers me to seriously think that I also would like to contribute to the aerodynamics community as a leading expert with unique aspects. While, of course, I am still on the way towards that goal, I again very much appreciate his patient guidance and here promise that I will also make my best efforts in pursuing my next academic journey. I would like to return the favor to Sam in some ways in the future.

Next, I also appreciate huge support and advice from my Bachelor's and Master's degrees supervisor, Professor Koji Fukagata (hereafter called Fukagata sensei) at Keio University. He was my first fluid mechanics teacher in my undergraduate study, which was a great introduction to me to dive into the field of fluid mechanics. While Fukagata sensei is always cheerful and has a bright personality (I was a bit surprised when he appeared in a class while wearing a Santa Claus cap one day), he dramatically becomes a true professional in tackling turbulent flow problems. Such a way of switching on and off while serving as a "professional" is simply cool and also one of my role models. Even after I came to UCLA, Fukagata sensei has kindly kept in touch and given me a range of positive influences to me.

During my Ph.D. study, I had great opportunities for research collaborations and fruitful discussions on data-driven fluid mechanics. While there are countless people who have shared positive

and insightful experiences with me, let me particularly express my gratitude to Byungjin An, Romit Maulik, Vedasri Godavarthi, Hiroya Nakao, and Susumu Goto.

I thank my committee members Professors Jeff Eldredge, Mitchell Spearrin, Jacob Bortnik, and Steven L. Brunton, for giving insightful suggestions. I am also thankful to the UCLA–Amazon Science Hub for Humanity and Artificial Intelligence for the support during the 2022-2023 academic year. The studies in this dissertation were supported by the U.S. Department of Defense Vannevar Bush Faculty Fellowship (N00014-22-1-2798), the Air Force Office of Scientific Research (FA9550-21-1-0178), the National Science Foundation (2129639), and Ebara Corporation.

Finally, I would like to end my acknowledgment section with special thanks to my parents, Takeshi Fukami and Naoko Fukami, my soul mate, Ramses and Nefertiti, and my partner, Azusa Shimizu, for their tremendous support and love.

I. Vita

Apr 2017-Mar 2018, Undergraduate Research Assistant, Keio University

Mar 2018, B.Eng. (Mechanical Engineering), Keio University

Aug 2018-Dec 2018, Visiting Research Student, Florida State University

Jan 2019-Aug 2019, Visiting Research Student, UCLA

Apr 2018-Sep 2020, Graduate Research Assistant (Master student), Keio University

Sep 2020, M.Eng. (Science for Open and Environmental System), Keio University

Sep 2020-Sep 2021, Visiting Researcher, Keio University

Sep 2020-Feb 2024, Graduate Research Assistant (Ph.D. student), UCLA

II. First author publications

1. **K. Fukami**, R. Maulik, N. Ramachandra, K. Fukagata, K. Taira, "Global field reconstruction from sparse sensors with Voronoi tessellation-assisted deep learning," Nature Machine Intelligence, 3, 945–951, 2021

2. **K. Fukami**, B. An, M. Nohmi, M. Obuchi, K. Taira, "Machine-learning-based reconstruction of turbulent vortices from sparse pressure sensors in a pump sump," Journal of Fluids Engineering, 144(12), 121501, 2022

3. **K. Fukami**, K. Fukagata, K. Taira, "Super-resolution analysis via machine learning: A survey for fluid flows," Theoretical and Computational Fluid Dynamics, 37, 421–444 (invited), 2023

4. **K. Fukami**, S. Goto, K. Taira, "Data-driven nonlinear turbulent flow scaling with Buckingham Pi variables," Journal of Fluid Mechanics, in Review, 2023

5. **K. Fukami**, K. Taira, "Grasping extreme aerodynamics on a low-dimensional manifold," Nature Communications, 14, 6480, 2023

6. **K. Fukami**, H. Nakao, K. Taira, "Phase-amplitude modeling and control of extreme aerodynamics on a machine-learned manifold," to be submitted, 2023

III. Co-authored publications

1. H. Odaka, **K. Fukami**, K. Taira, “Latent space representation of plunging airfoil wakes," in Review, 2024

2. L. R. Smith, **K. Fukami**, G. Sedky, A. R. Jones, K. Taira, “A cyclic perspective on transient gust encounters through the lens of persistent homology," Journal of Fluid Mechanics, 980, A18, 2024

3. D. Chen, F. Kaiser, J.-C. Hu, D. E. Rival, **K. Fukami**, K. Taira, “Sparse pressure-based machine learning approach for aerodynamic loads estimation during gust encounters," AIAA Journal, 62, 1, 275-290, 2024

4. Y. Zhong, **K. Fukami**, B. An, K. Taira, “Sparse sensor reconstruction of vortex-impinged airfoil wake with machine learning," Theoretical and Computational Fluid Dynamics, 37, 269–287, 2023

5. V. Anantharaman, J. Feldkamp, **K. Fukami**, K. Taira, “Image and video compression of fluid flow data," Theoretical and Computational Fluid Dynamics, 37, 61–82, 2023

6. R. Maulik, **K. Fukami**, N. Ramachandra, K. Fukagata, K. Taira, “Probabilistic neural networks for fluid flow surrogate modeling and data recovery,” Physical Review Fluids, 5 (104401), 2020

IV. Conference Papers

1. **K. Fukami**, K. Taira, “Extreme aerodynamics of vortex impingement: Machine-learning-based compression and situational awareness," in 13th International Symposium on Turbulence and Shear Flow Phenomena (TSFP13), Montreal, Canada, June 2024.

2. **K. Fukami**, K. Taira, “Learning the nonlinear manifold of extreme aerodynamics," in the 36th Conference on Neural Information Processing Systems (NeurIPS), Dec 2022.

3. **K. Fukami**, B. An, M. Nohmi, M. Obuchi, K. Taira, “Machine-learning-based turbulent state estimation from pressure sensors in a pump sump," in the 86th conference of turbomachinery society of Japan, 8608, May 2022.

4. **K. Fukami**, R. Maulik, N. Ramachandra, K. Fukagata, K. Taira, “Probabilistic neural network-based reduced-order surrogate for fluid flows," in the 34th Conference on Neural Information Processing Systems (NeurIPS), Dec 2020

CHAPTER 1

Introduction

Unsteady fluid flows are ubiquitous. Complex vortical structures emerge in various circumstances associated with automobile, airplane, and industrial fluid-based machines. Since the presence of vortical structures greatly contributes to the performance of fluid-based systems, unsteady fluid flows have been examined through theoretical, experimental, and numerical approaches (Gol69; MM98; WEA13).

Along with the recent developments in computational resources and digital tools such as processors, memory, data transfer, and hard drives, we are now in the age of fluid-flow big data. A large collection of computationally/experimentally measuring fluid flow data is becoming available. In fact, there exist some open-source databases that not only include time-averaged statistics but also cover unsteady, highly resolved flow snapshots, which can accelerate research activities in the community (LPW08; WM08; TDB23).

At the same time, this increase in data availability may become a cause of headaches in analyzing fluid flows. While being able to increase grid resolution as well as Reynolds number, the degree of freedom would be continuously large as the number of grid points to sufficiently resolve vortical flows scales on the order of $Re^{9/4}$ (KT16; KL24). Once we start to sweep in a parameter space composed of an infinite number of variables such as Reynolds number, flow configurations, shape of bodies, and actuator types, the data size quickly grows. Even if we can save them, monitoring all the time series of fluid flow data and analyzing them is impractical. In other words, we are now at a turning point to efficiently analyze such fluid flow big data.

To systematically tackle a range of challenging problems in fluid dynamics, the aforementioned

circumstance calls for data-driven approaches including machine learning. Machine learning, or recently referred to as deep learning (LBH15), has evolved in computer science, exhibiting the potential to extract features from a large pool of data sets (JM15). With such capabilities, data-driven techniques have been widely examined to extract underlying physics involved in the fluid flow big data to promote unsteady flow analyses (DIX19).

Applicabilities of machine-learning techniques to turbulence modeling have been of interest in the community (DIX19; VYA23). For large-eddy simulations (LES), Gamahara and Hattori (GH17) proposed a multi-layer perceptron-based subgrid-scale model of turbulent channel flows. Following their study, machine-learning-based LES modeling has been extended to a range of tasks not only in fluid mechanics (MS17; MSJ19a; MSR19; YZW19; ZHY21; MSF21; XWY23) but also in combustion problems (SNS21; PNS21; SHP22). While a fully-connected model is often used for LES modeling due to the advantage that local stencils on a grid can be reasonably handled (LB23), convolutional neural network (CNN)-based models have also been examined to accommodate spatial invariants of vortical flows (PSR20; LYH22; PSR23a; GSC23; MJW23; TH23).

As well as the efforts for LES modeling, machine-learning-based closure modeling for Reynolds-Averaged Navier–Stokes (RANS) simulations have been well investigated. The seminal study of machine-learning-based RANS modeling was performed by Ling et al. (LKT16) who developed the tensor-basis neural network (TBNN) guaranteeing the Galilean invariance. While extensions of TBNN are widely examined (MLE21; BC20; PSS20; TWW23), some studies augment the existing closure modeling such as the Spalart–Allmaras model (SMD17; YZC22; BHY23). However, most of the studies above for LES and RANS are based on supervised learning, implying that the solution obtained by high-fidelity simulations such as direct numerical simulations is generally needed for training (Spa23). From this aspect, reinforcement learning has also recently been considered towards low-cost and robust modeling (NLK21; BK22; MWG23).

Focusing on the capability to seek nonlinear relationships between input and output data, the community has revisited inverse problems including sparse-sensor-based reconstruction and state estimation with machine learning (YH19; DGP22; YBF23; Buz23; LBB23). Such problem set-

tings had been tackled with linear-theory-based techniques such as Gappy POD (BDW04), linear stochastic estimation (AM88), and Kalman filters (CCB11) for canonical flows. While they have encountered difficulty in reconstructing flows from limited measurements, nonlinear machine learning can often achieve qualitative vortical flow reconstruction (LLN22; XS23; HZW24). For example, Erichson et al. (EMY20) proposed a multi-layer perceptron-based global field reconstruction from local sensors considering a two-dimensional cylinder wake, ocean temperature fields, and homogeneous isotropic turbulence. In the context of wall-bounded turbulence, Guastoni et al. (GGI21) developed a CNN-based approach to estimate far-field conditions from only the wall information by combining with proper orthogonal decomposition (POD; Lum67). These off-wall state estimation studies with machine learning can be regarded as an extension of the well-examined "footprint" study by Bewley and Protas (BP04).

In addition to the studies with numerical data sets, applications to experiments are also performed (MWM23; DHL19; OPD21; LU22; ZLH23). Cai et al. (CZX19) used CNNs for estimating velocity fields from particle images. The proposed CNN-based model can provide a much finer spatial resolution of flow fields compared to the conventional correlation method and optical flow approach, suggesting the potential to find structures that cannot be captured with traditional techniques (GN20; FK20; OLS22). A similar method for flows around bluff bodies was also proposed by Morimoto et al. (MFF21), aiming to reduce measuring noise due to halation and reflection around immersed bodies. Furthermore, multi-layer perceptron-based sparse reconstruction was also examined with experimental data of NACA0012 airfoil flows at $Re_c = 75000$ by Carter et al. (CDS21).

Successful flow reconstruction from limited measurements suggests that a collection of flow snapshots over time may be expressed with a few dynamically important modes (THB20a; BHT20; THB20b). Along with this observation, machine learning, particularly nonlinear autoencoder, has also been considered to extract nonlinear modes while compressing unsteady flow data sets (CJK19; GKS20; XD20; PBK21; MLC23; FID23). Milano and Koumoutsakos (MK02) first applied a multi-layer perceptron-based autoencoder to the burgers equation and turbulent channel flows,

reporting its superior capability to linear compressions. To visualize nonlinear modal structures extracted by nonlinear autoencoder, Murata et al. (MFF20) developed a mode-decomposing CNN autoencoder and demonstrated it with flows around a circular cylinder. They also reported that a linear autoencoder is mathematically equivalent to POD, suggesting the importance of the use of nonlinear activation functions. Some advanced autoencoder models have been proposed to achieve better compression of fluid flows while extracting modes that align based on kinetic energy (LPB22; FNF20; ELH22).

Furthermore, the use of compressed representations obtained via nonlinear machine-learning techniques has also been examined to construct surrogate models for high-fidelity simulations. Similar to the idea of POD Galerkin projection model, another machine-learning model is prepared to integrate the dynamics of low-dimensional representations. As a temporal integrator model, a variety of machine-learning techniques has been investigated for unsteady flows including multi-layer perceptron (LW19; DG23), long short-term memory (MLB21; ASR21), echo state network (RDM23; CPL23), sparse identification of nonlinear dynamics (FMZ21; CGF23), transformer (YZY23; YW23; WSV24), Gaussian process regression (MBR21b), and neural ODE (SPM22; LG23).

Related to the neural network-based surrogate modeling for numerical simulations mentioned above, physics-informed neural networks (PINN) have also gained attention in the community (RPK19; RYK20; CMW22). PINN generally takes coordinates and time information as inputs while outputting flow variables at the corresponding input point. Contrary to regular machine-learning models, the governing equations are considered inside of the cost function in optimizing network parameters. It has been widely reported that this incorporation of physics from the equations can enhance the reliability of machine-learning-based prediction while ensuring robustness against noisy input measurements (JCL21; CWF21; SR23; SGD24). While the PINN was proposed in the fluid mechanics field, the use of PINN can be currently seen in a wide range of science and engineering (CDG22).

While flow variables and related coefficients are often used for the cost functions of the afore-

mentioned applications, one can also use a control objective as a cost function to design control strategies with machine learning. Currently, machine-learning-based control can be mainly categorized into two groups: namely, 1. combining with the existing control strategies and 2. deriving a new control law with reinforcement learning. An example in the former group is Lee et al. (LKB97) who used a multi-layer perceptron to learn the actuation pattern of opposition control (CMK94) in turbulent channel flows for drag reduction. Park and Choi (PC20) has recently combined a CNN-based off-wall velocity estimator and opposition control of turbulent channel flows. They reported that taking a low-pass filter can improve the drag reduction ability so that the effect of reconstruction error can be mitigated.

For the reinforcement learning-based control, Rabault et al. (RKJ19) first developed a multi-layer perceptron-based agent to reduce drag of flows around a cylinder. Following this seminal study, the applicability for bluff-body wake stabilization has been extensively examined in recent years (PBD21; GVL21; LZ22; PSR23b; NG23; ZFZ23; WFJ23). For wall-bounded turbulence, Sonoda et al. (SLI23) has recently applied reinforcement learning to blowing/suction control of turbulent channel flows. They reported that the linear model learned a similar actuation pattern as the opposition control (CMK94) while the nonlinear model provides more complex patterns, leading to a better drag reduction performance. Similarly, Lee et al. (LKL23) has also performed a reinforcement learning-based control for turbulent channel flows and compared it to a traditional suboptimal control (LKC98). These efforts exhibit the potential of machine-learning techniques to gain insights into unsteady flows, beyond what have been possible by relying on only human insights.

As reviewed above, nonlinear machine learning has been recognized as an attractive tool for a range of studies in fluid mechanics. From the aerodynamics viewpoint, of particular interest is their usage for extremely unsteady situations in which the spatiotemporal scales of the baseflow unsteadiness and disturbances reach almost the same level in magnitude. Such flight conditions would occur when modern small-scale aircraft such as drones operate in severe weather (JCS22). With the increased occurrence of extreme weather due to global warming, they are now asked to

fly during adverse situations (FW15; GW22). However, it is currently challenging to achieve stable flight since small air vehicles would encounter extremely strong gusts.

For steady or quasi-steady aerodynamic scenarios, there are a range of studies to analyze aerodynamics with respect to small perturbations and time-averaging flows (And91; Lei06). To extract dominant modes from a collection of fluid-flow data, linear modal analysis techniques such as POD (Lum67) and dynamic mode decomposition (DMD; Sch10; Sch11; Sch22) can be considered. These techniques provide physical insights as either modes or temporal coefficients, which has been demonstrated with a range of flow configurations (IR08; DHW16; RD17; RW17; LAN18a). However, both techniques are generally not robust for time-varying mean flows or transient dynamics due to their linear assumptions in the formulation. Although there are few methods to handle nonlinear, transient nature of flows with linear theories for particular flows, e.g., introducing a shift mode of flows around a circular cylinder (NAM03), it is challenging to develop a robust technique that can accommodate time-varying baseline dynamics.

Focusing on the linearized operator, stability analysis has also been leveraged over the past century to find characteristics of the flow dynamics about the given perturbation (SH01; The11). Moreover, Resolvent analysis has also gained attention to identify the input-output relationship of given flow dynamics (MS10). These operator-based techniques can reveal the underlying physical mechanism (SL07; SSM19; NMM21; RJF22; BHZ22) while being able to provide clues for controlling aerodynamic flows (LSM14; YT19; KNL19; JIS20; SYS22; MJC22; LTT23). However, their formulations generally assume that the given dynamics can be linearized with respect to time-averaging (mean) flow and small-amplitude perturbations. Since the baseflow under extreme aerodynamic conditions would always be time-varying while the magnitude of disturbance is almost a similar level to the unsteadiness of regular baseline flight operations, naïve applications of these linear theory-based techniques may not appropriate to extract key features of extreme aerodynamic flows.

While there exist a large number of parameters to determine the characteristics of gusts, the gust ratio $G \equiv u_g/u_\infty$, where u_g is the characteristic gust velocity and u_∞ is the cruise velocity,

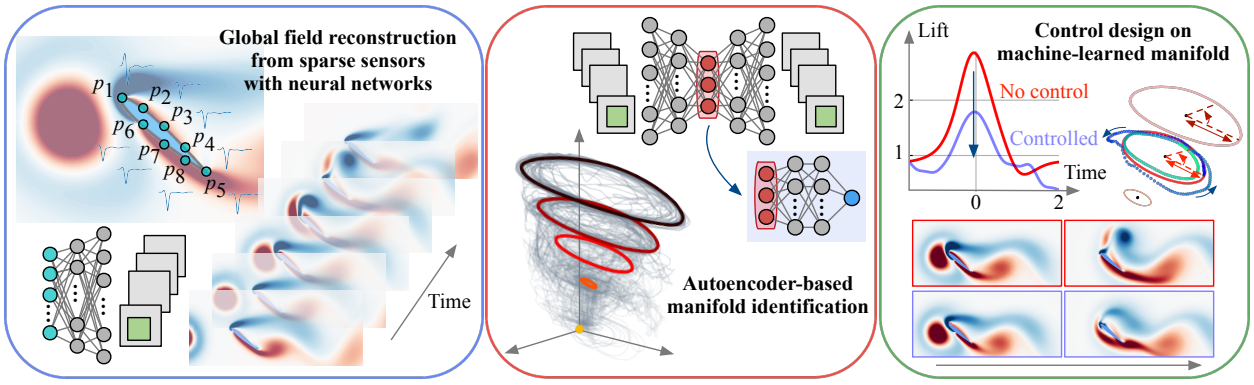

Figure 1.1: Overview of the current study.

is especially critical. Although operating aircraft under $G > 1$ is generally avoided, small air vehicles would experience it under extremely gusty situations in urban canyons, mountainous environments, and severe atmospheric turbulence. Furthermore, under the extreme aerodynamic condition of $G > 1$, a wing experiences massive flow separations due to complex interactions with extremely violent gusts. We also note that conventional vortex-gust airfoil interaction studies including a PIV-based flow visualization (QWG23), sparse reconstruction (ZFA23; CKH24), and gust mitigation control (HBP22; SGL23) are limited to $G \leq 1$. Since it is easily anticipated that traditional linear-theory-based techniques cannot accommodate extreme level of unsteadiness associated with transient effects, it is worth examining nonlinear data-driven approaches for taming extreme aerodynamic flows.

In this thesis, we develop a basic foundation of data-driven techniques to support analyses of extreme aerodynamic flows from the aspect of global field reconstruction, reduced-order modeling, and flow control. Particularly, this thesis considers a systematic approach to control unsteady fluid flows starting from only few sensor measurements in a data-driven manner, as graphically summarized in figure 1.1.

We first aim to develop a method for reconstructing a flow field from limited measurements with super-resolution analysis. Super resolution that originally emerged in image processing can spatially reconstruct a high-resolution flow field from a low-resolution counterpart (IP91). We

perform machine-learning-based super-resolution reconstruction in fluid flows with a survey study. We also examine its applicability to an example of industrial turbulent flows, vortical flows in a pump sump. Moreover, a Voronoi-tessellation-assisted neural network, which can deal with a situation where numbers and position of sensors are in motion, is also proposed to enhance practical uses of super-resolution models for unsteady flows.

Although machine-learning-based analyses can often provide reasonable performance beyond training conditions for unsteady flows, i.e., extrapolation, it is important to correctly identify interpolatory and extrapolatory conditions in the context of turbulent flows. To this end, we develop the Buckingham Pi theorem-assisted nonlinear scaling of turbulent flows to distinguish interpolatory and extrapolatory vortical structures in machine-learning applications. This enables the quantitative characterization of seen and unseen physics by extracting scale-invariant structures of turbulent flows across training and test data.

Once we obtain a sufficient amount of fluid flow information from limited measurements, we then aim to identify a control strategy of flows in a low-order manifold space identified by nonlinear machine-learning-based compression, autoencoder. Autoencoder can low-dimensionalize given fluid flow data into a low-order subspace while retaining the essential information that are energetically or dynamically important. The resulting low-dimensional representation can provide a compact form of fluid flow behavior in the low-dimensional space called latent space.

Our manifold identification is achieved using an observable-augmented autoencoder, providing a physically-explainable form of latent expression. This is particularly helpful in deriving control strategies by combining them with pre-existing mathematical tools. With an example of extreme vortex-airfoil interactions, this thesis performs phase-amplitude reduction on an autoencoder-based low-dimensional manifold to acquire efficient control strategies that can quickly modify unsteady flows to be a desired state.

This thesis is organized as follows: we survey machine-learning-based super-resolution reconstruction of fluid flows in chapter 2. Supervised machine-learning-based sparse reconstruction of vortical structures in a pump sump from pressure sensors is performed in chapter 3. The Voronoi

tessellation-assisted sparse reconstruction is expressed in chapter 4. The data-driven nonlinear scaling with Buckingham Pi variables is discussed in chapter 5. The autoencoder-based manifold identification and phase-amplitude reduction-assisted fast flow control with an example of extreme aerodynamic flows are respectively provided in chapters 6 and 7. Conclusions are remarked in chapter 8.

CHAPTER 2

Machine-learing-based super-resolution analysis for fluid flows

This section surveys machine-learning-based super-resolution reconstruction for vortical flows (FFT23). While super resolution can be regarded as an image-based data recovery technique, it is also a general framework for a broad range of applications in fluid mechanics. Hereafter, let us discuss recent studies, challenges, and outlooks of machine-learning-based super-resolution analysis for fluid flow applications.

2.1 Motivation

Super resolution reconstructs a spatially high-resolution field data $\boldsymbol{q}_{\mathrm{HR}}$ from its low-resolution counterpart $\boldsymbol{q}_{\mathrm{LR}}$ (IP91; Sal16; Ban09). This problem set has been traditionally tackled in computer visions with various techniques including interpolation (Key81; VSV06; JSK08; LK81), example-based internal learning (MI13; GBI09; ZMI13; SFI11), high-frequency transfer (FF11; YLC13; BK02; PPK03), neighbor embedding (RS00; BRG12; CYX04; FJP02; FPC00), and sparse coding (LBR06; YWH08; LYY12; YWH10; ZGT12). Although these implementations are effortless, it is generally challenging to reconstruct high-wavenumber contexts. To address this difficulty, machine learning has been used for accurate super-resolution reconstruction of images (DLH14; DLT16; YZT19). Machine learning can find a nonlinear relationship between input and output data even under ill-posed conditions. This approach can be applied to a pair of low- and high-resolution images, providing a finer level of images from extremely coarse images (DLH15).

Machine-learning-based techniques in general (BNK20; BHT20; BEF19) have been considered

for a range of applications in fluid mechanics including turbulence modeling (DIX19; MSJ19b; LKT16; NLK21; BK22), reduced-order modeling (LY19; CRL22; SM18; FMZ21; SGA19), data reconstruction (SSS20; MBK18; FFT20; KKL23), and flow control (RKJ19; BPB20; ZFZ20; PBD21; PC20; GVL21). Super-resolution reconstruction with machine learning is no exception. The lower barrier to access open source codes in image science and implement models also enables fluid mechanicians to apply methods for fluid flow data by replacing RGB components (red, green, and blue) with velocity components $\{u, v, w\}$.

While super resolution can be regarded as an image-based data recovery technique, it is also a general framework for a broad range of applications in fluid mechanics. For instance, a low-resolution fluid flow image can be interpreted as a set of sparse sensor measurements. In this aspect, the inverse problem of global field reconstruction from local measurements is an extension of super-resolution analysis (FMR21; GVD22; SW20). If we consider low-resolution fluid flow data as noisy experimental measurements, super-resolution analysis can also be extended to denoising problem (GSW21; FPB20; VS09). Furthermore, large-eddy simulation (LES) can incorporate super-resolution reconstruction to reveal finer structures inside a low-resolution grid cell (PD23; BGL21).

This paper surveys the current status and the challenges of machine-learning-based super-resolution analysis for vortical flows. We first cover several machine-learning models and their applications to super resolution of fluid flows. We then offer case studies using a supervised learning-based super resolution for an example of two-dimensional decaying isotropic turbulence. We consider embedding physics into the model design to successfully reconstruct a high-resolution vortical flow from low-resolution data. We further discuss the challenges and outlooks of machine-learning-based super resolution in fluid flow applications. The present paper is organized as follows. We introduce machine-learning approaches of super-resolution reconstruction for vortical flows in section 2.2. Applications of these machine-learning techniques are discussed in section 2.3. We perform case studies in section 2.4. Extensions of super-resolution analysis for fluid dynamics are discussed in section 2.5. Concluding remarks with outlooks are provided in section 2.6.

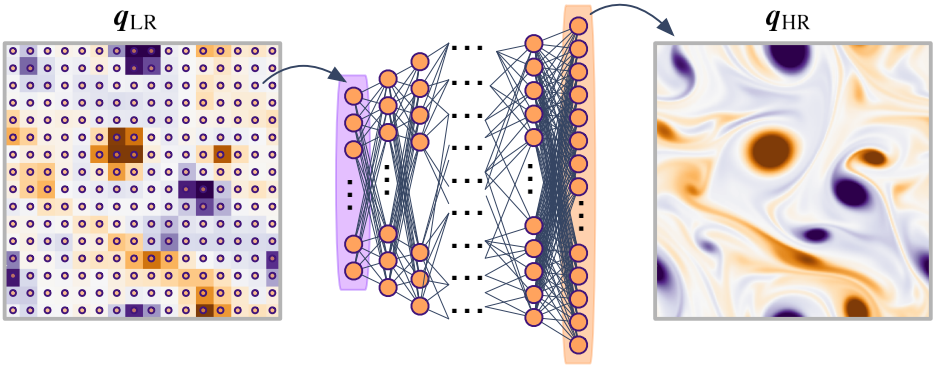

Figure 2.1: Fully-connected model-based super resolution.

2.2 Approaches

A variety of machine-learning models have been proposed for the super-resolution reconstruction of vortical flows. Machine-learning-based approaches can find a nonlinear relationship between the low-resolution input and the corresponding high-resolution output from a large collection of data through training. In super-resolution analysis, the dimension of the input (low-resolution data) $\boldsymbol{q}_{\mathrm{LR}} \in \mathbb{R}^m$ is smaller than that of the high-resolution output $\boldsymbol{q}_{\mathrm{HR}} \in \mathbb{R}^n$ with $m \ll n$,

$$\boldsymbol{q}_{\mathrm{HR}} = F(\boldsymbol{q}_{\mathrm{LR}}), \tag{2.1}$$

where F is the super-resolution model. Depending on the flow of interest and the size of data, the machine-learning model should be carefully chosen. In section 2.2.1, we introduce three types of machine-learning models that are widely used. We also discuss the use of physics-based loss functions in section 2.2.2.

2.2.1 Machine-learning models

2.2.1.1 Fully-connected network (multi-layer perceptron)

The fully-connected network, also called the multi-layer perceptron (RHW86), is the most basic neural network model. Nodes between layers are fully connected with each other, as illustrated in figure 2.1. The minimum unit of a fully-connected network is called perceptron. For each

perceptron, the linear combination of the inputs from layer $(l-1)$, $c_j^{(l-1)}$, is connected with weights $\boldsymbol{w}$ yielding the output at layer (l), $c_i^{(l)}$,

$$c_i^{(l)} = \varphi(\sum_j w_{ij}^{(l)} c_j^{(l-1)} + b_i^{(l)}), \tag{2.2}$$

where φ is the activation function and b is the bias added at each layer. We can choose a nonlinear function for φ, enabling the network to capture the nonlinear relationship between the input and the output.

A fully-connected model can be used for supervised machine learning-based super resolution. A training process for supervised machine-learning models is cast as an optimization problem to determine the weights $\boldsymbol{w}$ inside the model F. The weights $\boldsymbol{w}$ are optimized by minimizing the loss function $\mathcal{E}$ through backpropagation (KB14). This optimization procedure is described as

$$\boldsymbol{w} = \text{argmin}_{\boldsymbol{w}}\ \mathcal{E}(\boldsymbol{w}). \tag{2.3}$$

Since super-resolution reconstruction aims to obtain a high-resolution image $\boldsymbol{q}_{\text{HR}}$ from the corresponding low-resolution data $\boldsymbol{q}_{\text{LR}}$, the loss function (error) can be formulated as

$$\mathcal{E} = ||\boldsymbol{q}_{\text{HR}} - F(\boldsymbol{q}_{\text{LR}})||_P, \tag{2.4}$$

where P indicates the norm. While the L_2 norm is widely used, we can instead consider other norms such as L_1 norm and logarithmic norm depending on the data characteristics. The L_1 norm can be used for model construction that is not as sensitive for outliers in the data. The logarithmic norm is suitable for cases where underestimation should be avoided.

As mentioned above, the difference of data dimension between the input and the output in the super-resolution analysis is substantial. Hence, models generally comprise the decoder-type structure (EMY20; WZK22), meaning that the number of nodes gradually increases towards the output layer. This is especially the case for high-dimensional inverse problems such as super-resolution reconstruction of fluid flows. This leads to the number of nodes and their connections to drastically increase, leading to the prohibitively expensive computational cost and the failure of

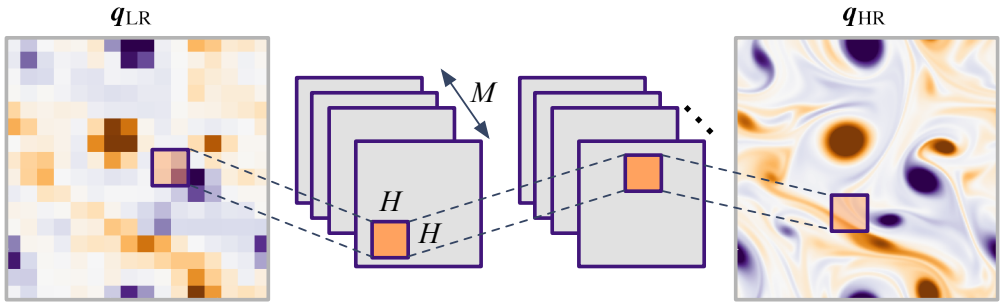

Figure 2.2: Convolutional neural network-based super resolution.

non-convex optimization known as the curse of dimensionality (Dom12). Users should be mindful of computational time and memory requirements for fully-connected models.

2.2.1.2 Convolutional neural network

To address the issue of the computational burden associated with the fully-connected models, convolutional neural networks (CNNs) (LBB98) have been widely utilized in super-resolution analysis of fluid flows. CNNs incorporate a function called filter sharing, enabling the processing of large vortical flow data without encountering the curse of dimensionality (MFZ21).

A CNN is generally comprised of the convolutional layer, pooling layer, and upsampling layer. The convolutional layer depicted in figure 2.2 captures the nonlinear relationship between input and output data by extracting spatial features of supplied data through filtering operations. This operation is expressed as

$$q_{ijn}^{(l)} = \varphi\left(\sum_{m=1}^{M}\sum_{p=0}^{H-1}\sum_{q=0}^{H-1} h_{pqmn}^{(l)} q_{i+p-G,j+q-G,m}^{(l-1)} + b_n^{(l)}\right), \tag{2.5}$$

where $G = \lfloor H/2 \rfloor$, H is the width and height of the filter, M is the number of input channel, n is the number of output channel, b is the bias, and φ is the activation function. As in the fully-connected models, a nonlinear function can be chosen for φ to account for nonlinearlities in the machine-learning model.

In addition to the convolutional layer, a pooling layer also plays an important role in CNN-based

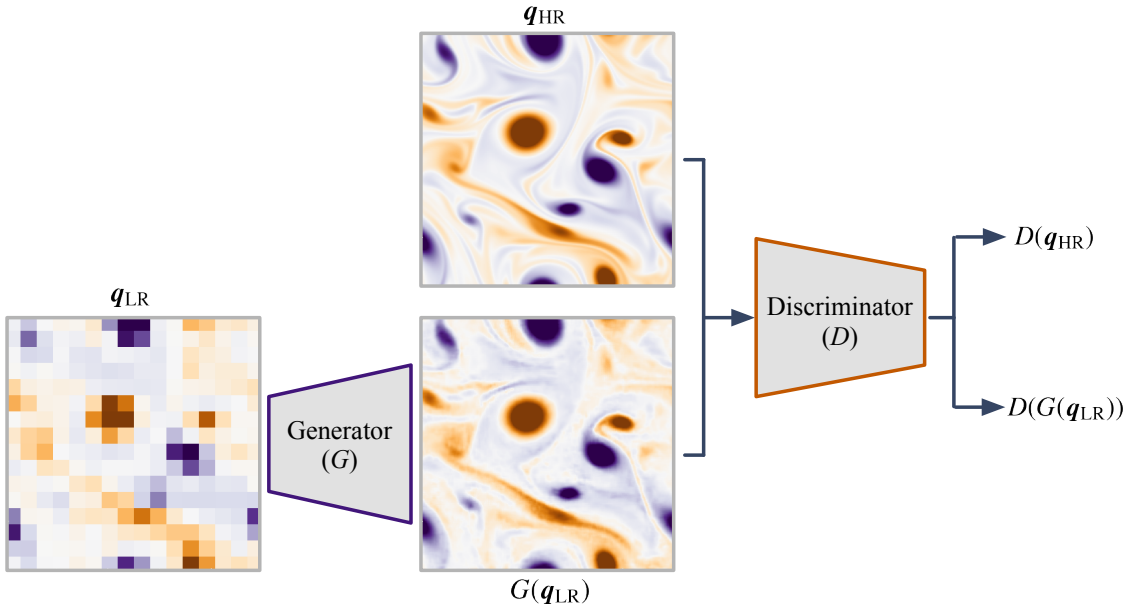

Figure 2.3: Generative adversarial network-based super resolution.

analysis. The pooling layer downscales the data, reducing data dimension. For regression tasks, it is useful for reducing spatial sensitivity, producing a robust CNN model against noisy inputs (NF22). It is also possible to expand the data dimension through the upsampling layer. Upsampling copies the value onto an arbitrary region to expand the dimension. This function is especially useful to align the data dimension inside the network.

For super resolution in which the dimension of the output $\mathbb{R}^n$ is larger than that of the input $\mathbb{R}^m$, there are several ways to treat the difference of the dimensions between the input and the output. For example, the upsampling can be used inside a network to expand the dimension (WGS22). One can also implement a resize or interpolation function for the input data to align the size with that of the output (DLH15; FFT19b; RIM16). This can avoid the use of pooling or upsampling operations, reducing the complexity of the model.

2.2.1.3 Generative adversarial network

In addition to supervised fully-connected networks and convolutional networks, unsupervised learning with generative adversarial network (GAN) (GPM20) has also been proposed for super-resolution analysis of fluid flows (XFC18; BGK19; KKW21; GDI21; MTK23). GAN is attractive for cases in which it is difficult to prepare paired input and output data. For example, the application of super resolution with LES can correspond to this scenario. A model trained with a pair of high-fidelity DNS and subsampled low-resolution data may not directly support super-resolution reconstruction for LES data. Super resolution of PIV measurements with limited spatio-temporal resolution (without corresponding high-resolution solution images) also needs to be carefully considered.

GAN is composed of two networks, namely, a generator (G) and a discriminator (D). A generator produces a fake image which is similar to the solution from random noise $\boldsymbol{n}$. In contrast, a discriminator judges the generated (fake) image as whether it is likely to be a realistic image by returning a probability between 0 (fake) and 1 (real). A generator usually possesses a decoder-type structure to expand the data dimension from noise to images, while a discriminator is composed of an encoder-type network towards reducing the data size from images to the probability. Throughout the training process, the weights inside the generator are being updated to deceive the discriminator toward the direction of minimizing the probability by generating images increasingly similar to the real data. Fake images produced by the generator eventually become high-quality images that cannot be distinguished from the real image.

These processes can be mathematically expressed with regard to the cost function $V(D, G)$,

$$\min_{G}\max_{D} V(D,G) = \mathbb{E}_{\boldsymbol{d}\sim p_{\text{data}}(\boldsymbol{d})}[\log D(\boldsymbol{d})] + \mathbb{E}_{\boldsymbol{n}\sim p_{\boldsymbol{n}}(\boldsymbol{n})}[\log(1 - D(G(\boldsymbol{n})))], \tag{2.6}$$

where $\boldsymbol{d}$ is a real data set and p_{data} is the probability distribution of the real data. The parameters in the generator G are trained towards the direction in which $D(G(\boldsymbol{n}))$ becomes 1. On the other hand, the weights in the discriminator D are updated so that $D(\boldsymbol{d})$ returns a value close to 1. Since the discriminator becomes wiser through training, $D(G(\boldsymbol{n}))$ provides a value close to 0.

Summarizing, the parameter inside the generator G is optimized by minimizing the loss function while that for the discriminator D is adjusted by maximizing the loss function, referred to as competitive learning (RZ85). Once the training ends, the trained generator can produce an output with indistinguishable quality compared to the real data. For super-resolution problems, we can use low-resolution data as the input for the generator G instead of random noise $\boldsymbol{n}$, as illustrated in figure 2.3. A generator in super-resolution reconstruction provides a statistically plausible high-resolution output by learning the relationship between the input low-resolution data set and the high-resolution data set, which need not be paired.

2.2.2 Choice of loss function

Here, let us discuss the choice of loss (cost) function for machine-learning-based super-resolution analysis. In standard formulation, we can have the cost function defined by equations 2.4 and 2.6. However, super-resolved flow fields with direct applications of machine-learning models do not satisfy physical conditions, such as the conservation laws. To address such an issue, loss functions that embed physics laws can be utilized (LLF98; RPK19). Together with the original data-based cost $\mathcal{E}_d$ from equation 2.4 or 2.6, the loss function $\mathcal{E}$ incorporating a physics-inspired loss function $\mathcal{E}_p$ for super-resolution analysis can take the form of

$$\mathcal{E} = \mathcal{E}_d + \beta \mathcal{E}_p, \tag{2.7}$$

where β provides a scale between $\mathcal{E}_d$ and $\mathcal{E}_p$.

There are several approaches to introduce the physics-based loss term for fluid flows. For instance, we can directly substitute a reconstructed high-resolution field $\boldsymbol{q}_{\mathrm{HR}}$ into the governing equation (RPK19) if we have all data for the state variables to have,

$$\mathcal{E}_p = ||\mathcal{N}(\boldsymbol{x}, \boldsymbol{q}_{\mathrm{HR}}(\boldsymbol{x}, t))||_P, \tag{2.8}$$

where $\mathcal{N}$ is an operator from governing equations. Minimizing a loss function incorporating only

certain terms of the Navier–Stokes equation (LY19) can also be considered,

$$\mathcal{E}_p^j = ||\mathcal{N}_j(\boldsymbol{q}_{\mathrm{Ref}}) - \mathcal{N}_j(\boldsymbol{q}_{\mathrm{HR}})||_P, \quad \mathcal{N} = \sum_j \mathcal{N}_j, \tag{2.9}$$

where $\mathcal{N}_j$ is a term in the governing equation and $\boldsymbol{q}_{\mathrm{Ref}}$ is a reference data. It is known that these physics-based loss functions help in reconstructing flows with a small amount of data (GSW21). What these terms in the loss function do is to better constrain the solution space (KKL21; CMW22). This is a similar concept to semisupervised learning which combines a small amount of labeled data with a large amount of unlabeled data (ZG09). In the present paper, we demonstrate the effectiveness of training with small data set for super-resolution reconstruction of turbulent vortices in section 2.4. We should however note that the so-called physics-inspired analysis can suffer from large numerical error if $\boldsymbol{q}_{\mathrm{HR}}$ contains error or noise. This approach should be used with caution as it assumes that $\boldsymbol{q}_{\mathrm{HR}}$ can be used to evaluate certain terms.

2.3 Applications

In this section, we survey recent super-resolution applications for fluid flows through supervised (section 2.3.1) and semisupervised-/unsupervised learning (section 2.3.2).

2.3.1 Supervised learning

In machine-learning-based super-resolution reconstruction of fluid flows, supervised techniques are often used. Supervised learning requires a pair of input and output flow field data as training data. For super-resolution analysis, a high-resolution reference flow field and the corresponding low-resolution data need to be available for training models. To avoid the curse of dimensionality, CNN models are often used for image-based super resolution of fluid flows rather than fully-connected models.

Fukami et al. (FFT19b; FFT19a; FFT21) proposed a CNN-based super-resolution reconstruction for fluid flows in a supervised manner. The CNN-based model was applied to examples of

a two-dimensional cylinder wake, two-dimensional isotropic turbulence, and three-dimensional turbulent channel flow. To capture multi-scale physics in turbulent vortical flows, they also proposed the hybrid downsampled skip-connection/multi-scale (DSC/MS) model based on the CNN. The model is composed of the up-/downsampling operations, the skip connection (HZR16), and CNNs with various sizes of filters. While up-/downsampling operations support robustness against rotation and translation of vortical structures, the skip connection provides stability of the learning process (HZR16). Moreover, the multi-scale CNN aims to capture a variety of length scales in turbulent flows. Especially for the examples of turbulence, it was shown that the DSC/MS model is effective in accurately preserving the energy spectrum.

Following this study, supervised CNN-based super-resolution analysis has been actively studied for a range of flows. Obiols-Sales et al. (OVM21) proposed a CNN-based super-resolution model called SURFNet and tested its performance for wakes around various NACA-type airfoils, ellipses, and cylinders. SURFNet includes a transfer learning-based augmentation (PY09). The model is first trained using only low-resolution flow data, and then the pre-trained weights are transferred in training with high-resolution data sets. Transfer learning over multiple levels of spatial-resolution flow field can improve the accuracy of super-resolution reconstruction (GGI21), which is also related to multi-fidelity learning (LPB22). U-Net-based model (illustrated in figure 2.4) can also reduce the training cost for super-resolution reconstruction of turbulent flows since the size of fluid flow data is reduced through an autoencoder-type model structures (PF20).

Incorporating physical insights and domain knowledge into model construction further supports or enhances supervised-learning-based super-resolution reconstruction in vortical flows. For instance, accounting for spatial length scales of the flow structures in the models improves reconstruction (FFT19b). Kong et al. (KCL20) developed a multiple path super-resolution CNN with several connections inside the model to capture variations of spatial temperature distribution in a supersonic combustor. They reported that the proposed multiple-path CNN provides enhanced reconstruction of temperature fields compared to a regular CNN. Incorporating the time history of flow fields is also useful for super-resolving vortical flows in a supervised manner. Liu et

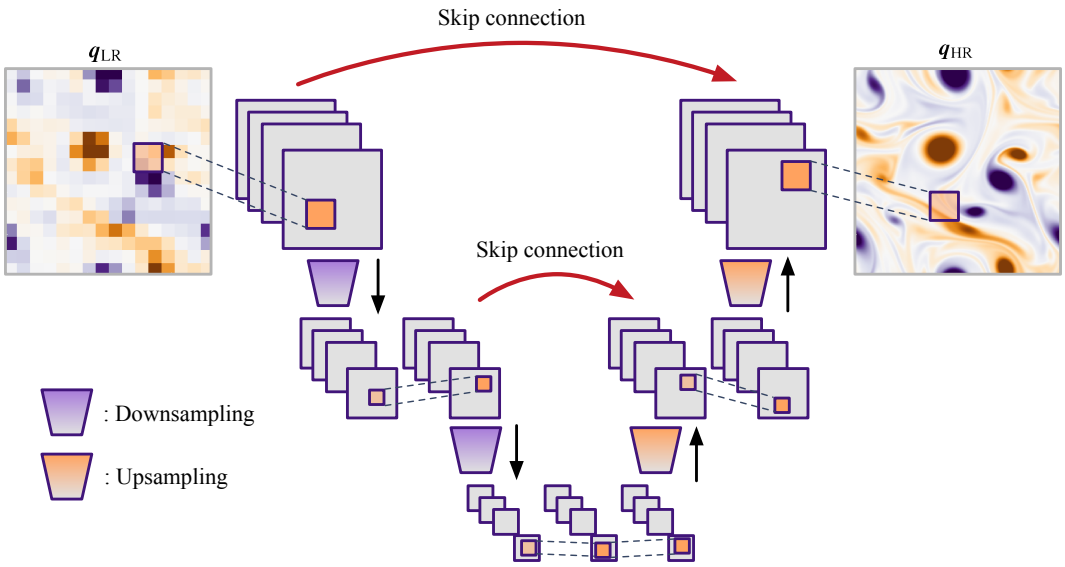

Figure 2.4: U-Net-based model for super-resolution reconstruction of vortical flows.

al. (LTH20) compared two types of supervised CNN-based models for super-resolution analysis: namely the static CNN (SCNN) and the multiple temporal paths CNN (MTPC). While the SCNN model uses instantaneous flow snapshots as the input, the MTPC model considers a time series of velocity fields as the input to read spatial and temporal information simultaneously. With examples of forced isotropic turbulence and turbulent channel flow, they found that the MTPC model can improve the reconstruction of turbulence statistics such as kinetic energy spectra and the second and third invariants of the velocity gradient tensor.

Once supervised models are trained, machine-learning models can be used for data compression since we only need to save only the input data to recover high-resolution flow fields. Matsuo et al. (MFN24) proposed an adaptive super-resolution analysis. They focused on how a low-resolution field is prepared in training a supervised learning-based model. While max- and averaging pooling operations are generally used for preparing low-resolution data sets, they considered the spatial standard deviation in arbitrary subdomains in a flow field to determine the local degree of down-sampling. This can account for the importance of flow structures in generating low-resolution data sets. They reported that supervised CNN models can reconstruct a high-resolution field of three-

dimensional square cylinder wake from adaptive low-resolution data, achieving approximately 0.05% data compression against the original data.

Compressing fluid flow data in the time direction can also be considered. Fukami et al. (FFT21) used the DSC/MS model to reconstruct high-resolution turbulent flows from coarse flow data in space and time inspired by a concept of super-resolution analysis and inbetweening (LRT19). In their formulation, two spatial coarse flow fields at $t = n\Delta t$ and $t = (n + k)\Delta t$ are taken as the input of the first machine-learning model. Once the spatial-reconstruction model provides two super-resolved high-resolution flow fields, these outputs are then fed into the second model to perform inbetweening that provides high-resolution snapshots between the beginning and the end frames. By combining these two models, spatio-temporal high-resolution vortical flows can be obtained from only two coarse snapshot data. It should be note that linear interpolation in time cannot capture advective physics. They demonstrated the model capability with turbulent channel flows and reported that the flow field can be quantitatively reconstructed, achieving 0.04% data compression. Arora and Shrivastava (AS22) have recently combined this super-resolution/inbetweening idea with physics-informed neural network (RPK19) to improve the reconstruction accuracy and demonstrated it with an example of a mixed-variable elastodynamics system.

Furthermore, supervised super-resolution reconstruction can be used to examine how machine learning extracts the relationship between small and large-scale vortical structures. Kim and Lee (KL20) considered a CNN-based estimation of the high-resolution heat flux field in a turbulent channel flow from poorly-resolved wall-shear stresses and pressure. They revealed that the CNN model focuses on the relationship between vortical structures and pressure distribution in channel turbulence to estimate the local heat flux from the wall-shear stress. Morimoto et al. (MFZ22) has recently examined the effect of inter- and extrapolation with machine-learning-based super-resolution reconstruction with respect to flow parameters. They considered two-staggered cylinder wakes whose flow dynamics are characterized based on the diameters and the distance between two cylinders. They found that the supervised CNN-based model can quantitatively reconstruct a vortical flow even for untrained parameter cases by preparing flow field data based on the

information of lift coefficient spectrum.

Supervised super-resolution techniques have also been applied to larger-scale meteorological flows (OSM19; YOH22). Onishi et al. (OSM19) proposed a CNN-based model for super-resolution analysis of temperature fields in urban environment. The proposed model provides a high-resolution temperature field at reduced computational time than the corresponding high-fidelity simulation, suggesting the potential use of machine-learning models as a surrogate for large-scale numerical simulations. To improve the model performance, Yasuda et al. (YOH22) extended their model by incorporating skip connection (HZR16) and channel attention (HSS18). While skip connection (HZR16) helps stabilize the learning process of deep CNNs, channel attention (HSS18) can discover the crucial and irrelevant spatial regions of fluid flow regressions. The model trained with temperature fields in one city (Tokyo) provides quantitative reconstruction for test temperature data for another city with similar climate (Osaka). They also observed that including building height information as a part of the input of the machine-learning model is important for successful temperature reconstruction.

In addition to the aforementioned studies with numerical data, applications to experiments have also been considered (DL23). For such cases, the effects of noise in the input data must be carefully considered. Deng et al. (DHL19) developed a machine-learning model to super-resolve PIV measurements. For training the model based on CNN, a pair of high-resolution experimental velocity data collected by PIV with cross-correlation method and downsampled low-resolution data is used. The model was tested for turbulent flows around a single cylinder and two cylinders. For more complex turbulent flows, Wang et al. (WYL20) proposed a super-resolution neural network for two-dimensional PIV (PIV2DSR) based on CNNs. Once they trained the model with velocity fields of turbulent channel flow at $Re_\tau = 1000$ obtained by direct numerical simulation (DNS), the model is assessed with not only numerical channel flow field data at a much higher Reynolds number of 5200 but also real experimental PIV data for a turbulent boundary layer at $Re_\tau = 2200$.

For the preparation of training data in these experimental studies, cross-correlation methods (Adr05) are generally used to obtain velocity fields from particle images. Instead of giving a

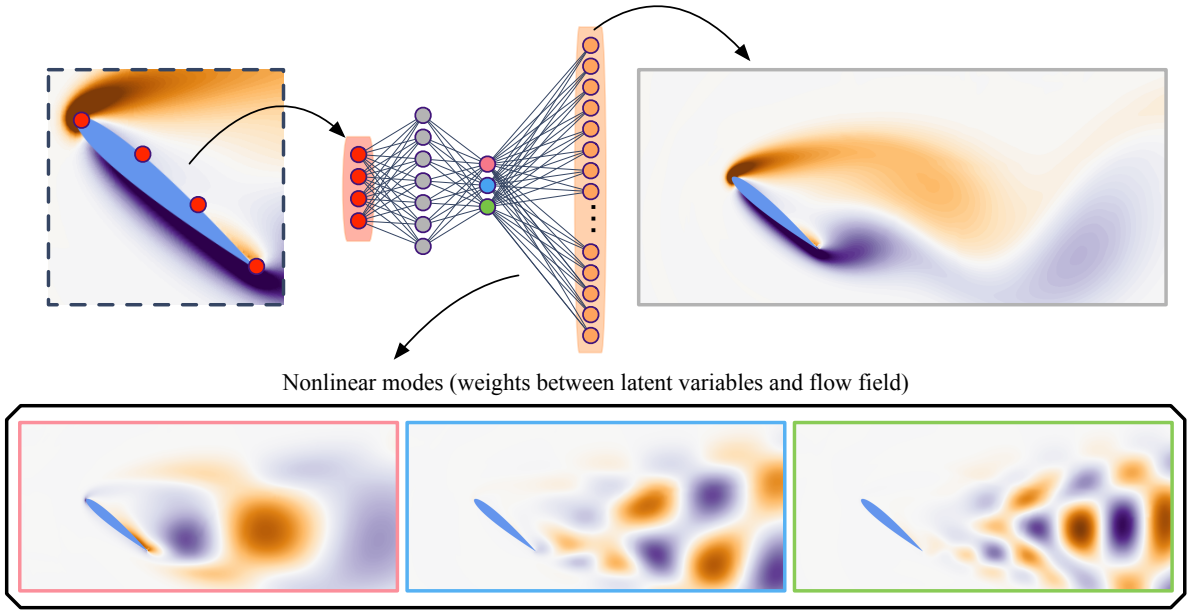

Figure 2.5: Extraction of nonlinear modes (MFF20) from shallow decoder (EMY20) in super-resolution reconstruction for an example of two-dimensional incompressible flow (vorticity field) over a NACA0012 airfoil ($Re = 100$ and $\alpha = 40$ deg).

velocity field from the correlation method, one may consider providing a particle image directly into a model to obtain a higher-resolution flow field. Cai et al. (CZX19) used FlowNetS (DFS19) to estimate velocity fields of cylinder wake, backward-facing step flow, and isotropic turbulence from synthetic particle images. They exhibited that a machine-learning model provides higher-resolution flow field data than the conventional PIV. The proposed method was also tested with experimental particle images of a turbulent boundary layer. Reconstructed flows based on machine learning may capture phenomena that cannot be observed with conventional techniques. This FlowNetS-based method has recently been commercialized as AI-PIV (MWK20). The super-resolution approach with particle images has also been applied to a wake around bluff bodies to remove the influence of reflection and halation in PIV measurements (MFF21).

Alternatively, a set of sparse sensor measurements can be considered as input to machine-learning models instead of the low-resolution flow data. For instance, Erichson et al. (EMY20) used

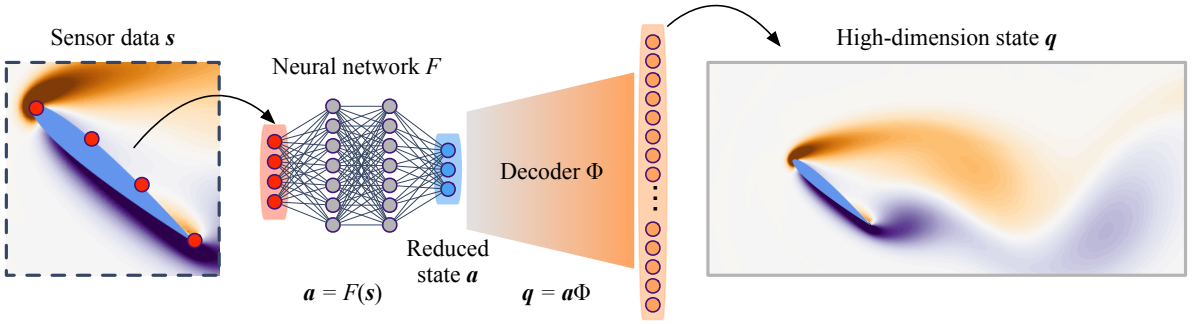

Figure 2.6: Reduced-order modeling-assisted super-resolution reconstruction (NG20; DGP22).

a fully-connected model to reconstruct a global flow field from local sensors. The model was applied to geophysical flow and forced isotropic turbulence. Their fully-connected model is a shallow decoder – the model that incorporates a dimension compression to nonlinearly extract key features from sensors, after which the whole field is recovered from these latent representations of the input sensors, as illustrated in figure 2.5. By visualizing the weight distribution between the latent space representation and the whole field, the shallow decoder provides nonlinear modes that represent the contribution of each latent variable for super-resolution reconstruction, which are analogous to those captured by nonlinear autoencoders (MFF20; FT22; FNF20; ELH22; FHN21; LG20; FT23).

As mentioned above, fully-connected network-based reconstruction is prohibitively expensive for global flow field reconstruction due to the very large number of parameters in the network (WPC20). To address this issue, there are also some efforts to estimate low-order representations such as coefficients obtained through proper orthogonal decomposition (POD) from sparse sensor measurements (CDS21; GA20; MFR20). For instance, Nair and Goza (NG20) proposed a fully-connected model-based estimator of POD coefficients and applied it to a laminar wake around a flat plate. Their fully-connected model takes vorticity sensors on the airfoil surface and then outputs POD coefficients, as illustrated in figure 2.6. They considered wakes with two different angles of attacks, and reported that the neural-network model outperforms conventional linear techniques such as Gappy POD (ES95; BDW04) and linear stochastic estimation (AM88). Similarly, Manohar et al. (MMZ22) has also recently performed a fully-connected model and POD-

based sparse reconstruction for wake interactions of two cylinders. Their model considers the time history of sensor measurements with long short-term memory (LSTM) (HS97), achieving more robustness against noisy inputs compared to a regular MLP model. These reduced-order strategies in machine-learning-based vortical flow reconstruction are summarized in Dubois et al. (DGP22). With flow examples of two- and three-dimensional cylinder wakes and a spatial mixing layer, they discussed pros and cons of a variety of techniques such as POD (Lum67; HLB12; TBD17), regular autoencoder (HS06), variational autoencoder (RMW14), linear/nonlinear fully-connected networks, support vector machine (SS04), gradient boosting (Fri01), and library-based reconstruction (BPK16a; CMB19).

From the aspect of reducing the number of parameters inside machine-learning models, a combination of a fully-connected model and CNNs has also been leveraged to overcome the limitation of fully-connected networks. Morimoto et al. (MFM22) considered a combination of multi-layer perceptron (MLP) and CNN (called MLP-CNN-based estimator) to estimate vortical flows around urban structures and temperature data (DayMET) across North America from sparse sensors. The sensor inputs are first given into the part of a fully-connected model and the model extracts the features from the input sensors. The feature vectors extracted from it are then given to the convolutional layers. Compared to solely using fully-connected layers, the computational cost can be significantly reduced while maintaining the reconstruction accuracy. A similar MLP-CNN model was also considered by Zhong et al. (ZFA22; ZFA23) for a vortex-airfoil gust interaction problem. The model estimates a two-dimensional vorticity field from pressure sensor measurements on an airfoil surface. They reported that transfer learning (PY09; LYF22) can help in reducing the required amount of training data, while recurrent neural network (long short-term memory, LSTM (HS97)) also improves the reconstruction performance of complex transient wake problems.

2.3.2 Semisupervised- and unsupervised learning

In addition to supervised-learning-based efforts, semisupervised- and unsupervised learning can be used in super-resolution analysis of fluid flows. Semisupervised learning combines a small

amount of labeled data with a large amount of unlabeled data, which can also be augmented with prior knowledge incorporated into the loss function. Gao et al. (GSW21) proposed a semisupervised CNN-based super-resolution analysis for fluid flows. Through the investigation of a two-dimensional laminar flow and a cardiovascular flow, they showed that the constraints based on the conservation laws and boundary conditions enable successful super-resolution reconstruction without high-resolution labeling. These physics-law-based augmentations inspired by physics-informed neural network (PINN) (LLF98; RPK19; RYK20) achieve accurate reconstruction while reducing the required amount of training data (YYL21; YYH22).

There are also a couple of studies on semisupervised super resolution. Bode et al. (BGL21) proposed the physics-informed enhanced super-resolution generative adversarial network (PIESRGAN) for applications to subgrid-scale modeling of LES. To incorporate a physics-based loss function, they used the following cost function $\mathcal{E}$ for training,

$$\mathcal{E} = \mathcal{E}_{\text{adv}} + \beta_{\text{reg}}\mathcal{E}_{\text{reg}} + \beta_{\text{grad}}\mathcal{E}_{\text{grad}} + \beta_{\text{cont}}\mathcal{E}_{\text{cont}}, \tag{2.10}$$

where β_{reg}, β_{grad}, and β_{cont} are weighting coefficients for the different loss term contributions. The first loss term $\mathcal{E}_{\text{adv}}$ corresponds to a regular adversarial loss used in GAN-based models, introduced in equation 2.6 (WYW18). The second term $\mathcal{E}_{\text{reg}}$ is a regular supervised loss function, which is equivalent to equation 2.4. The PIESRGAN also includes the gradient loss $\mathcal{E}_{\text{grad}}$ defined as the L_2 error norm of the gradient of state variables (BGK19). Weighting the gradient of the flow field promotes a smooth and physically-plausible reconstruction (HFM20b; HFM20a). They also considered $\mathcal{E}_{\text{cont}}$, the divergence-free error for incompressible flow. Similarly, a combination of physics-based loss and U-Net (figure 2.4) was proposed by Esmaeilzadeh et al. (EAK20) as MeshfreeFlowNet and was applied for the Rayleigh-Bénard instability problem. Due to the U-Net-based augmentation, the training for MeshfreeFlowNet takes only less than 4 minutes with 128 GPUs while achieving quantitative reconstruction. To improve the generalizability of MeshfreeFlowNet (EAK20) for a wide variety of problems, Wang et al. (WZG22) have recently proposed TransFlowNet which weakens the constraint of initial and boundary conditions compared to MeshfreeFlowNet. TransFlowNet was tested with examples of shallow water equation and Rayleigh-Bénard convection. The

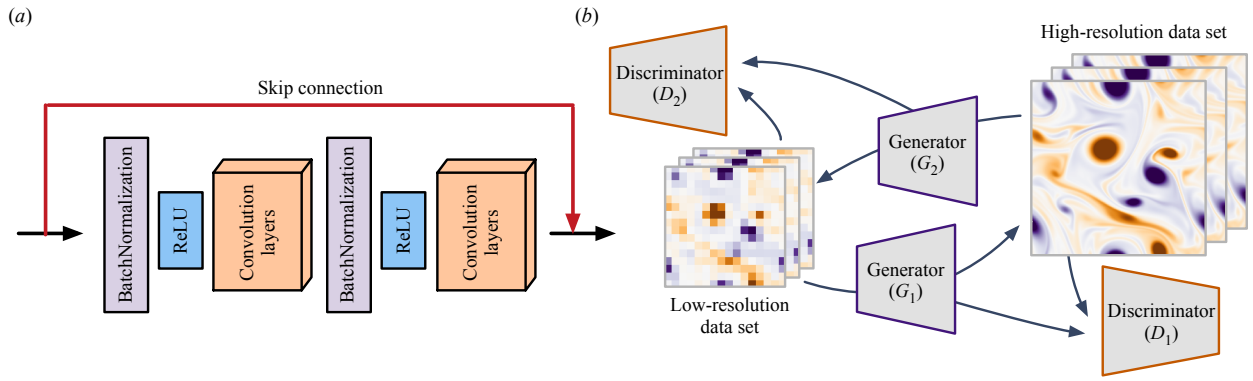

Figure 2.7: (a) ResBlock (HZR16) comprised of BatchNormalization layer, ReLU activation, and convolutional layer. (b) Cycle GAN (cGAN) (ZPI17; MTK23).

model provides better reconstruction than the original MeshfreeFlowNet, although the instability of training process is also observed due to the complexity of model.

While incorporating the aforementioned physics loss can promote a physically-plausible super-resolution solution, we should be mindful of the fact that finding an appropriate balance between the weighting coefficients is challenging. We can consider the use of optimization for finding an optimal set of coefficients, although it is computationally expensive (PKK22). The influence of balancing between an adversarial error and a regular L_2 reconstruction error for sparse flow reconstruction is discussed in detail by Zhang et al. (ZOK22) for an example of a flow around building models. Moreover, achieving stable convergence during training is also difficult with such complex loss functions. To avoid this issue, additional machine-learning functions such as skip connection (HZR16) and BatchNormalization (IS15) can be leveraged. In fact, the aforementioned models such as PIESRGAN (BGK19), MeshfreeFlowNet (EAK20), and TransFlowNet (WZG22) are composed of ResBlock (HZR16) (illustrated in figure 2.7(a)), which includes both BatchNormalization and skip connection, for stable and successful learning.

In contrast to supervised and semisupervised learning, unsupervised learning, which does not require labeled data sets, is also used for super-resolution analysis. Kim et al. (KKW21) proposed a cycle generative adversarial network (cGAN)-based framework for unsupervised super-

resolution reconstruction of turbulent flows. While a regular GAN is composed of one generator and one discriminator as presented in section 2.2.1.3, cGAN possesses two generators (G_1 and G_2) and two discriminators (D_1 and D_2), as illustrated in figure 2.7(b). One generator G_1 attempts to reconstruct a high-resolution data $\boldsymbol{q}_{\mathrm{HR}}$ from a low-resolution flow field $\boldsymbol{q}_{\mathrm{LR}}$, while another generator G_2 provides low-resolution fields from the generated high-resolution flow data through G_1. The discriminators D_1 and D_2 are trained to distinguish the real data from the generated data, as depicted in figure 2.7(b). This operation allows the cGAN model to learn common features between low- and high-resolution data, that need not be paired (ZPI17). The proposed model can reconstruct a velocity field of turbulent channel flow from its low-resolution field. They also demonstrated that the model trained with data from DNS can be applied to the LES data.

Following the study by Kim et al. (KKW21), the unsupervised GAN-based super resolution has recently been examined for a variety of flows. Wurster et al. (WSG21) proposed a hierarchical GAN to perform super resolution of fluid flows. Analogous to SURFNet (OVM21), a hierarchical GAN is first trained with low-resolution data sets. The model weights are then transferred to training with higher-resolution flow fields. Güemes et al. (GDI21) combined a GAN-based super-resolution reconstruction and state estimation (BMT01; CHB06; CCB11; SH06) from the wall sensor measurements of turbulent channel flow. They first perform super-resolution reconstruction for wall-shear stresses and wall pressure. Another GAN model is then constructed to estimate wall-parallel velocity fields at several wall-normal locations from the super-resolved wall measurements. The GAN models are able to provide reasonable agreement with the reference simulation data up to $y^+ \approx 50$. Yousif et al. (YYL22b) extended a super-resolution GAN model by combining it with multi-scale CNN (FFT19b) and applied it to a turbulent channel flow with large longitudinal ribs. The reconstructed flow fields are shown to retain the temporal correlations and high-order spatial statistics.

Moreover, the use of a CNN-based GAN for three-dimensional super-resolution analysis was examined by Xu et al. (XLW20) for computed tomography (CT) of turbulent jet combustor. With an example of turbulent atmospheric flow, Hassanaly et al. (HGS22) has comprehen-

sively compared various models for super-resolution reconstruction, including a super-resolution GAN (LTH17), stochastic estimation, a deconvolution GAN (SGH20), and diversity-sensitive conditional GAN (YHJ19). Although GAN-based models have issues with stability during the learning process, these models hold potential for high-wavenumber reconstruction of turbulent flows.

2.4 Case study: super-resolution reconstruction of turbulence

This section offers details of CNN-based super-resolution reconstruction for fluid flows through a case study. As an example, we consider two-dimensional decaying isotropic turbulence, which serves as a canonical turbulent flow. The flow field data to be studied is generated by a two-dimensional DNS (TNB16), which numerically solves the two-dimensional vorticity transport equation,

$$\frac{\partial \omega}{\partial t} + \boldsymbol{u} \cdot \nabla \omega = \frac{1}{Re_0} \nabla^2 \omega, \tag{2.11}$$

where $\boldsymbol{u} = (u, v)$ and ω represent the velocity and vorticity fields, respectively. The computational domain is a biperiodic square with $L_x = L_y = 1$. The initial Reynolds numbers for training/validation and test data sets are respectively set to $Re_0 \equiv u^* l_0^* / \nu = \{451, 442\}$. Here, u^* is the characteristic velocity defined as the square root of the spatially averaged initial kinetic energy, $l_0^* = [2\overline{u^2}(t_0)/\overline{\omega^2}(t_0)]^{1/2}$ is the initial integral length, and ν is the kinematic viscosity. The numbers of computational grid points used by DNS are $N_x = N_y = 512$. For training the baseline networks, we use 1000 snapshots over an eddy turn-overtime of $t \in [2, 6]$ with a time interval of $\Delta t = 0.004$. We consider a vorticity field ω as the variable of interest.

We note that our previous studies (FFT19b; FFT21) on machine-learning-based super-resolution reconstruction was performed with two-dimensional decaying turbulence but at lower Reynolds numbers ($Re_0 \approx 80$) with smaller numbers of the grid points ($N = 128$). The present case study examines how the model can be improved with regard to not only reconstruction accuracy but also a large amount of necessary training data at a higher Reynolds number.

For the present study, we consider super-resolution reconstruction with a regular CNN and

the hybrid downsampled skip-connection/multi-scale (DSC/MS) model (FFT19b). The design of the DSC/MS model is illustrated in figure 2.8. The red portion of the downsampled skip connection (DSC) model is composed of up-/downsampling operations and skip connection. The up-/downsampling operations provide robustness against rotational and translational invariance. The skip connection plays a crucial role in learning hierarchically the relationship between the high-resolution output and the low-resolution input, while providing numerical stability during the learning process of the CNN (HZR16). The present model also incorporates the multi-scale model (MS) model (DQH18), corresponding to the blue portion of figure 2.8. This part of the model performs filtering operations across three different sizes, capturing a range of spatial length scales in vortical flows.

To accurately reconstruct two-dimensional higher Reynolds number turbulent flow, we provide additional internal skip connections between the DSC model and MS model, as depicted in the green and orange boxes in figure 2.8. Each green box in the DSC model connects with each of the orange boxes in the MS model, hence nine connections are present. With these interconnections, this interconnected DSC/MS model enables the intermediate input/output from both submodels to correlate with each other through the learning process. Since coverage of spatial length scales increases with the Reynolds number, the interconnections are expected to be important in learning the relationship between small and large vortical elements by the model. For the activation function φ, this study uses the ReLU function (NH10) to avoid vanishing gradients of weights during the training process.

Furthermore, we consider a physics-based loss function to examine its effects on machine-learning-based super-resolution reconstruction of turbulent vortical flows. As discussed in section 2.2.2, the use of physics-inspired loss function may not only promote the physical validity of reconstruction but also reduce the amount of necessary training data in a semisupervised manner (GSW21; YYL21; EAK20; RRL22). Here, we use the nonlinear advection term and the linear viscous diffusion term in equation 2.11 for the physics-based loss function. The present cost

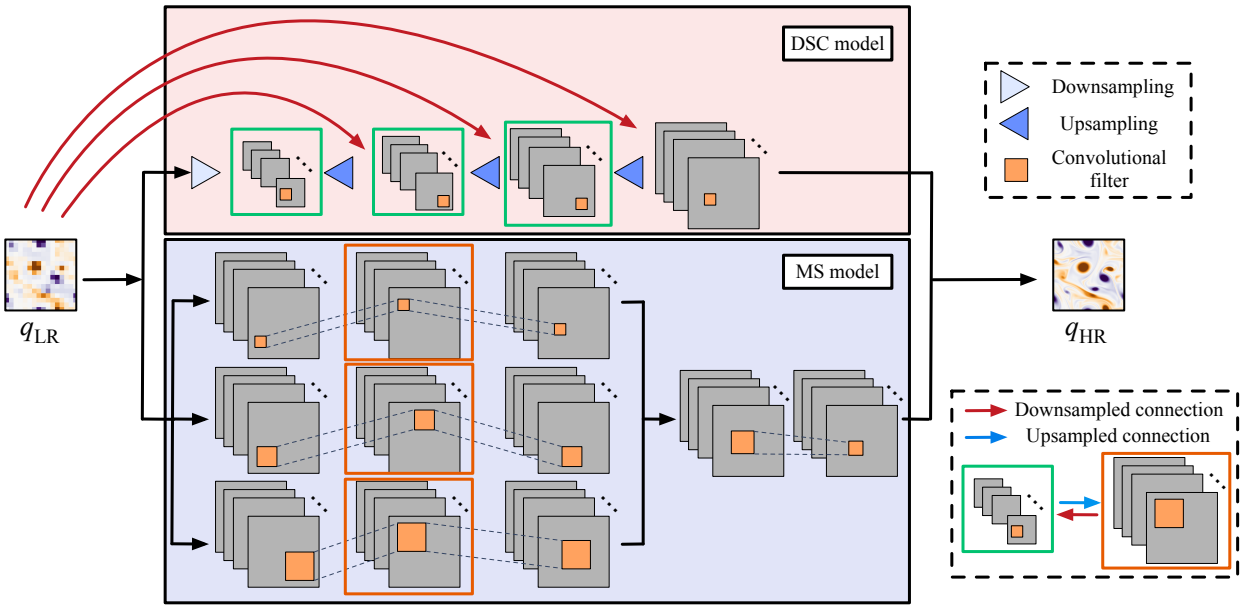

Figure 2.8: Interconnected DSC/MS model for super-resolution reconstruction of turbulent flows.

function $\mathcal{E}$ is hence defined as

$$\mathcal{E} = \mathcal{E}_\omega + \beta_{\mathrm{adv}}\mathcal{E}_{\mathrm{adv}} + \beta_{\mathrm{visc}}\mathcal{E}_{\mathrm{visc}}, \quad \text{where} \tag{2.12}$$

$$\mathcal{E}_\omega = ||\omega_{\mathrm{DNS}} - F(\omega_{\mathrm{LR}})||_2,$$

$$\mathcal{E}_{\mathrm{adv}} = ||\boldsymbol{u}_{\mathrm{DNS}} \cdot \nabla\omega_{\mathrm{DNS}} - \boldsymbol{u}_{\mathrm{ML}} \cdot \nabla\omega_{\mathrm{ML}}||_2,$$

$$\mathcal{E}_{\mathrm{visc}} = ||\nabla^2\omega_{\mathrm{DNS}} - \nabla^2\omega_{\mathrm{ML}}||_2,$$

in which ω_{DNS} and ω_{LR}, respectively, represent the reference (high-resolution) DNS field and the low-resolution input flow field. The coefficients β_{adv} and β_{visc} determine the balance of the terms in the loss function. The terms $(\cdot)_{\mathrm{ML}}$ inside $\mathcal{E}_{\mathrm{adv}}$ and $\mathcal{E}_{\mathrm{visc}}$ are computed with the super-resolved vorticity field $F(\omega_{\mathrm{LR}})$.

In what follows, we assess six different machine-learning models:

1. CNN-L_2: a regular CNN model with $\mathcal{E} = \mathcal{E}_\omega$,

2. CNN-L_{phys}: a regular CNN model with $\mathcal{E} = \mathcal{E}_\omega + \beta_{\mathrm{adv}}\mathcal{E}_{\mathrm{adv}} + \beta_{\mathrm{visc}}\mathcal{E}_{\mathrm{visc}}$,

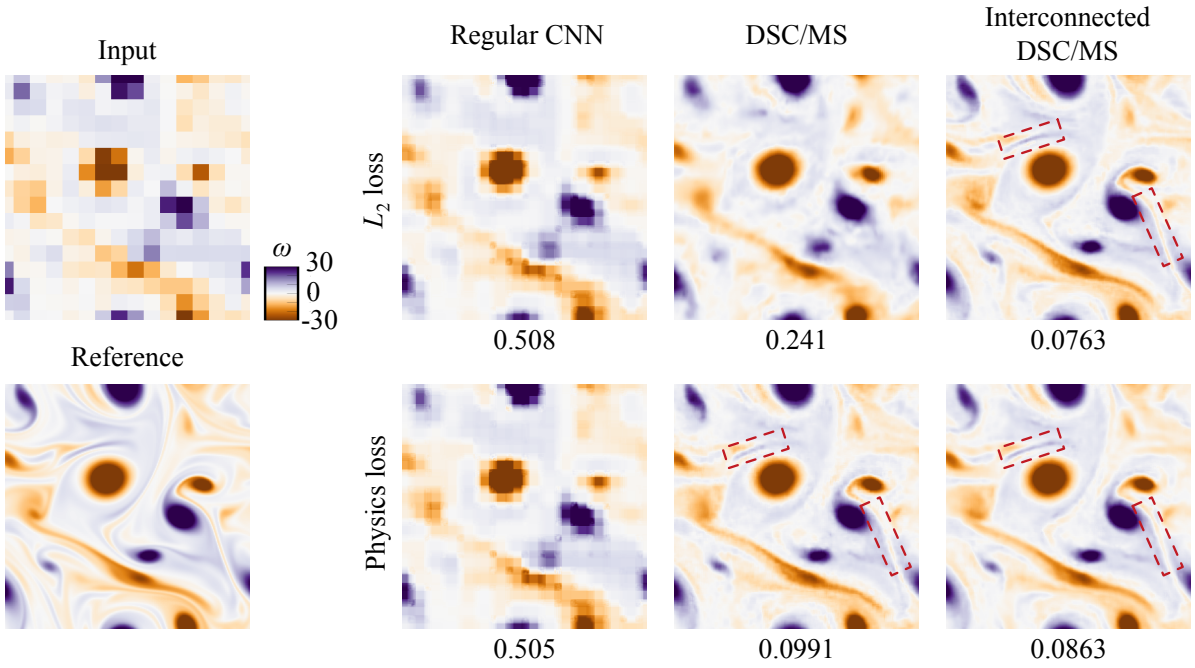

Figure 2.9: Super-resolution reconstruction of two-dimensional decaying homogeneous isotropic turbulence. The value underneath each vorticity contour plot presents the L_2 norm of reconstruction error ϵ.

3. DSC/MS-L_2: the original DSC/MS model (FFT19b) with $\mathcal{E} = \mathcal{E}_\omega$,
4. DSC/MS-L_{phys}: the original DSC/MS model with $\mathcal{E} = \mathcal{E}_\omega + \beta_{\text{adv}}\mathcal{E}_{\text{adv}} + \beta_{\text{visc}}\mathcal{E}_{\text{visc}}$,
5. IDSC/MS-L_2: the interconnected DSC/MS model with $\mathcal{E} = \mathcal{E}_\omega$,
6. IDSC/MS-L_{phys}: the interconnected DSC/MS model with $\mathcal{E} = \mathcal{E}_\omega + \beta_{\text{adv}}\mathcal{E}_{\text{adv}} + \beta_{\text{visc}}\mathcal{E}_{\text{visc}}$.

These six machine-learning models are tasked to reconstruct the high-resolution vortical flow field of size 512^2 from the corresponding low-resolution data of size 16^2, generated by average-pooling operations (FFT19b). We set $\beta_{\text{adv}} = \beta_{\text{visc}} = 0.1$ to the balance of the order for each term.

Let us consider the reconstructed vorticity fields from machine-learing-based super-resolution approaches in figure 2.9. The large-scale vortices can be reconstructed with the regular CNN models. However, the reconstructed fields are pixelized around rotation and shear-dominated

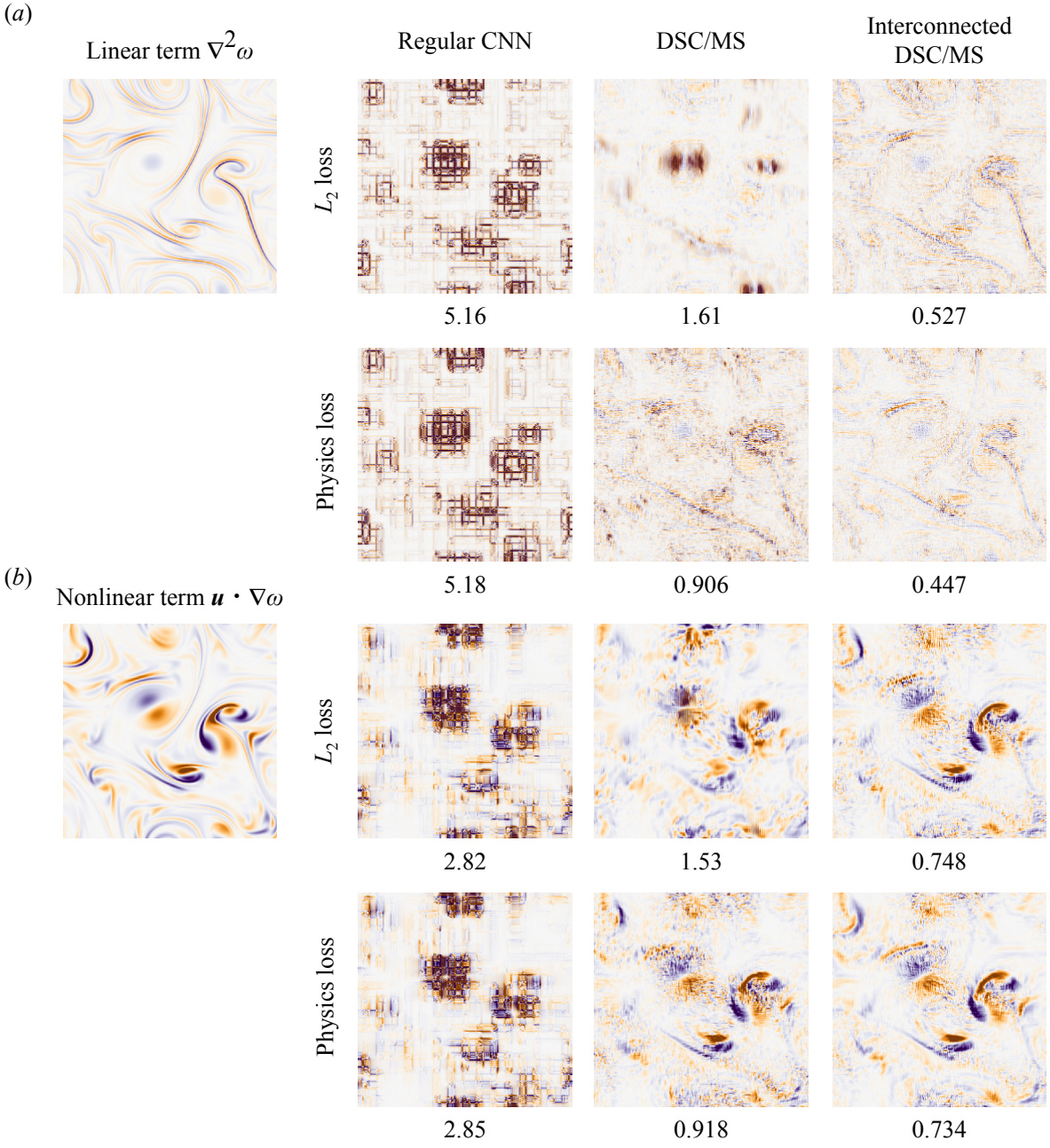

Figure 2.10: (a) The linear term $\nabla^2\omega$ and (b) the nonlinear term $\boldsymbol{u} \cdot \nabla\omega$, computed from the reconstructed flow fields for each machine-learned model. The value underneath each contour presents the L_2 norm error ϵ. Shown results are from the same case as the vorticity snapshots presented in figure 2.9.

structures, which was also observed with a regular CNN-based super-resolution reconstruction in our previous study (FFT19b). The L_2 norm error, $\epsilon = ||f_{\mathrm{DNS}} - f_{\mathrm{ML}}||_2 / ||f_{\mathrm{DNS}}||_2$, is found to be larger than 0.5 with the regular CNNs. The DSC/MS model with the L_2-based optimization provides a better and clear reconstruction for large vortical structures with an L_2 norm error of 0.241. This indicates that embedding the physics-inspired DSC functions and the MS filters enables accurate reconstruction of vortical flows.

While the DSC/MS model achieves a qualitative reconstruction for vortical structures, finer scales of shear layers that appear around large rotational elements cannot be recovered well. The reconstruction over these scales that emerge in higher Reynolds number flows can be improved by introducing either the physics-based loss function or the interconnection inside the DSC/MS model, as presented in figure 2.9. With DSC/MS-L_{phys}, IDSC/MS-L_2, and IDSC/MS-L_{phys}, these shear layers are more accurately reconstructed compared to the reconstruction with the regular model, as highlighted by the red boxes in figure 2.9. Hence, both the physics-inspired optimization and model design greatly assist in the reconstruction of higher Reynolds number flows. Note that the difference between the interconnection-based model enhancement and using the physics-based loss function is in their robustness against noisy low-resolution input, as it will be discussed later.

We here examine each term in the physics-loss function; namely the linear term $\nabla^2\omega$ and the nonlinear term $\boldsymbol{u} \cdot \nabla\omega$ of the present super-resolution reconstruction, as shown in figure 2.10. These results are from the same case as the vorticity snapshots presented in figure 2.9. Examination of these terms is a strict test since higher-order derivations can amplify errors greatly for high wavenumbers. Let us first focus on the estimated linear viscous diffusion term visualized in figure 2.10(a). The regular CNN completely fails to estimate $\nabla^2\omega$, as evident from the pixelized vorticity reconstruction in figure 2.9. Using the DSC/MS model with the regular L_2 optimization, the linear term field also exhibits erroneous profiles comprised of pairwise structures that cannot be observed in the reference field. These derivative-based assessments are again very sensitive and also affected by the reconstruction of surrounding local structures. As expected, estimation is improved by including the physics-based term in the loss function (DSC/MS-L_{phys}). The accuracy of $\nabla^2\omega$ can be further

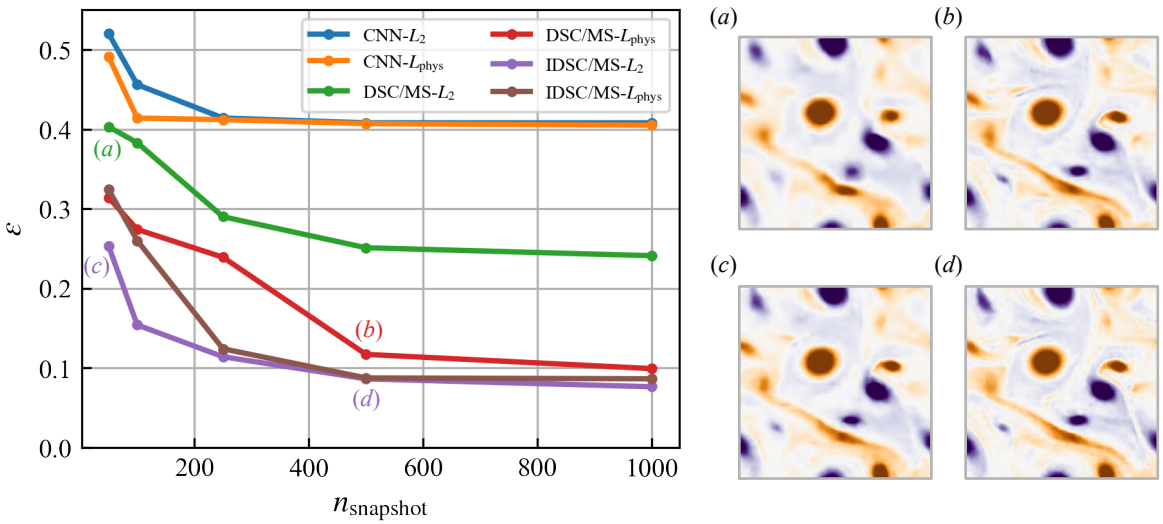

Figure 2.11: Dependence of the reconstruction accuracy on the number of the training snapshots.

enhanced by using the interconnected DSC/MS models, presenting fine-scale structures in the high-order derivation field. This indicates that adding the interconnections inside the machine-learning model enables physically-compatible super-resolution reconstruction of turbulent flows in addition to the physics-loss-based optimization.

The estimation of the nonlinear term is shown in figure 2.10(b). The whole trend in reconstruction is analogous to that for the linear term, hence the interconnected DSC/MS models well reconstruct the nonlinear term fields compared to the reference field. The L_2 errors for the nonlinear term with DSC/MS-L_{phys}, IDSC/MS-L_2, and IDSC/MS-L_{phys} are higher than that of the linear term. This suggests that the estimation for the nonlinear term is more difficult than the linear term.

We also investigate the dependence of the reconstruction error on the number of the training snapshots n_{snapshot}. For all models, the error decreases as n_{snapshot} increases, as shown in figure 2.11. Both the interconnection and the physics-based loss enable a qualitative reconstruction with a reduced number of training snapshots. The observation that a physics-inspired optimization reduces the required amount of training data has also been reported in previous studies (GSW21; RYK20). The interconnected DSC/MS model reconstructs fine vortical structures even with only $n_{\text{snapshot}} =$

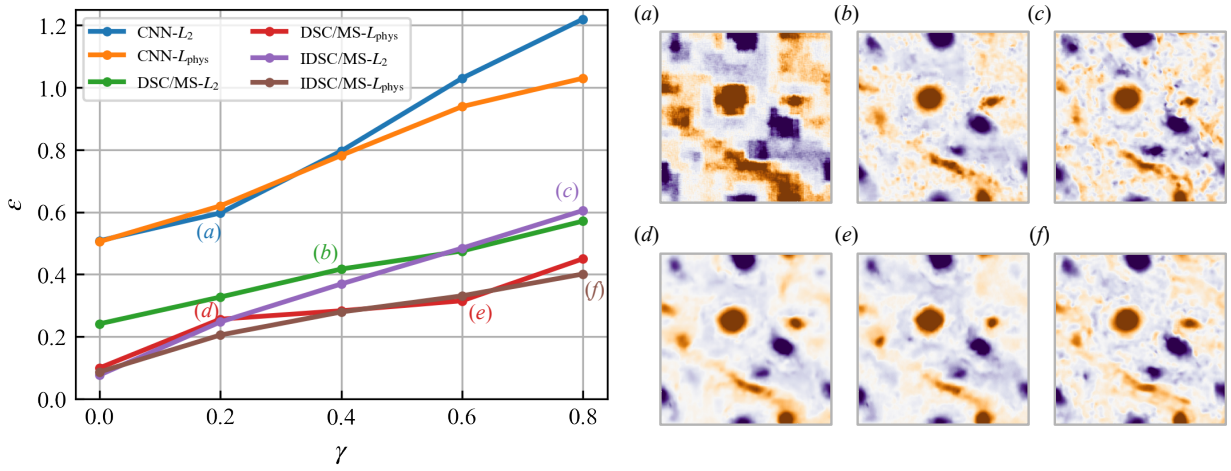

Figure 2.12: Dependence of the reconstruction accuracy on the magnitude of noisy input.

50 (figure 2.11(c)), while the original DSC/MS model provides only large-scale structures, as shown in figure 2.11(a). This suggests that the present machine-learning model efficiently captures a nonlinear relationship between the under-resolved input and the high-resolution vortical flow from a small amount of training data by capitalizing on the interconnected skip connections.

The use of the physics-based loss function can lead to robustness against noisy inputs. Here, let us examine the influence of noise on super-resolution reconstruction. We add the Gaussian noise $\boldsymbol{n}$ to the low-resolution input ω_{LR}, and assess the reconstruction L_2 error $\epsilon = ||\omega_{\text{HR}} - F(\omega_{\text{LR}} + \boldsymbol{n})||_2/||\omega_{\text{HR}}||_2$, where the magnitude of the noise is given as $\gamma = ||\boldsymbol{n}||/||\omega||$. Here, the models trained with 1000 snapshots are used. The relationship between the error and the noise magnitude is shown in figure 2.12. For all cases, the error increases with increasing magnitude γ. The reconstructed flow fields generally reveal the large-scale vortices, while the finer scales are affected by the noisy input. Especially for $\gamma > 0.3$, the DSC/MS models with the physics-based loss function are observed to be more robust than models trained with the simple L_2 error optimization. Hence, it can be argued that physics-based loss function helps in devising robust models against noisy measurements.

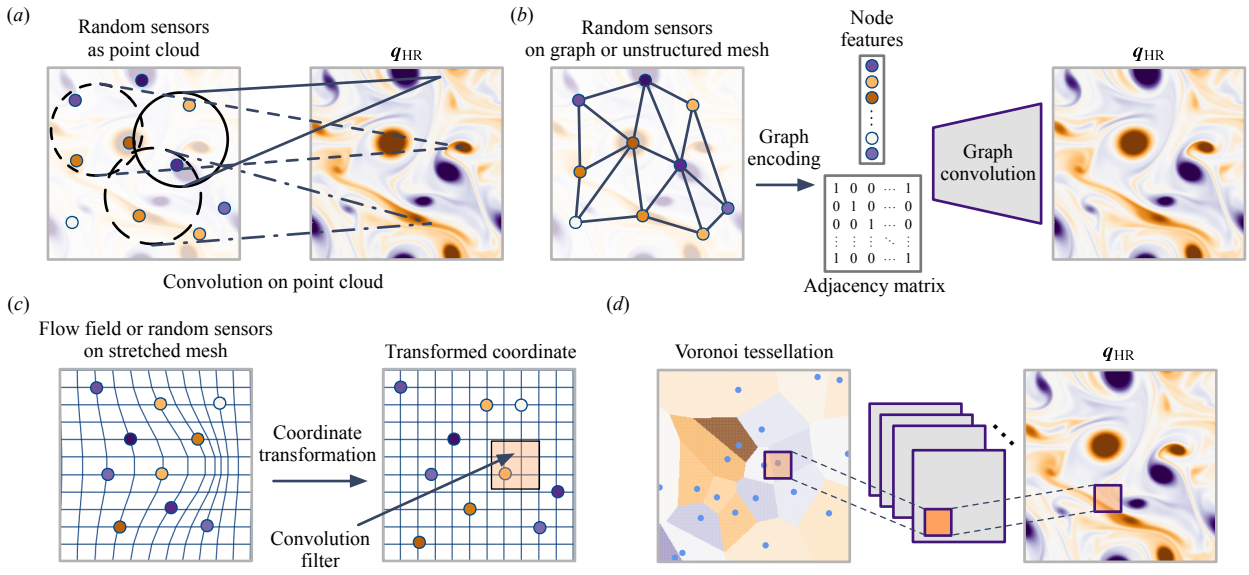

Figure 2.13: Applications of machine-learning-based super-resolution analysis for moving sensor and unstructured grid conditions. (a) Convolution on point clouds (KRG21; QSM17). (b) Graph neural network (LZJ22; GGJ22). (c) Coordinate transformation (GSW20). (d) Voronoi tessellation-based projection (FMR21).

2.5 Extensions

In the above sections, we surveyed various machine-learning-based super-resolution approaches and their applications to vortical flows. Here, we discuss extensions of machine-learning-based super-resolution analysis beyond their basic applications.

2.5.1 Changing input variable setups

When a machine-learning model is trained, the size of the input and output variables or more specifically the setup of the input and output variables is fixed. If the setup is changed, the machine-learning model generally needs to be completely retrained, which is a heavy burden. This issue is in fact a limitation of many machine-learning models, and machine-learning-based super-resolution models are no exceptions. If the number of pixels or their locations is different from that used in

the training process, the trained model cannot be used without retraining the model with the input variable size changed. Preprocessing the different-size input data with interpolation may work, but care should be taken since such an approach generally loses information. Unstructured grid and randomly sampled data also require some care since standard CNN-based models may not be appropriate.

There are several approaches to address these challenges. For instance, PointNet (QSM17) is able to handle unorganized and sparse data with a point cloud. Although this was originally used for image classification and segmentation tasks, Kashefi et al. (KRG21) has recently applied it to fluid flows. In their formulation, sensors on the grid can be directly treated and a model can learn the relationship between the sensors and outputs, as illustrated in figure 2.13(a).

To handle spatially irregular sensor arrangements, graph neural network (GNN) (WPC20) can be considered. GNN is able to perform a convolutional operation on unstructured mesh data, which is similar to that inside of CNNs. Such GNN-based methods can be applied for machine-learning-based super-resolution reconstruction by modifying the setup for data dimensions between input and output, as shown in figure 2.13(b).

Coordinate transformation can also be considered to simply use regular machine-learning models for vortical flows. PhyGeoNet (GSW20) includes coordinate transformation from an irregular domain to a structured mesh space for fluid flow regression, allowing us to convolve on flow fields, as illustrated in figure 2.13(c). Finding the appropriate coordinate transformation may be a challenge for complex flow field domain geometry.

We can also generalize super-resolution analysis by considering sensor measurements in the flow field as the input for machine-learning models to reconstruct the flow field. For a fixed number of sensors with their positions unchanged, regular machine-learning models developed in image science can often be directly used. However, when sensors go online or offline changing the number of sensors and moving spatially over time, the machine-learning models cannot be applied without special care. Voronoi-tessellation-based CNN (FMR21) can handle an arbitrary number of moving sensors in a single model. In this formulation, sparse sensor measurements are projected onto grids

generated from Voronoi tessellation, as illustrated in figure 2.13(*d*). The flow field discretized with Voronoi tessellation is then used as an input for CNN-based super-resolution reconstruction. This approach provides robust real-time super-resolution analysis for vortical flows.

2.5.2 Super resolution for turbulent flow simulations

With the ability to recover fine-scale flow structures from coarse images of the flow field, it is natural to ask whether machine-learning-based super-resolution analysis can be incorporated into numerical simulations to improve turbulent flow simulations. From a broader perspective, this question translates to whether super-resolution analysis can be implemented in a simulation of multi-scale physical phenomena to accurately reconstruct the subgrid-scale physics (PD23; BGL21).

For super-resolution analysis to reconstruct a physically accurate high-resolution flow field, it is generally necessary that the low-resolution input data is accurate on its own coarse grid. If the coarse flow field input is provided by some turbulent flow simulation (e.g., large-eddy simulation, detached eddy simulation, and Reynolds-averaged Navier-Stokes simulation (KT16)), it is important that the coarse flow be accurate to begin with. The super-resolved field would not be a physically accurate if the low-resolution flow field (input) is deviated from the true solution. Conservatively speaking, turbulent flow statistics may be predicted well with super resolution but highly-accurate reconstruction of each and every instantaneous flow would likely be a major difficulty, if not impossible (KSA21). In other words, we should not expect that LES results (or those from other solvers with turbulence models) can be transformed to yield DNS results.

A worthy question to ask is whether super-resolution analysis can support the development of subgrid-scale models. This could be different from other turbulence modeling approaches that use applied regressions to directly determine the subgrid-scale models for turbulent flow simulations. Similar to an approximate deconvolution model (SAK01) which considers inverse mapping of spatial filters, super resolution could be used to augment the subgrid-scale models. Furthermore, it remains to be seen whether super-resolution analysis can simultaneously nudge the low-resolution

field and recover the subgrid-scale flow structures. Again, the success of such simultaneous corrections will likely require the low-resolution flow field to be fairly accurate on its own grid. Alternatively, GAN-based techniques may also provide interesting approaches to achieve super resolution for turbulence.

Ongoing research developments in super-resolution analysis of turbulent flows and data-driven turbulence models (LKT16; DIX19) may address the issues identified here in the coming years. As super-resolution methods are extended and incorporated into turbulent flow analysis and simulations, it is important to ensure that the derived super-resolution method is generalizable over a range of Reynolds numbers and turbulent flow problems to confirm robust and reliable performance. This is critical if these techniques are to be implemented in general-use turbulent flow simulators.

2.5.3 Applications to real-world problems

Super-resolution analysis holds great potential for fluid dynamics as discussed above. However, there still exists some challenges, especially toward applications to real-world problems. This section discusses the current challenges and possible future directions of machine-learning-based fluid flow super resolution.

One of the major challenges of machine-learning-based super-resolution reconstruction for fluid flows is the necessity for a certain amount of training data. While unsupervised learning used for GANs and semisupervised learning assisted with physics-inspired loss functions introduced in the present survey can mitigate this issue, existing techniques still require learning the relationship between coarse data and high-resolution vortical flows from either unpaired or paired training data for successful reconstruction. Since the majority of real-world problems do not have access to ground truth and only sparse and noisy measurements are available, one can consider the use of data assimilation (DWZ23; DMB20; DMB18) to improve super-resolution reconstruction by incorporating the latest observations with a short-range real-time forecast.

Yasuda and Onishi (YO22) has recently proposed a four-dimensional super-resolution data

assimilation and demonstrated its performance with a two-dimensional periodic channel flow. The proposed method considers the temporal evolution of a system from low-resolution simulations with the aid of an ocean model, while a trained machine-learning model is simultaneously used to perform data assimilation and super resolution. Since there is a huge amount of historical weather and climate reanalysis data available, the unification of super resolution with data assimilation or pre-existing models would be an interesting research direction.

In addition, most of the existing studies focus on designing a reconstruction model for a particular flow problem, variable, or data shape. From this aspect, it would be desired to simultaneously leverage a variety of multi-modal data such as point-wise measurements, image-based data, and online measurements such as LiDAR-type data. Prediction of unavailable parameters from such sparse and noisy but available measurements may also become an interesting direction of super-resolution studies of fluid dynamics.

2.6 Conclusions

We provided a survey on machine-learning-based super-resolution reconstruction of vortical flows. Several machine-learning approaches and the use of physics-based cost functions for super-resolution analysis were discussed. We further performed case studies of super-resolution reconstruction of turbulent flows with convolutional neural network (CNN)-based methods. We demonstrated that a super-resolution model with physics-based loss function or physics-inspired neural network structures can reconstruct vortical flows even with limited training data and noisy inputs. We also discussed extensions and challenges of machine-learning-based super resolution for fluid flows from the aspects of changing input variable setups and applications for turbulent flow simulations.

The insights obtained through the present survey can be leveraged for a variety of machine-learning-based super-resolution models. For instance, the use of multi-scale filters inside CNN can be generalized not only in supervised learning but also in unsupervised techniques (YYL22a).

Physics-informed loss functions can also be extended for various machine-learning models. Moreover, it may also be interesting to develop super-resolution models in wavespace to incorporate certain spectral properties.

We remind that studies surveyed in the present paper are generally based on clean training data. Preparing high-quality input data is essential for successfully reconstructing turbulent flows. However, it is necessary to assess the robustness and sensitivity of the models against noisy inputs (NFF22). This point will be important as machine-learning-based super-resolution analyses become utilized in industrial applications (FAN22). Together with the accuracy of the models, quantifying uncertainties in machine-learning prediction is also required to assess their reliability and limitations. For these reasons, making computational and experimental fluid-flow databases (LPW08; WM08; TDB23) available is critically important to advance studies on data-driven analysis of vortical flows. We hope that this survey paper provides some guidance in advancing algorithms and applications of machine-learning-based super-resolution analysis for a variety of fundamental and industrial fluid flow problems.

CHAPTER 3

Sparse pressure sensor-based vortical flow reconstruction in a pump sump with machine learning

Here, we present a supervised machine-learning technique to reconstruct turbulent vortical structures in a pump sump from sparse surface pressure measurements (FAN22), which is an example of the industrial applications of our techniques.

3.1 Motivation

Chaotic dynamics caused by turbulent vortices can make operations of industrial machines challenging. Large-scale turbulent vortices produce noise, energy loss, and vibrations, affecting the performance of machines. Hence, it is critical that engineers are mindful of the large-scale turbulent vortices for safe and efficient operations of fluid-based systems (LAN20; Bre05; Bre11; HKK14; KYK19).

Achieving accurate awareness of the flow state is important. Thus far, linear-theory-based techniques have served a crucial role in reconstructing fluid flows from limited measurements. Linear stochastic estimation (LSE) had often been used for flow state estimation of canonical flows (AM88; NFF22). Kalman filter-based approaches have also been considered for fluid flow reconstruction of wall-bounded turbulence (CHB06; CCB11) and airfoil wakes (HES14; LE21). In addition, Gappy POD (ES95) has been utilized for global flow field reconstruction in both numerical (BDW04; Wil06) and experimental studies (MU07). Although these linear techniques provide insights from fluid flow data, they have limitations in extracting features from fluid flows

with strong nonlinearities.

Recent advancement in machine learning paves a new way for data-driven fluid flow reconstruction (BNK20; Dur21). Callaham et al. (CMB19) performed a library-based flow field reconstruction from sparse sensors for flows, including a periodic cylinder wake, a mixing layer, and geophysical flows. The global flow field is reconstructed through a linear combination of basis vectors from the training library. They also reported the robustness of the linear sparsity-promoting technique against noisy measurements. Such sparse sensing framework based on linear analysis is also useful for identifying flow regimes and bifurcation phenomena in thermo-fluid flow problems (KGB17). Moreover, nonlinear neural networks have been used for fluid flow reconstruction (BEF19; BBD21; FFT19b; LY19; LY21). Erichson et al. (EMY20) utilized a fully-connected neural network for sparse turbulent flow reconstruction of a geophysical flow and forced isotropic turbulence. Nair and Goza (NG20) also proposed a flow estimation technique based on multi-layer perceptron by combining with low-dimensional representation of flows obtained through proper orthogonal decomposition. In the context of super resolution which reconstructs a high-resolution signal from its low-resolution counterpart, convolutional neural networks have also been considered for fluid flow reconstruction (FFT19b; FFT21).

While the aforementioned studies focused on the application to structured grid data, the extension of neural network models to unstructured data is more recent. For instance, Leer and Kempf (LK21) used a radial-logarithmic filter mask to handle unstructured data with a multi-layer perceptron based estimator. They estimated flows around airfoils and ground vehicles. Fukami et al. (FMR21) have recently proposed a Voronoi tesselation-assisted machine learning technique for global flow field reconstruction from sparse sensors with arbitrary time-varying sensor locations and number of sensors.

These recent data-driven efforts are generally limited to academic problems. Of particular interest in this paper is the applicability of the aforementioned machine learning models to industrial turbulent flows that contain a broad range of spatio-temporal scales. This study presents a neural network-based fluid flow estimator. As an example, we consider turbulent flow in a pump sump

which can experience the emergence of air-entraining vortices and submerged vortices. These vortices are harmful to pump operations as they cause unbalanced loading and loud noise with the possibility of structural damage (Bre11; Zha10; ALT18; Yan17). Here, we consider a global field reconstruction from sparse pressure sensors located on the surface of the pump inlet to detect the aforementioned harmful vortices. We use a combination of multi-layer perceptron and three-dimensional convolutional neural network for the present flow reconstruction. This network structure enables us the handling of complex flow in a computationally efficient manner.

The present paper is organized as follows. The data set used in the present study is described in section 3.2.1. We then introduce the basic principles of machine learning models in section 3.2.2. Results of the present reconstruction with discussions are provided in section 3.3. At last, we offer concluding remarks in section 3.4.

3.2 Methods

3.2.1 Data preparation of pump sump flow

We perform a large-eddy simulation (LES) with an incompressible flow solver in OpenFOAM (WTJ98) to simulate the single-phase vortical flow in a pump sump. Wall-adapting local eddy-viscosity model (WALE) (ND99) is adopted for the subgrid scale stress tensor in the present LES. The computational setup and grid of a pump sump are illustrated in figure 3.1(a). The flow enters to the sump area from the left inlet of the rectangular domain and leaves from the top outlet, as depicted in figure 3.1(a). The steady-velocity boundary condition of 0.384 m/s and the static pressure boundary condition (0 Pa) are applied at the inlet and outlet boundary, respectively. The flow rate is set to 1.73 m^3/min. A no-slip wall boundary condition is imposed along the bottom wall and side walls of the rectangular domain, and the wall of cylindrical domain. Along the top wall of the rectangular domain, i.e., the free surface of water, we apply the slip wall boundary condition. The characteristic Reynolds number is 16000 based on the bulk velocity V at the bell mouth of 0.122 m/s and the diameter of the pump inlet of 0.15 m. The present grid size is approximately

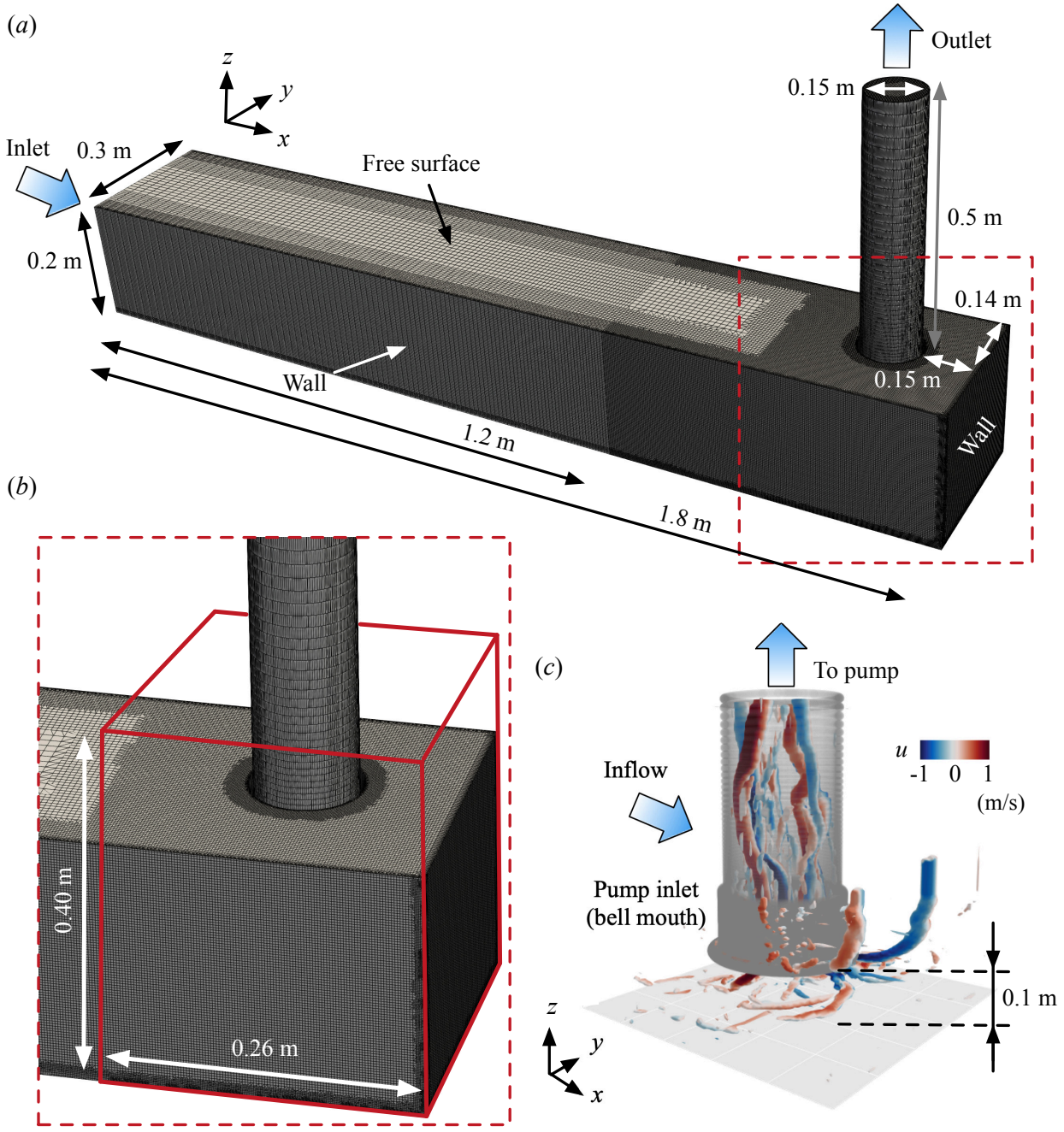

Figure 3.1: (a) and (b) Computational setup and grid used in the present study. (c) Vortical flow in a pump sump. Turbulent vortices are visualized using the second invariance of the velocity gradient tensor (Q = 1500).

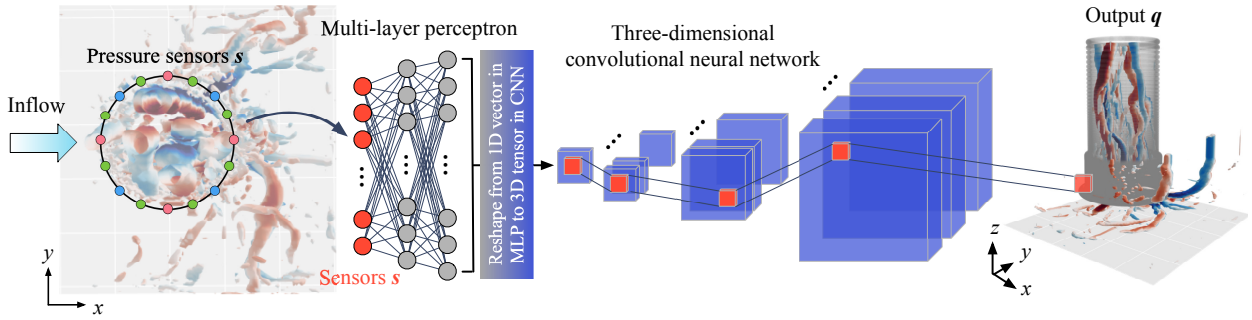

Figure 3.2: The combination of multi-layer perceptron and three-dimensional convolutional neural network for pump sump flow reconstruction from sparse sensors. Flow fields are visualized using the second invariance of the velocity gradient tensor (Q = 1500).

5 million with trimmed mesh. The accuracy of the LES computation has been checked to ensure that relevant turbulent physics in the pump sump are well-captured (ALN19).

The present study aims to reconstruct a global vortical flow field shown in figure 3.1(c) from sensors on the bell mouth using supervised machine learning. For training the present supervised machine learning $\mathcal{F}$, a set of inputs $\boldsymbol{s}$ and output $\boldsymbol{q}$ is prepared (FFT20). We prepare the training data as a set of pressure sensor measurements on the bell mouth as the input and the second invariant of the velocity gradient tensor as the output. The second invariant of the velocity gradient tensor is known as the Q-criterion (HWM88) which is used to identify vortex cores. For the output domain of the interest, we focus on the region of 1.54 m $\leq x \leq$ 1.8 m and 0 m $\leq y \leq$ 0.4 m, as shown in figure 3.1(b).

3.2.2 Machine learning models

The objective of the present study is to develop a machine learning model that takes a limited number of pressure sensor measurements as inputs to accurately reconstruct the global turbulent flow field (Q). We use a combination of multi-layer perceptron (MLP) (RHW86) and three-dimensional convolutional neural network (CNN) (LBB98) for the present model, as illustrated in figure 3.2. The pressure measurements are first provided as input to the MLP portion of the network. Through

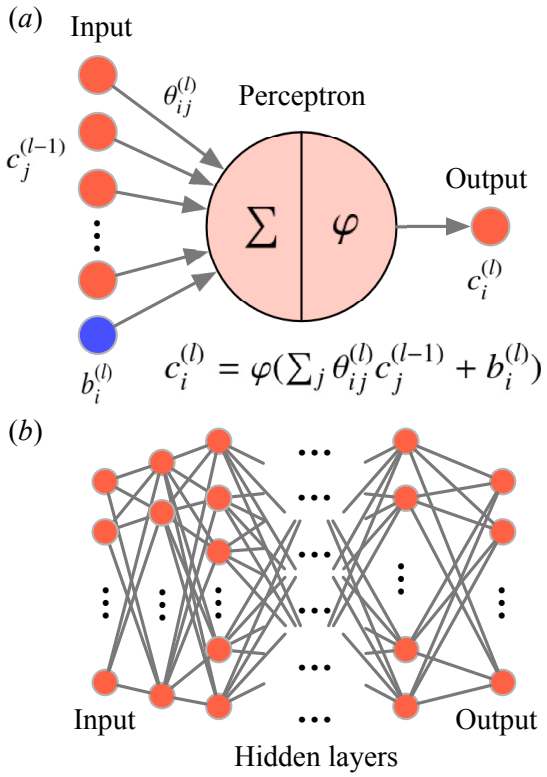

Figure 3.3: (a) A single perceptron and (b) a multi-layer perceptron.

the nonlinear operations within the MLP, the model can acquire the high-dimensional representation of input sensor measurements as the output of the hidden layers. This data is then fed to the CNN section, which extracts the relationship between the representation of the input sensors and the three-dimensional flow field with a manageable computational cost. Note that reconstructing a three-dimensional turbulent flow field with a large number of grid points, such as the present flow, is prohibitively expensive solely with MLP due to its fully-connected structure (WPC20). The use of CNN can address this computational cost while maintaining accuracy. Below, we briefly present the formulations of MLP and CNN, and discuss the hybrid MLP-CNN model.

3.2.2.1 Multi-layer perceptron (MLP)

Let us introduce the multi-layer perceptron (MLP) (RHW86). MLP can learn the nonlinear relationship between the input and the output. MLP is an aggregate of perceptrons, as shown in

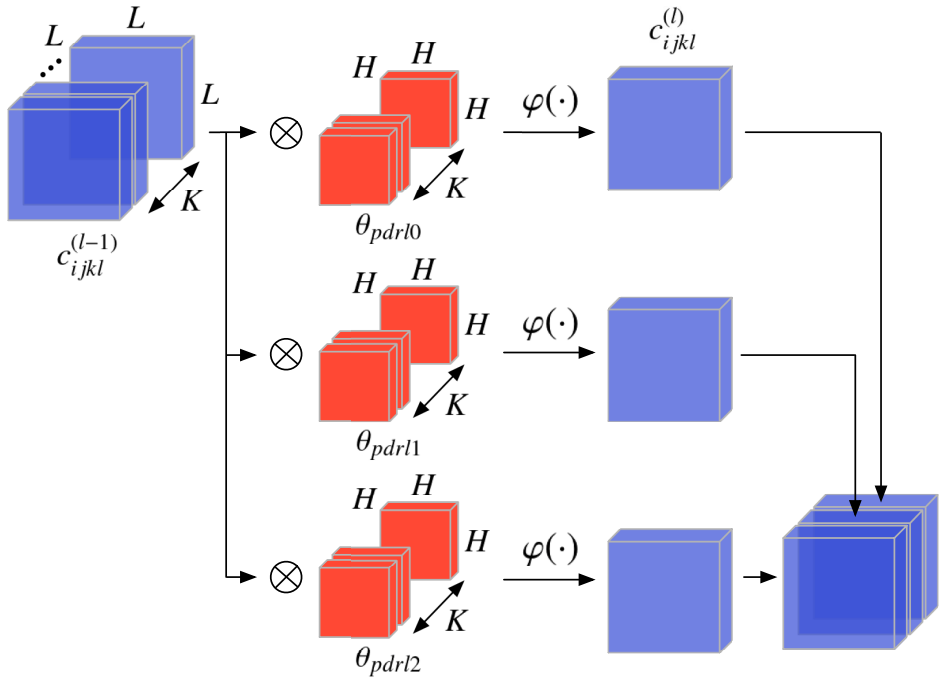

Figure 3.4: Three-dimensional filter operations in a convolutional neural network.

figure 3.3. For each perceptron, the linear combination of the inputs from layer $(l-1)$, $c_i^{(l-1)}$, is connected with weights $\boldsymbol{\theta}$ toward the output at layer (l), $c_j^{(l)}$,

$$c_i^{(l)} = \varphi\left(\sum_j \theta_{ij}^{(l)} c_j^{(l-1)} + b_i^{(l)}\right). \tag{3.1}$$

Here, φ is the activation function and b is the bias added at each layer. By choosing a nonlinear function for φ, MLP can perform nonlinear regressions (and classifications), well beyond what can be achieved by linear reconstruction techniques. The present study uses the ReLU function (NH10), which is robust against vanishing gradients during the training of neural networks.

3.2.2.2 Three-dimensional convolutional neural network (CNN)

Convolutional neural network (CNN) (LBB98) is widely used for image recognition. Filter operations inside the CNN enable us to process high-dimensional data without being limited by the curse of dimensionality (the problem of having enormously large number of weights). This capability is especially attractive to manage fluid flow data that has large grid size (high degrees of

freedom) (MFZ21; GGI21; KL20). The operation of a three-dimensional CNN can be expressed as

$$c_{ijkm}^{(l)} = \varphi\left(\sum_{l=0}^{K-1}\sum_{p=0}^{H-1}\sum_{d=0}^{H-1}\sum_{r=0}^{H-1}\theta_{pdrlm}^{(l)}c_{i+p-G,j+d-G,k+r-G,l}^{(l-1)} + b_m^{(l)}\right), \tag{3.2}$$

where H is the width and height of the filter, $G = \text{floor}(H/2)$, K is the number of channels in the convolution layer, b_m is the bias, and φ is the activation function. The convolutional layer provides the output through the filters θ by giving the input data $c^{(l-1)}$, as illustrated in figure 3.4. Similar to the MLP, the nonlinear activation function φ is then taken for each output. The ReLU function (NH10) is also chosen as the activation function here. Through the training process of CNN, filter coefficients θ_{pdrlm} for the filter are optimized to acquire an input-output relationship in a supervised manner. Since this filter (weights) is shared over the whole field within the same layer (l), the number of weights is much smaller than what is needed for a fully-connected MLP for the same degrees of freedom. In addition to the filtering operations, we also incorporate upsampling operations to recover the dimension of data towards the final layer of the CNN.

3.2.2.3 MLP-CNN based state estimator

We combine the aforementioned two machine learning models for the present reconstruction. Pressure sensor measurements on the bell mouth $\boldsymbol{s}$ are fed into an MLP. The feature vectors extracted through the MLP are supplied to the three-dimensional convolutional layers, as depicted in figure 3.2. To provide a one-dimensional feature vector from the MLP into the CNN, the vector is here reshaped into a three-dimensional tensor. The training process of the present MLP-CNN based state estimator $\mathcal{F}$ is expressed as,

$$\boldsymbol{w}^* = \text{argmin}_{\boldsymbol{w}}||\boldsymbol{q} - \mathcal{F}(\boldsymbol{s};\boldsymbol{w})||_2. \tag{3.3}$$

This problem is solved to optimize weights $\boldsymbol{w}$ by minimizing the L_2 error function between the reference field $\boldsymbol{q}$ and the estimated field $\mathcal{F}(\boldsymbol{s})$. We use the Adam algorithm (KB14) for updating weights $\boldsymbol{w}$ in the present model. To prevent overfitting the data, we incorporate an early stopping criteria (Pre98) into the present training process.

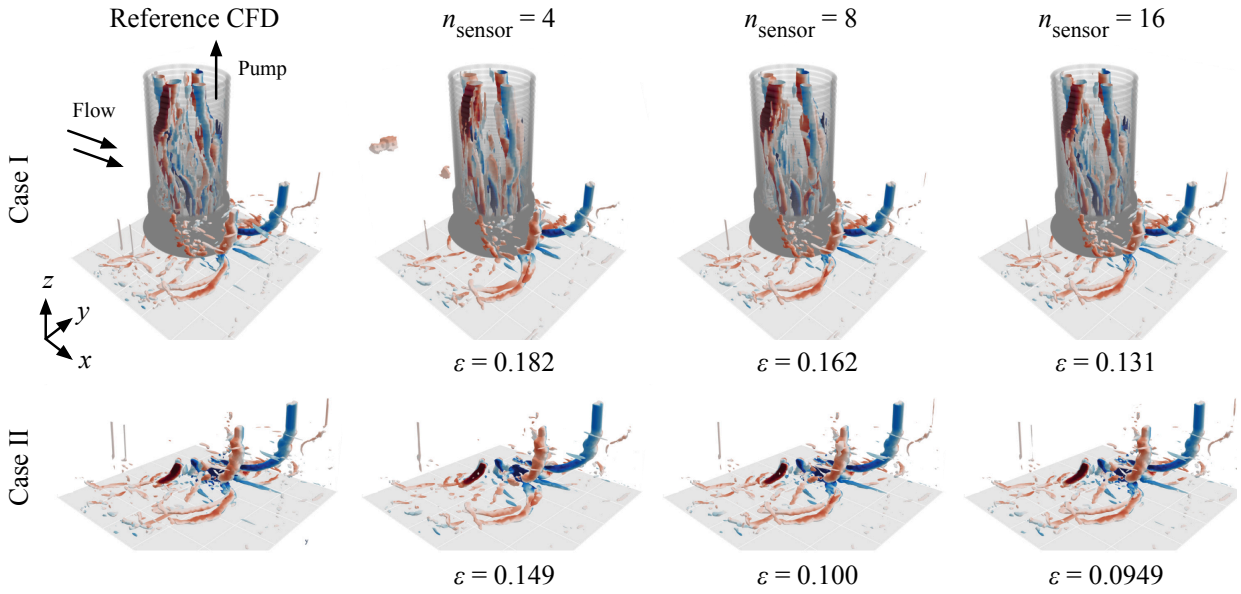

Figure 3.5: Machine-learning-based reconstruction of pump sump flow. Flow fields are visualized using the second invariance Q of characteristic equation with respect to a velocity gradient tensor with the threshold of $Q_{\text{th}} = 1500$. The structures are colored by the streamwise velocity u. The values underneath each subfigure represent the L_2 error norm ϵ.

3.3 Results

Let us discuss the present machine-learning-based pump sump flow reconstruction. Here, two different sizes of the output variable are considered:

Case I. the domain with flow inside the pump inlet (bell mouth) such that $\boldsymbol{q}_1 \in \mathbb{R}^{100\times100\times100}$,

Case II. the domain without flow inside the pump inlet (bell mouth) such that $\boldsymbol{q}_2 \in \mathbb{R}^{100\times100\times50}$.

We prepare two machine-learning models for each of these cases. As for the input sensors $\boldsymbol{s}$, we consider the pressure p. We choose the second invariant Q of the velocity gradient tensor (CPC90; JH95) as an output variable $\boldsymbol{q}$ to capture vortical structures in the pump sump.

Let us present in figure 3.5 the reconstructed flow fields from pressure sensor measurements. We consider different numbers of input pressure sensors $n_{\text{sensor}} = \{4, 8, 16\}$. As for the sensor

placements, we use pink sensors for $n_{\text{sensor}} = 4$, pink and blue sensors for $n_{\text{sensor}} = 8$, and all (blue, pink, and green) sensors for $n_{\text{sensor}} = 16$, as indicated in figure 3.2. These sensors are placed around the bell mouth in equispacing at the height of $y = 0.103$ m. The reconstructions shown in figure 3.5 are performed using models trained with 1400 snapshots spanning over $t \in [8, 15]$ seconds. For the present model training, it takes approximately 3.5 hours with an NVIDIA Tesla V100 graphics processing unit. We will revisit the dependence of the reconstruction performance on the number of snapshots n_{snapshot} later.

For all cases, the reconstructions are in agreement with the reference data. To quantify the present reconstruction, we define the L_2 error as $\epsilon = ||\boldsymbol{q}_{\text{Ref}} - \boldsymbol{q}_{\text{ML}}||_2 / ||\boldsymbol{q}_{\text{Ref}} - \overline{\boldsymbol{q}}||_2$, where $\boldsymbol{q}_{\text{Ref}}$, $\boldsymbol{q}_{\text{ML}}$, and $\overline{\boldsymbol{q}}$ denote a reference variable, a machine-learning-based estimation, and the time-average value of the reference, respectively. With $n_{\text{sensor}} = 16$, the models achieve an L_2 error of $\epsilon = 0.131$ (Case I) and 0.0949 (Case II), exhibiting almost indistinguishable vortical flow reconstruction from the reference field. Although some spurious structures are observed, primary structures can be captured even with $n_{\text{sensor}} = 4$. We also observe improvements in the reconstruction by removing the flow inside the bell mouth, as shown in figure 3.5. This is likely because the weights inside the model only cover the region only around the bell mouth where complex vortical structures appear.

We further examine the probability distribution of the Q variable, as shown in figure 3.6. We consider the models trained with $\{n_{\text{snapshot}}, n_{\text{sensor}}\} = \{1400, 8\}$. The probability distributions obtained by the machine-learning based reconstruction match the trends to that of the reference data, which are consistent with the observations from the flow visualization in figure 3.5. We also find that structures inside the inlet, that are removed in Case II, i.e., $2 \times 10^6 \lessapprox Q \lessapprox 6 \times 10^6$, correspond to lower probabilities. It is known that supervised machine learning models with the L_2 optimization preferentially learn structures that appear with high probability (FFT21). This observation can also be considered as the reason of the accuracy improvement for the case without the interior flow.

The demonstrations above were performed using machine learning models trained with 1400 snapshots spanning over $t \in [8, 15]$ seconds. Next, let us investigate the dependence of the

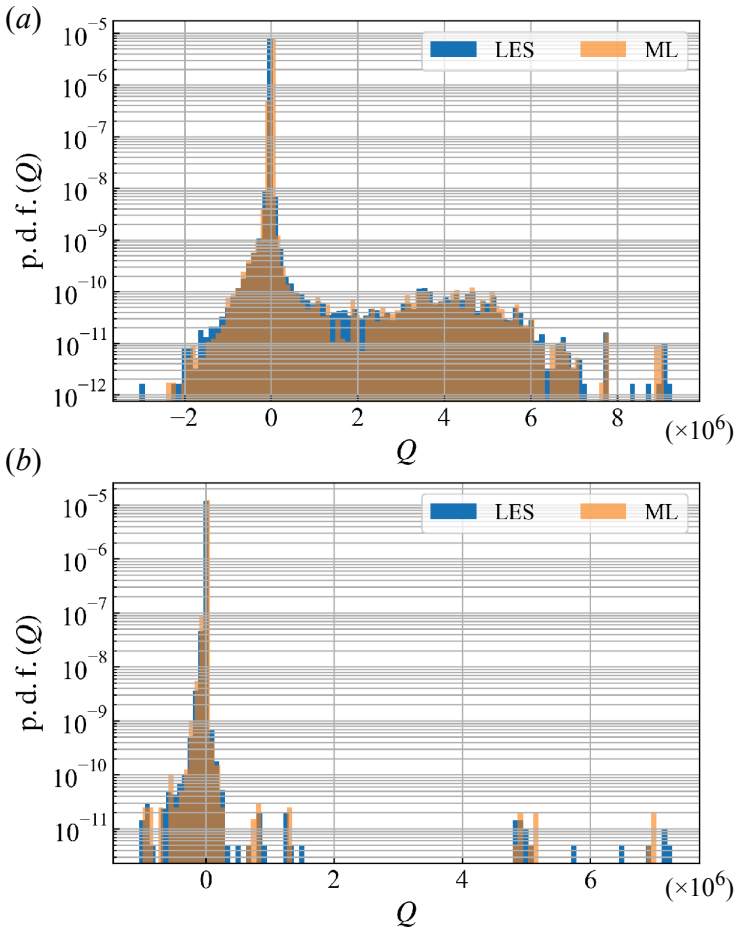

Figure 3.6: Probability density function of Q for (a) Case I and (b) Case II.

reconstruction accuracy on the number of training snapshots n_{snapshot}. Here, we consider $n_{\text{sensor}} = 8$ for both cases with and without the flow inside the inlet. For this investigation, the number of snapshots is varied while fixing the time step to $\Delta t = 0.005$ seconds. Hence, the increment of the number of snapshots corresponds to that of the time window over the training data regime. As shown in figure 3.7, the error decreases as the number of snapshots increases for both cases. Moreover, reasonable reconstruction can be achieved even inside the bell mouth, with as little as 250 snapshots spanning over $t \in [8, 9.25]$ seconds. It is also worth pointing out that the L_2 norm error used here is a strict measurement that does not account for translational or rotational similarities (FFT19b). Although the cases with $n_{\text{snapshot}} = 250$ report approximately 20% error, it is mainly caused by the slight structural offsets between the reference and the reconstruction.

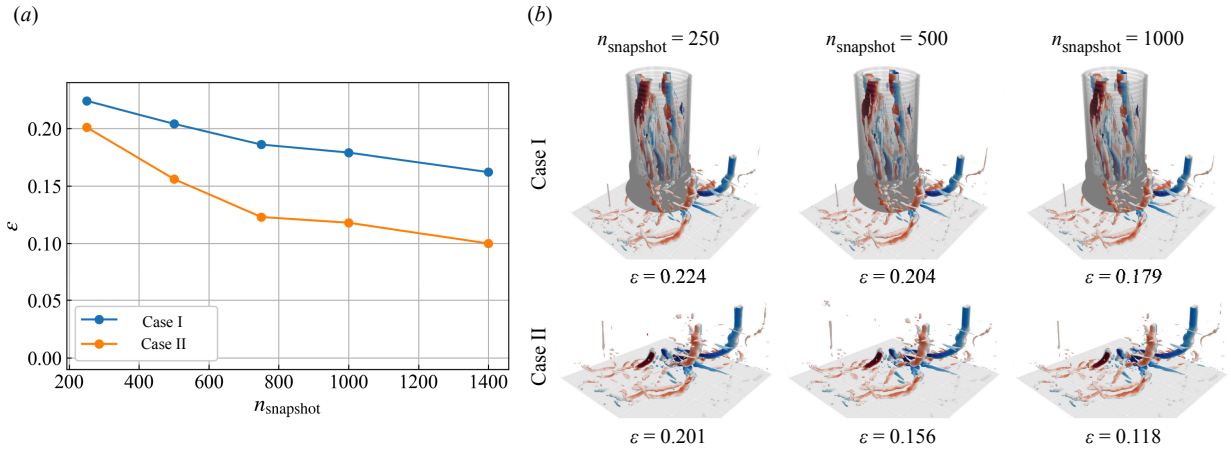

Figure 3.7: Dependence of the reconstruction accuracy on the number of training snapshots. (a) The relationship between the number of training snapshots and the reconstruction error. (b) Representative snapshots with the L_2 error.

The large-scale structures are captured well with the present model despite the small numbers of training snapshots.

At last, let us examine the influence of noise on the reconstruction. Here, we add noise $\boldsymbol{n}$ to the sensor input $\boldsymbol{s}$ as

$$\boldsymbol{q} = \mathcal{F}(\boldsymbol{s} + \gamma \boldsymbol{n}), \tag{3.4}$$

where $\mathcal{F}$ denotes the model trained without the noisy input, $\gamma = ||\boldsymbol{s}||/||\boldsymbol{n}||$ is the magnitude of noise, and $\boldsymbol{q}$ represents the output of the model. As for the noise $\boldsymbol{n}$ ($||\boldsymbol{n} = 1||$), we use colored noise whose power spectral density P varies over frequency such that $P \propto 1/f^{\beta}$. Changing the coefficient β, various types of noise can be generated. The present study considers $\beta \in \{-2\ \text{(purple)}, -1\ \text{(blue)}, 0\ \text{(white)}, 1\ \text{(pink)}, 2\ \text{(brown)}\}$. Note that the flat distribution is offered with $\beta = 0$, while the positive/negative β produces the large spectral density at the low/high frequency. This setup evaluates the robustness of the present machine learning model in terms of both magnitude and frequency of the noisy input. For the present demonstration, we use models trained with 1400 snapshots spanning over $t \in [8, 15]$ seconds, and then assess the performance using test snapshots over $t \in [16, 17]$ seconds.

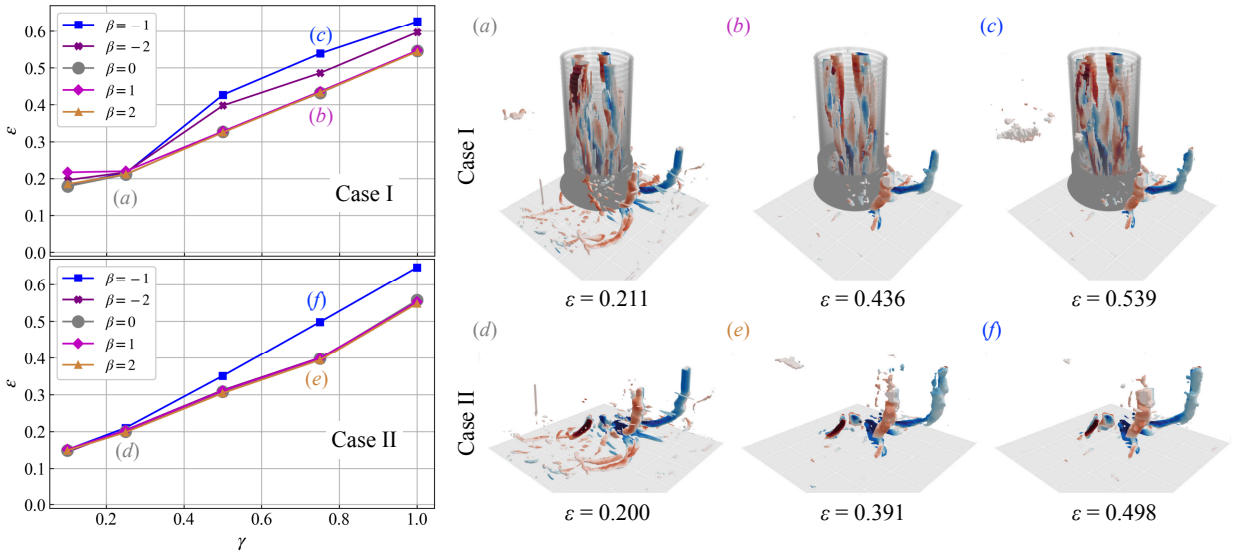

Figure 3.8: Dependence of the reconstruction accuracy on the magnitude and frequency of input noise.

The robustness of our model against noise is summarized in figure 3.8. For both cases with and without the interior domain of the bell mouth, the error increases with increasing magnitude γ. Even with $\gamma = 0.25$, large vortical structures are well-captured, while finer scales remain in the reconstructed field. Notably, the model is robust for large-scale reconstruction even for $\gamma = 0.75$, although small scales and the interior of the bell mouth cannot be estimated due to the large noise level over a broad range of frequency.

3.4 Concluding remarks

We presented a machine-learning-based technique to reconstruct turbulent vortical flows in a pump sump. To reconstruct the turbulent flow structures from sparse sensor measurements collected along the bell mouth, the proposed model combined two types of supervised machine learning techniques; namely, the multi-layer perceptron and the convolutional neural network. This proposed network was able to reconstruct the chaotic vortical flow over a three-dimensional domain with manageable computational costs for both training and online estimations. We also examined the dependence of

the model performance with the presence of noise. The present model can be robust for situations with the limited availability of training data and noisy sensor data.

We envision a broad range of industrial applications for the present machine learning technique to gain situational awareness of complex turbulent flows. Since the current technique identifies the location of vortical structures, it can be combined with existing control methods that can effectively mitigate adverse vibrations and present structural damage (LAN18b; LAN20). Moreover, combining the present approach with modal analyses may promote understanding of turbulent flow analyses (TBD17; THB20b). The applicability to flows of other pump sump shapes and at different Reynolds numbers can be examined in the future. We believe that the present technique can serve as a flow estimation tool to enhance the performance and safety of industrial fluid-based machines.

CHAPTER 4

Voronoi tessellation-assisted flow field reconstruction

While convolutional neural network-based supervised machine learning has been considered for space-time data recovery of turbulent flows (FFT21), they have often been limited to use for only fixed grid/sensor data and are not suited for local sensor measurements placed randomly and in motion. To enhance the practicability of the method, we develop a Voronoi-tessellation-assisted approach, which solves issues associated with existing schemes of global field reconstruction from limited measurements (FMR21).

4.1 Motivation

Spatial field reconstruction from limited local sensor information is a major challenge in the analysis, estimation, control, and design of high-dimensional complex physical systems. For complex physics including geophysics (MBK18), astrophysics (AAA19), atmospheric science (ALM10; MKK14), and fluid dynamics (FFT20), traditional linear theory-based tools, including Galerkin transforms (BD11; NE94), linear stochastic estimation (AM88; SH06) and Gappy proper orthogonal decomposition (BDW04), have faced challenges in reconstructing global fields from a limited number of sensors. Neural networks have emerged as hopeful nonlinear alternatives to reconstruct chaotic data from sparse measurements in an efficient manner (LBH15; BNK20). However, there are key limitations associated with neural networks for field reconstruction. One of the biggest difficulties is the applicability of neural network-based methods to unstructured grid data. Almost all practical experimental measurements or numerical simulations rely on unstructured grids or non-uniform/random sensor placements. These grids are not compatible with convolutional

neural network (CNN)-based methods which are founded on training data being *structured* and *uniformly* arranged (LBB98; FFT19b). While a multi-layer perceptron (MLP) (RHW86) can handle unstructured data, its use is sometimes impractical due to their globally connected network structure. Moreover, MLPs cannot handle sensors that may go offline or move in space. On the other hand, graph convolutional networks (GCNs) have been utilized to perform convolutions on unstructured data (WPC20). However, GCNs are also known to scale poorly and their state-of-the-art applications have been limited to the order of 10^5 degrees of freedom (MBR21a). Even such applications of GCNs have required distributed learning on several hardware accelerators. This restricts their utilities for practical field reconstructions. A greater limitation stems from the fact that all methods fail to handle spatially moving sensors. This implies that applications of these conventional tools are limited to a fixed sensor arrangement as that used in a training process. This limitation is a major hindrance to practical use of these reconstruction techniques, since experimental sensor locations commonly evolve over time. The framework that integrates convolutional architectures with time-varying unstructured data is crucial for bridging the gap between structured field reconstructions and practical problems (CGL20).

In response to the aforementioned challenges, we propose a method that incorporates sparse sensor data into a CNN by approximating the local information onto a structured representation, while retaining the information of spatial sensor locations. This is achieved by constructing a Voronoi tessellation of the unstructured data set and adding the input data field corresponding to spatial sensor locations through a mask. Voronoi tessellation projects local sensor information onto the structured-grid field based on the Euclidean distance. The currently technique achieves accurate field reconstructions from arbitrary sensor locations and varying numbers of sensors with existing CNN architectures. The present formulation will impact a wide range of research fields that rely on fusing information from discrete sensors, e.g, buoy-based sensors and tracers in particle tracking velocimetry (MHC19).

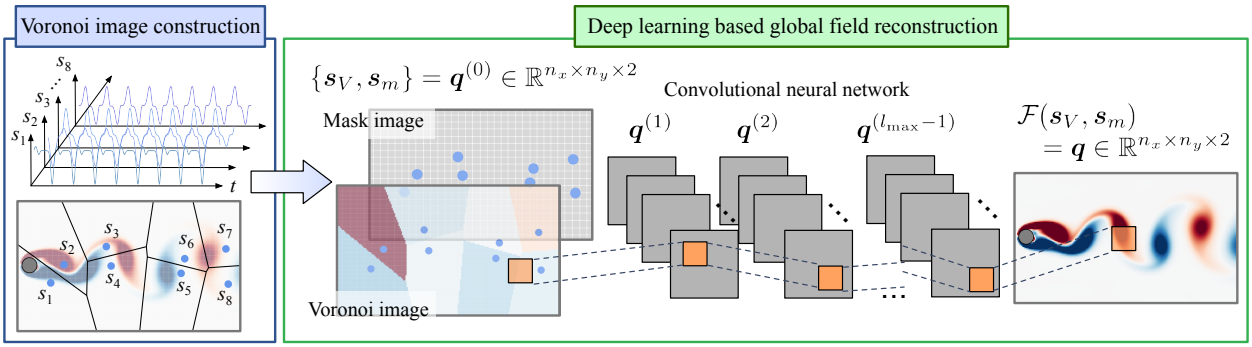

Figure 4.1: Voronoi tessellation aided global data recovery from discrete sensor locations for a two-dimensional cylinder wake. Input Voronoi image is constructed from 8 sensors. The Voronoi image is then fed into a convolutional neural network with the mask image. In the mask image, a grid having a sensor (blue circle) has 1 while otherwise 0.

4.2 Problem setup and approach

Our objective is to reconstruct a two-dimensional global field variable $\boldsymbol{q} \in \mathbb{R}^{n_x \times n_y}$ from local sensor measurements $\boldsymbol{s} \in \mathbb{R}^n$ at locations $\boldsymbol{x}_{si} \in \mathbb{R}^2, i = 1, \ldots, n$. Here, n_x and n_y respectively denote the number of grid points in the horizontal and vertical directions on a high-resolution field, and n indicates the number of local sensor measurements. The challenge here is to handle arbitrary numbers of sensors at any location over the field. The number of sensors can be changed in time and the sensors can be moving. The reconstruction process should be performed with only a single machine-learning model to avoid retraining when sensors move or change their numbers.

To achieve the goal of the present study, we utilize two input data files (images) for the CNN:

1. Local sensor measurements projected on Voronoi tessellation $\boldsymbol{s}_V = \boldsymbol{s}_V(\boldsymbol{s}) \in \mathbb{R}^{n_x \times n_y}$.

2. Mask image $\boldsymbol{s}_m = \boldsymbol{s}_m(\{\boldsymbol{x}_{si}\}_{i=1}^n) \in \mathbb{R}^{n_x \times n_y}$ which contains the local sensors positions, defined as

$$\boldsymbol{s}_m(\{\boldsymbol{x}_{si}\}_{i=1}^n) = \begin{cases} 1 & \text{if } \boldsymbol{x} = \boldsymbol{x}_{si} \text{ for any } i, \\ 0 & \text{otherwise.} \end{cases}$$

The two input images above are provided to a machine learning model $\mathcal{F}$ such that $\boldsymbol{q} = \mathcal{F}(\boldsymbol{s}_V, \boldsymbol{s}_m) \in \mathbb{R}^{n_x \times n_y}$, where $\boldsymbol{q}$ is the desired high-resolution field. With these two input vectors holding magnitude and position information of the sensors, the present idea can deal with arbitrary sensor locations and arbitrary numbers of sensors. It should be noted that reconstruction cannot be achieved with conventional methods, including MLPs and CNNs due to their structural constraints. In what follows, we introduce Voronoi tessellation and machine learning framework, which are the two key components in the present approach.[1]

To use a machine learning framework, the sensor data needs to be projected into an image file in an appropriate manner. Voronoi tessellation (Vor08) is a simple and spatially optimal projection of local sensor measurements onto the spatial domain. This tessellation approach optimally partitions a given space E into n regions $G = \{g_1, g_2, ..., g_n\}$ using boundaries determined by distances d among n number of sensors s (Aur91). Using a distance function d, Voronoi tessellation can be expressed as

$$g_i = \{s_i \in E | d(s_i, g_i) < d(s_i, g_j),\ j \neq i\}. \tag{4.1}$$

Hence, for a Euclidean domain, the Voronoi boundaries between sensors are their bisectors.

Voronoi tessellation has two important characteristics which provide the foundation for the present approximation constructed with local sensor measurements (Aur91). One is that each area in a Voronoi tessellation is convex. This property enables us to establish a Voronoi tessellation using bisections in a simple manner. The other is that a Voronoi tessellation does not include other sensors inside it when a circle centered at the vertex of a Voronoi region g passes neighboring sensors (Empty-circle property). This implies that each Voronoi region g is optimal for each sensor s in a Voronoi tessellation. Note that the Voronoi discretization is influenced by the computational domain size. Experimental setups are also influenced in analogous manner with their finite fields of view. Additional details on the mathematical theory of Voronoi tessellation can be seen in the study of Aurenhammer (Aur91).

[1] Sample codes are available on `https://github.com/kfukami/Voronoi-CNN`.

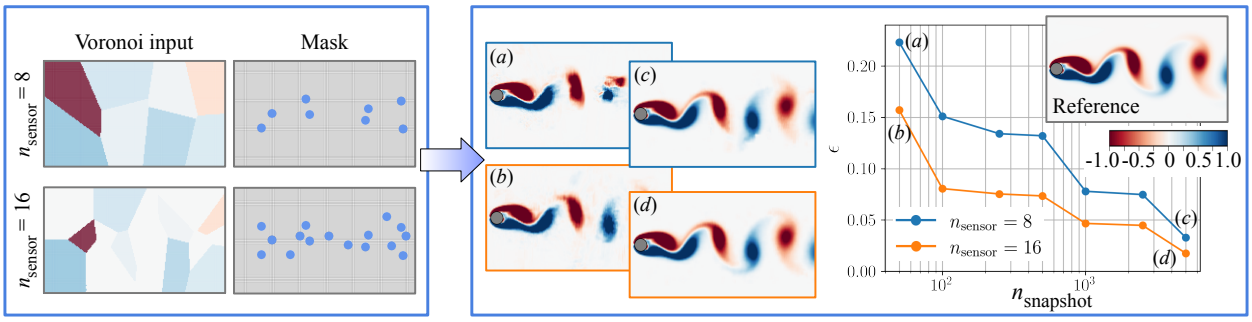

Figure 4.2: Voronoi-tessellation aided spatial data recovery of a two-dimensional cylinder wake with $n_{\mathrm{sensor}} = 8$ and 16. The input Voronoi image, input mask image holding sensor locations, and the reconstructed vorticity field are shown. Dependence of the reconstruction ability on the number of training snapshots is also shown. (a) $\{n_{\mathrm{sensor}}, n_{\mathrm{snapshot}}\} = \{8, 50\}$, (b) $\{n_{\mathrm{sensor}}, n_{\mathrm{snapshot}}\} = \{16, 50\}$, (c) $\{n_{\mathrm{sensor}}, n_{\mathrm{snapshot}}\} = \{8, 5000\}$, and (d) $\{n_{\mathrm{sensor}}, n_{\mathrm{snapshot}}\} = \{16, 5000\}$.

The spatial domains to be discretized by Voronoi tessellation and the high-resolution data are taken to be the same size. All grid points in each portion of the Voronoi image have its representative sensor value. Since Voronoi tessellation provides a structured-grid representation of measurements from arbitrary placed sensors, the present approach enables us to use existing CNNs devised for structured grid data. Note that a Voronoi tessellation needs to be performed solely once if sensors are stationary. If the number of sensors change over time, only local regions in direct vicinity of added or removed sensors need to undergo tessellation in an adaptive manner.

4.3 Applications

We demonstrate the use of the present Voronoi-based CNN for global fluid flow reconstruction. Our examples include laminar cylinder wake, geophysical data, and three-dimensional wall-bounded turbulence, which contain strong nonlinear dynamics over a wide range of spatio-temporal scales.

4.3.1 Example 1: two-dimensional cylinder wake

We first consider the Voronoi-based fluid flow reconstruction for a two-dimensional unsteady laminar cylinder wake at a diameter-based Reynolds number $Re_D = 100$. The training data set is prepared with a direct numerical simulation (DNS) (TC07; CT08) which numerically solves the incompressible Navier–Stokes equations. In this study, we consider the flow field data around a cylinder body for the training and demonstration, i.e., $((x/D)^*, (y/D)^*) = [-0.7, 15] \times [-5, 5]$ and $(N_x, N_y) = (192, 112)$. The vorticity field is used for both input and output attributes to the CNN model in this case. The training data spans approximately 4 vortex shedding periods. We examine the dependence of the reconstruction on the amount of training data. The number of sensors n_{sensor} is set to 8 and 16 with fixed input sensor locations for both training and testing.

The reconstructed fields are shown in figure 4.2. The reconstructed vorticity fields are in excellent agreement comparing to the reference vorticity field ω and in terms of the L_2 error norm $\epsilon = ||\omega_{\text{ref}} - \omega_{\text{ML}}||_2/||\omega_{\text{ref}}||_2$, where ω_{ref} and ω_{ML} denote the reference and the reconstructed vorticity fields, respectively. It can be seen from the reconstructed vorticity field that the vortices and shear layers in the near and far wakes are provided by the present deep learning technique with great accuracy and detail. The vorticity field for $n_{\text{sensor}} = 8$ shows some low-level reconstruction error due to the low number of sensors. When n_{sensor} is doubled to 16, we observe the error in the reconstruction is reduced by half with accurate recovery of the global flow field. Furthermore, reasonable data recovery can be achieved with $n_{\text{sensor}} = 16$ using as few as 50 training snapshots.

4.3.2 Example 2: NOAA sea surface temperature

Next, let us consider the NOAA sea surface temperature data collected from satellite and ship-based observations (`http://www.esrl.noaa.gov/psd/`). The data is comprised of weekly observations of the sea surface temperature with a spatial resolution of 360×180. We use 1040 snapshots spanning from 1981 to 2001, while the test snapshots are taken from 2001 to 2018. For this example, we take the sensors to be placed randomly over the water. The number of

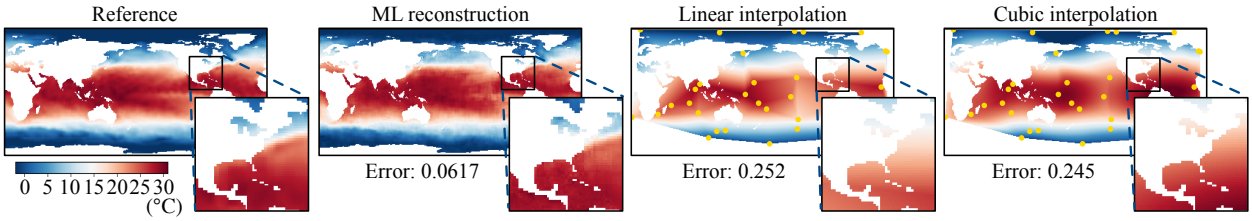

Figure 4.3: Comparison of spatial data recovery for NOAA sea surface temperature with $n_{\text{sensor}} = 30$.

sensors for training is set to $n_{\text{sensor,train}} = \{10, 20, 30, 50, 100\}$ with 5 different arrangements of sensor locations, amounting to 25 cases. The sensor locations are randomly provided for each snapshot. For the test data, we also consider unseen cases with 70 and 200 sensors such that $n_{\text{sensor,test}} = \{10, 20, 30, 50, 70, 100, 200\}$. These numbers of sensors for the test data correspond to $\{0.0154\%, 0.0309\%, 0.0463\%, 0.0772\%, 0.108\%, 0.154\%, 0.309\%\}$ against the number of grid points over the field. Both seen and unseen sensor locations for all numbers of sensors are considered for the present test demonstrations. We emphasize that only a *single* machine learning model is trained and used for all combinations of sensor numbers and sensor placements.

Let us demonstrate the global sea surface temperature reconstruction in figure 4.3. As a test case, we use a low $n_{\text{sensor}} = 30$. The reconstructed global temperature field by the present model shows great agreement with the reference data. This figure also reports the L_2 error norm $\epsilon = ||T_{\text{ref}} - T_{\text{ML}}||_2/||T_{\text{ref}}||_2$, where T_{ref} and T_{ML} are respectively the reference and reconstructed temperature fields. We here also compare our results to standard linear and cubic interpolation. Since those are simple methods, fine structures cannot be recovered and the L_2 errors are larger than that of the present method. These trends are noticeable from comparing the zoomed-in temperature contours. The interpolation schemes are unable to reconstruct the fine-grained features of the temperature fields accurately. However, the proposed technique performs very well. In addition to enhanced reconstruction, the present method is able to recover the whole field, while classical interpolation methods cannot extrapolate beyond the convex hull covered by the sensors, as evident from figure 4.3. This observation also speaks to the significant advantage of the present model.

Next, let us assess how the current approach performs when the number of sensors are changed

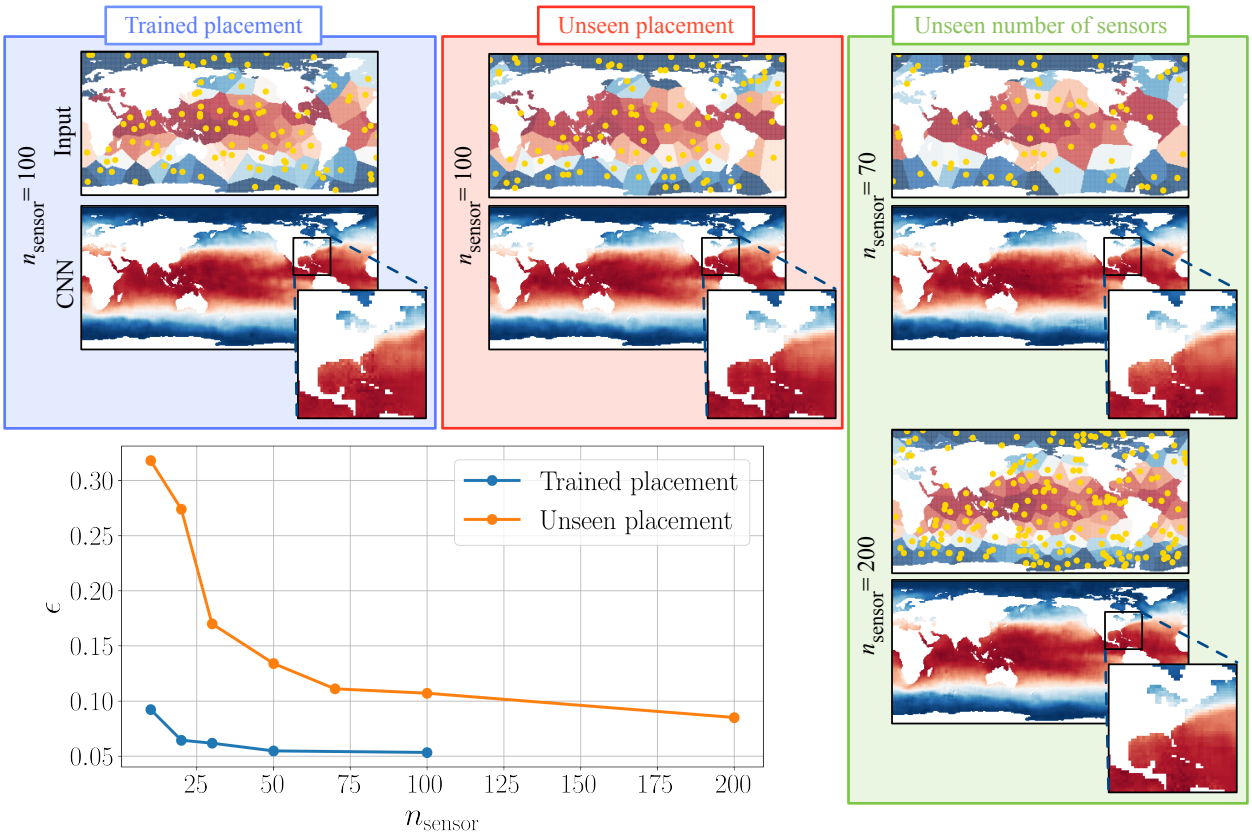

Figure 4.4: Voronoi based spatial data recovery of NOAA sea surface temperature. We show the representative reconstructed fields with $n_{\text{sensor}} = 100$ which corresponds to the number of sensors contained in the training data and $n_{\text{sensor}} = \{70, 200\}$ which correspond to cases not available in the training data set.

and when the sensors are in motion. We present the results for these cases in figure 4.4. With $n_{\text{sensor}} = 100$ being the number of sensors observed during training, the reconstructed sea surface temperature field is in agreement with the reference field for both trained (left) and unseen sensor (middle) placements. Cases of unseen placements correspond to instances of sensors coming online or offline during development and being in motion. Despite that the input Voronoi tessellation being significantly modified with the displaced sensors, the reconstruction is still successful. This highlights the effective use of the mask image holding information on sensor locations. What is also noteworthy is that successful reconstructions can be achieved with $n_{\text{sensor}} = 70$ and 200, which are numbers of sensors unseen during training. This corresponds to situations where sensors may

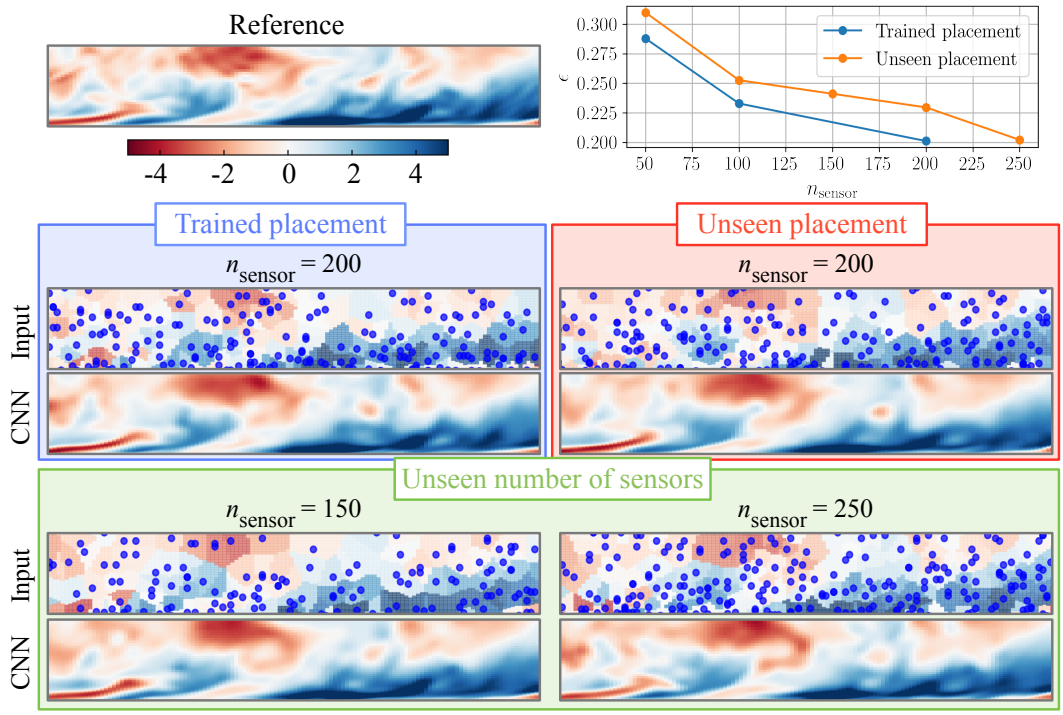

Figure 4.5: Voronoi tessellation-aided data recovery of turbulent channel flow. Considered are $x - y$ cross sections of streamwise velocity fluctuation u' reconstructed with $n_{\mathrm{sensor}} = 200$ (trained number of sensors) and $n_{\mathrm{sensor}} = \{150, 250\}$ (untrained number of sensors). The error convergence over n_{sensor} is also shown.

come online or go offline during deployment.

The relationship between the number of input sensors and the L_2 error norm is also investigated. The error level of the test data with unseen placements (orange curve) is higher than that with trained placements (blue curve) as shown in figure 4.4. However, the present model achieves a reasonable estimation with an L_2 error being less than 0.1, even when the number of unseen sensors reaches 200. This result suggests that the present approach employing the Voronoi input and the mask image is robust for data sets where the number of sensors and the sensor placements vary considerably. It also demonstrates the advantage of the present idea that a single trained model alone can handle the global field reconstruction for arbitrary number of sensors and time-varying positions.

4.3.3 Example 3: turbulent channel flow

The above two problems contain strong periodicity in time, appearing as periodic vortex shedding and seasonal periodicity. To further challenge the present approach, let us consider a chaotic and dynamically rich phenomenon of turbulent channel flow. The flow field data is obtained by a direct numerical simulation of incompressible flow in a channel at a friction Reynolds number of $Re_\tau = 180$. Here, x, y, and z directions are taken to be the streamwise, wall-normal, and spanwise directions. The size of the computational domain and the number of grid points are $(L_x, L_y, L_z) = (4\pi\delta, 2\delta, 2\pi\delta)$ and $(N_x, N_y, N_z) = (256, 96, 256)$, respectively, where δ is the half width of the channel. Details of the simulation can be found in Fukagata et al. (FKK06). For the present study, $x-y$ section of a subspace is used for the training process, i.e., $x, y \in [0, 2\pi\delta] \times [0, \delta]$ with $(N_x^*, N_y^*) = (128, 48)$. The extracted subdomain maintains the same turbulent characteristics of the channel flow over the original domain, due to the symmetry of statistics in the y direction and homogeneity in the x direction. We consider here the fluctuating component of an $x - y$ sectional streamwise velocity u' as the variable of interest. For training, we use $n_{\text{snapshot}} = 10\,000$. The numbers of sensors for training data are chosen to be $n_{\text{sensor,train}} = \{50, 100, 200\}$ with 5 different cases of sensor placements. For the test data, we also consider the use of 150 and 250 sensors with both trained and untrained sensor placements such that $n_{\text{sensor,test}} = \{50, 100, 150, 200, 250\}$. This setting allows us to assess the robustness of our approach for varied numbers of sensor inputs analogous to Example 2, with consideration of both seen and unseen sensor locations for all numbers of sensors.

The performance of Voronoi-assisted CNN-based spatial data recovery for turbulent channel flow is summarized in figure 4.5 for $n_{\text{sensor}} = \{150, 200, 250\}$. These numbers of sensors amount to 2.44%, 3.26%, and 4.07% with respect to the number of grid points over the field. We observe that finer flow features can be accurately reconstructed from just 200 sensors indicating a remarkable degree of sparsity in measurement. Although error levels for unseen placement (i.e., the same number of sensors but at different locations) is higher than that for trained sensor placement, similar trends are obtained. Notably, reasonable reconstruction for both unseen number of sensors

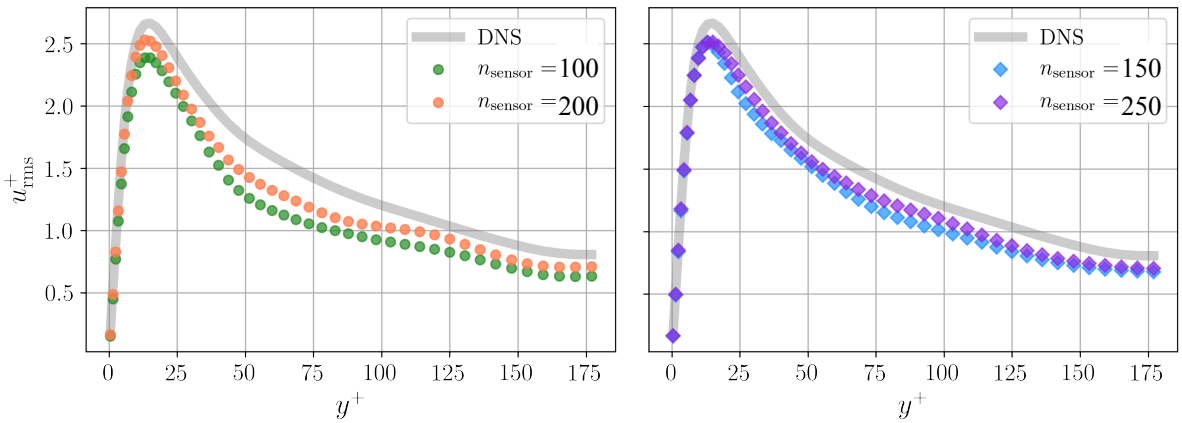

Figure 4.6: Root mean squared value of streamwise velocity fluctuation in turbulent channel flow.

and unseen input sensor placement as shown in the results for $n_{\text{sensor}} = \{150, 250\}$. As these results suggest, the present approach is a powerful tool for global reconstruction of complex flow fields from sparse sensor measurements.

To quantitatively analyze reconstructed flow field, we examine the root-mean-square of the streamwise velocity fluctuations, as shown in figure 4.6. The peak in the near-wall region and profile are captured well for all considered numbers of sensors. The underestimations against the reference DNS curve are likely due to the use of fluctuation components and the use of an L_2 minimization during the training process (FNK19). Since the supervised model minimizes a loss function through a training process, the machine learning model tends to provide solution near the average value of training data to reduce the loss function. This implies that the present machine learning model underestimates the fluctuations. Note that this is due to the supervised machine learning framework and is not an issue imposed by the unstructured grid placements or the use of Voronoi tessellation. This issue can be mitigated by using a loss function augmentation to the data, such as through z-scoring.

To further assess the practical application of the present model, we analyze the effect of input noise on reconstruction. Here, we consider the influence of two types of perturbations to the training data. Case I: Add noise to local sensor measurements $\boldsymbol{s}_m$ before performing the Voronoi tessellation; and Case II: Add noise to the Voronoi tessellation input $\boldsymbol{s}_V$. For Cases I and II, the

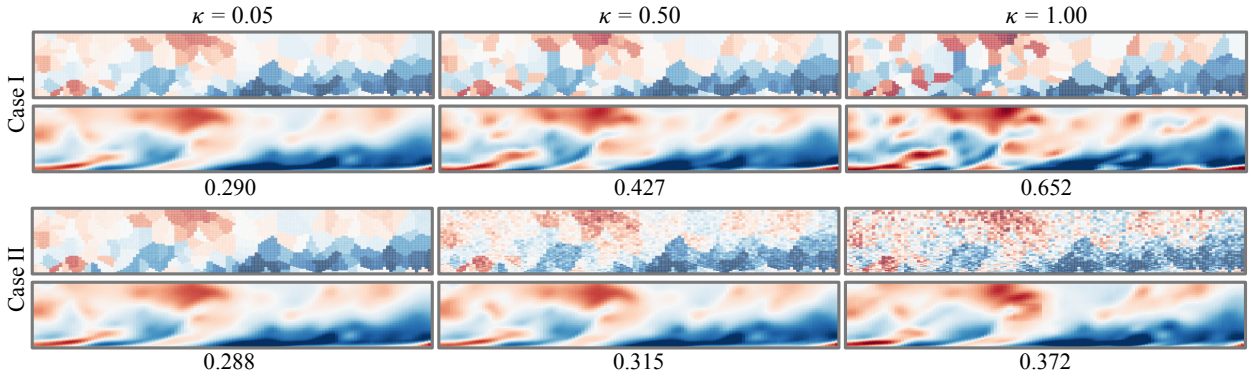

Figure 4.7: Robustness of the present reconstruction technique for noisy input for the example of turbulent channel flow. Input Voronoi tessellations (top) and reconstructed $x-y$ sectional flow fields (bottom) are shown for Cases I and II with $\kappa = 0.05, 0.5$, and 1.0. Reference solution is shown in figure 4.5.

error is assessed as

$$\epsilon_{\mathrm{I}} = ||\boldsymbol{q}_{\mathrm{ref}} - \mathcal{F}(\boldsymbol{s}_V(\boldsymbol{s} + \kappa\boldsymbol{n}), \boldsymbol{s}_m)||_2/||\boldsymbol{q}_{\mathrm{ref}}||_2, \tag{4.2}$$

$$\epsilon_{\mathrm{II}} = ||\boldsymbol{q}_{\mathrm{ref}} - \mathcal{F}(\boldsymbol{s}_V + \kappa\boldsymbol{n}, \boldsymbol{s}_m)||_2/||\boldsymbol{q}_{\mathrm{ref}}||_2, \tag{4.3}$$

respectively, where κ is the magnitude of the noise and $\boldsymbol{n}$ is the Gaussian distributed noise.

The reconstructed turbulent flows for $n_{\mathrm{sensor}} = 200$ with the noisy inputs are summarized in figure 4.7. As shown, the input Voronoi tessellations defined by Case II exhibit noisy features compared to those utilized by Case I since the noise for Case II is added after the preparation of the Voronoi tessellations. The influence of noise for Case I is larger than that of Case II. This is caused by the fact that the present CNN is trained for learning the relationship between the input Voronoi images and high-resolution flow fields, which implies that large perturbations to the sensor measurements produce greater error to the input images. If robustness is desired, we recommend adding noise to the sensor measurements prior to the preparation of the Voronoi-based input images during the training process. Overall, the present reconstruction technique is found to be robust against noise.

4.4 Discussion

Reconstruction of a global field variable from an arbitrary collection of sensors has been a long-standing challenge in engineering and the sciences. In order to address this problem, we presented a data-driven global reconstruction technique comprised of Voronoi tessellation and CNN. The present method relies on inputs of mask images holding the sensor location and Voronoi images representing the sensor measurements. The use of Voronoi tessellation translates the input sensor data to be represented on a uniform grid, which then enables the applications of CNNs to derive deep learning based reconstruction models. Three examples of global flow reconstruction from local sensor measurements demonstrated the accuracy and robustness of the current method.

Since CNNs have a large collection of toolsets from the image processing community, the present reconstruction approach is significant from the point of view of merging image processing with sensor data analytics. This perspective now allows engineers and scientists to move through the wealth of local and global measurements using data-driven techniques. Furthermore, Voronoi tessellation has the beneficial property of being able to discretize the spatial information in an adaptive manner only where sensor arrangements change in time. This provides computational savings and an opportunity to develop spatially adaptive techniques.

The present approach can be extended to enforce physical constraints and properties (RPK19; RYK20; HFM20b; LY19). For example, evolutional deep neural network (DZ21) has been able to enforce the divergence free constraint for incompressible flow. Another possible extension is the construction of robust models with regard to physical parameters by preparing proper training data sets (MFZ22; HFM20a; KKW21). To obtain generalizable models for turbulent data sets, unsupervised learning may also be helpful (KKW21).

The present data-driven approach was demonstrated with a set of local sensor measurements. As this method performs spatial field reconstruction at each time, changes in the number of sensors or motion of the sensors are easily accommodated. Having this flexibility allows for extensions to incorporate other types of measurements, such as under-resolved satellite based measurements or

particle image velocimetry. The current formulation also opens a path to incorporate intelligent sensor placements (MBK18) to further reduce reconstruction error and enhance the robustness with data redundancy. Moreover, the present method can be applied to cases where output attributes are different from the input data attributes. In such a scenario, the Voronoi-tessellation is akin to a projection operation to extend learning one step further. While we use the Voronoi CNN solely for flow reconstruction in the present paper, high-order turbulence statistics, e.g., root-mean-squared values of velocity fluctuations, can be extracted as well. The power and simplicity of the present approach will support scientific endeavor across a wide range of studies for complex data structures.

CHAPTER 5

Exploring interpolatory and extrapolatory vortical structures with data-driven nonlinear scaling with Buckingham Pi variables

The above studies have shown that nonlinear machine learning is powerful enough to reconstruct a global flow field from sparse sensors, they can often provide reasonable performance beyond training conditions in turbulent flow studies. While these cases may appear as extrapolations, of particular interest here is how interpolation and extrapolation for turbulent flows should be defined. In part of this question, this section examines how machine-learning models extract scale-invariant structures of turbulent flows across training and test data with the assistance of a data-driven nonlinear scaling (FGT23).

5.1 Motivation

Trained fluid mechanicians can identify similarities in vortical structures for a variety of turbulent flows. Even if there are scale or rotational differences, we can visually extract similar structures due to their geometrical features across spatial and temporal scales. Analogously, recent machine-learning models have capitalized on such structural similarities to achieve reliable performance for the given training data. However, it is also known that machine-learning models often achieve satisfactory performance even in untrained situations. Examples of models performing successfully beyond the training data include, turbulence modeling (GCS22), state estimation (GGI21), and

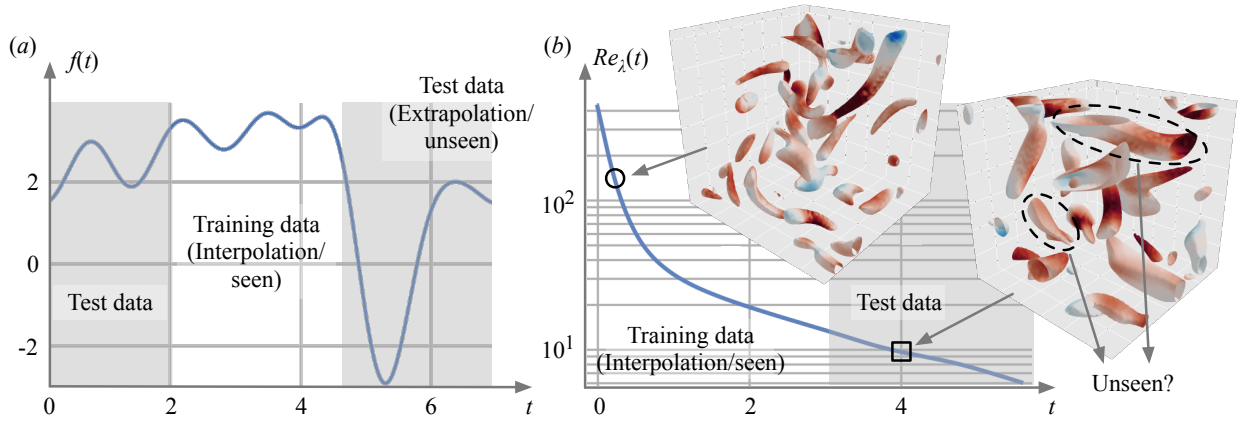

Figure 5.1: Concept of interpolation and extrapolation. (a) A one-dimensional example. (b) Evolution of three-dimensional decaying isotropic turbulence over $Re_\lambda(t)$.

super-resolution (KKW21). This suggests that machine-learning models are able to incorporate scale-invariant properties of the flows while optimizing the output to meet their objectives.

These observations imply that nonlinear machine-learning models are capturing data characteristics in a more holistic manner. Traditionally, interpolation and extrapolation of models have been associated with a particular variable or parameter (Dom12; Mar18), as illustrated in figure 5.1(a). In this example, test data outside of the training data is captured by the temporal variable t. In the case of more complex data set, such as turbulent flows, describing whether a certain type of vortical structure appears in training data or not requires additional considerations, beyond a single parameter such as the Reynolds number.

Given this motivation, we revisit the idea of interpolation and extrapolation in the context of turbulent flow structures. Here, we consider the capturing vortical structures that have certain similarities across training and test data to be "interpolation" and their structural features to be "seen." On the other hand, capturing structures in the test data that do not share similarities with those in the training data are referred to as "extrapolation" and their structures as "unseen." With machine-learning models known to perform well for approximating the nonlinear relationship between the input and output from a large collection of data, the presence of seen (or common) features can provide robust performance under untrained flow situations (KKW21; GCS22). The

current study presents a data-driven scaling approach to reveal seen/unseen structures of turbulent flow data in machine learning.

To assess rotational and shear similarities between small- and large-length scales in turbulent flows, we examine the flow field data in terms of the invariants of the velocity gradient tensor. In the present analysis, the scaled invariants are found through sparse nonlinear regression using non-dimensional parameters from the Buckingham Pi theorem (Buc14). The present approach offers the optimal nonlinear scalings of the invariants, uncovering scale-invariant vortical structures in a turbulent flow field. Analyzing the data distribution of the present scaled invariants reveals what types of flow structures are seen and unseen. Furthermore, the findings from this study provide guidance in the choice of machine-learning functions to offer robustness for scale-invariant vortical structures. The present paper is organized as follows. The proposed Buckingham-Pi sparse nonlinear scaling of the invariants is introduced in section 5.2. We demonstrate the current approach for three-dimensional isotropic turbulence in section 5.3. Concluding remarks are provided in section 5.4.

5.2 Methods

Machine-learning models for turbulent flow structures are known to remain accurate beyond the coverage of training data. This is the case especially when the nonlinear machine-learning models have scale and rotational invariances embedded in their formulations. To explain this extended validity of machine-learning models, this study aims to uncover nonlinear scalings that capture the similarities in turbulent vortical structures across a range of Reynolds numbers. The central hypothesis of this study is that the existence of such scalings enables nonlinear machine-learning techniques to effectively perform across different flow fields beyond the range of Reynolds numbers provided in the training data. With these identified scalings, turbulent flow structures that linearly and nonlinearly span across a range of scales may be considered *seen* beyond the training data due to their structural similarities.

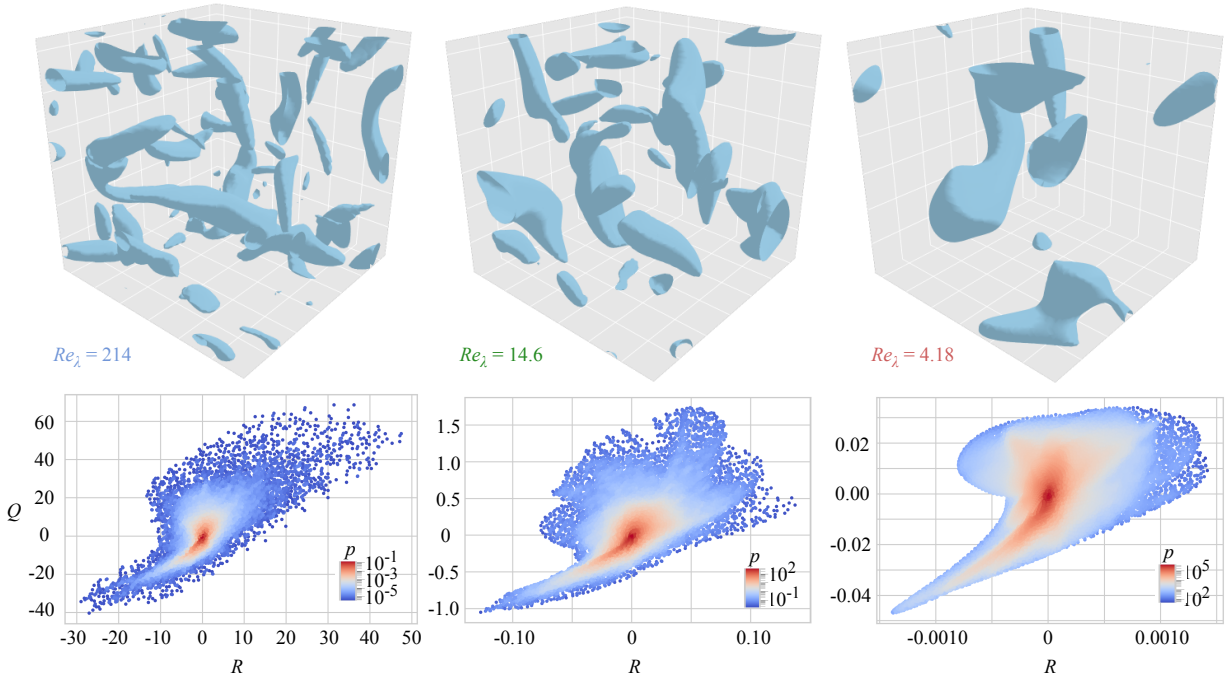

Figure 5.2: Example flow snapshots with $Q - R$ distributions of three-dimensional decaying turbulence at (a) $Re_\lambda = 214$, (b) 14.6, and (c) 4.18. Each distribution is colored by density. Turbulent vortices are visualized with (a) $Q = 10$, (b) 0.3, and (c) 0.02.

To examine turbulent flows, we consider the invariants of the velocity gradient tensor $\boldsymbol{A} = (\nabla \boldsymbol{u})^T$ such that the observations are independent of the frame of reference (CPC90). These invariants are $P = \text{trace}(\boldsymbol{A})$, $Q = \frac{1}{2}[P^2 - \text{trace}(\boldsymbol{A}^2)]$, and $R = \det(\boldsymbol{A})$. For the present study, we consider incompressible turbulent flows, which makes $P = \nabla \cdot \boldsymbol{u} = 0$. The remaining two invariants of Q and R characterize the local rotation and shear, respectively (OMS99). According to these invariants, the flow can experience vortex compression $(Q > 0, R < 0)$, vortex stretching $(Q > 0, R > 0)$, biaxial strain $(Q < 0, R < 0)$, and axial strain $(Q < 0, R > 0)$ (Dav15). These invariants will be nonlinearly scaled with non-dimensional Pi groups using a data-driven approach.

In this study, we consider three-dimensional incompressible decaying isotropic turbulence. The flow field data is obtained from direct numerical simulation with a Taylor microscale-based Reynolds number of $0.85 \leq Re_\lambda \leq 252$ (Chu08; GT21), satisfying $k_{\max}\eta \geq 1$, where $k_{\max}$ is the maximum resolvable wavenumber of the grid and η is the Kolmogorov length scale, to resolve all

important scales of motion. We present representative flows with their corresponding invariants on the Q–R plane over time in figure 5.2. The Reynolds number decreases as vortical structures evolve as their characteristic size increases. Even at a large time when $Re_\lambda = 4.18$, large-scale structures are still observed while the flow is under decay. During this process, invariants Q and R decrease in magnitude while the probability density functions of these invariants remain geometrically similar. This suggests that there is some level of scale invariance in the distributions of the turbulent vortical structures over the Q–R plane. That is, the decaying isotropic turbulence holds similar rotational and shear structures whose sizes vary over the Reynolds number.

Linear scaling for the Q–R distributions based on the kinematic viscosity ν and dissipation ϵ such as $Q/(\epsilon/\nu)$ and $R/(\epsilon/\nu)^{3/2}$ do not completely collapse the distributions, given their long tails especially at high Reynolds number, as presented in figure 5.2. This seems to be caused by the wide range of Reynolds numbers and strong unsteadiness contained in the present decaying turbulence data, implying that Kolmogorov's similarity hypotheses do not hold in an instantaneous manner. For example, skewness S_R of the linearly-scaled distribution for R in figure 5.2 is 2.74, 0.299, and 0.186 for $Re_\lambda = 214$, 14.6 and 4.18, respectively. These observations suggest that nonlinear scaling needs to be considered to accommodate non-equilibrium effects. Identifying such nonlinear scalings of Q and R distributions with data-driven techniques can also reveal how nonlinear machine learning extracts *seen* (or *common*) vortical structures that share similarities with structures outside of the training data sets. Moreover, *unseen* structures can be captured by uncovering the invariant space that do not overlap for the scaled data.

Let us consider scaling the invariants Q and R in a nonlinear manner using non-dimensional Pi groups from the Buckingham Pi theorem (1914), which distills a number of dimensional parameters into a smaller number of dimensionless groups (XSG22; BCB22). We assume that the scaling can be obtained through superposing appropriate polynomials of the Pi variables. Denoting these invariants as ϕ (either Q and R), the candidate polynomials are assumed to have the form of

$$\theta_k(\boldsymbol{x}, t) = \Pi_i^m(t)\Pi_j^n(t)\phi(\boldsymbol{x}, t), \quad \text{where} \quad i, j = 1, 2, \ldots, \quad m, n \in \mathbb{Z}, \quad k = 1, \ldots, n_L. \tag{5.1}$$

Here, n_L is the number of library-basis functions. Given these library candidates θ_k, we can express

the scaled invariants $\phi^*(\boldsymbol{x}, t)$ as

$$\phi^*(\boldsymbol{x}, t) = \sum_{k=1}^{n_L} a_k \theta_k(\boldsymbol{x}, t) \tag{5.2}$$

with $\boldsymbol{a} = (a_1, a_2, \ldots, a_{n_L})^T \in \mathbb{R}^{n_L}$. Spatiotemporal discretization of this equation yields $\boldsymbol{\Phi}^* = \boldsymbol{\Theta}\boldsymbol{a}$, where

$$\boldsymbol{\Phi}^* = \begin{bmatrix} \boldsymbol{\phi}^*(t_1) \\ \boldsymbol{\phi}^*(t_2) \\ \vdots \\ \boldsymbol{\phi}^*(t_{n_t}) \end{bmatrix} \in \mathbb{R}^{n_x n_t}, \quad \boldsymbol{\Theta} = \begin{bmatrix} \boldsymbol{\theta}_1(t_1) & \boldsymbol{\theta}_2(t_1) & \ldots & \boldsymbol{\theta}_{n_L}(t_1) \\ \boldsymbol{\theta}_1(t_2) & \boldsymbol{\theta}_2(t_2) & \ldots & \boldsymbol{\theta}_{n_L}(t_2) \\ \vdots & \vdots & \ddots & \vdots \\ \boldsymbol{\theta}_1(t_{n_t}) & \boldsymbol{\theta}_2(t_{n_t}) & \ldots & \boldsymbol{\theta}_{n_L}(t_{n_t}) \end{bmatrix} \in \mathbb{R}^{n_x n_t \times n_L} \tag{5.3}$$

with $\boldsymbol{\phi}(t) = (\phi(x_1, t), \ldots, \phi(x_{n_x}, t))^T \in \mathbb{R}^{n_x}$ and $\boldsymbol{\theta}_k(t) = (\theta_k(x_1, t), \ldots, \theta_k(x_{n_x}, t))^T \in \mathbb{R}^{n_x}$ being the scaled invariant and the library candidate, respectively, discretized in space. Here, the invariants are spatiotemporally stacked into a tall vector. The coefficients $\boldsymbol{a}$ are determined through the sequential threshold least squares method (BPK16a), promoting sparsity of the coefficient matrix in a computationally efficient manner (FMZ21).

For the present decaying turbulence, the Taylor length scale λ can be expressed as the function of the characteristic velocity u (the square root of the spatially averaged kinetic energy), the kinematic viscosity ν, the computational domain size L, and viscous dissipation ϵ such that $\lambda = f(u, \nu, L, \epsilon)$. Through the use of Buckingham Pi theorem, we can find three Pi variables, which namely are $\Pi_1 = u\lambda/\nu$, $\Pi_2 = uL/\nu$, and $\Pi_3 = \epsilon\nu/u^4$. The first Pi variable Π_1 is the Taylor Reynolds number Re_λ. In the present study, we take these Pi variables as a function of time. Given these Pi variables, we can construct the library candidates for equation (5.1) as first and second-order polynomials of the Pi variables such that

$$\begin{aligned} \{&\Pi_1,\ \Pi_2, \Pi_3,\ \Pi_1^{-1},\ \Pi_2^{-1},\ \Pi_3^{-1},\ \Pi_1^2,\ \Pi_2^2,\ \Pi_3^2,\ \Pi_1^{-2},\ \Pi_2^{-2},\ \Pi_3^{-2}, \\ &\Pi_1\Pi_2,\ \Pi_2\Pi_3,\ \Pi_3\Pi_1,\ \Pi_1^{-1}\Pi_2,\ \Pi_2^{-1}\Pi_3,\ \Pi_3^{-1}\Pi_1, \ldots,\ \Pi_i^m\Pi_j^n,\ \ldots\}, \end{aligned} \tag{5.4}$$

where $|m| + |n| \leq 2$.

With the Buckingham Pi-based library matrix $\boldsymbol{\Theta}$, we seek coefficients $\boldsymbol{a}$ by maximizing the similarity of data distributions of the invariants over space and time. Here, we utilize the Kullback–Leibler (KL) divergence (KL51) to assess the difference between a probability distribution f_1 and

the reference probability distribution f_2. For two probability (data) distributions, the KL divergence is defined as

$$D(f_1||f_2) \equiv \int_{-\infty}^{\infty} f_1(\boldsymbol{\phi}^*)\log\frac{f_2(\boldsymbol{\phi}^*)}{f_1(\boldsymbol{\phi}^*)}\mathrm{d}\boldsymbol{\phi}^*. \tag{5.5}$$

The minimization of the KL divergence finds the optimal coefficients $\boldsymbol{a}^*$ for maximum similarity of the scaled invariant distributions, which yields an optimization problem of $\boldsymbol{a}^* = \mathrm{argmin}_{\boldsymbol{a}}[D(f_1||f_2)]$. Below, the data distribution from a snapshot at high Re_λ is used as the reference f_2.

5.3 Results

We apply the present nonlinear scaling analysis to three-dimensional decaying isotropic turbulence over $0.85 \leq Re_\lambda \leq 252$. The present data is comprised of 800 snapshots over time and 64^3 grid points in a tri-periodic cubic domain. Here, we aim to (1) uncover the nonlinear influence of characteristic variables on the evolution of the invariants Q and R, (2) identify common (seen) vortical flow features through the scaled invariants, and (3) provide guidance on proper training and formulation of machine-learning models.

Based on sparse regression, we find the scaling factors for Q and R to be

$$Q^* = (5.76\Pi_1 + 4.17\Pi_2^{-2} - 3.59\Pi_2\Pi_3)Q, \tag{5.6}$$

$$R^* = (5.53\Pi_1 - 0.826\Pi_2^{-1} + 4.42\Pi_2^{-2} - 3.44\Pi_2\Pi_3)R. \tag{5.7}$$

While isotropic turbulence is complex, the nonlinearly scaled invariants turn out to be surprisingly compact in their expressions. For both scaled invariants, we have Π_1 which is the Taylor Reynolds number Re_λ. This reflects the decaying nature, corresponding to the fact that the data spread on the Q–R plane shrinks with decreasing Taylor Reynolds number over time, as shown in figure 5.3(a). The present scaling also identifies the influence of $\Pi_2 = uL/\nu$, the box-size-based Reynolds number, revealing that the computational domain size influences the turbulent flow, especially as time advances and vortical structures become comparable in size to the computational domain. This is evident from the inverse and quadratic inverse nature of the scalings. The size of the periodic

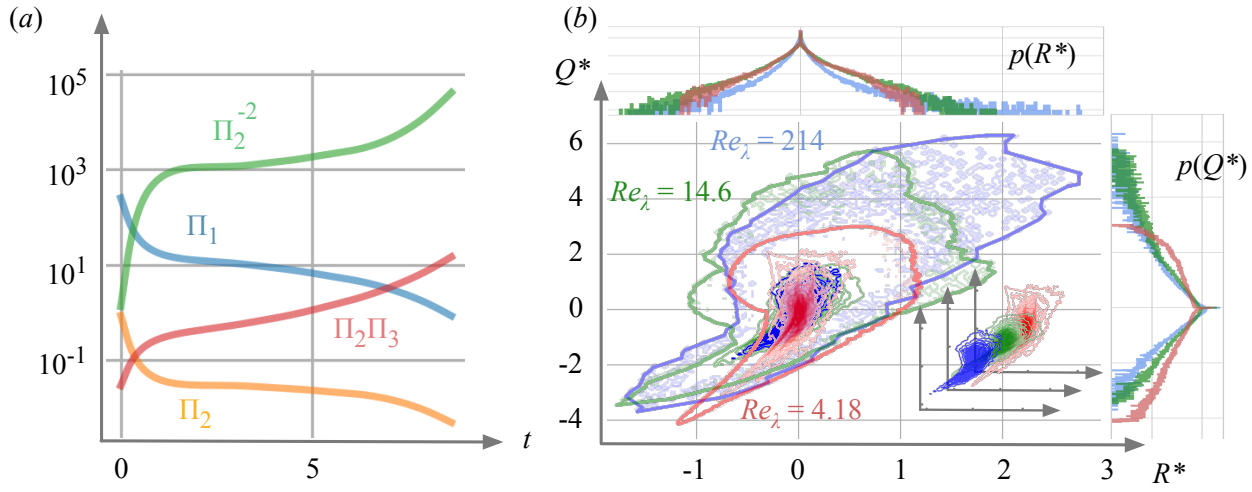

Figure 5.3: The data-driven Buckingham Pi scaling for three-dimensional decaying turbulence. (a) The time series of the identified non-dimensional variables. (b) Scaled Q^* and R^* invariants with their probability density functions.

box affects not only the large-scale vortical motion over the domain but also the energy dissipation of turbulence (Dav15).

Furthermore, the present analysis uncovers the importance of $\Pi_2\Pi_3 = uL/\nu \cdot \epsilon\nu/u^4 = \epsilon L/u^3$, which is the ratio between the instantaneous energy dissipation rate determined by small length scales and the cascading energy flux from the system-size vortices. Thus, $\Pi_2\Pi_3$ plays a similar role to the dissipation coefficient $C_\epsilon \equiv \epsilon l/u^3$, quantifying the degree of non-equilibrium (Vas15), i.e., the violation of Kolmogorov's similarity. Although $\Pi_2\Pi_3$ is constant when the energy flux of large-scale vortices and energy dissipation are in balance, that is not the case for the present decaying turbulence (GV16). The present $\Pi_2\Pi_3$ accounts for the time delay of energy-cascade process between energy flux and dissipation due to strong nonlinearities in decaying turbulence. This is achieved by correcting non-equilibrium effects in a nonlinear manner.

Next, the identified scalings are applied to the original Q and R data distributions, as shown in figure 5.3(b) along with their probability density functions. The identified factors in equations 5.6 and 5.7 yield the optimal overlap of Q^* and R^* over space and time. The scaled data distribution for the high Reynolds number flow spreads over a larger area than that for the low Reynolds number,

especially for $Q^* > 0$. This implies high occurrence of vortex stretching and compression at high Reynolds number.

Let us focus on the vortical structures for overlapping and non-overlapping regions of the data over the Q^*–R^* plane, as illustrated in figure 5.4. For $Q^* > 1$, similar shapes of vortical elements can be observed across a range of length scales. These identified vortical structures are assessed as 'interpolatory' (common) with the present scaling approach. The isosurfaces of $Q^* > 3$ are also visualized in figure 5.4. These strong rotational elements that barely appear in low Reynolds number flows are 'extrapolatory' structures. Moreover, such 'extrapolatory' vortical structures against the low-Re flow field can be seen in the portion of $R^* < -1.2$ and $R^* > 1.2$. The region of $Q < 0$ and $R < 0$ corresponds to biaxial strain, while that of $Q > 0$ and $R > 0$ reflects vortex stretching (Dav15). Hence, the scaled data distribution suggests that these structures caused by strong biaxial strain and vortex stretching correspond to 'extrapolation' for the present turbulence data. The scaled Q–R data distribution gives insights into turbulent flows, in addition to the identified scaling.

The present Buckingham-Pi-based sparse nonlinear scalings can identify interpolatory and extrapolatory vortical structures in isotropic turbulence. Nonlinear machine-learning models are likely to capture the characteristics and behavior of what we refer to as the interpolatory structures even in untrained situations. This explains why well-trained machine-learning models may perform well beyond their training data. However, we caution that when the test data includes extrapolatory structures, machine-learning models are no longer guaranteed to be valid. With regard to these points, classifying interpolatory and extrapolatory structures solely by Re_λ is not encouraged for assessing nonlinear machine-learning models.

Based on the insights from the scaled invariants above, let us consider machine-learning-based super-resolution reconstruction of turbulent flows (FFT23). Super resolution reconstructs the high-resolution flow field $\boldsymbol{q}_{\mathrm{HR}}$ from its low-resolution data $\boldsymbol{q}_{\mathrm{LR}}$ with a reconstruction model $\mathcal{F}$ through $\boldsymbol{q}_{\mathrm{HR}} = \mathcal{F}(\boldsymbol{q}_{\mathrm{LR}})$. Recently developed machine-learning-based super-resolution analysis captures the nonlinear relationship between small (unresolved) and large-scale (resolved) structures. This

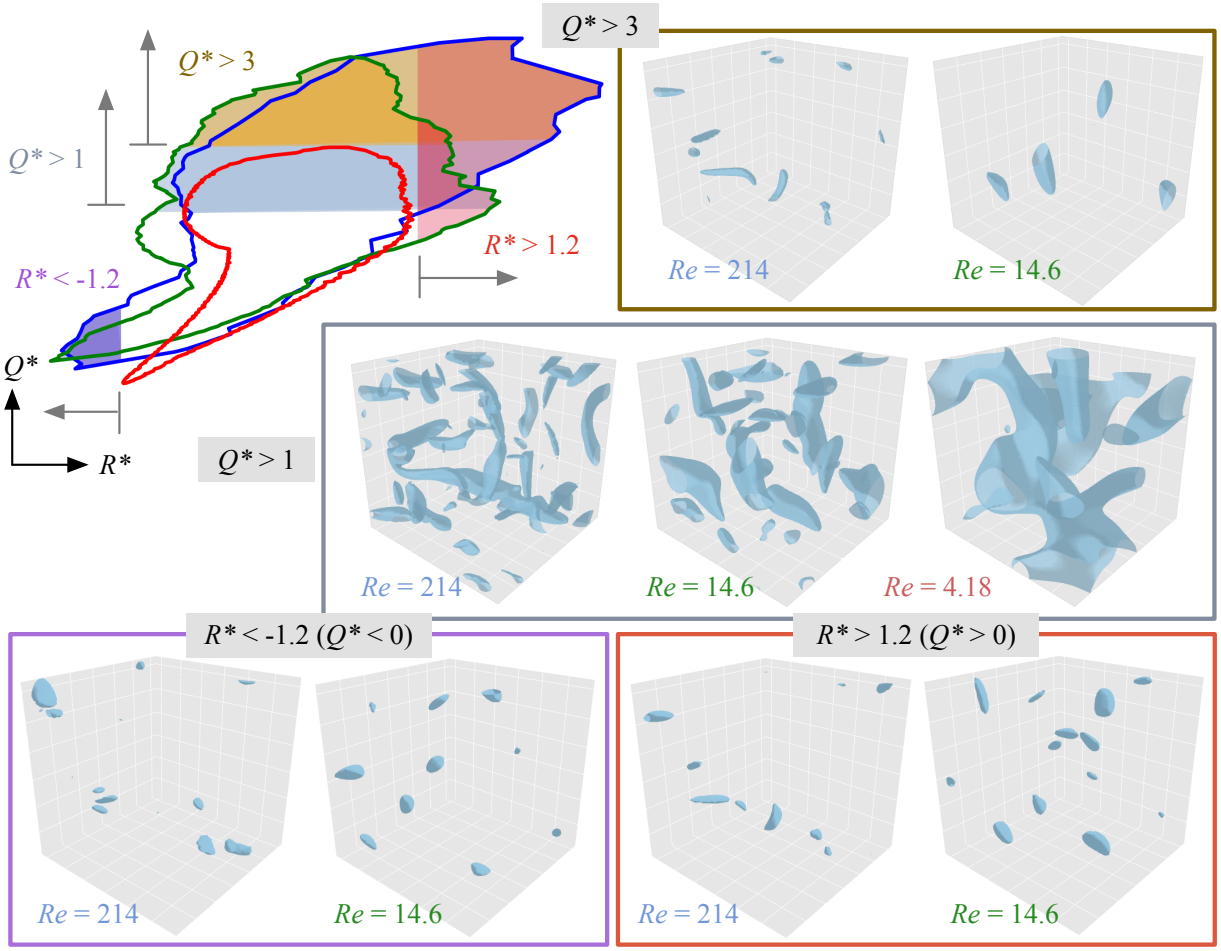

Figure 5.4: Interpolatory and extrapolatory vortical structures in three-dimensional decaying isotropic turbulence.

study considers the ability of machine-learning-based reconstruction to recognize and reconstruct *common* turbulent flow structures for a variety of flow field snapshots, even outside of the training data.

For super-resolution reconstruction of turbulent flows, a machine-learning model should be carefully constructed to account for a range of spatial length scales while enforcing rotational and translational invariance of vortical structures. To satisfy these properties, we use the hybrid downsampled skip-connection/multi-scale (DSC/MS) model (FFT19b). The DSC/MS model based on convolutional neural network (LBB98) is composed of three main functions: namely, (A) up/downsampling

operations, (B) skip connection, and (C) multi-scale filters. The up/downsampling provides robustness against rotation and translation of vortical structures. The skip connection allows communication between the input low-resolution data and the intermediate output of the DSC model, which is crucial in learning a step-by-step internal process towards the high-resolution output from the low-resolution input while expanding the dimension of the flow field snapshot (HZR16). The multi-scale filters apply filtering with a number of different sizes of them (e.g., three here) in parallel to capture a broad range of scales in turbulent flows. Further details on the present neural network model are in Fukami et al. (FFT19b). We will discuss which function inside the present model contributes to gaining robustness for scale invariance later.

Here, we consider two cases of training and testing for super-resolution reconstruction of turbulent flows: (1) a model trained with a low-Re_λ data set and tested with a high-Re_λ data set (low-Re_λ training); (2) a model trained with a high-Re_λ data set and tested with a low-Re_λ data set (high-Re_λ training). We expect that the low-Re_λ training cannot cover the non-overlapping portion of the scaled invariants, which corresponds to extrapolation. The high-Re_λ training, which covers a wide portion of the scaled invariants, may amount to interpolation in terms of the turbulent flow structures. For the present analysis with the two training scenarios, the threshold Re_λ between the low- and high-Re_λ training cases is set to $Re_\lambda = 15$. The velocity vector is used as data attributes $\boldsymbol{q}$ with $\mathcal{F}$ reconstructing the high-resolution flow field on 64^3 grids from the low-resolution data on 4^3 grid.

The reconstructed flow fields are shown in figure 5.5(a). The vortical flows are visualized using Q-criteria and colored by the third invariant R computed from the reconstructed velocities. For the low-Re_λ training case, the model reconstructs the vortical structures for the training Re_λ with an L_2 error of approximately 0.1. In contrast, the visualized Q variable at the high-Re_λ exhibits significant level of error rendering the reconstruction grossly incorrect. Such high errors can be explained using the scaled variables in figure 5.5(b) due to the flow features residing over the non-overlapping region on the present plane. The high error is also observed around the bottom left of figure 5.5(b). This extrapolation region cannot be reconstructed with the low-Re_λ training

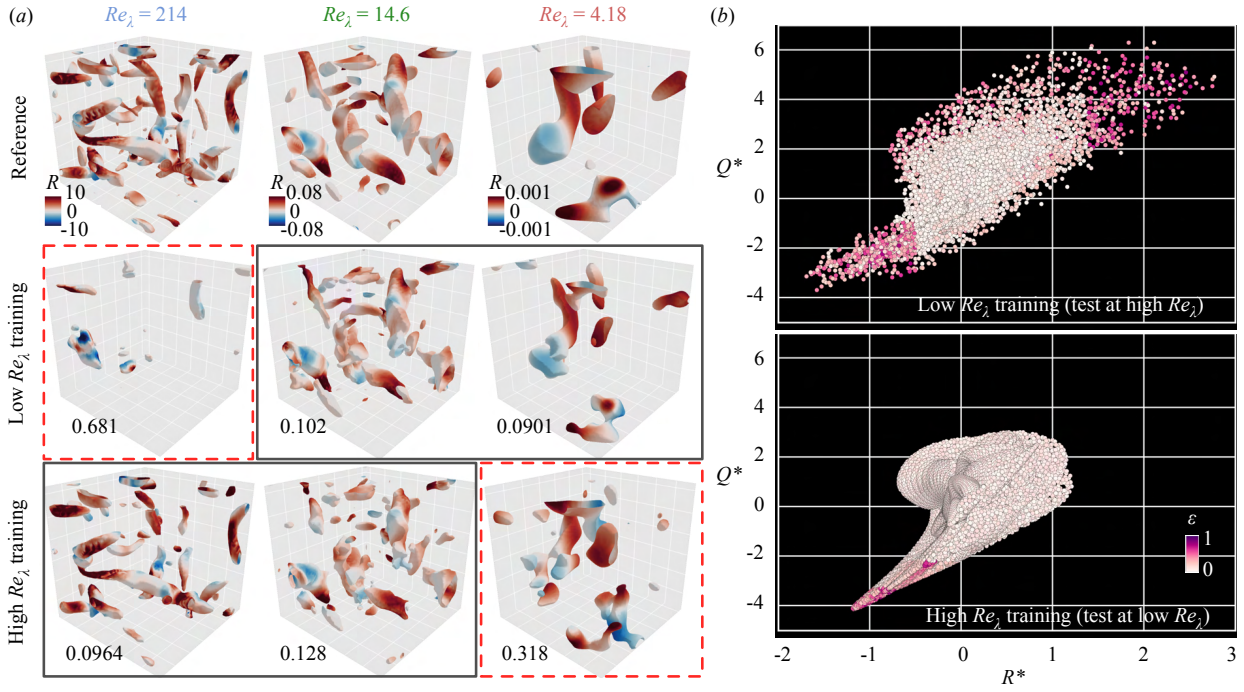

Figure 5.5: (a) Super-resolution reconstruction of three-dimensional decaying turbulence. The reconstructed flow fields are visualized with the Q-criteria, colored by R. The values underneath each figure represent the L_2 error norm. The gray and red boxes respectively highlight snapshots for training and testing Re_λ regime. (b) Scaled Q^* and R^* at test Re_λ's for low- and high-Re_λ training cases, colored by the spatial L_2 reconstruction error.

because these structures are barely seen in the low-Re_λ data sets, as presented in figure 5.4.

Next, let us consider the high-Re_λ training case. The reconstructed flow from the overlapping case (interpolation) is in agreement with the reference data. In contrast to the extrapolatory low-Re_λ training, reasonable reconstruction can still be achieved at $Re_\lambda = 4.18$. This suggests that the high-Re_λ training data holds insights into a wider range of vortical structures that also appear in the low Re_λ regime, which is confirmed from the scaled Q^* and R^* data. It is worth pointing out that the scaled invariants at the low Re_λ include some non-overlapping portion (scale-variant structures) in the region of $Q^* < 0$ and $R^* < 0$. This implies that the model trained with only the high-Re_λ regime cannot cover vortical structures of $Q^* < 0$ and $R^* < 0$. For better reconstruction over this regime, we need to include training data that covers $Q^* < 0$ and $R^* < 0$. Such an

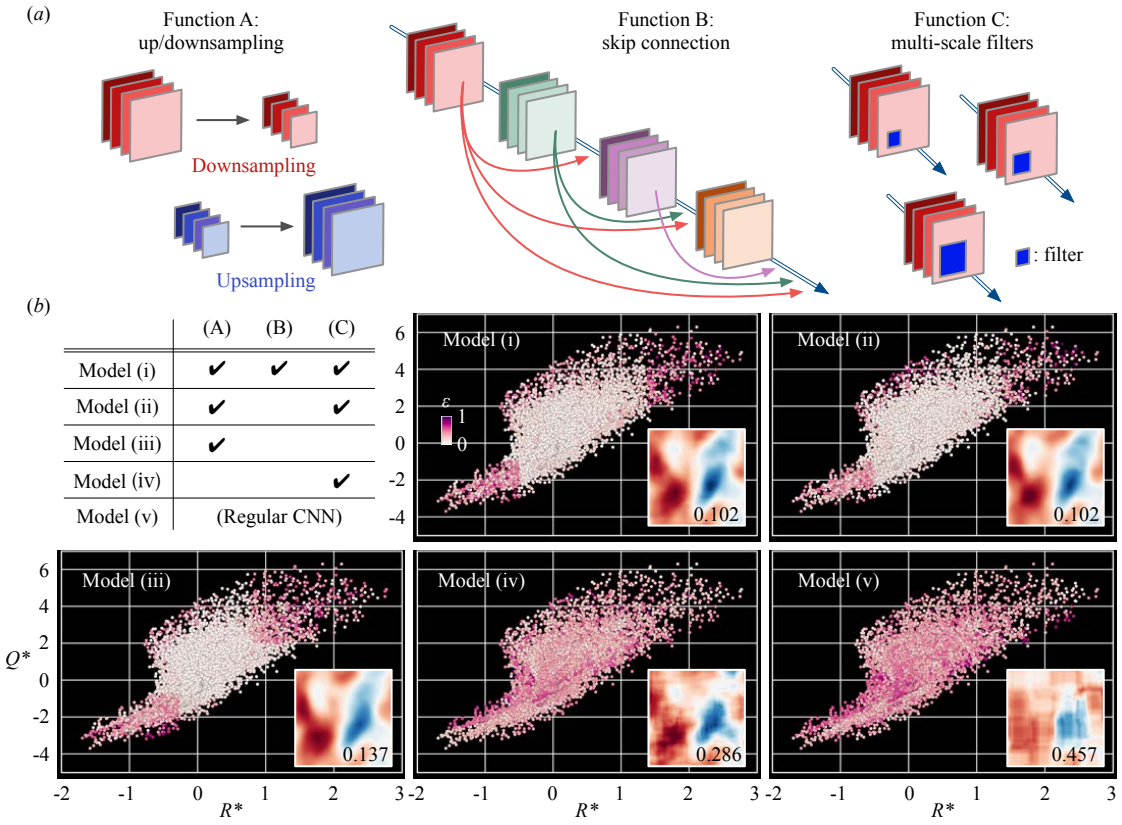

Figure 5.6: (a) The three functions used in the DSC/MS super-resolution model. (b) The scaled Q^*-R^* data for five models. The two-dimensional sections of the reconstructed streamwise velocity are also shown with velocity errors.

observation provides guidance on how the vortical flow data should be prepared to enable reliable reconstruction.

We further examine the nonlinearly scaled invariants to assess which inner functions of the machine-learning models contribute to robustness for scale-invariant regression. We here consider five models using the aforementioned functions A, B, and C (figure 5.6(a)):

1. the original DSC/MS model (functions A, B, and C),

2. the original model without the skip connection (functions A and C),

3. the original model with up/downsampling only (function A),

4. the original model with multi-scale only (function C),

5. a regular convolutional neural network (without any of the functions above).

We perform the low-Re_λ training for all of these five cases. The corresponding error distributions are presented in figure 5.6(b). For model (ii) which removes the skip-connection function from the baseline model, the error behavior on the scaled data is similar to that of the original model. A similar observation is seen for model (iii) which has no multi-filter functions. Since both models (ii) and (iii) include function A, up/downsampling operations are crucial for robust super-resolution reconstruction of turbulent flows.

This can be further confirmed with model (iv) which is comprised only of the multi-scale filters (function C). The reconstruction error is significantly higher without the up/downsampling operations. Including dimension compression and expansion plays an important role in obtaining robustness for scale-invariant characteristics, which agrees with a number of studies on CNNs for scale invariance characteristics in image science (JKR09; VP17). In contrast, multi-scale filters have secondary importance in reconstructing the flow (model (iv)) as evident from its comparison to the results from CNN (model (v)). While the regular CNN without functions A, B, and C returns pixelized flow fields, model (iv) achieves qualitative reconstruction. These findings suggest that robust turbulent flow reconstruction can be achieved by selecting machine-learning functions based on the implication of scaled invariants. Model effectiveness and accuracy should be carefully examined in terms of its construction and the richness of training data.

5.4 Concluding remarks

For nonlinear machine-learning models for turbulent flows, there is generally not a single parameter that can reveal whether such models are performing an interpolation or extrapolation. This is due to the turbulent flow data containing similarities in flow structures across a range of spatiotemporal scales. These properties contribute to machine-learning models being accurate beyond the coverage

of training data in some cases. To shed light on the validity of machine-learning models, we nonlinearly scaled the invariants of the velocity gradient tensor Q and R with non-dimensional parameters using a Buckingham Pi theorem-based sparse regression, which maximizes the similarity of invariant data distributions over space and time across Reynolds numbers. As a canonical turbulent flow example, we considered three-dimensional decaying isotropic turbulence for $0.85 \leq Re_\lambda \leq 252$. The present approach found nonlinear scalings that express the influence of the decaying nature of the present flow, domain size of the simulation, and non-equilibrium effects of energy cascade on the invariants Q and R. With the scaled invariants Q^* and R^*, we were able to determine that the training data lacked flow structures associated with strong biaxial strain and vortex stretching.

We further analyzed which types of machine-learning functions contribute to gaining robustness for scale-invariant vortical structures within the context of super-resolution reconstruction. We found that fluid flow reconstruction can be achieved for data of the overlapping portion on the scaled Q^*–R^* plane even under untrained Re_λ with an appropriate construction of machine-learning models. The present findings suggest that transfer learning could be effective for training nonlinear machine-learning models of turbulent flow across Reynolds number provided that extrapolatory structures do not alter the physics significantly (IG20; GGI21). Including fractional exponents for Pi variables would likely enhance the generalizability of the present method for discovering additional nonlinear scaling in turbulent flows. The present procedure to examine nonlinear scalings of turbulent flow structures provides guidance on how to develop robust machine-learning models and compile the necessary training data, enabling us to depart from naïve training and being unaware of the validity of these complex models.

CHAPTER 6

Low-dimensional manifold of vortical flows: an example of extreme aerodynamics with vortex-gust airfoil interaction

Successful reconstruction of vortical flows from sparse sensors suggests that flow fields possessing a large degree of freedom may be expressed with a few important variables. Once we find low-dimensional coordinates that can express the dynamics of given fluid flows while holding the essence of the original high-dimensional state, such low-dimensional representations can be used for a variety of applications such as reduced-complexity modeling and flow control. This section examines how we can optimally find low-dimensional representations of fluid flows using unsupervised machine learning with an example of extreme aerodynamic flows (FT23).

6.1 Motivation

Since the Wright brothers accomplished the first human-powered and controlled flight in 1903, a wide variety of aircraft has been developed for transportation, defense, observation, search, and rescue missions. What makes these aircraft uniquely different from other modes of transportation is their ability to stay aloft by taking advantage of aerodynamics. To support the development of these aircraft, the field of aerodynamics has undergone tremendous growth over the past century. Despite its expansive theory, the current aerodynamics is generally based on steady (cruise) or quasi-steady flight conditions with linear analysis or its nonlinear extensions for small perturbations (And91; KP01; Lei06).

We are now at an important transition point for aerodynamics. With novel materials and

enhanced powerplants/batteries becoming available over the past couple of decades, there have been tremendous efforts in developing and operating smaller size personalized air vehicles and unmanned air systems (PB06; SCC22; MAW16; PFM18; GMM18). They can traverse unconventional terrain, including mountainous and urban environments (FGD21; Gro14; WBM20) that were traditionally avoided by conventional aircraft. As a matter of fact, flight demonstrations of such air vehicles in calm weather have taken place in recent years (GGL21). These new and amazing flying vehicle concepts will likely revolutionize air-based transportation (LAD21; SCC22; STM21) and have already been realized for some cases (YYJ18; Kug19).

However, there are major challenges in operating small-scale aircraft under these complex airspace when adverse weather generates highly turbulent environments (FW15; JCS22; GHF21; DDD22; DMS20). Moreover, the increased occurrence of extreme weather caused by global warming limits the operations of aircraft. Flying small-scale aircraft near large natural or man-made structures in adverse weather face additional complications as these vehicles need to navigate through severe turbulence comprised of gusts and vortical disturbances, as illustrated in figure 6.1. These disturbances come in a variety of forms (MMW23) and are far more disruptive than what present-day commercial aircraft experience in inclement weather (Hob88). These extreme aerodynamic environments can be characterized by a manifestation of a large number of strong vortices with different strengths, sizes, and orientations generated by the surrounding structures (SHB23). Such a flight environment has been off-limits due to the fact that there is virtually no available theory for extreme aerodynamic problems and to avoid possible loss of aircraft.

With infinite scenarios of large and strong atmospheric disturbances hitting a flying vehicle, we cannot only focus on a single cruise condition but must also consider a whole array of cases in which wings experience extreme aerodynamic disturbances. These disturbances are characterized by a variety of parameters, including the size, strength, orientation, position, and geometry of the disturbances, necessitating massive experimental and computational campaigns if approached naively. With a single extreme aerodynamic simulation already producing a very large amount of flow field data, extensive parametric sweeps lead to an enormous collection of aerodynamic

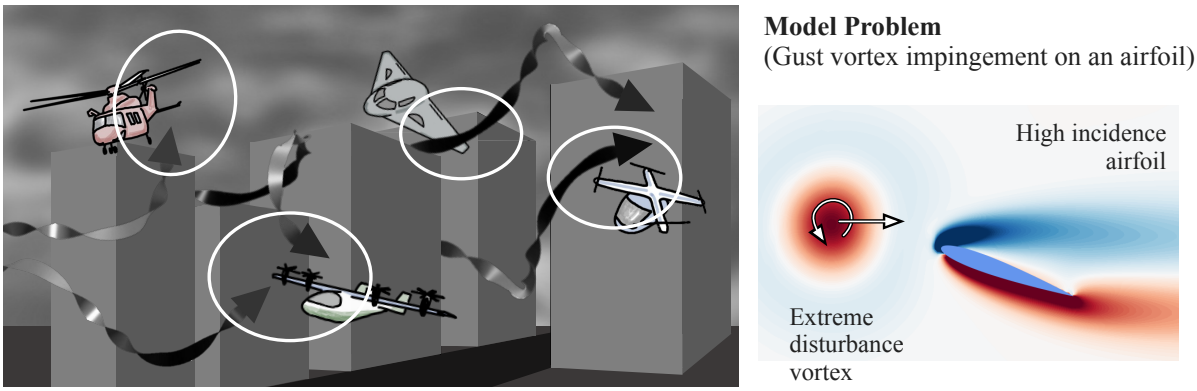

Figure 6.1: (Left) Illustration of possible extreme aerodynamic encounters by modern air vehicles in urban environment during adverse weather. Air vehicles operating in such an environment experience extreme level of unsteady aerodynamic forces due to strong gusts with spatial variations comparable to their vehicle size. (Right) Model problem of strong disturbance vortex impinging on an airfoil with vorticity distribution being visualized.

flow data and calls for significant computational and experimental resources. These extreme aerodynamic flows exhibit rich nonlinear behavior over a range of spatiotemporal scales that cannot be easily analyzed and modeled with existing theories.

One of the important parameters under such extreme aerodynamic situations is the gust ratio $G = u_{\text{gust}}/u_\infty$, which is ratio between the characteristic gust velocity u_{gust} and the translational velocity of the wing u_∞. For conditions of $G \gtrsim 1$, sustaining stable flight becomes challenging (JCS22; JC21). In the present work, we consider high levels of aerodynamic disturbance with $0 \leq G \leq 10$, and refer to cases of $G > 1$ as *extreme aerodynamics*. Strong gusts with $G > 1$ can be encountered in urban canyons, mountainous environments, and severe atmospheric turbulence. The goal of this study is to identify the unifying dynamics that a wing experiences from extreme gust disturbances. At the most fundamental level, the present problem requires the identification of the underlying nonlinear dynamics of the complex separated flows from an enormous amount of data in an efficient manner while gaining physical insights into extreme aerodynamics.

Although the aerodynamic influence of large-scale disturbances on lifting bodies take various

forms, the underlying dynamics are generally shared. In this study, we seek these dominant dynamics embedded in complex extreme aerodynamic flows. To achieve this objective, we examine the reduction of massive fluid flow data into a low-dimensional space in which the right set of variables describe the underlying extreme aerodynamic physics. This process is enabled by incorporating physical observables and ensuring that the gained insights are interpretable and beneficial for future aircraft operations and designs. In fact, we find that extreme aerodynamic flows can be compressed by a carefully designed nonlinear machine-learning technique to only three variables for a model problem of a strong vortex hitting a canonical airfoil. The present findings further suggest that the discovered manifold holds potential to support downstream tasks such as real-time flow estimation, dynamical modeling, flow control, and vehicle design.

6.2 Results

6.2.1 Extreme Vortex-Airfoil Interactions

We consider a strong vortex gust impacting an airfoil as a representative model problem for wings experiencing extreme atmospheric disturbances. The present model problem involves wake vortices shedding from a high-rise building, ships in rough seas, and mountain ridges (JCS22). The size of such strong vortices can be comparable to the size of the wing, exerting tremendously large lift and drag forces. In this study, we simulate two-dimensional incompressible flows with a vortex placed upstream of the wing with varied vortex size, strength, and initial position, as shown in figure 6.1. Because the airfoil wake responds differently for each combination of these disturbance settings, the resulting flow fields exhibit vastly different wake patterns and aerodynamic forces from case to case due to the nonlinear vortex dynamics, as presented in figure 6.2. As the vortex passes around an airfoil, the wing experiences massive flow separation (stall), which also causes the emergence of additional vortical structures. All of these flow structures interact nonlinearly, making the dynamics complex and difficult to predict and control.

This study considers two-dimensional extreme aerodynamic flows around a NACA 0012 airfoil

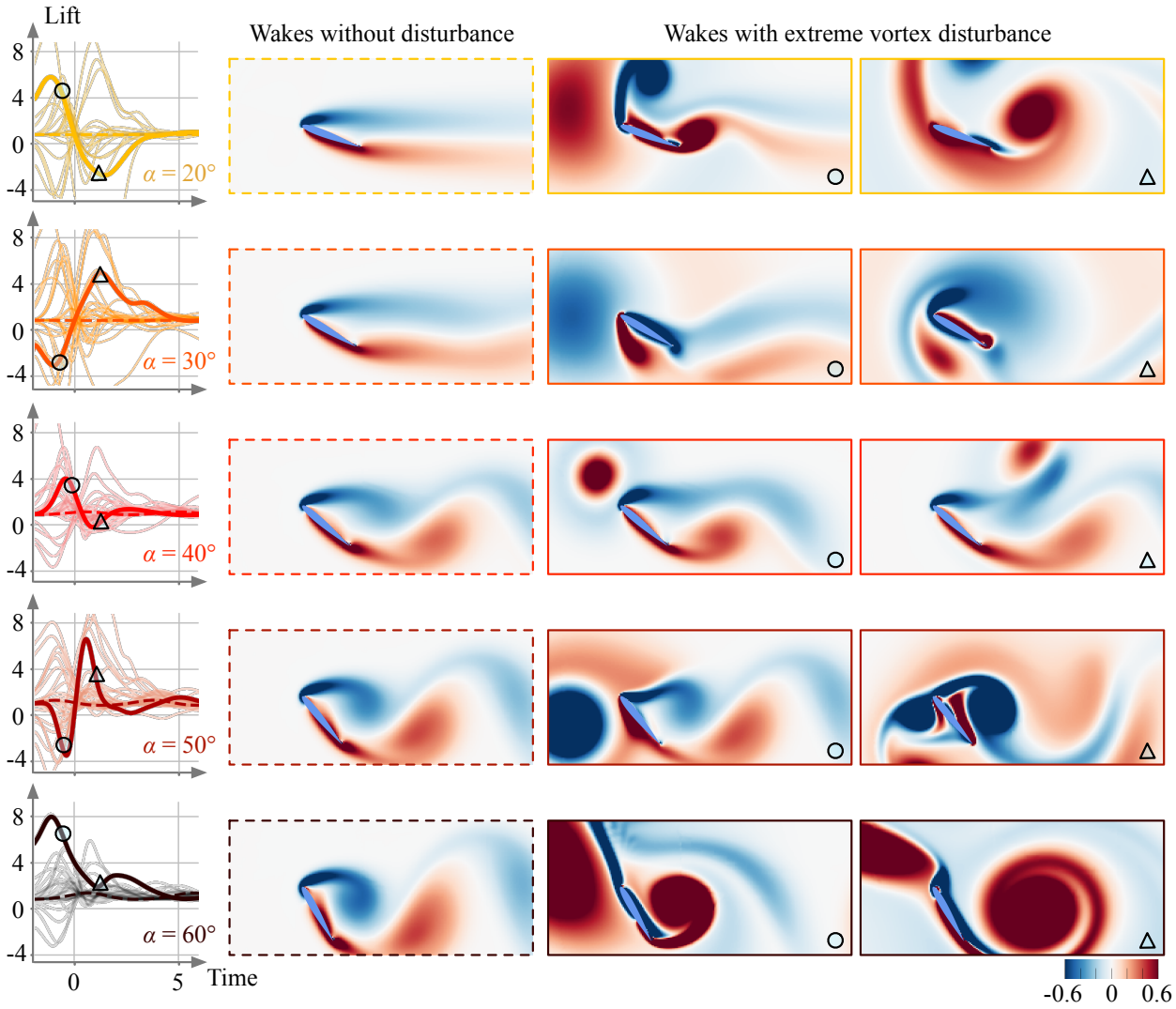

Figure 6.2: Examples of lift responses and vortical flows. Visualizations of the vorticity fields from times indicated by symbols ∘ and △ on the lift responses (thick lines associated with the visualized cases). The light-colored lift curves correspond to all lift responses considered in the present study. The shown color for each angle of attack is shared with other figures.

at a chord-based Reynolds number $\mathrm{Re} = u_\infty c/\nu = 100$. Here, u_∞ is the free-stream velocity, c is the chord length, and ν is the kinematic viscosity. The flow field is obtained with direct numerical simulation using an incompressible flow solver (HI04; HMI06). The airfoil is positioned in the free stream with its leading edge at the origin with angles of attack of $\alpha \in [20°, 60°]$, enabling us to cover cases of steady and unsteady wakes in undisturbed (baseline) cases. These wakes are disturbed with a gust vortex having an angular velocity profile (Tay18) of $u_\theta = u_{\theta,\max}(r/R)\exp[1/2 - r^2/(2R^2)]$, where the radius of the vortex is R.

The present disturbance vortex is characterized by the gust ratio $G \equiv u_{\theta,\max}/u_\infty \in [-10, 10]$ with its size relative to the wing chord $L \equiv 2R/c \in [0.5, 2]$ and is introduced upstream of the wing at $x_0/c = -2$ and $y_0/c \in [-0.5, 0.5]$. The combinations of these parameters provide a wide range of large and strong gust vortices hitting the wing at various locations. The flow field around the airfoil exhibits a rich dynamical response to the disturbance vortex characterized by a large parameter space comprised of $(\alpha, G, L, y_0/c)$. To fully resolve the dynamics over this parameter space, a substantial number of flow cases for different combinations of these parameters would be required. In general, Re is also another parameter but is fixed for this study at 100. While the gust vortices contained in actual atmospheric turbulence can be much more complex than what is considered here, the primary dynamics of large vortex core interacting with the wing is captured well at this Re at least in a two-dimensional manner. What is particularly important is to resolve the large vorticity source from the surface under local flow acceleration (WMZ07). These phenomena have relatively short time-scales compared to the much longer viscous scales associated with $\mathrm{Re} = 100$, making the current problem setup an appropriate test bed. In this study, we set the convective time to be zero when the center of the vortex arrives at the leading edge of the wing $x_0/c = 0$. The snapshots of the vorticity field and the lift history are examined in detail with data-driven analyses in what follows.

Without any external disturbances, the wing experiences steady aerodynamic lift forces at low angles of attack ($\alpha \lesssim 20°$) and moderate unsteady aerodynamic force fluctuations at higher angles of attack ($\alpha \gtrsim 30°$). These lift values are shown by the dashed lines for the different angles of

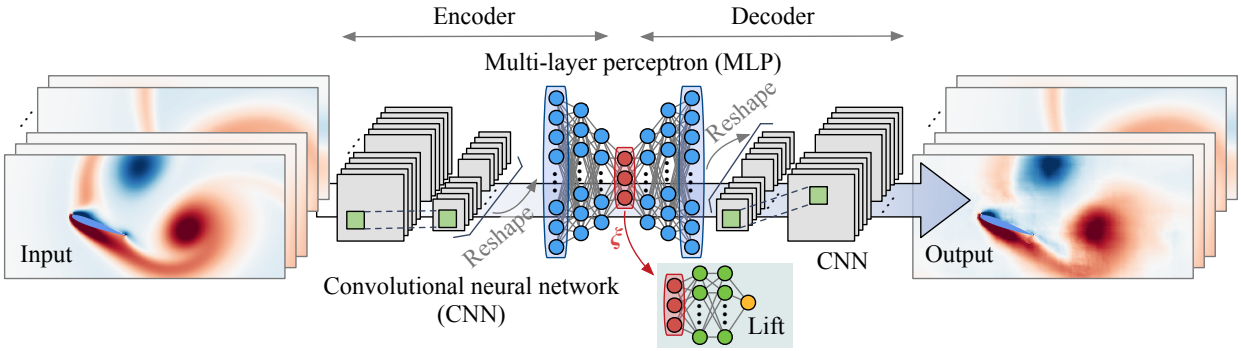

Figure 6.3: Nonlinear autoencoder. The vorticity field is taken as the input and output. The green shaded portion becomes active when embedding lift into the compression process.

attack in figure 6.2. The unsteady lift fluctuations are exerted by the von Karman vortices shedding from the leading and trailing edges, as visualized in figure 6.2. At this Reynolds number, these cases are periodic in time and constitute limit cycles.

When the wing encounters a strong gust vortex, the flow around the wing is significantly modified. The approaching vortex strongly influences the vorticity field around the wing and triggers large-scale vortex formation. For example, let us consider the flow field for a case shown in figure 6.2 for which a strong positive vortex with $G = 3.8$ hits a wing at $\alpha = 20^{\circ}$. Due to this disturbance, two large vortices are formed shortly after impact, generating massive separation due to the interaction of the gust vortex and the wing wake. These dramatic transient wake dynamics exert sharp increase in aerodynamic forces on the wing. In fact, the lift force increases 714% and drops 656% within a short duration of 1.8 convective time. Such a significant variation in the lift force makes controlling air vehicles tremendously difficult. While not shown, the moment experienced by the wing also undergoes a tremendous change. We also display a total of 100 force histories for cases of flows disturbed by extreme levels of gust vortices in figure 6.2. In all of these cases, the airfoil wake dynamics undergo large transient changes within a short amount of time with large aerodynamic force fluctuations with similar order of magnitudes. These violent disturbances not only destabilize flight but can also damage vehicle structures, making the analysis of these flows critically important.

Because of the nonlinear nature of the dynamics, flow around the airfoil responds differently to each different gust vortex with massive flow separation and large-scale formation of additional vortices, as visualized in figure 6.2. There is no aerodynamic model or theory that can easily describe the highly nonlinear nature of the extreme gust-airfoil interactions. What is especially challenging is that there is no simple scaling that collapses the collection of lift curves or the vortical flow fields due to the strong nonlinearity. This is an enormous burden for studying extreme aerodynamic flows since each and every case needs to be examined through painstaking computational or experimental campaigns that require significant resources. We re-emphasize that even for the present problem setup, there are a good number of parameters (vortex strength G, size L, position y_0/c, and airfoil angle of attack α) that necessitate a very large number of cases of extreme aerodynamic flows to map out the response dynamics. Practically speaking, such a campaign may not be possible for all gust encounters with limited computational resources. Therefore, it is desirable to capture the underlying dominant dynamics that form the basis of extreme gust response characteristics without having to rely on expensive simulations with a very large degree of freedom, which in this case is proportional to 2.88×10^4 grid (spatial) points to describe the instantaneous flow field and 1.26×10^5 temporal frames for sufficient spatiotemporal solutions for all cases. While we do have the Navier–Stokes equations as the governing partial differential equations to fully describe the dynamics, solving them in real time for practical air vehicle operations is out of the question.

For the aforementioned reasons, it is important to extract the dominant low-dimensional dynamics from the possible collection of extreme aerodynamic data sets. The rich responses to different gust vortices appear uniquely different from one snapshot to another but possess some common and identifiable features, including the disturbance vortex, flow separation, wake vortices, secondary vortices, shear layers, vortex roll-up, vortex pinch-off, and vortex deformation. The fact that these features are indeed identifiable by the trained eyes of fluid dynamicists suggests that there is likely some underlying low-dimensional representation of the high-dimensional complex dynamics. Thus, we aim to capture the key dynamics in a space comprised of a very small number of variables that can estimate the full state of the flow field and offer insights into the nonlinear dynamics of the

vortex-gust interaction. We find that a nonlinear autoencoder with physical observables illustrated in figure 6.3 achieves the present objective.

6.2.2 Identification of Extreme Aerodynamic Manifold

To find a low-dimensional space that captures the essential physics of extreme aerodynamic interactions between the gust vortex and the airfoil wake, we perform data-driven compression of the flow field. Herein, we consider cases with randomly-sampled parameters from $G \in [-4, 4]$, $L \in [0.5, 2]$, and $y_0/c \in [-0.5, 0.5]$.

First, let us consider the most commonly used linear dimensionality reduction technique, namely the principal component analysis (PCA), which is also known as the proper orthogonal decomposition (POD) (Jol02; BHL93; TBD17). With this method, the low-dimensional representation of a fluctuating variable is found by identifying the primary modes (or vectors) that best capture the variance about the mean. In the present study, we first analyze the vorticity fields over $(x, y)/c \in [-1.4, 4] \times [-1.2, 1.2]$, shown in figure 6.2 by applying PCA to determine the most vortically energetic components of the flow field.

Shown in figure 6.4 are the temporal variations of the first three PCA components ($\xi_1(t)$, $\xi_2(t)$, and $\xi_3(t)$) of the vorticity field data. The gray curves represent the whole collection of extreme aerodynamic data plotted in this coordinate space. Also highlighted are undisturbed baseline cases for $\alpha = 20°$ to $60°$. Here, we observe that the gray curves span a range of values over ξ_1, ξ_2, and ξ_3 in a seemingly incoherent manner. What is further problematic with this compression is the overlap of the baseline cases. These observations reveal that PCA struggles to compress the extreme aerodynamic data in a meaningful manner while keeping different angles of attack cases distinct. Because different flows over different angles of attack are collapsed as the same, the overlapping low-dimensional representations produced by PCA cannot distinguish important flow characteristics and yield grossly inaccurate flow reconstructions, as shown in figure 6.8.

The challenges of reducing degrees of freedom (dimension) of extreme vorticity dynamics

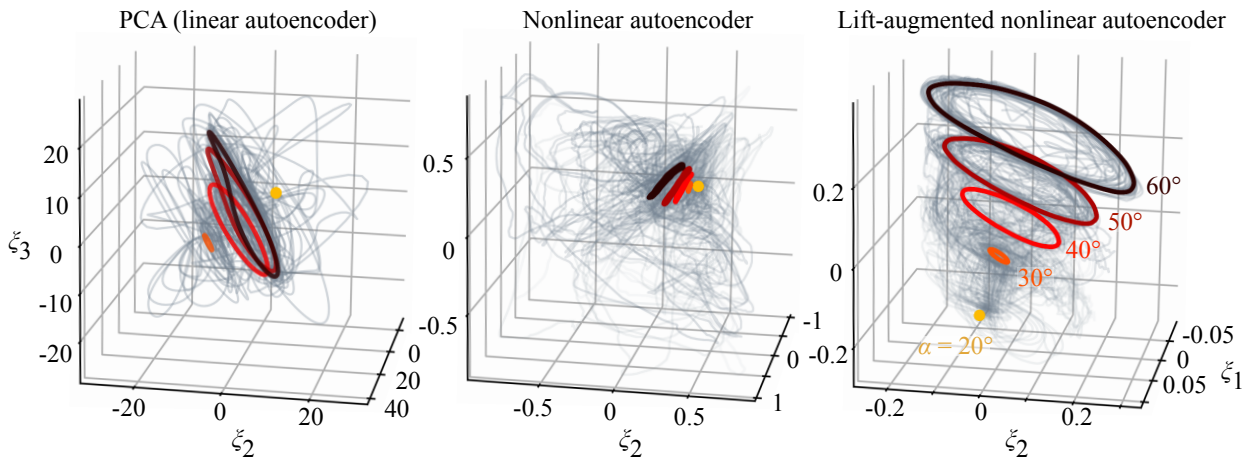

Figure 6.4: Compression of extreme aerodynamic flow data using (left) PCA (linear autoencoder), (middle) nonlinear convolutional autoencoder, and (right) lift-augmented nonlinear convolutional autoencoder. The undisturbed cases are highlighted in color while all disturbed wake cases used for training are shown with light gray curves. The lift-augmented convolutional autoencoder identifies the extreme gust-airfoil interaction manifold.

by PCA can be mitigated by utilizing a nonlinear compression technique. For this purpose, we utilize a nonlinear convolutional autoencoder, presented in figure 6.3 (excluding the green-shaded side network), to reduce a large number of vorticity field data to very few variables. An autoencoder is a neural network composed of an encoder and a decoder with a bottleneck in the middle (HS06; MFF20; OS19). Generally, this neural network framework is used to take an input data and replicate the same data at the output. The variables that lie in the middle are referred to as latent variables (red circles in figure 6.3), which hold the compressed information about the input data. When the nonlinear autoencoder can replicate the same input data at the output, this means that both the encoder and the decoder function effectively to nonlinearly transform the full data set to a low-dimensional latent variable $\boldsymbol{\xi}$ and vice versa effectively. The present autoencoder first compresses a flow field using a convolutional neural network (CNN) (LBB98) to capture global features of the vortical flow field. The compressed vector (extracted feature) through the CNN is then flattened at the reshape layer in figure 6.3 to pass into a multi-layer perceptron

(MLP) (RHW86) towards the latent space. A similar operation is performed for the decoder side to expand the dimension of the latent variable back to the size of the original flow field. The present autoencoder is trained with the same data sets as that used for PCA. The details of the autoencoder setup used in the present study are provided in Supplemental Material.

The nonlinear autoencoder is able to compress the flow field data and reproduce the flow field accurately, as shown in figure 6.8. We also present the latent space comprised of only three latent variables (ξ_1, ξ_2, and ξ_3) in figure 6.4 (middle). The ability of the nonlinear autoencoder to compress the vorticity field to mere three variables is not only surprising but also reaffirms that the flow field is indeed comprised of common flow features. The compression capability offered by a nonlinear autoencoder is promising to capture violent flow physics that appears tremendously rich. Nonetheless, we should note that the full data set shown in figure 6.4 is distributed over the latent space without a meaningful collapse of the latent variables. This is sufficient if the objective is to ensure that data in latent space are distinct, thus covering as much space as necessary to ensure uniqueness of the information. However, with regard to this study, we are aiming not only to compress the extreme aerodynamic flow data but also to identify universal features among the large number of flow field data holding dynamical information.

The above autoencoder analysis was performed purely from a data-centric perspective. Instead, let us consider incorporating a physical measurement (observable) into the autoencoder to facilitate the identification of a low-dimensional subspace defined by the appropriate latent variable coordinates. Capturing the low-dimensional nature of extreme aerodynamic flows can support the flight stabilization of air vehicles in extreme levels of turbulence. For this reason, we weigh the latent space variables $\boldsymbol{\xi}$ with lift force acting on the wing. This is achieved by supplementing the autoencoder with a multi-layer perceptron that outputs the lift force for each vorticity field over time, as shown by the green-shaded network in figure 6.3. In this case, training is performed to compress the vorticity field to the latent variables and to estimate the lift force accurately from the latent variables.

Incorporating lift into the learning process of the autoencoder assists in effectively extracting

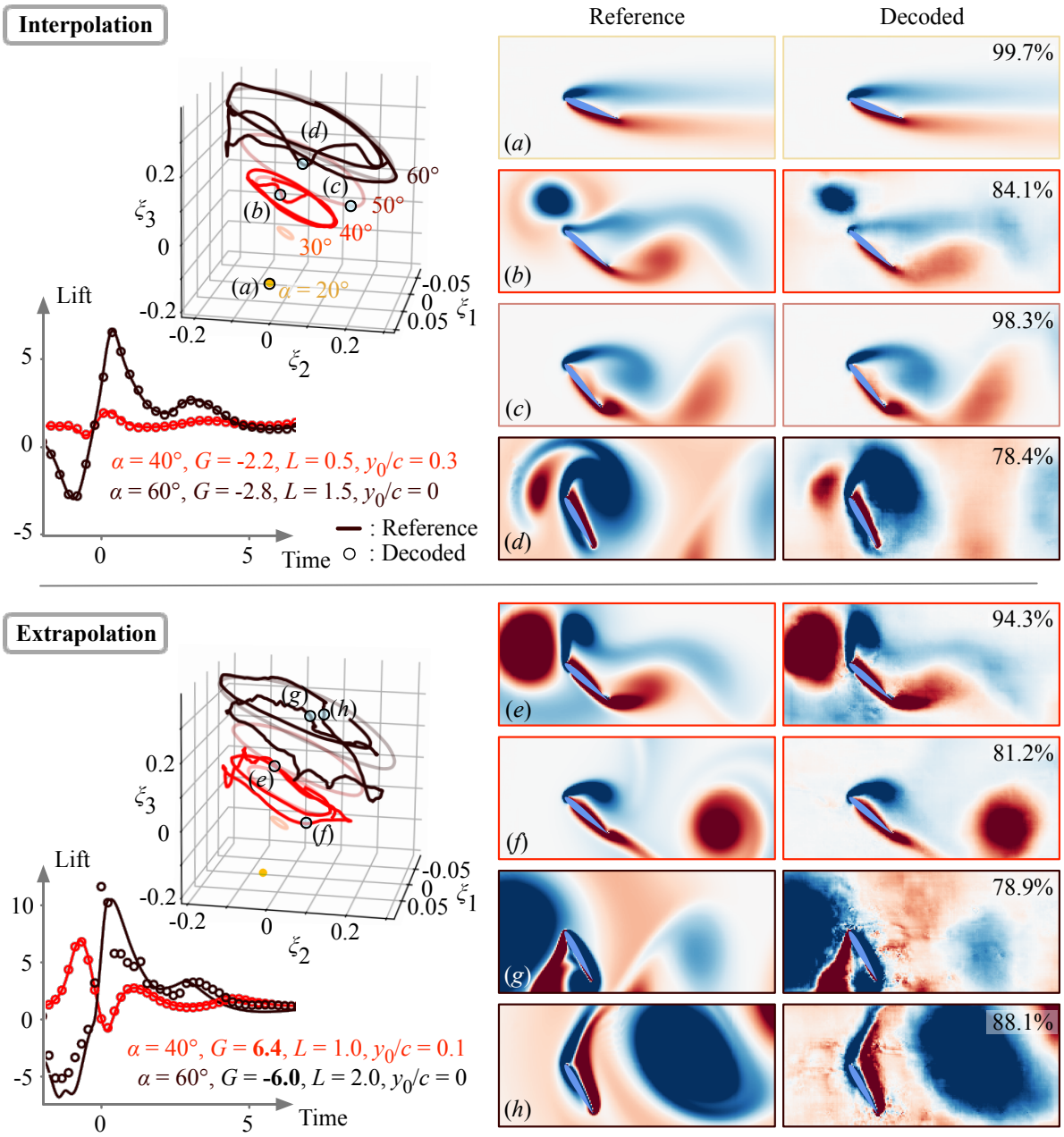

Figure 6.5: The lift-augmented autoencoder-based manifold expression and its output for a variety of wakes around a wing. Interpolation ($|G| < 4$) and extrapolation ($|G| > 4$) cases with regard to training data are shown. The trajectories for the undisturbed cases are shown in light color in latent space. The value presented on each decoded flow field corresponds to the time-averaged structural similarity index between the decoded and reference fields.

the essence of extreme aerodynamics due to three main reasons. First, using the lift force with the vorticity input comes as a natural choice since vorticity is theoretically known as the main mechanism for generating lift on a body. We take advantage of this intimate relationship between the vorticity field and lift. Second, the latent variables are guided to retain important information held by the vorticity field correlated with the lift force. This means that vortical structures that apply large vortical forces are well-captured by the lift-augmented autoencoder. Because extreme aerodynamic disturbances exert enormous amounts of transient forces as presented in figure 6.2, the autoencoder weights these extreme event appropriately and is able to accurately identify the responsible vortical structures. Third, the latent variables are encouraged to distinguish cases that yield different lift responses to impinging gust vortices. This is crucial to avoid latent variables from overlapping unnecessarily as observed in the struggling cases of PCA.

Now, let us examine the compression results from the lift-augmented autoencoder. The latent space comprised of three variables ξ_1, ξ_2, and ξ_3 is presented in figure 6.4. We observe that the entire collection of extreme aerodynamic cases collapses well in these latent space coordinates, confirming that the extreme aerodynamic responses to gust vortices possess a fundamentally low-dimensional behavior if captured appropriately with a nonlinear compression method. Here, the asymptotic periodic shedding states of the airfoil wakes provide shows a "cone" or a "chocolate cornet" like structure with the extreme aerodynamic trajectories lying in its vicinity in the three-dimensional latent space. As the dynamical trajectories converge to the cone-shaped structure, this structure serves as the inertial manifold (FMT88; Tem89; DG23). This manifold geometry can be considered as an hour-glass shape since there is a mirrored manifold for negative angle of attack cases. It should be noted that the geometry of this structure is not specified a priori and is discovered in an unsupervised manner. Here, this surface constitutes a manifold on which the key dynamics of extreme gust response reside. That is, the trajectories of the presently considered extreme aerodynamic flows are mapped onto the discovered geometry or to its vicinity.

Given the lift-augmented autoencoder collapsing all extreme aerodynamic response data onto this cone-shaped manifold, let us examine the accuracy of state reconstruction for the disturbed

flow and lift based on the three latent variables (ξ_1, ξ_2, ξ_3). As representative examples, we present the performance of the autoencoder for the cases of $(\alpha, G, L, y_0/c) = (40°, -2.2, 0.5, 0.3)$ and $(60°, -2.8, 1.5, 0)$, which are unused in training but chosen from the training parameter range. Here, the gust ratios G for these two cases are much higher than what are traditionally considered in gust response studies, but are within the training data range of $|G| \leq 4$. The latent variable trajectories for these cases and the reconstruction of lift and vortical flows are also shown in figure 6.5. To assess the reconstruction performance, we evaluate the structural similarity index (SSIM) (WBS04) between the reference and the decoded flow fields. The SSIM value for each decoded flow field is listed under the visualized flow reconstruction. Even the flow states exhibiting nonlinear interactions between the wing and the extreme vortex gust can be reconstructed well by the present autoencoder, as presented in figures 6.5 and 6.8. Note that the structural similarity index for a regular autoencoder without lift being higher compared to that for the lift-augmented autoencoder is expected. This is because a regular autoencoder is able to tune its weights solely to obtain accurate reconstruction of the flow field from the latent variables. It is also possible to reconstruct lift solely from the vorticity field. However, the lift-augmented autoencoder is critical for revealing the manifold for extreme aerodynamic response dynamics. These successful reconstructions indicate that high-dimensional extreme aerodynamic flows can be compressed into only three variables without significant loss of key physics.

The trajectory in the present latent space for the disturbed cases reflects key features of nonlinear vortex-gust interaction appearing in the high-dimensional space. For the extreme aerodynamic case of $\alpha = 40°$, the latent vector first drops towards the direction of the undisturbed periodic orbit of $\alpha = 30°$ then comes back to the original undisturbed orbit of $\alpha = 40°$. This is due to the approach of negative vortex disturbance to the wing, decreasing the effective angle of attack. This indicates that the lift-augmented autoencoder captures the relationship between high-dimensional extreme aerodynamic flows and lift force in the low-order space. In fact, the reduction in ξ_3 towards the direction of $\alpha = 30°$ in the latent space coincides with the temporal evolution of lift responses, as shown in figure 6.4. A similar trend is also observed in the case of $\alpha = 60°$ in which the latent

vector first heads to the direction of the periodic orbit of $\alpha = 50°$ corresponding to the decrease of the lift response. Being able to capture the extreme aerodynamic response of the wing on this manifold enables us to relate the instantaneous dynamics to the effective angle of attack, which is critically important for the flight stability of air vehicles. It is particularly encouraging that only three values in latent space are required to accurately estimate the state of the violent flow around the wing and transient lift force, which is promising for future development of sensors.

The discovered manifold captures dynamics beyond the trained gust strength G. Let us demonstrate how the present autoencoder approach is able to capture even more severe vortex gust conditions with $|G| \geq 4$ by presenting two cases $(\alpha, G, L, y_0/c) = (40°, 6.4, 1.0, 0.1)$ and $= (60°, -6.0, 2.0, -0.3)$, as shown in figure 6.5. The trajectory of these seemingly extrapolative cases exhibits a larger radius on the $\xi_1 - \xi_2$ plane compared to the variables of the interpolation cases while also presenting the effective angle of attack as the latent vector moves in the ξ_3 direction. The wider radial trajectory is due to the stronger disturbance, which produces a higher level of fluctuations in the vortical flow response likely away from the body without affecting lift. The present decoder can also recover the high-dimensional flow states while estimating the very large transient lift dynamics as presented in figure 6.5. This indicates that the present autoencoder can be robustly applied for such extreme gust vortex-airfoil interactions while achieving a nearly lossless compression of high-dimensional data. These findings also suggest that even under the extrapolating condition of $|G| > 4$, the underlying vortex dynamics shares common physics and can be nonlinearly compressed to a low-dimensional and universal manifold. This provides hope in estimating the flow states for cases that were not part of the extreme aerodynamic training data.

To further examine the robustness of the identified manifold and the autoencoder, let us consider cases that are different from the training cases, namely flows with noise and two extreme vortices, as shown in figure 6.6. Here, the noisy flow field is generated by adding Gaussian noise that is 30% of the original extreme aerodynamic flow field (same as the case shown in figure 6.5(b)). The present lift-augmented autoencoder not only reconstructs a vortical flow but also estimates the lift response well from a noisy flow. The autoencoder noise rejection characteristics is beneficial in

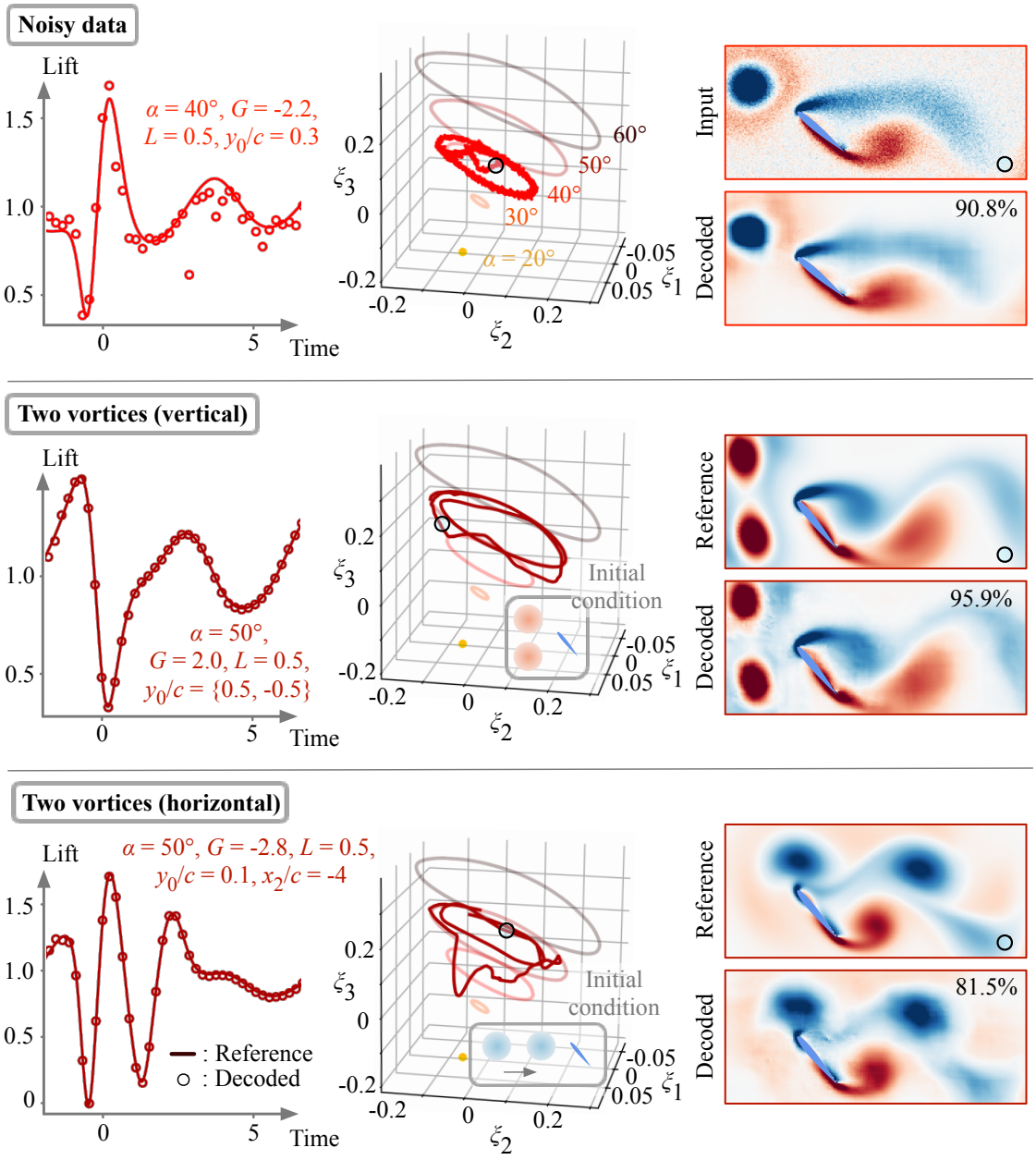

Figure 6.6: Extrapolation assessments of the present nonlinear autoencoder with lift augmentation. Three extrapolating cases are considered: 1. noisy data, 2. two vortex gusts (vertically arranged), and 3. two vortex gusts (horizontally arranged). The initial condition for the cases with two vortices is illustrated in the plot of each latent space. The trajectories for the undisturbed cases are shown in light color in latent space. The value presented on each decoded flow field corresponds to the time-averaged structural similarity index between the decoded and reference fields.

obtaining real-time situational awareness and working with turbulent flows in which less influential smaller-scale structures may also be present around the extreme gust vortices.

We also consider cases of vortex-dominated gust flows that are challenging for most reconstruction techniques trained only with single-gust disturbances. Here, we take two vortices that are introduced vertically and horizontally upstream of the airfoil, as depicted in figure 6.6. In both cases, the dynamical lift responses can be accurately estimated while the decoder reproduces the presence of two vortex disturbances very well, as shown in figures 6.6 and 6.9. We can also notice from the latent space that the trajectory of the two-horizontal-vortex case presents two inflections at $\xi_2 \approx 0$. This coincides with the observation in the lift dynamics which possesses two valleys due to the impingement of two negative vortices. We note that these particular examples are difficult for linear techniques, including PCA which completely fails to reconstruct the flow field as shown in figure 6.9.

Finally, let us demonstrate the potential of the present lift-augmented autoencoder for handling a more challenging and realistic extreme flight condition. In this last example, we introduce randomly generated five strong vortices upstream of the wing to simulate severe wake turbulence striking the airfoil, as shown in figure 6.7 (top left). The decoded lift, reconstructed flow fields, and latent trajectory are presented in figure 6.7. Even under this extreme operating condition, the present autoencoder robustly provides accurate reconstruction of the flow variables despite the model being trained only with single-gust disturbances. This success in flow compression/reconstruction and lift estimation corroborates that the discovered low-dimensional manifold universally captures the extreme gust vortex-airfoil interaction dynamics. This discovery provides great hope in establishing flight in extreme gusts, which was traditionally considered impossible.

6.3 Discussion

Small-scale air vehicles flying in urban or mountainous environments need to maneuver through a highly unsteady wake field full of strong vortices generated by manmade or natural obstacles. The

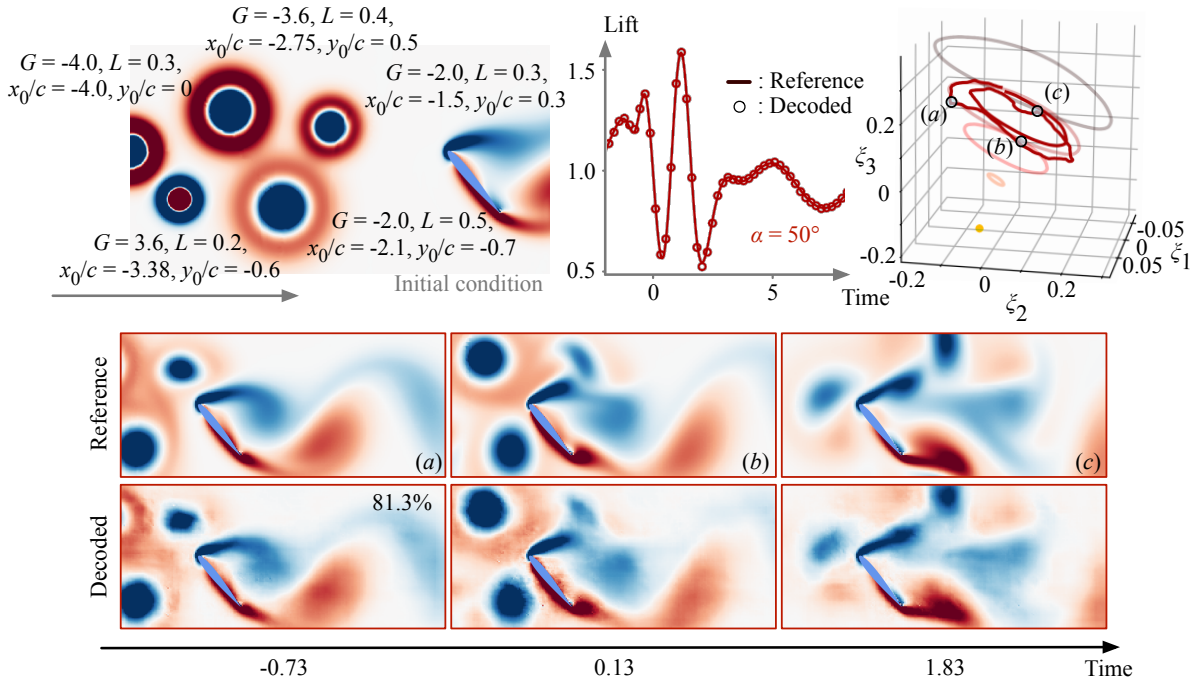

Figure 6.7: Application of the present nonlinear autoencoder with lift augmentation to extreme gust disturbance situation with multiple vortices, simulating severe wake turbulence striking the airfoil. The initial condition with the gust parameters for each vortex is provided (top left). The decoded lift history and the latent space dynamics are shown (top right). The trajectories for the undisturbed cases are shown in light color in latent space. The value presented on the decoded flow field corresponds to the time-averaged structural similarity index between the decoded and reference fields (bottom).

interaction of these vortices with flying vehicles requires an understanding of extreme aerodynamic flows, for which there are no established theories. In the current study, we presented a data-driven approach to identify a low-dimensional manifold on which the key dynamics between strong gust vortices and airfoil wakes can be collapsed. This manifold was found with an autoencoder designed to retain the knowledge of aerodynamic lift as part of the latent variables. The existence of this low-dimensional manifold is significant in a few ways.

First, the fact that only three variables can represent the complex vortical flow field confirms

the low-dimensional nature of the strong gust vortices interacting with the airfoil wakes. While the present study distilled the dynamics to only three variables, it actually can be further reduced to two variables if the three variables are projected on the identified manifold. This significant compression of the extreme aerodynamic flow fields was enabled with a nonlinear autoencoder-based approach that incorporates aerodynamic insights embedded into its formulation. We also note that noisy experimental data encountering a different type of gust can also be coincidentally low-dimensionalized to be three-dimensional variables through a nonlinear autoencoder with the assistance of a topology-based concept (SFS23). Second, this low-dimensional representation of the extreme aerodynamic flows suggests that only a small number of sensors on the airfoil may be able to accurately reconstruct the surrounding flow field in real time. In fact, decoder-type neural networks, that take sparse sensors as the input and high-resolution aerodynamic flows as the output, have been recently developed to perform real-time fluid flow state estimation (EMY20; FMR21; ZFA23; AW21). The observations in these studies imply that low-dimensional extreme aerodynamic latent vectors can also be estimated from sparse sensor information, enabling us to track the high-dimensional dynamics in a low-order, real-time manner. Third, given the present findings, it is possible to develop a reduced-order model that can capture the dynamics in the latent space to desired level of accuracy and complexity. While we could model the latent dynamics using other data-driven techniques such as sparse regression (BPK16a), modeling and controlling the high-dimensional extreme aerodynamic flows on the present manifolds from the perspective of phase-amplitude space appears interesting (Nak16; TN18; KSN13). It can be anticipated the phase-reduction analysis on the present nonlinear manifold offers a new aspect in modifying wake dynamics by providing the optimal timing and locations of actuation.

With the discovered manifold, active flow control and vehicle stability control strategies can be developed for mitigating the effects of extreme aerodynamic disturbances. While this study focused on extreme two-dimensional vortex-airfoil interactions, there are other types of gust disturbances present in severe atmospheric turbulence that require three-dimensional analysis (FGD21). Three-dimensional flow extensions are important to further examine the potential of the present approach.

As shown in this study, nonlinear data-driven compression techniques appear promising to support the identification of other manifolds that capture the complex extreme aerodynamic interactions between these other types of gusts and the aircraft. The present findings offer a new perspective on modeling and taming extreme aerodynamic flows in support of next-generation air vehicle operations in conditions traditionally considered unflyable.

6.4 Methods

6.4.1 Simulations of Extreme Vortex-Airfoil Interactions

The present study considers the unsteady flow field generated by the extreme gust vortex-airfoil interactions. The flow fields examined in this study are obtained from direct numerical simulations of flows over a NACA 0012 airfoil at a chord-based Reynolds number $\mathrm{Re} \equiv u_\infty c/\nu = 100$. Here, u_∞ is the free-stream velocity, c is the chord length, and ν is the kinematic viscosity. The simulations are performed with an incompressible flow solver (HI04; HMI06) for an airfoil at six different angles of attack of $\alpha = 20°, 30°, 40°, 50°$, and $60°$. For the undisturbed cases, the flow at $\alpha = 20°$ is steady while that at $\alpha \geq 30°$ exhibits unsteady periodic wake shedding. The computational domain extends over $(x, y)/c \in [-15, 30] \times [-20, 20]$ with the leading edge of the wing positioned at the origin.

To study the gust-airfoil interactions, a very strong vortex with an angular velocity profile prescribed by equation (Tay18) is introduced upstream of the airfoil at $x_0/c = -2$ and $y_0/c \in [-0.5, 0.5]$. The present disturbance vortex is parameterized by the gust ratio $G \equiv u_{\theta,\max}/u_\infty \in [-10, 10]$, its size $L \equiv 2R/c \in [0.5, 2]$, and the vertical position of the disturbance y_0/c. From the parameter space composed of these three variables, 40 randomly-sampled cases of the disturbed flows are simulated for each angle of attack. For the purpose of learning the extreme aerodynamics with the autoencoder, 20 cases are used for training and the remaining 20 cases are used for testing. The simulated flows were validated with previous studies (ZFA23; Kur15; LLZ12; DCU18), in particular with a study that considered a vortex-airfoil interaction problem (ZFA23).

For each of the cases considered in the present study, we prepare 1200 snapshots of vorticity field over 10.2 non-dimensional convective time $t^* \equiv u_\infty t/c$. We refer to this convective time as simply 'time' in the main text. Of the entire flow field, a subdomain $(x, y)/c \in [-1.4, 4] \times [-1.2, 1.2]$ with spatial grid points $(N_x, N_y) = (240, 120)$ is considered for the data-driven analysis since vortex-airfoil interactions primarily occur in this region. Moreover, the history of the lift fluctuations is provided by the numerical simulations. The non-dimensional lift coefficient $C_L \equiv F_{\text{lift}}/(\frac{1}{2}\rho u_\infty^2 c)$, where F_{lift} is the lift force on the wing body and ρ is the density. In the main text, C_L is referred to as 'lift.' Overall, the training data used for the present models amounts to 1.26×10^5 frames comprised of 100 extreme aerodynamic gust response cases and 5 undisturbed wake cases with 1200 snapshots for each case.

Autoencoder Setup

To discover the universal nonlinear manifold that represents the high-dimensional extreme aerodynamic flows in a low-dimensional latent space, we use an autoencoder (HS06) (see figure 6.3). Here, we consider a convolutional neural-network-based autoencoder $\mathcal{F}$, which is trained to output $\hat{\boldsymbol{q}}$ to be the same data as the input $\boldsymbol{q} \in \mathbb{R}^n$ such that $\hat{\boldsymbol{q}} \approx \mathcal{F}(\boldsymbol{q}; \boldsymbol{w})$, where $\boldsymbol{w}$ denotes the weights inside the autoencoder. This autoencoder is comprised of an encoder $\mathcal{F}_e$ and a decoder $\mathcal{F}_d$ connected through a low-dimensional variable $\boldsymbol{\xi} \in \mathbb{R}^m$ in the middle, where $m \ll n$. Here, the high-dimensional input $\boldsymbol{q}$ can be compressed into the latent vector $\boldsymbol{\xi}$ if the autoencoder $\mathcal{F}$ successfully recovers the data accurately. That is, we seek to have an autoencoder that achieves

$$\boldsymbol{q} \approx \hat{\boldsymbol{q}} = \mathcal{F}(\boldsymbol{q}; \boldsymbol{w}) = \mathcal{F}_d(\boldsymbol{\xi}) = \mathcal{F}_d(\mathcal{F}_e(\boldsymbol{q})). \tag{6.1}$$

The autoencoder $\mathcal{F}$ is found based on data such that its weights $\boldsymbol{w}$ are optimized to minimize a desired cost (loss) function $\mathcal{E}$, yielding the following optimization problem

$$\boldsymbol{w} = \text{argmin}_{\boldsymbol{w}} [\mathcal{E}(\boldsymbol{q}, \mathcal{F}(\boldsymbol{q}; \boldsymbol{w}))] = \text{argmin}_{\boldsymbol{w}} \|\boldsymbol{q} - \hat{\boldsymbol{q}}\|_2. \tag{6.2}$$

The weights $\boldsymbol{w}$ are determined with the Adam optimizer (KB14).

We use an autoencoder composed of convolutional neural networks (CNN) (LBB98) and multi-layer perceptrons (MLP) (RHW86), as illustrated in figure 6.3. In the encoder, the CNN captures global features of the extreme aerodynamic flow field and the MLP is used to extract features from the CNN while further reducing the size of the data. By leveraging nonlinear activation functions, an autoencoder can achieve better compression than linear compression techniques such as principal component analysis (PCA) (HS06). Note that using autoencoder with linear activation functions is mathematically equivalent to performing principal component analysis (PCA) (HS06; MFF20). As for the nonlinear activation function, we use the hyperbolic tangent function $\varphi(s) = (e^s - e^{-s})/(e^s + e^{-s})$, enabling us to consider the positive and the negative gust influence in latent space. The hyperparameters used in the MLP and CNN follow previous work with similar settings (MFF20; FNF20).

In addition to PCA and a regular autoencoder, we develop a lift-augmented convolutional autoencoder in this study. The present lift-augmented autoencoder trains the model with a lift coefficient $C_L(t)$ in addition to a vorticity field $\boldsymbol{q}(t)$ such that $[\hat{\boldsymbol{q}}(t), \hat{C}_L(t)] = \mathcal{F}(\boldsymbol{q}(t))$. The additional side network based on an MLP is illustrated in the green-shaded portion of figure 3. This additional network ensures that the latent vector $\boldsymbol{\xi}(t)$ holds relevant information related to the lift coefficient $C_L(t)$ to support the manifold identification. The cost function in this case becomes

$$\boldsymbol{w}^* = \text{argmin}_{\boldsymbol{w}} \left[||\boldsymbol{q} - \hat{\boldsymbol{q}}||_2 + \beta ||C_L - \hat{C}_L||_2 \right], \tag{6.3}$$

where β balances the vorticity field and lift reconstruction losses. In this study, we choose $\beta = 0.05$ based on the L-curve analysis (HO93). With the lift decoder $\mathcal{F}_L$, the reconstructed lift coefficient $\hat{C}_L(t)$ is given by

$$\hat{C}_L(t) = \mathcal{F}_L(\boldsymbol{\xi}(t)) = \mathcal{F}_L(\mathcal{F}_e(\boldsymbol{q}(t))). \tag{6.4}$$

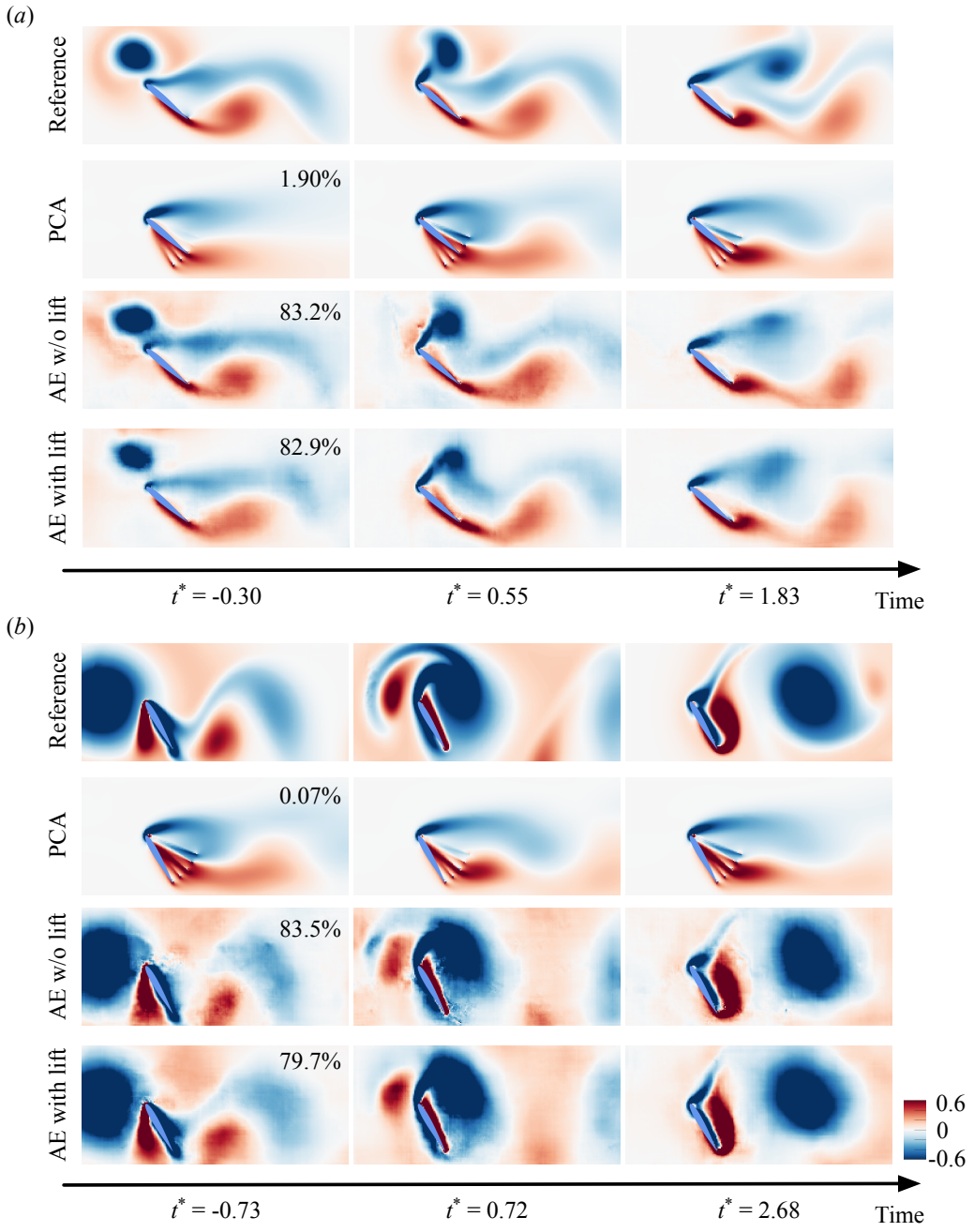

Figure 6.8: Reconstructed vorticity fields by PCA, a regular autoencoder, and the present lift-augmented autoencoder for the cases of (a) $(\alpha, G, L, y_0/c) = (40°, -2.2, 0.5, 0.3)$ and (b) $(60°, -2.8, 1.5, 0)$. The values listed on the decoded flow fields are the time-averaged structural similarity indices between the decoded and reference fields.

6.5 Appendix: Reconstruction of vorticity fields

Comparative assessment of the reconstructed flow fields using different techniques is offered in this section. Here, we compare the reconstructed vorticity field from PCA, a regular autoencoder, and the lift-augmented autoencoder. To quantitatively assess the reconstruction performance, we evaluate the accuracy of the structural similarity index (SSIM) (WBS04) between the reference and the decoded flow fields. The SSIM χ is defined as

$$\chi' = \frac{(2\mu_r\mu_d + C_1)(2\sigma_{rd} + C_2)}{(\mu_r^2 + \mu_d^2 + C_1)(\sigma_r^2 + \sigma_d^2 + C_2)}. \tag{6.5}$$

Here, subscripts r and d are used for the reference and decoded flow fields, μ and σ are the mean and standard deviation of given data, respectively, σ_{rd} is the covariance of the reference and decoded flow fields, and the constants $(C_1, C_2) = (0.16, 1.44)$ are used to stabilize division [41]. The SSIM χ lies between 0, representing no similarity, and 1, representing an identical image. The value of the SSIM is provided on every reconstructed vorticity field plot of the main text.

In this supplemental material, we present two cases of $(\alpha, G, L, y_0/c) = (40°, -2.2, 0.5, 0.3)$ and $(60°, -2.8, 1.5, 0)$ in figures 6.8(a) and (b), respectively. We compare the performance of PCA, regular autoencoder, and the lift-augmented autoencoder all with the number of the latent vector being set to 3. As evident from these figures, PCA struggles to reconstruct high-dimensional states over time for both cases of extreme aerodynamic flows. PCA completely fails to detect the incoming gust vortex. In addition to the failure of reconstruction for the presence of the vortex disturbance upstream of the wing and the wake structures, limitations of linear reconstruction techniques are also observed around the wing with superpositions of wings appearing incorrectly.

In contrast, the reconstruction can be greatly improved with a nonlinear convolutional autoencoder, as shown in figure 6.8. The position of extreme vortex disturbance is estimated very accurately over time including when a vortex gust impinges the wing causing strong nonlinear interactions among the wing, gust, and wake. This observation shows that the collection of the present extreme aerodynamic flow fields can be significantly compressed into only three variables using a nonlinear autoencoder. The improvement of the reconstruction by the nonlinear model can

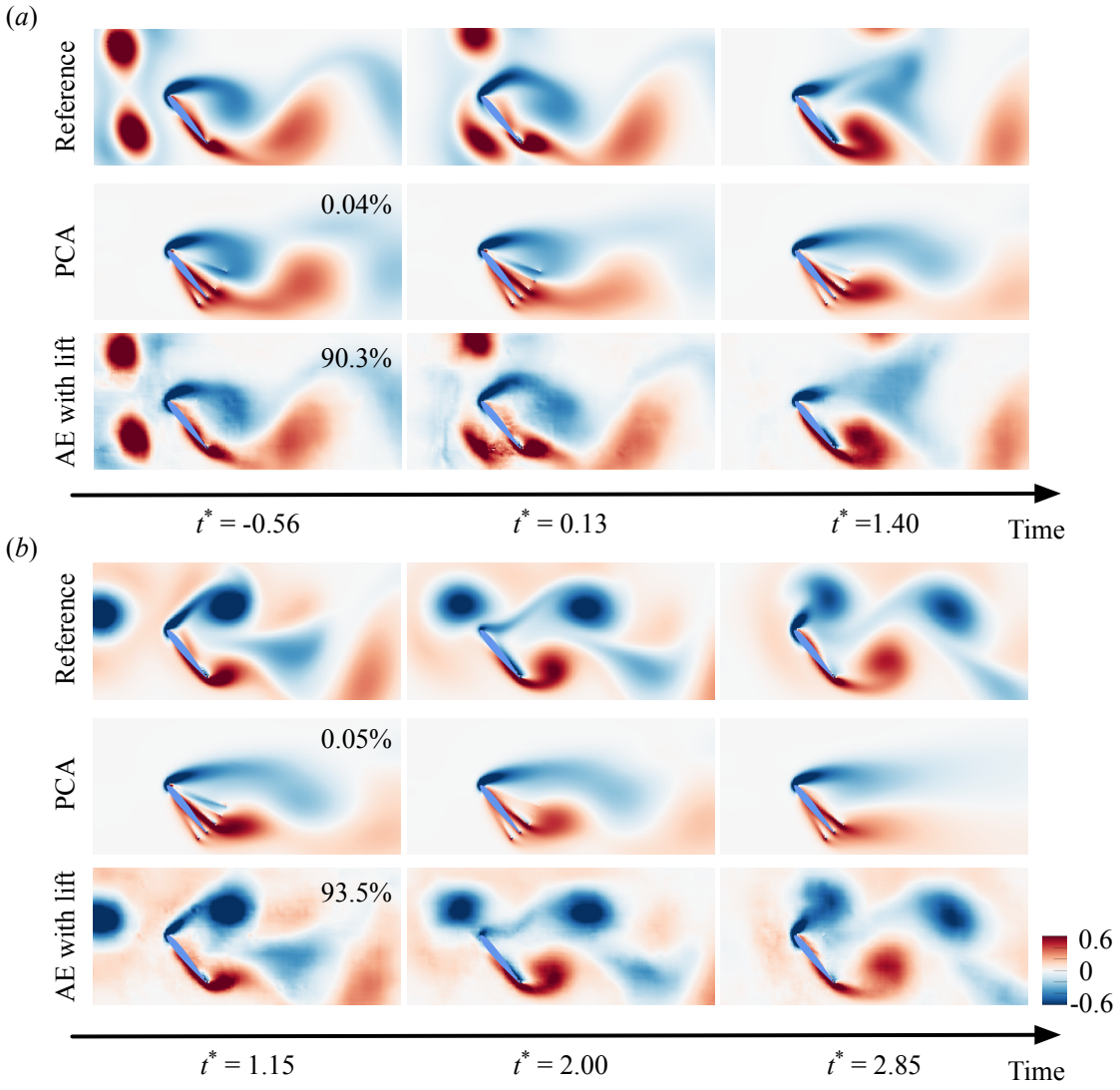

Figure 6.9: Reconstructed vorticity fields by PCA and the present lift-augmented autoencoder for the cases of two gust vortices that are (a) vertically arranged and (b) horizontally arranged. The values listed on the decoded flow fields are the time-averaged structural similarity indices between the decoded and reference fields.

also be observed with an example of disturbed flow fields with two extreme gust vortices.

The impingement with these multiple gust vortices causes challenges to stable flight with extreme levels of nonlinear lift responses than single-gust cases. These unseen situations cannot be generally analyzed with conventional linear analysis. The reconstructed flow fields with two different types of vortex gust placements, (1) vertical and (2) horizontal arrangements, using PCA and the lift-augmented autoencoder are shown in figure 6.9. As expected, PCA cannot detect the presence of two vortices and also completely fails to capture the influence of extreme disturbance on the wake over time. On the other hand, the present lift-augmented autoencoder is able to reconstruct the flow states, achieving over 90% SSIM for both examples. The ability to reconstruct such unseen complex gust situations based on a variety of single-vortex disturbed flow training data suggests that the discovered manifold space is indeed capturing the underlying extreme aerodynamic responses in not only a low-dimensional manner but also in a universal fashion. It is hence anticipated that the present manifold expression can be extended to wings flying into a wide range of extreme vortex-dominated gusts.

CHAPTER 7

Controlling unsteady flows on a machine-learned manifold: vortex-gust airfoil interaction

Here, we demonstrate that control laws can be designed in a latent space identified by nonlinear machine learning to modify unsteady fluid flows. We take an example of extreme aerodynamic flows and use the extreme aerodynamic manifold to derive a control strategy to mitigate the impact of vortex gust leveraging phase-amplitude reduction (FNT23).

7.1 Motivation

Small-scale air vehicles are used in a range of operations including transportation (CDS14), rescue (HJ11), agriculture (ZK12) and media reporting (HLL15). Although such small-scale aircraft typically fly in favorable conditions, they are now being tasked to navigate in challenging environments such as urban canyons, mountainous areas, and turbulent wakes created by ships. As the occurrence of these extreme scenarios has increased due to global warming, real-time and low-cost control strategies are critical to achieving stable flight under sizeable and violent atmospheric disturbances (JCS22; MMW23). In response, this study presents a data-driven control technique for flows around a wing experiencing extreme levels of vortical gusts.

In violent and turbulent airspace, small-scale air vehicles encounter various forms of vortex disturbance characterized by a number of parameters including strength, size, and orientation (BSJ21; SHB23). In studying vortex-gust airfoil interaction, the gust ratio $G \equiv u_g/u_\infty$ is a particularly important factor, where u_g is the characteristic gust velocity and u_∞ is the freestream

velocity or cruise velocity. Flight condition of $G > 1$ is traditionally avoided, which can occur in urban canyons, mountainous environments, and severe atmospheric turbulence (JCS22). Large-scale aircraft do not encounter conditions of $G > 1$ due to their high-cruise velocity. However, such a condition becomes a critical matter for small-scale aircraft such as drones because of its low cruise velocity, leading to potentially large G.

Previous studies of vortex-gust airfoil interaction have mainly focused on scenarios with $G \leq 1$. For example, (QWG23) experimentally investigated vortex-gust airfoil interaction under $G \leq 0.5$. They examined the effect of various parameters such as gust ratio, angle of attack, and sweep angle of the wing on vortical flows and aerodynamic forces through PIV measurements. (HBP22) considered gust mitigation of flows around a DLR-F15 airfoil under vortex gusts with $G \leq 0.1$. With trailing-edge flaps and a combined proportional-integral feedback/model-based feedforward approach, they achieved 64% reduction in the lift deviation during quasirandom gust encounters. For conditions of $G \leq 0.71$, (SGL23) has recently developed a closed-loop pitch control strategy to mitigate lift fluctuation for transverse gust encounters.

The complex dynamics of vortex-airfoil interactions are driven not only by the gust ratio but also by other factors such as the Reynolds number, wing geometry, disturbance size, and orientation. Since different combinations of these parameters create diverse patterns of vortex-airfoil interactions, covering infinite scenarios with numerical and experimental studies by naïve parameter sweeps is impractical. This calls for a smart way to sample and extract the fundamental nonlinear dynamics. There is also a need to control these violent flows to achieve some form of stable flight.

We have recently proposed a data-driven technique called a nonlinear lift-augmented autoencoder that uncovers the low-dimensional dynamics of vortical flows experiencing extreme levels of vortex disturbances over a wide parameter space (FT23). Our previous study considered extremely high levels of aerodynamic disturbances with $0 < G \leq 10$. For aerodynamics with $G > 1$, we refer to it as extreme aerodynamics due to the presence of violently strong gusts. We have found that time-varying vortical flow fields spanning over the large parameter space can be compressed

to only three variables using nonlinear machine learning. Furthermore, the compressed three latent variables can hold the essence of the original high-dimensional flow physics, forming a low-dimensional manifold that captures the influence of extreme vortex disturbance about the baseline flow dynamics.

This study considers leveraging the machine-learned low-order manifold for gust mitigation control. However, controlling such violent flows is challenging due to their inherent transient nature. In response, this study applies phase-amplitude reduction (Nak21; SKN17) to a low-dimensional manifold to design a control law. Phase-amplitude reduction is a mathematical technique to analyze oscillatory signals or waveforms in a wide range of nonlinear dynamics (WLT13; WM16). This analysis can model a given complex dynamics with its constituent components of phase and amplitude. Phase can be thought of as the timing information of a signal, referring to the position of a waveform at a particular point over time relative to a reference point. On the other hand, amplitude represents the intensity of a waveform at a specific point in time, hence providing information about the energy of a given signal (MM18; KOS20; MZN23).

A simplified form of a given complex dynamics with the reduction to its phase and amplitude can facilitate various analyses from the aspect of dynamical modeling and system control (Nak16; KSN13; MMM13; TIK23). Phase-reduction analysis has recently been used to characterize and control fluid flows, including the periodic vortex shedding around cylinders (TN18; Iim19; KT20; KKT21; LNJ21; LZK23), a flat plate (Iim21; Iim23), and airfoil (NTB21; KGT22; GKT23). Synchronization characteristics to various forms of periodic perturbations in fluid flows can also be examined via phase-reduction analysis, demonstrated with vortex shedding for a circular cylinder (TN18; KT20; KKT21; NTB21). For laminar-separated airfoil wakes, phase-reduction-based control design has also exhibited potential not only to reveal responsible flow physics (KGT22) but also to optimally modify wake behaviors (GKT23).

This study develops a feedforward control strategy to quickly mitigate the impact of extreme vortex gusts by performing the phase-amplitude reduction on the extreme aerodynamic manifold. The overview of the present study is shown in figure 7.1. There is a step-by-step procedure for

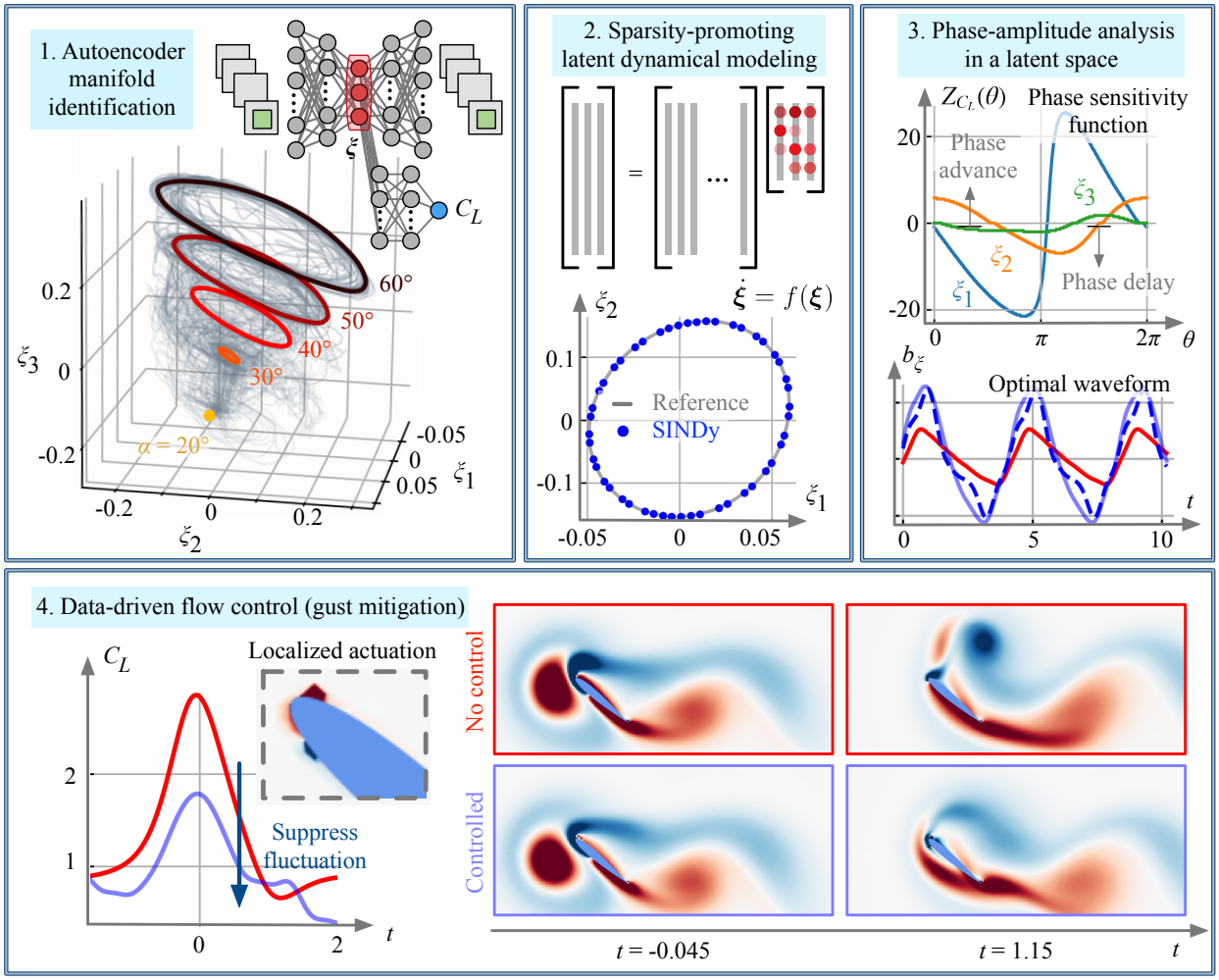

Figure 7.1: Overview of the present study. 1. Nonlinear autoencoder-based manifold identification of extreme aerodynamic flows (in section 7.2). 2. Sparsity-promoting latent dynamical modeling (in sections 7.3.1 and 7.4.1). 3. Phase-amplitude reduction in a latent space (in sections 7.3.2 and 7.4.2). 4. Data-driven flow control with optimal waveform for gust mitigation (in sections 7.3.3 and 7.4.3).

preparing the optimal control actuation, aiming to quickly modify the flow state.

The present paper is organized as follows. Extreme aerodynamic flow physics and their low-dimensioalization through a machine-learning technique are introduced in section 7.2. Methods used to prepare the optimal control actuation are described in section 7.3. Results and discussion are provided in section 7.4. Conclusions are lastly remarked in section 7.5.

7.2 Extreme vortex-airfoil interactions on a low-dimensional manifold

This study considers extremely strong vortex-gust and airfoil interaction, exhibiting inherently transient and nonlinear nature. To control such violent aerodynamic flows with minimal costs, we develop a data-driven strategy assisted with phase-amplitude reduction analysis in a low-dimensional manifold, as illustrated in figure 7.1.

The first step is to obtain a universal, low-dimensional representation of extreme aerodynamic flows. This is achieved by a nonlinear machine-learning-based technique referred to as a lift-augmented autoencoder (FT23). Once we obtain the low-dimensional expression, we model the latent dynamics using sparsity-promoting regression. The identified dynamical model here is needed to perform phase-amplitude reduction. Through the phase-amplitude reduction, we can measure phase- and amplitude sensitivity functions that are used to derive a control law. In this study, we aim to achieve significant control effects within a very short time duration because the impact of the gust quickly generally appears within only 2–3 convective time. The phase-amplitude reduction enables us to optimally gain a control actuation that can quickly modify the flow state while suppressing the amplitude modulation of the dynamics. The derived time-varying control actuation is finally applied to extreme aerodynamic flows.

This section first discusses complex transient flow physics appearing in extreme aerodynamics while introducing a model problem. We also show how complex, high-dimensional vortical flows under extreme aerodynamic conditions can compactly be expressed in a manifold space while covering a principle of nonlinear autoencoder used for the present manifold identification.

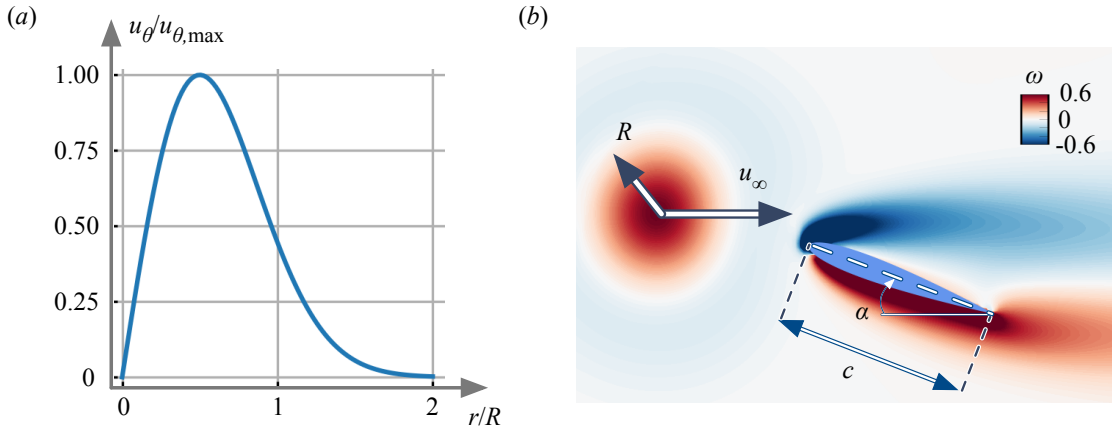

Figure 7.2: (a) The velocity profile of the vortex gust. (b) An example vorticity snapshot with a vortex gust. The parameters considered in the present study are also shown.

7.2.1 Flow physics: extreme vortex-gust airfoil interaction

In this study, extremely strong vortex-gust airfoil interaction is considered to model a situation in which a wing experiences a significant level of disturbance during flight operations. Such a strong vortex gust induces a large excitation of aerodynamic forces within a very short time duration while exhibiting highly nonlinear transient dynamics. Furthermore, the flow fields involve a variety of wake patterns depending on a parameter combination of the vortex-gust setting such as vortex size, strength, and initial position. Due to the nonlinear interaction between the vortex gust and a flow around an airfoil, there are massive flow separations creating additional vortical structures with a range of length scale. This study aims to mitigate the impact of such a strong vortex gust with a data-driven control.

To model the aforementioned extreme aerodynamic conditions, we consider a vortex-gust airfoil interaction around a NACA0012 airfoil with angle attacks $\alpha \in [20, 60]^\circ$ at a chord-based Reynolds number of 100. The data sets are produced by direct numerical simulations (HI04; HMI06). Without the presence of a vortex gust, a wake at $\alpha = 20^\circ$ is steady while wakes at $\alpha \geq 30^\circ$ exhibit unsteady periodic shedding (limit-cycle oscillation). For the disturbed wake cases, an extremely strong gust is introduced upstream of a wing at $x_0/c = -2$ and $y_0/c \equiv Y \in [-0.5, 0.5]$, as illustrated

in figure 7.2. A Taylor vortex (Tay18) is used to model the disturbance with a velocity profile of

$$u_\theta = u_{\theta,\max}\frac{r}{R}\exp\left[\frac{1}{2}(1-\frac{r^2}{R^2})\right], \tag{7.1}$$

where R is the radius at which u_θ reaches its maximum rotational velocity $u_{\theta,\max}$. The vortex gust is parameterized by the gust ratio $G \equiv u_{\theta,\max}/u_\infty \in [-10, 10]$, its size $D \equiv 2R/c \in [0.5, 2]$, and the vertical position of the disturbance Y. Note that the gust ratio G considered herein is much larger than that traditionally thought of as flyable (JCS22).

A parameter combination of the vortex-gust setting generates diverse patterns of violent vortex-airfoil interaction (FT23). Let us exhibit in figure 7.3 the entire collection of lift responses in the present data set with representative vortical flow snapshots. Here, the convective time is set to zero when the center of the vortex arrives at the leading edge of the airfoil. The present data set includes a variety of wake behaviors and lift waveforms over time, occurring due to complex vortex-gust airfoil interactions.

Let us first take an example case at $\alpha = 30°$ shown in figure 7.3 which is disturbed by a strong positive vortex gust with the parameters of $(G, D, Y) = (3.4, 0.5, 0.1)$. With the approach of positive disturbance, the lift drastically first increases from the undisturbed state. Once this positive vortex gust impinges on the airfoil, the interaction between the gust and the airfoil wake triggers massive separation.

A negative vortex disturbance conversely decreases the lift first, and then the lift value recovers towards that of the original limit-cycle case in a transient manner, as shown in the case of $\alpha = 50°$ in figure 7.3. The amplitude of lift fluctuation generally becomes larger as the size of the vortex gust increases, as evident from the showcased example of $\alpha = 20°$ and $40°$ in figure 7.3. However, the lift time series with a large, strong vortex gust such as the case of $\alpha = 60°$ in figure 7.3 with the parameter combination of $(G, D, Y) = (3.2, 1.5, -0.3)$ presents a different asymptotic wave pattern, due to the massive separation which additionally generates vortical structures around an airfoil.

These sharp lift responses with extreme vortex-gust airfoil interaction occur within only two

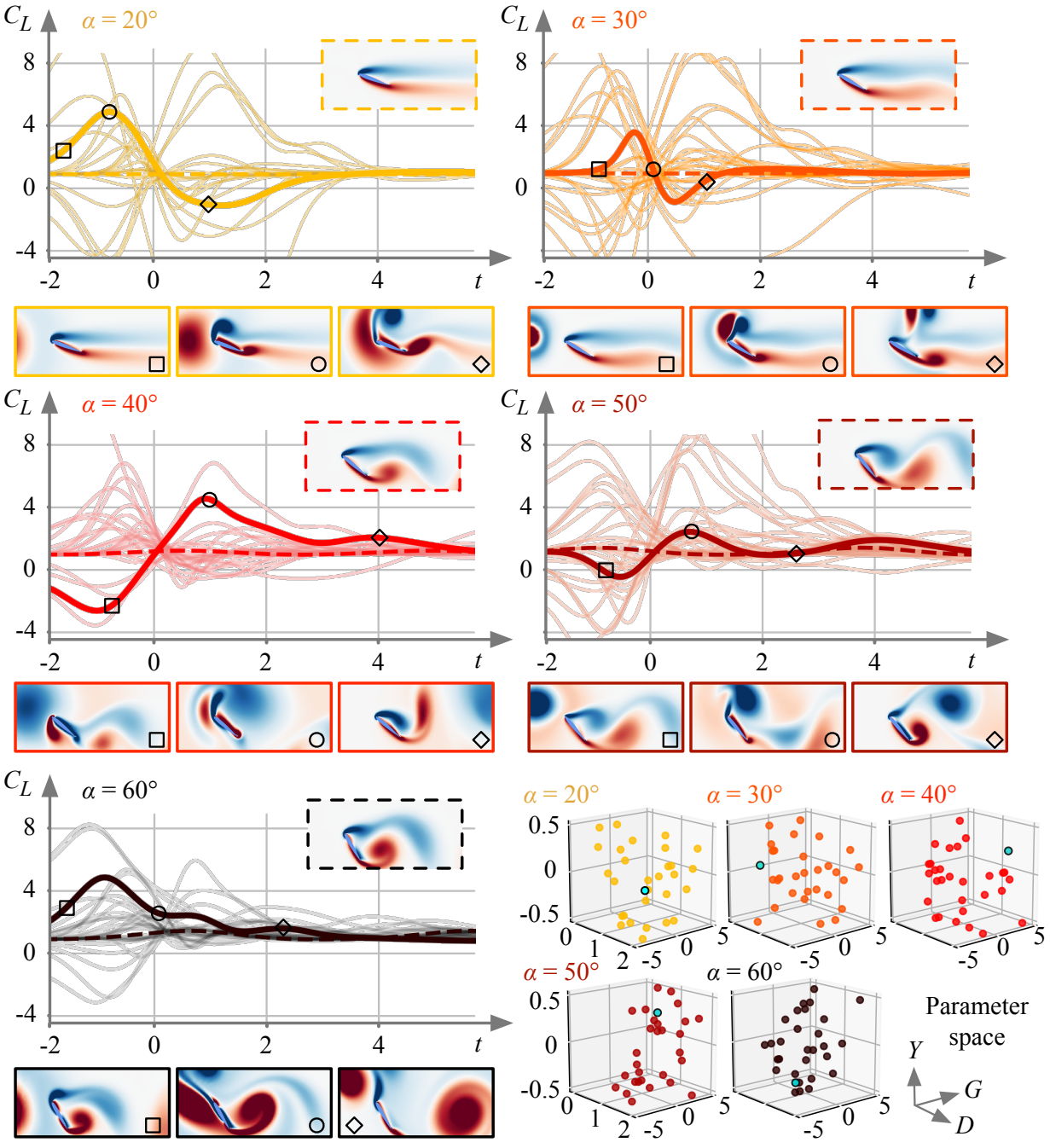

Figure 7.3: Extreme aerodynamic flow data sets. The entire collection of lift history across the parameter space of (α, G, D, Y) and representative vorticity fields are presented. The vorticity field surrounded by the dashed line is the undisturbed reference flow for each angle of attack. The light-blue circles in the parameter spaces correspond to the representative cases chosen for the vorticity field visualizations.

convective time for almost all considered cases. While we easily recognize the difficulty of controlling air vehicles under such a significant variation in the lift force, it also implies that a controller for the present extreme aerodynamic flows would be asked to quickly modify the flow to attenuate the lift responses. This calls for a control that reacts in a fast manner.

For the present data-driven manifold identification, we use 1200 vorticity snapshots over 10.2 convective time per case, resulting in 1.26×10^5 collective snapshots. A subdomain of $(x, y)/c \in [-1.4, 4] \times [-1.2, 1.2]$ with spatial grid points $(N_x, N_y) = (240, 120)$ is extracted from the computational domain of $(x, y)/c \in [-15, 30] \times [-20, 20]$ with the leading edge of the wing positioned at the origin, capturing the primarily vortex-airfoil interactions.

7.2.2 Lift-augmented nonlinear autoencoder

The analysis of the present extreme aerodynamic flows is challenging due to their complexity and nonlinearity. Furthermore, it is impractical to perform either numerical simulations or experiments for studying vortex-airfoil interaction across a very large parameter space with limited resources. Hence, it can be anticipated that the analysis can be facilitated with a reduced-order model that universally captures the essential physics of extreme aerodynamics without necessitating expensive simulations and experiments.

To this end, we have recently developed a lift-augmented nonlinear autoencoder (FT23) that can compress a collection of extreme aerodynamic vortical flow data across a large parameter space into few variables while holding the essence of the original vortex-airfoil interaction. Herein, we introduce a principle of the lift-augmented nonlinear autoencoder.

Autoencoder (HS06) is a neural-network-based model reduction technique. As illustrated in figure 7.4, an autoencoder is composed of an encoder $\mathcal{F}_e$ and a decoder $\mathcal{F}_d$ while having the bottleneck called latent vector $\boldsymbol{\xi}$. The autoencoder model is generally trained to output the same data as a given input data. In other words, a given high-dimensional input data can be compressed into the latent vector $\boldsymbol{\xi}$ if the autoencoder $\mathcal{F}$ can successfully decode the original high-dimensional

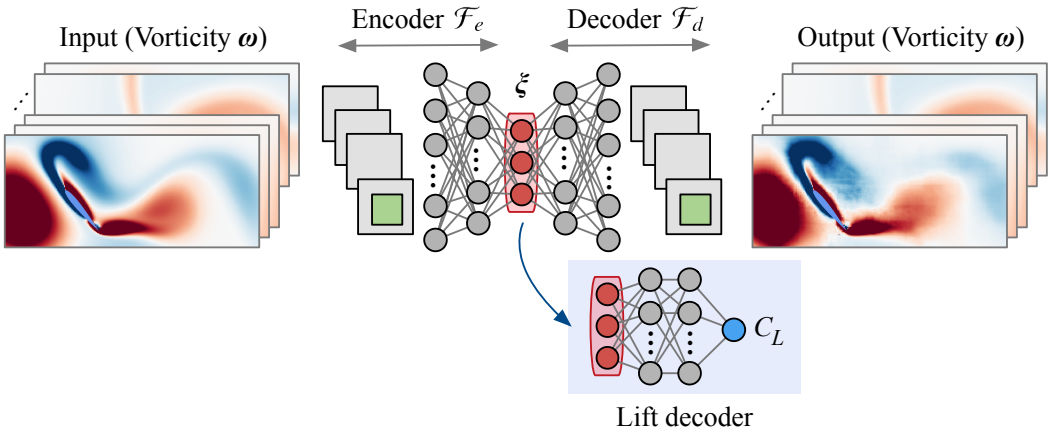

Figure 7.4: Lift-augmented nonlinear autoencoder (FT23).

data.

In this study, a discrete vorticity field $\boldsymbol{\omega}$ is compressed through the autoencoder such that

$$\boldsymbol{\xi} = \mathcal{F}_e(\boldsymbol{\omega}), \quad \boldsymbol{\omega} \approx \hat{\boldsymbol{\omega}} = \mathcal{F}_d(\boldsymbol{\xi}), \tag{7.2}$$

where $\hat{\boldsymbol{\omega}}$ is a decoded vorticity field. The weights inside a regular autoencoder are optimized by solving the following minimization problem,

$$\boldsymbol{w}^* = \text{argmin}_{\boldsymbol{w}} \|\boldsymbol{\omega} - \hat{\boldsymbol{\omega}}\|_2 = \text{argmin}_{\boldsymbol{w}} \|\boldsymbol{\omega} - \mathcal{F}(\boldsymbol{\omega}; \boldsymbol{w})\|_2, \tag{7.3}$$

where $\boldsymbol{w}$ is the weights of the autoencoder. With nonlinear activation functions inside neural networks, autoencoder can nonlinearly compress high-dimensional data into a low-order subspace, which often achieves better compression than linear techniques.

While nonlinear autoencoders can be used to compress a variety of vortical flow data (FHN21; OS19; XD20), we have found that the regular formulation expressed in equation 7.3 does not guarantee to obtain a physically-interpretable data distribution in the latent space. Especially, extracting low-order coordinates associated with aerodynamic features is important in considering not only the understanding of extreme aerodynamic flows but also downstream tasks such as developing control strategies. To facilitate the identification of a low-dimensional subspace from the aspect of aerodynamics, the proposed model referred to as a lift-augmented nonlinear autoencoder incorporates a lift coefficient $C_L(t)$ for manifold identification.

In the present formulation, the additional branch network connected with the latent variables $\boldsymbol{\xi}$ (lift decoder, the blue-shade portion in figure 7.4) simultaneously outputs $C_L(t)$ with a vorticity field $\boldsymbol{\omega}(t)$. This can weigh the latent variables $\boldsymbol{\xi}$ with the lift coefficient C_L. The optimization for the weights inside the lift-augmented autoencoder is described as

$$\boldsymbol{w}^* = \text{argmin}_{\boldsymbol{w}} \left[||\boldsymbol{\omega} - \hat{\boldsymbol{\omega}}||_2 + \beta ||C_L - \hat{C}_L||_2 \right], \tag{7.4}$$

where β balances the vorticity field and lift reconstruction loss terms. By adding this lift decoder, the latent vector $\boldsymbol{\xi}(t)$ can be relevant to the lift coefficient $C_L(t)$ in identifying a low-dimensional manifold. More details on the autoencoder setup are referred to (FT23).

7.2.3 Vortex-airfoil interaction on a low-dimensional manifold

With the nonlinear lift-augmented autoencoder, the time series of extreme aerodynamic vortical flows spanning over a large parameter space can be compressed into only three latent variables. The latent variables $\boldsymbol{\xi}(t)$ in the present three-dimensional space are visualized in figure 7.5(a). Here, undisturbed baseline cases are shown in color while gray lines correspond to all the trajectories mapped from the disturbed vorticity flow field data. A variety of vortical flows with and without gust disturbances across five different angles of attack are considered. Each of the extreme aerodynamic cases can reside in the vicinity of the undisturbed base states while representing how much they are different (or similar) from the baseline conditions across angle of attack in a low-order manner, converging to the inertial manifold (FMT88; Tem89; DG23).

Let us first focus on the latent trajectories of the undisturbed flows. The latent vectors for the undisturbed flows across the angle of attack are aligned along the ξ_3 direction. While the different angles of attack can be distinguished in a low-order space, the shape of the trajectory for each angle also reflects the wake behavior of the original high-dimensional space. The case of $\alpha = 20°$ is mapped as a single dot while the other baseline cases possessing unsteady periodic shedding at $\alpha \geq 30°$ exhibit cyclic trajectories. This corresponds to the steady flow at $\alpha = 20°$ and unsteady limit-cycle oscillations at $\alpha \geq 30°$ of vorticity fields.

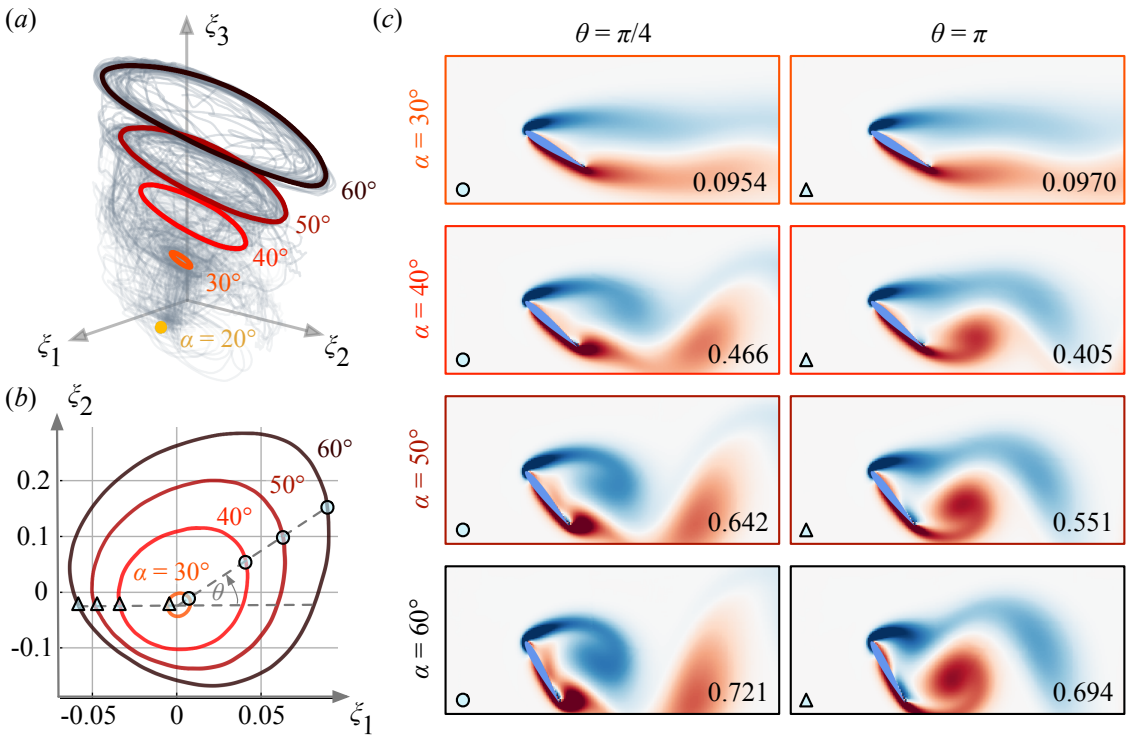

Figure 7.5: Extreme aerodynamic trajectories in (a) the three-dimensional latent space and (b) its two-dimensional view for the undisturbed baseline cases. (c) Undisturbed vorticity fields at $\theta = \pi/4$ and π for $\alpha \in [30, 60]°$. The values inside each snapshot report an unsteadiness factor norm $\epsilon_\omega = ||\omega(t) - \overline{\omega}||_2/||\overline{\omega}||_2$.

The two-dimensional view of the latent space and representative vorticity fields with $\alpha \in [30, 60]°$ at two different phases $\theta = \pi/4$ and π are shown in figures 7.5(b) and (c), respectively. The radius of each circle for the undisturbed cases of $\alpha \geq 30°$ increases with the angle of attack. To quantitatively examine this point, we assess an unsteadiness factor norm $\epsilon_\omega = ||\omega(t) - \overline{\omega}||_2/||\overline{\omega}||_2$, where $\overline{\omega}$ is a time-averaged vorticity field, and report it for each of the representative snapshots with $\alpha \in [30, 60]°$ in figure 7.5(c). As shown, the value increases with the angle of attack. In other words, the expansion of the radius is due to the increases in flow unsteadiness for each angle of attack case. Furthermore, undisturbed vorticity fields at each phase depicted in figure 7.5(c) present a similar wake shedding pattern across the angle of attack. These observations suggest that the undisturbed wakes can be successfully low-dimensionalized while preserving the information

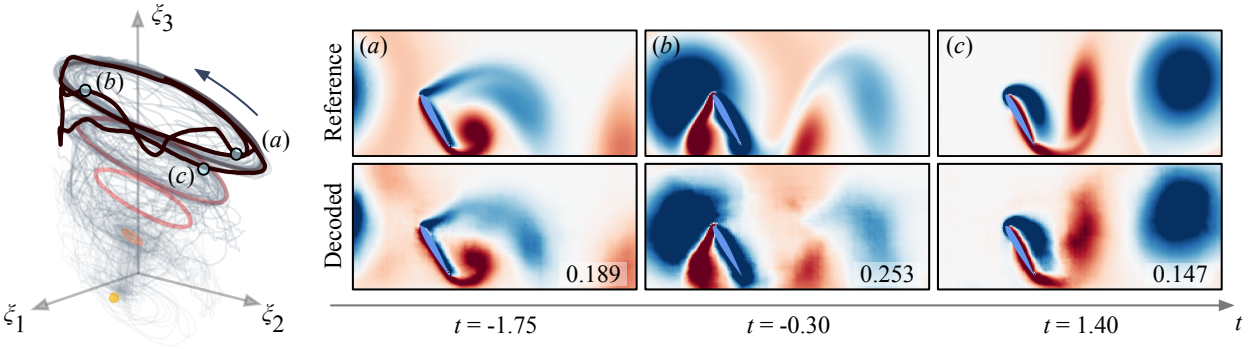

Figure 7.6: Extreme aerodynamic trajectories in the three-dimensional latent space and vortical flow snapshots for $(\alpha, G, D, Y) = (60°, -2.8, 1.5, 0)$. The value inside of each decoded snapshot reports the L_2 spatial reconstruction error norm.

of phase (time) and amplitude (fluctuation) in the original high-dimensional space.

Next, let us examine the trajectories for disturbed wake flows. All gray trajectories corresponding to extreme aerodynamic flows reside around the orbits of the undisturbed cases in a coherent manner. To investigate the implication of low-dimensionalized extreme aerodynamic trajectories, we take an example case of $(G, D, Y) = (-2.8, 1.5, 0)$ for which a strong, large vortex gust impinges an airfoil at $\alpha = 60°$.

The latent variable trajectory and the reconstructed flow fields over time are also shown in figure 7.6. The value shown in each decoded flow contour reports the spatial reconstruction error norm $\varepsilon = ||\boldsymbol{\omega}_{\text{ref}} - \boldsymbol{\omega}_{\text{dec}}||_2 / ||\boldsymbol{\omega}_{\text{ref}}||_2$, where $\boldsymbol{\omega}_{\text{ref}}$ and $\boldsymbol{\omega}_{\text{dec}}$ are the reference and decoded vorticity fields, respectively. Nonlinear interaction between the airfoil and vortex gust can be reconstructed over time through the autoencoder-based compression of the three variables. This successful reconstruction indicates that the three-dimensional latent variables retain the essence of high-dimensional vortical flows without significant loss of key physics.

The extreme aerodynamic trajectory depicted in figure 7.6 reflects the effect of nonlinear vortex-gust interaction in the high-dimensional space about the undisturbed baseline flow. From the points (a) to (b) in figure 7.6, the latent vector dynamically rises and drops in the ξ_3 direction.

This is likely because of the approach of negative vortex disturbance to the airfoil, drastically and dynamically changing the effective angle of attack α_{eff} (And91; SJL20), i.e., $\xi_3 \propto \alpha_{\text{eff}}$. In other words, the present lift-augmented autoencoder can express the relationship between extreme aerodynamic flows and lift force in a low-order manner.

Such physically-interpretable low-dimensional representations of extreme aerodynamic flows can be obtained due to the lift-augmented network while a regular autoencoder cannot provide understandable latent data distributions (FT23). We emphasize that expressing extreme disturbance effects about the undisturbed baseline dynamics is critical in developing flow control strategies because it enables us to identify the desired direction (or control objective) in the low-order coordinates to mitigate the strong impact of extreme vortex gusts.

7.3 Phase-amplitude reduction and optimal control

With the uncovered space representation, we can quantitatively assess the influence of extreme vortex gusts on the dynamics in a low-order manner. While being able to avoid the collection of expensive time-history data, this coordinate also offers the possibility to examine the dynamics in the vicinity of the three-dimensional manifold.

In particular, the present nonlinear coordinate transformation suggests that the extracted dynamics of violent vortex-airfoil interaction can be analyzed through the viewpoint of dynamics expressed with phase θ and amplitude r, as illustrated in figure 7.7. The latent variable captures similar wake structures at the same phase θ while showing the amplitude difference caused by the vortex-airfoil interaction, as exhibited in figure 7.7(b). This observation suggests that control strategies that push the extreme aerodynamic trajectory towards the direction of the undisturbed baseline state in the latent space may mitigate the influence of vortex disturbance in the flow field.

In this study, we analyze and control extreme aerodynamic flows with the assistance of phase-amplitude modeling. The procedure can be divided into three steps, namely;

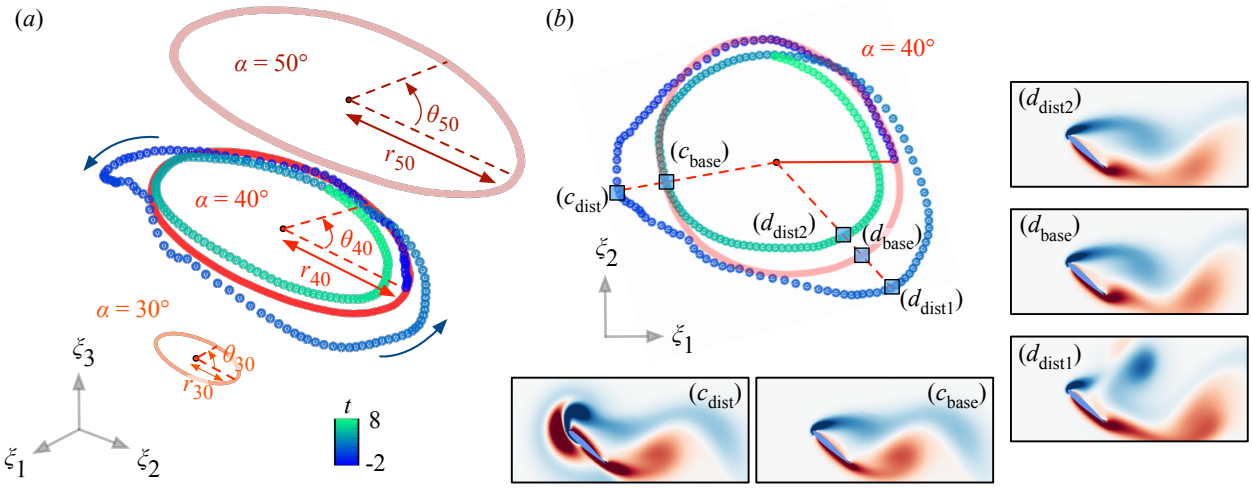

Figure 7.7: (a) Concept of phase-amplitude space on extreme aerodynamic manifold. The extreme aerodynamic trajectory colored by convective time for the case of $(\alpha, G, D, Y) = (40°, 2.8, 0.5, -0.3)$ is shown in addition to the undisturbed baseline orbits of $\alpha = 30°$, 40°, and 50°. (b) Two-dimensional phase-amplitude plane for $\alpha = 40°$. Flow fields at the same phase but different amplitudes chosen from undisturbed and disturbed wakes are visualized.

1. dynamical modeling in the latent space using sparse regression (section 7.3.1),

2. performing phase-amplitude reduction to measure phase- and amplitude sensitivity functions (section 7.3.2), and

3. controlling extreme aerodynamic flows with amplitude-constrained optimal waveform for fast synchronization (section 7.3.3).

Throughout these steps, we aim to derive a control law to suppress the large fluctuation of lift force due to the vortex disturbance within a very short time duration. Hereafter, let us introduce approaches used at each step of the present control strategies.

7.3.1 Sparsity-promoting low-dimensional dynamical modeling

Here, the dynamics of the latent vector $\boldsymbol{\xi}$ is modeled with a system of ordinary differential equations (ODE) using sparse identification of nonlinear dynamics (SINDy) (BPK16a). This data-driven technique can identify nonlinear governing equations from given time-series data. Let us consider a dynamical system for the latent vector $\boldsymbol{\xi}(t) \in \mathbb{R}^3$,

$$\dot{\boldsymbol{\xi}}(t) = \boldsymbol{F}(\boldsymbol{\xi}(t)). \tag{7.5}$$

The temporally discretized data of $\boldsymbol{\xi}$ are collected to prepare a data matrix $\boldsymbol{\Xi}$,

$$\boldsymbol{\Xi} = \begin{pmatrix} \boldsymbol{\xi}^T(t_1) \\ \boldsymbol{\xi}^T(t_2) \\ \vdots \\ \boldsymbol{\xi}^T(t_m) \end{pmatrix} = \begin{pmatrix} \xi_1(t_1) & \xi_2(t_1) & \xi_3(t_1) \\ \xi_1(t_2) & \xi_2(t_2) & \xi_3(t_2) \\ \vdots & \vdots & \vdots \\ \xi_1(t_m) & \xi_2(t_m) & \xi_3(t_m) \end{pmatrix} \in \mathbb{R}^{m\times 3}. \tag{7.6}$$

Similarly, the time-series data of the time-differentiated value $\dot{\boldsymbol{\xi}}(t)$ is arranged to construct a time-differentiated data matrix $\dot{\boldsymbol{\Xi}}$. We also prepare a library matrix $\Phi(\boldsymbol{\Xi})$ including nonlinear terms of $\boldsymbol{\Xi}$. This study uses sine and cosine functions for the library matrix construction,

$$\Phi(\boldsymbol{\Xi}) = \begin{pmatrix} | & | & | & | & | & & | & | \\ \sin(\boldsymbol{\Xi}) & \sin(\boldsymbol{\Xi}/2) & \sin(\boldsymbol{\Xi}/4) & \sin(2\boldsymbol{\Xi}) & \sin(4\boldsymbol{\Xi}) & \cdots & \cos(2\boldsymbol{\Xi}) & \cos(4\boldsymbol{\Xi}) \\ | & | & | & | & | & & | & | \end{pmatrix}, \tag{7.7}$$

where we include sine and cosine functions of ξ_i, $\xi_i/2$, $\xi_i/4$, $2\xi_i$, and $4\xi_i$. While polynomials constructed by given variables are often considered for the library matrix construction (BPK16a; BPK16b; KKB18; LKL19), we have found that a trigonometric function-based library can provide a more accurate solution. A coefficient matrix Ψ can be obtained by solving the following regression problem,

$$\dot{\boldsymbol{\Xi}}(t) = \Phi(\boldsymbol{\Xi})\Psi, \tag{7.8}$$

with

$$\Psi = (\psi_{\xi_1} \;\; \psi_{\xi_2} \;\; \psi_{\xi_3}) = \begin{pmatrix} \psi_{(\xi_1,\,1)} & \psi_{(\xi_2,\,1)} & \psi_{(\xi_3,\,1)} \\ \psi_{(\xi_1,\,2)} & \psi_{(\xi_2,\,2)} & \psi_{(\xi_3,\,2)} \\ \vdots & \vdots & \vdots \\ \psi_{(\xi_1,\,l)} & \psi_{(\xi_2,\,l)} & \psi_{(\xi_3,\,l)} \end{pmatrix}, \tag{7.9}$$

where the subscript l denotes the row index of the library matrix. In this study, the adaptive Lasso (Zou06; FMZ21) is used to optimize the coefficient matrix Ψ.

Once we obtain an accurate low-dimensional dynamical model $\dot{\boldsymbol{\xi}}$, the model is then used to perform the phase-amplitude reduction which can provide the optimal timing and location of control actuation to efficiently and quickly modify the dynamics. For the present analysis, we model the undisturbed baseline dynamics (i.e., periodic limit-cycle oscillation) using SINDy with some auxiliary training data picked up in the vicinity of the limit cycle to obtain a dissipative and non-Hamiltonian low-dimensional model, which we explain in details later.

7.3.2 Phase-amplitude reduction analysis

As illustrated in figure 7.7, the current low-dimensional latent variables $\boldsymbol{\xi}$ can be analyzed through the lens of phase θ and amplitude r. Here, let us introduce the phase-amplitude reduction for the periodic, stable limit-cycle oscillator $\dot{\boldsymbol{\xi}}(t) = \boldsymbol{F}(\boldsymbol{\xi}(t))$ obtained through the SINDy for each angle of attack case. It is assumed that this ODE has an exponentially stable limit-cycle solution $\boldsymbol{\xi}_0(t) = \boldsymbol{\xi}_0(t+T)$, where $T = 2\pi/\omega_\xi$ with the natural frequency ω_ξ of the latent variable $\boldsymbol{\xi}$ for the undisturbed baseline case at each angle of attack.

Given the aforementioned ODE system, the phase and amplitude in the basin of χ can be expressed with the phase function $\Theta(\boldsymbol{\xi})$ and the amplitude functions $R_i(\boldsymbol{\xi})$. Here, the generalized phase and amplitude dynamics are described as

$$\begin{aligned} \dot{\Theta}(\boldsymbol{\xi}) &= \langle \nabla\Theta(\boldsymbol{\xi}), \dot{\boldsymbol{\xi}} \rangle = \langle \nabla\Theta(\boldsymbol{\xi}), \boldsymbol{F}(\boldsymbol{\xi}) \rangle = \omega_\xi, \\ \dot{R}_i(\boldsymbol{\xi}) &= \langle \nabla R_i(\boldsymbol{\xi}), \dot{\boldsymbol{\xi}} \rangle = \langle \nabla R_i(\boldsymbol{\xi}), \boldsymbol{F}(\boldsymbol{\xi}) \rangle = \lambda_i R_i(\boldsymbol{\xi}), \end{aligned} \tag{7.10}$$

where λ_i $(i = 0, 1, 2)$ denotes the Floquet exponents. Using them, we define the phase and amplitude variables of the latent system state $\boldsymbol{\xi}$ for each angle of attack case,

$$\theta = \Theta(\boldsymbol{\xi}), \quad r_i = R_i(\boldsymbol{\xi}). \tag{7.11}$$

Now considering an external input $\boldsymbol{f}(t)$ to the system, the oscillator dynamics is described as

$$\dot{\boldsymbol{\xi}}(t) = f(\boldsymbol{\xi}(t)) + \boldsymbol{f}(t). \tag{7.12}$$

For this perturbed system, the dynamics of phase θ and amplitudes r_i can be derived as

$$\begin{aligned} \dot{\theta}(t) &= \omega_{\boldsymbol{\xi}} + \langle \nabla\Theta(\boldsymbol{\xi}(t)), \boldsymbol{f}(t) \rangle, \\ \dot{r}_i(t) &= \lambda_i r_i(t) + \langle \nabla R_i(\boldsymbol{\xi}(t)), \boldsymbol{f}(t) \rangle, \end{aligned} \tag{7.13}$$

where the control input $\boldsymbol{f}(t)$ is sufficiently weak such that of the order of $O(\epsilon)$ with $0 \leq \epsilon \ll 1$. In other words, these equations can be approximated by neglecting the terms of order $O(\epsilon^2)$,

$$\dot{\theta} = \omega_{\boldsymbol{\xi}} + \langle \boldsymbol{Z}(\theta), \boldsymbol{f}(t) \rangle, \quad \dot{r}_i = \lambda_i r_i + \langle \boldsymbol{Y}_i(\theta), \boldsymbol{f}(t) \rangle, \tag{7.14}$$

where $\boldsymbol{Z}(\theta) = \nabla\Theta|_{\boldsymbol{\xi}=\boldsymbol{\chi}(\theta)}$ and $\boldsymbol{Y}_i(\theta) = \nabla R_i|_{\boldsymbol{\xi}=\boldsymbol{\chi}(\theta)}$ are the phase and amplitude sensitivity functions, respectively.

The phase sensitivity function $\boldsymbol{Z}(\theta)$ exhibits how the system is sensitive with respect to the phase shift against an external forcing over dynamics, while the amplitude sensitivity function $\boldsymbol{Y}_i(\theta)$ tells us how much the amplitude of system becomes excited from the periodic orbit due to a given forcing. Although it is generally difficult to measure the phase and amplitude sensitivity functions, they can be analytically obtained by assessing the left Floquet eigenvectors if a dynamical model is explicitly given (Kur84; TKN21).

Since we now have a low-order model through the SINDy as expressed above, we can analytically obtain the phase and amplitude sensitivity functions Θ and R_i with the Floquet theory. With the T-periodic solutions of the following equations,

$$\begin{aligned} \dot{\boldsymbol{U}}_i(t) &= [\mathcal{J}(\boldsymbol{\xi}_0(t)) - \lambda_i]\boldsymbol{U}_i(t), \\ \dot{\boldsymbol{V}}_i(t) &= -[\mathcal{J}(\boldsymbol{\xi}_0(t))^\dagger - \lambda_i^\dagger]\boldsymbol{V}_i(t), \end{aligned} \tag{7.15}$$

where the superscript † represents the Hermitian conjugate and $\mathcal{J}$ is a T-periodic Jacobian matrix of $\boldsymbol{F}$ evaluated about $\boldsymbol{\xi} = \boldsymbol{\xi}_0(t)$. Here, $\boldsymbol{U}$ and $\boldsymbol{V}$ are respectively the right and left Floquet eigenvectors. The phase and amplitude sensitivity functions $\boldsymbol{Z}(\theta)$ and $\boldsymbol{Y}_i(\theta)$ can be expressed as

$$\boldsymbol{Z}(\theta) = \boldsymbol{V}_0(\theta/\omega_{\boldsymbol{\xi}}), \quad \boldsymbol{Y}_i(\theta) = \boldsymbol{V}_i(\theta/\omega_{\boldsymbol{\xi}}), \tag{7.16}$$

for $0 \leq \theta < 2\pi$. Hence, the phase and amplitude sensitivity functions $\boldsymbol{Z}(\theta)$ and $\boldsymbol{Y}_i(\theta)$ can be obtained by numerically solving the adjoint linear equations (7.15) so that $\boldsymbol{U}$ and $\boldsymbol{V}$ can be calculated.

7.3.3 Optimal fast flow control with amplitude constraint

Next, we consider a feedforward control based on the phase and amplitude sensitivity functions $\boldsymbol{Z}(\theta)$ and $\boldsymbol{Y}_i(\theta)$. The present controller is designed to quickly modify the dynamics to be at the target frequency while suppressing the amplitude modulation in the low-dimensional latent dynamics $\boldsymbol{\xi}$. As exhibited in figure 7.7, the latent trajectory departs from the baseline (undisturbed) periodic dynamics when the airfoil encounters an extreme aerodynamic gust. Hence, modifying the latent space dynamics towards the direction of the periodic limit cycle while suppressing the amplitude modulation in the latent space corresponds to the mitigation of the impact from vortex gusts in a high-dimensional vortical flow field.

The above objective is achieved by leveraging the optimal-synchronization waveform with amplitude suppression (TKN21). The present control considers the alignment between the original system frequency and the target frequency, i.e., phase locking. The optimal waveform provides the actuation pattern over the dynamics to achieve the fastest synchronization (HTH10; ZNK16).

To begin with, let us introduce the concept of the relative phase (phase difference) $\phi(t) = \theta(t) - \omega_f t$ where ω_f is the forcing signal frequency. We assume that the the control input $\boldsymbol{f}$ is given in the form of $\boldsymbol{f}(t) = \boldsymbol{b}_{\boldsymbol{\xi}}(\omega_f t)$. The governing phase dynamics becomes

$$\dot{\theta} = \omega_{\boldsymbol{\xi}} + \langle \boldsymbol{Z}(\theta), \boldsymbol{b}_{\boldsymbol{\xi}}(\omega_f t) \rangle. \tag{7.17}$$

With the averaging methods (Kur84; HI97), the dynamics of the relative phase is provided as

$$\dot{\phi}(t) = \Delta\Omega + \frac{1}{T_f}\int_0^{T_f} \langle \boldsymbol{Z}(\phi + \omega_f \tau), \boldsymbol{b}_\xi(\omega_f \tau)\rangle d\tau \tag{7.18}$$

where T_f is a period of the periodic forcing input and $\Delta\Omega = \omega_\xi - \omega_f$. The asymptotic behavior of the relative phase dynamics can be approximated as

$$\dot{\phi}(t) = \Delta\Omega + \Gamma(\phi), \quad \Gamma(\phi) = \int_0^{T_f} \langle \boldsymbol{Z}(\phi + \Omega_p \tau), \boldsymbol{b}_\xi(\Omega_p \tau)\rangle d\tau, \tag{7.19}$$

where $\Gamma(\phi)$ is called the phase coupling function. In other words, phase locking can be achieved if the relative phase becomes a constant such that $\dot{\phi} \to 0$. This phase locking (synchronization) condition is given as $-\max\Gamma(\phi) < \Delta\Omega < -\min\Gamma(\phi)$, uncovering the Arnold tongue used in synchronization studies of nonlinear dynamical systems (SIM07).

Now, let us seek the optimal input to synchronize the system to a forcing (target) frequency as quickly as possible while suppressing the excitation from the limit-cycle dynamics in the latent space. In other words, the rate of convergence of ϕ to a fixed point ϕ^* needs to be maximized to satisfy $\dot{\phi}^* = \Delta\Omega + \Gamma(\phi^*) = 0$. To derive the periodic waveform that can satisfy the above condition, we consider the following cost function to formulate optimization maximizing $|\dot{\phi}|$,

$$\mathcal{L}(\boldsymbol{b}_\xi) = -\Gamma'(\phi^*) + \nu(P - \langle \boldsymbol{b}_\xi \cdot \boldsymbol{b}_\xi\rangle) + \mu(\Delta\Omega + \Gamma(\phi^*)) - k_i[\langle \boldsymbol{Y}_i(\phi^* + \omega_f t), \boldsymbol{b}_\xi(\omega_f t)\rangle^2]_t, \tag{7.20}$$

where $i = 1, \ldots, M$ with the first M amplitude variables, ν and μ are Lagrangian multipliers, and P is a constant satisfying $\sqrt{P} \sim O(\omega_\xi \delta)$. The first term contributes to maximizing the synchronization speed, the second term can constrain the energy of actuation, and the third term corresponds to the increment of the rate of convergence of ϕ. In addition, we can also penalize the excitation of the ith amplitude variable of amplitude sensitivity function with the weight k_i.

The above optimization can be analytically solved using the calculus of variations (ZCK13; TKN21) once we obtain the phase and amplitude sensitivity functions $\boldsymbol{Z}(\theta)$ and $\boldsymbol{Y}_i(\theta)$ through the Floquet analysis for the latent governing equation derived by SINDy. We can finally derive the optimal waveform as

$$\boldsymbol{b}_\xi(\omega_f t) = \frac{1}{2}\left\{\nu \boldsymbol{I} + k_i \boldsymbol{Y}_i(\phi^* + \omega_f t)\boldsymbol{Y}_i^\dagger(\phi^* + \omega_f t)\right\}^{-1} \cdot \{-\boldsymbol{Z}'(\phi^* + \omega_f t) + \mu \boldsymbol{Z}(\phi^* + \omega_f t)\}, \tag{7.21}$$

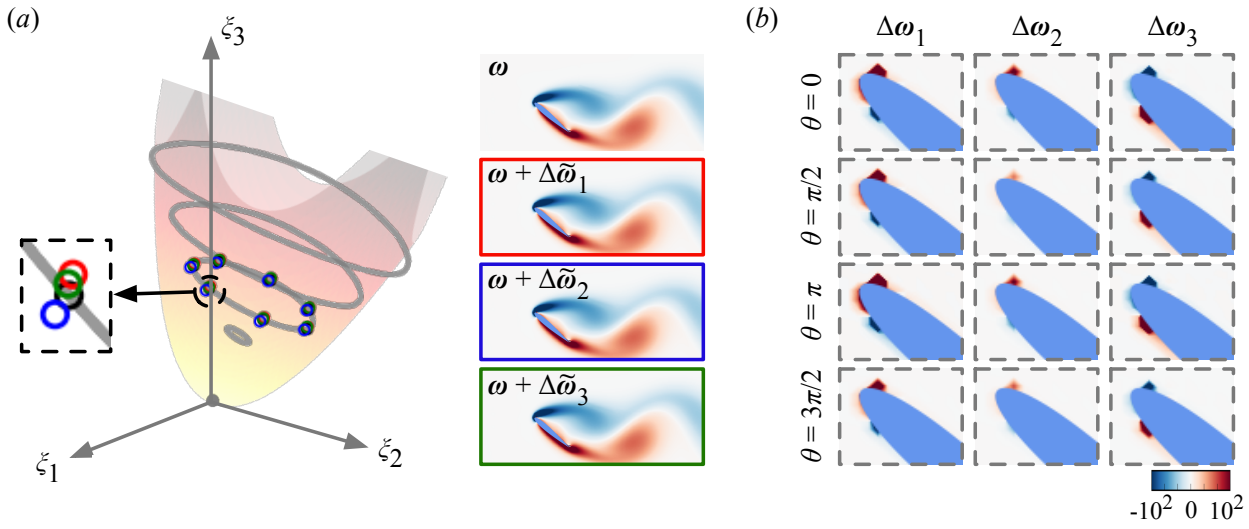

Figure 7.8: Conversion from latent perturbation to forcing in the original space. (a) Examples of perturbed vorticity fields $\boldsymbol{\omega} + \Delta\omega$ and the corresponding latent vector $\boldsymbol{\xi} + \Delta\tilde{\boldsymbol{\xi}}$. (b) The perturbation in the high-dimensional space toward a particular direction $\Delta\boldsymbol{\omega}_i$.

where $i = 1, ..., M$ and $\boldsymbol{I}$ is an identity matrix. Note that the weight value k_i is empirically chosen so that the effect of the input on the ith amplitude becomes sufficiently small (TKN21).

Because the optimal waveform in equation 7.21 provides how the actuation dynamically varies for controlling the latent system, it is also necessary to convert the latent perturbation to the forcing in the original latent space. We derive the relationship of the perturbation between the latent and physical spaces. For this, we assume that the encoder $\mathcal{F}_e$ is continuously differentiable. Given an input vorticity field $\boldsymbol{\omega}(t^*)$ with a perturbation in the high-dimensional space $\Delta\tilde{\boldsymbol{\omega}}(t^*)$, the corresponding latent vector can be approximated with the Jacobian matrix $\mathcal{J}_{\boldsymbol{\xi}}(\boldsymbol{\omega})$ of $\mathcal{F}_e$ evaluated at time t^* such that

$$\begin{aligned} \boldsymbol{\xi} + \Delta\tilde{\boldsymbol{\xi}} &= \mathcal{F}_e(\boldsymbol{\omega} + \Delta\tilde{\boldsymbol{\omega}}) \\ &\simeq \mathcal{F}_e(\boldsymbol{\omega}) + \mathcal{J}_{\boldsymbol{\xi}}(\boldsymbol{\omega})\Delta\tilde{\boldsymbol{\omega}}. \end{aligned} \tag{7.22}$$

For the current model yielding a three-dimensional latent vector from the given vorticity field, we consider giving three different patterns of perturbation to the original input $\Delta\tilde{\boldsymbol{q}}_m$ $(m = 1, 2, 3)$. The

deviation of the latent vector from the evaluation point is expressed as

$$\Delta\tilde{\boldsymbol{\xi}}_m = \mathcal{J}_{\xi}\Delta\tilde{\boldsymbol{\omega}}_m, \quad \text{where} \;\; m = 1, 2, 3. \tag{7.23}$$

With these deviations, a set of unit vectors $(\boldsymbol{e}_1, \boldsymbol{e}_2, \boldsymbol{e}_3)$ can be expressed as

$$\begin{aligned}\begin{pmatrix} | & | & | \\ \boldsymbol{e}_1 & \boldsymbol{e}_2 & \boldsymbol{e}_3 \\ | & | & | \end{pmatrix} &= \begin{pmatrix} | & | & | \\ \Delta\tilde{\boldsymbol{\xi}}_1 & \Delta\tilde{\boldsymbol{\xi}}_2 & \Delta\tilde{\boldsymbol{\xi}}_3 \\ | & | & | \end{pmatrix} \begin{pmatrix} H_{11} & H_{12} & H_{13} \\ H_{21} & H_{22} & H_{23} \\ H_{31} & H_{32} & H_{33} \end{pmatrix} \\ &= \boldsymbol{D}_{\xi}\boldsymbol{H}, \end{aligned} \tag{7.24}$$

where $\boldsymbol{H} \in \mathbb{R}^{3\times3}$ is a coefficient matrix. To individually perturb the latent system in the $\boldsymbol{e}_1$, $\boldsymbol{e}_2$, and $\boldsymbol{e}_3$ directions, the perturbation in the high-dimensional space toward a particular direction $\Delta\boldsymbol{\omega}_i$ $(i = 1, 2, 3)$ is prepared as

$$\Delta\boldsymbol{\omega}_i = H_{ji}\Delta\tilde{\boldsymbol{\omega}}_j, \tag{7.25}$$

where $j = 1, 2, 3$ and the coefficient matrix can be determined as $\boldsymbol{H} = \boldsymbol{D}_{\xi}^{-1}$.

In the present study, the three different perturbations in the physical space (for equation 7.23) are prepared by momentum injection at the leading edge of the airfoil with 45°, 90°, and 135° about the local tangential direction (NTB21). The actuation cost with the steady momentum coefficient c_μ is set to be 0.016. At each θ over the periodic dynamics, three perturbations are individually prepared so that the relationship of the perturbation in the latent and high-dimensional spaces can be obtained at each timing used for the linearization.

The perturbed flow fields and latent vectors (in equation 7.22) and the derived forcing in the high-dimensional space corresponding to a perturbation for each direction in the latent space (in equation 7.25) are shown in figure 7.8. The magnitude and shape of forcing structures vary over the dynamics and across the latent variables. Due to the assumption in equation 7.22 and small injections in preparing the three different patterns of $\Delta\boldsymbol{\omega}$, the designed forcing is very localized. This actuation enables us to examine whether extreme aerodynamic flows can be controlled by

such localized actuation spanning over a very small area with the assistance of optimal waveform analysis within a very short time duration.

Note that the identified relationship of the perturbation in the latent and high-dimensional spaces is also used to verify the phase sensitivity function $\boldsymbol{Z}(\theta)$ which is analytically derived in equation 7.16, which we explain in detail later. The designed perturbation $\boldsymbol{K}_\omega(\boldsymbol{x},t) = \epsilon \boldsymbol{b}_{\boldsymbol{\xi}}(t)\Delta\boldsymbol{\omega}(\boldsymbol{x},t)$ is added to the vorticity transport equation as

$$\partial_t \boldsymbol{\omega}(\boldsymbol{x},t) = -\boldsymbol{u}\cdot\nabla\boldsymbol{\omega} + Re^{-1}\nabla^2\boldsymbol{\omega} + \boldsymbol{K}_\omega(\boldsymbol{x},t), \tag{7.26}$$

where the designed perturbation in the velocity form $\boldsymbol{K}_{\boldsymbol{u}} = \nabla\times\boldsymbol{K}_\omega$ is used for performing the present simulations (KGT22). In the next section, we assess how much extreme aerodynamic flows can be controlled with the present localized forcing and the optimal waveform.

7.4 Results and discussion

This section demonstrates the present data-driven and phase-amplitude-inspired modeling and control of extreme aerodynamic flows. We consider cases at $\alpha = 40°$ as an example of complex vortex-airfoil interaction whose undisturbed baseline wake dynamics is time-periodic. A low-dimensional dynamical model identified by SINDy is first introduced. Once the phase and amplitude sensitivity functions are evaluated from the Floquet analysis for the identified low-order model, we apply the present control strategy to the extreme aerodynamic flows for gust mitigation.

7.4.1 Identification of low-dimensional latent dynamics

Here, let us discuss the SINDy-based low-dimensional latent dynamical modeling. As expressed in section 7.3.1, SINDy requires a data matrix $\boldsymbol{\Xi}$ and its time derivative $\dot{\boldsymbol{\Xi}}$ to approximate the dynamics in a least-square manner. While the periodic limit-cycle dynamics only need to be learned to measure both the phase and amplitude sensitivity functions from the model, giving only the data of the undisturbed periodic oscillation for training SINDy cannot achieve accurate

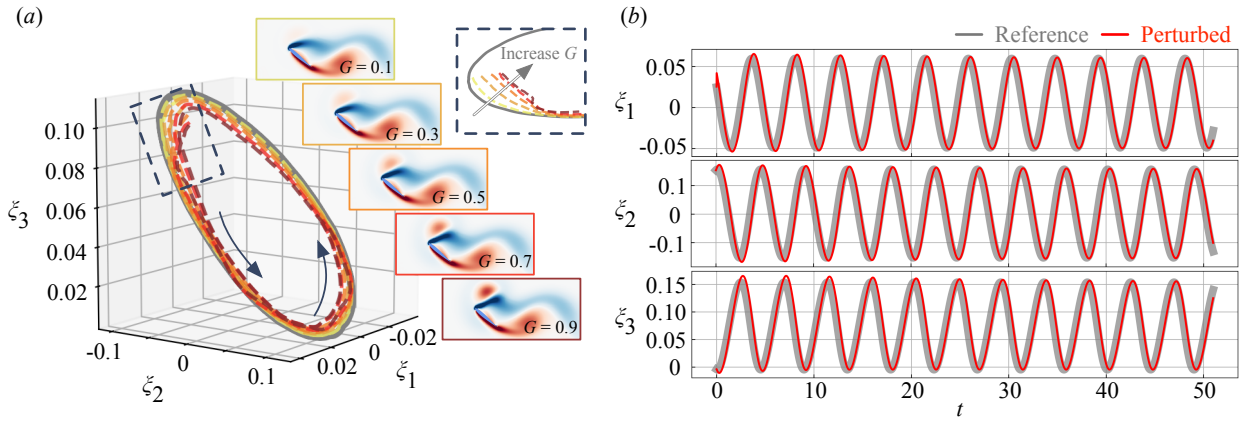

Figure 7.9: (a) Weakly-disturbed transient data used for SINDy training. The latent variables and the initial vorticity snapshot for cases with a positive vortex gust with $Y = 0.1$ are visualized. (b) SINDy-based latent dynamics identification.

modeling. This is simply because an identified model does not incorporate information off from the limit cycle. The SINDy-based modeling with periodical latent vectors generally finds the energy-conserving Hamiltonian system which cannot cover dissipative nature appearing in a high-dimensional flow physics (FMZ21). This indicates that the time trajectory of the Hamiltonian system does not return to the original limit cycle after the perturbation and would create a new periodic oscillation with a different radius. Since phase-amplitude reduction analysis assumes a T-periodic, stable limit cycle function, correctly identifying the non-Hamiltonian dynamics in a low-order manner is critical.

To this end, the present training data for SINDy includes not only the periodic oscillation but also the transient process of weakly disturbed cases with a vortex gust. Examples of training vorticity snapshots and corresponding latent vectors are shown in figure 7.9(a). To consider the transient process, the latent vector $\boldsymbol{\xi}$ and their time derivatives $\dot{\boldsymbol{\xi}}$ corresponding to twenty cases with a parameter combination of $G = (\pm 0.1, \pm 0.3, \pm 0.5, \pm 0.7, \pm 0.9)$, $Y = (-0.3, 0.1)$, and $D = 0.5$ are prepared. The snapshots after $t = 0.34$, when the vortex disturbance starts to impinge an airfoil, are used, enabling the SINDy model to accurately learn how the dynamics can return to the periodic

limit-cycle orbit.

The time-integrated results using the identified model equation $\dot{\boldsymbol{\xi}} = f(\boldsymbol{\xi})$ with perturbations are shown in figure 7.9(b). After the perturbation at $t = 0$, the amplitude gradually returns to the original level across all latent vectors. This reflects the given airfoil wake physics in the high-dimensional space in which the effect of perturbation dies out over the convection and the wake dynamics come back to the undisturbed periodic shedding oscillation.

7.4.2 Phase-amplitude-based modeling of latent dynamics

Next, we apply the phase-amplitude model reduction to the identified equation above to obtain the phase and amplitude sensitivity functions $\boldsymbol{Z}(\theta)$ and $\boldsymbol{Y}_i(\theta)$. As expressed in equations 7.15 and 7.16, these functions can be analytically obtained by assessing the left Floquet eigenvectors. These two functions for the present latent dynamics over $0 \leq \theta < 2\pi$ are depicted in figures 7.10(a) and (b). We find that the relative magnitudes of the sensitivities among the latent variables reflect the high-dimensional wake physics mapped into the low-order latent space.

The phase sensitivity functions $\boldsymbol{Z}(\theta)$ in the ξ_1 and ξ_2 directions are much larger than that for ξ_3. This is because the latent variables ξ_1 and ξ_2, which mainly compose the phase plane as illustrated in figure 7.7, possess a larger variation over the dynamics compared to ξ_3 capturing the effective angle of attack on the present manifold. This indicates that perturbing the system in the ξ_1 and ξ_2 directions is effective in modifying the dynamics from the aspect of phase delay or advancement.

On the other hand, the relative magnitude of the amplitude sensitivity function $\boldsymbol{Y}(\theta)$ for ξ_3 is of a similar order to that for the other two variables. This implies that the perturbation in the ξ_3 direction can contribute to the amplitude modulation of the latent dynamics. This also coincides with the aerodynamic observation in a high-dimensional space in which pitching the wing (in the ξ_3 direction) greatly modifies the fluctuation from the mean state of periodic wake shedding.

While being able to analytically derive the phase and amplitude sensitivity functions, these model-based sensitivity functions can be verified by perturbing the vorticity field in a numerical

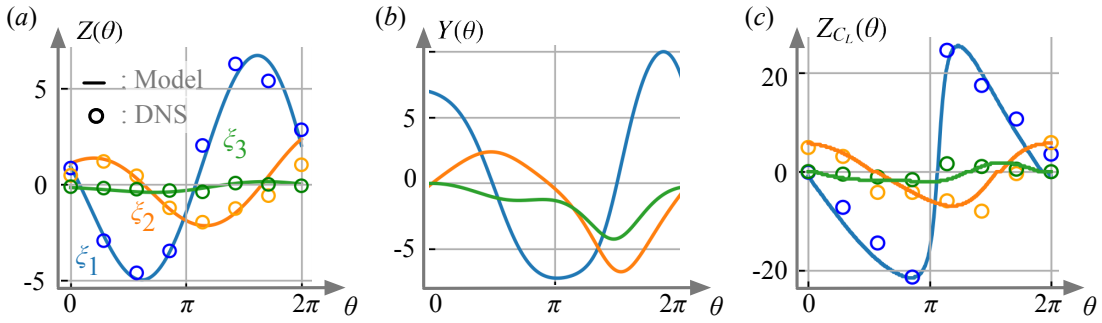

Figure 7.10: (a) Phase sensitivity function $\boldsymbol{Z}(\theta)$ and (b) amplitude sensitivity function $\boldsymbol{Y}(\theta)$ for the latent vector $\boldsymbol{\xi}$. (c) Phase sensitivity function $\boldsymbol{Z}_{C_L}(\theta)$ for the lift coefficient C_L. For the phase sensitivity functions, the analytical result through the Floquet analysis ($-$: Model) and the verified result with the forcing in equation 7.25 ($\circ$: DNS) are also shown.

simulation with the conversion via equation 7.25 and directly measuring the phase shift over the dynamics. The phase sensitivity functions evaluated in this way are also plotted with circles in figure 7.10. The verified results with the forcing are in agreement with the model-based phase sensitivity function, indicating that the SINDy-based model successfully captures the asymptotic flow behavior in a low-order manner.

Although we have discussed the phase sensitivity function for the latent variables, we can also measure the phase shift of the lift coefficient C_L since the present nonlinear autoencoder includes a lift decoder that estimates C_L from the latent variables $\boldsymbol{\xi}$. The phase sensitivity function for C_L is shown in figure 7.10(c). The overall trend of $\boldsymbol{Z}_{C_L}(\theta)$ is similar to that of $\boldsymbol{Z}(\theta)$, implying that the latent dynamics highly correlates with the vorticity field and lift coefficient. The verified results with the forcing quantitatively match the model-based sensitivity functions, similar to the case of the latent variables. The accurate estimation of phase sensitivity function for C_L also suggests that the present low-order model-based phase reduction can serve as a surrogate for the conventional phase analysis of fluid flows requiring expensive computational campaigns.

7.4.3 Amplitude-constrained fast synchronization control

With the phase and amplitude sensitivity functions $\boldsymbol{Z}(\theta)$ and $\boldsymbol{Y}(\theta)$ at hand, we are ready to derive the optimal waveform through equations 7.20 and 7.21. In this section, we demonstrate how the present method can mitigate the gust impact within a very short time by adding the forcing shown in figure 7.8 with the optimal waveform.

We first apply the present control to the case of $(\alpha, G, D, Y) = (40°, 2.8, 0.5, -0.3)$. Similar to the representative cases shown in figure 7.3, the lift coefficient in this case is violently affected due to the approach of the extreme vortex gust and shows significant fluctuation over a short time of less than 1 convective time. Our aim is to suppress such a sharp force fluctuation within a short time range. We imitate actuation at $t = -1.58$ when a vortex gust appears at the left edge of the domain of the interest.

To quantify the control effect, we consider the percentage change of lift fluctuation,

$$\eta = (\Delta C_{L,\mathrm{cont}} - \Delta C_{L,\mathrm{nocont}})/\Delta C_{L,\mathrm{nocont}}, \tag{7.27}$$

where $\Delta C_L \equiv \max(C_L) - \min(C_L)$ over $-1.58 < t < 2$ (during a vortex gust impinges a wing) with the subscripts $(\cdot)_{\mathrm{nocont}}$ and $(\cdot)_{\mathrm{cont}}$ being uncontrolled and controlled variables, respectively. Hence, a negative η corresponds to suppression of the lift fluctuation.

To derive the optimal waveform through equation 7.21, the ratio between the natural frequency ω_ξ and the target frequency ω_f, $H = \omega_f/\omega_\xi$, is set to be 1.5 in this case. The choice of target frequency ω_f is motivated to quickly modify a flow state since the actuation with $H > 1$ provides faster flow modification than that with $H < 1$ (GKT23). In the context of vortex-gust airfoil interaction, it is anticipated that the impact of the gust can be mitigated in a fast manner by changing the vortex-shedding frequency while suppressing the lift excitation due to the approach of vortex gust. Hereafter, we consider the waveform and forcing derived by the latent variable ξ_3 based on our aerodynamic knowledge that the effective angle of attack captured by ξ_3 strongly relates to the lift coefficient. This study chooses an actuation amplitude of $\epsilon = 0.12$ to achieve entrainment for extreme aerodynamic flows.

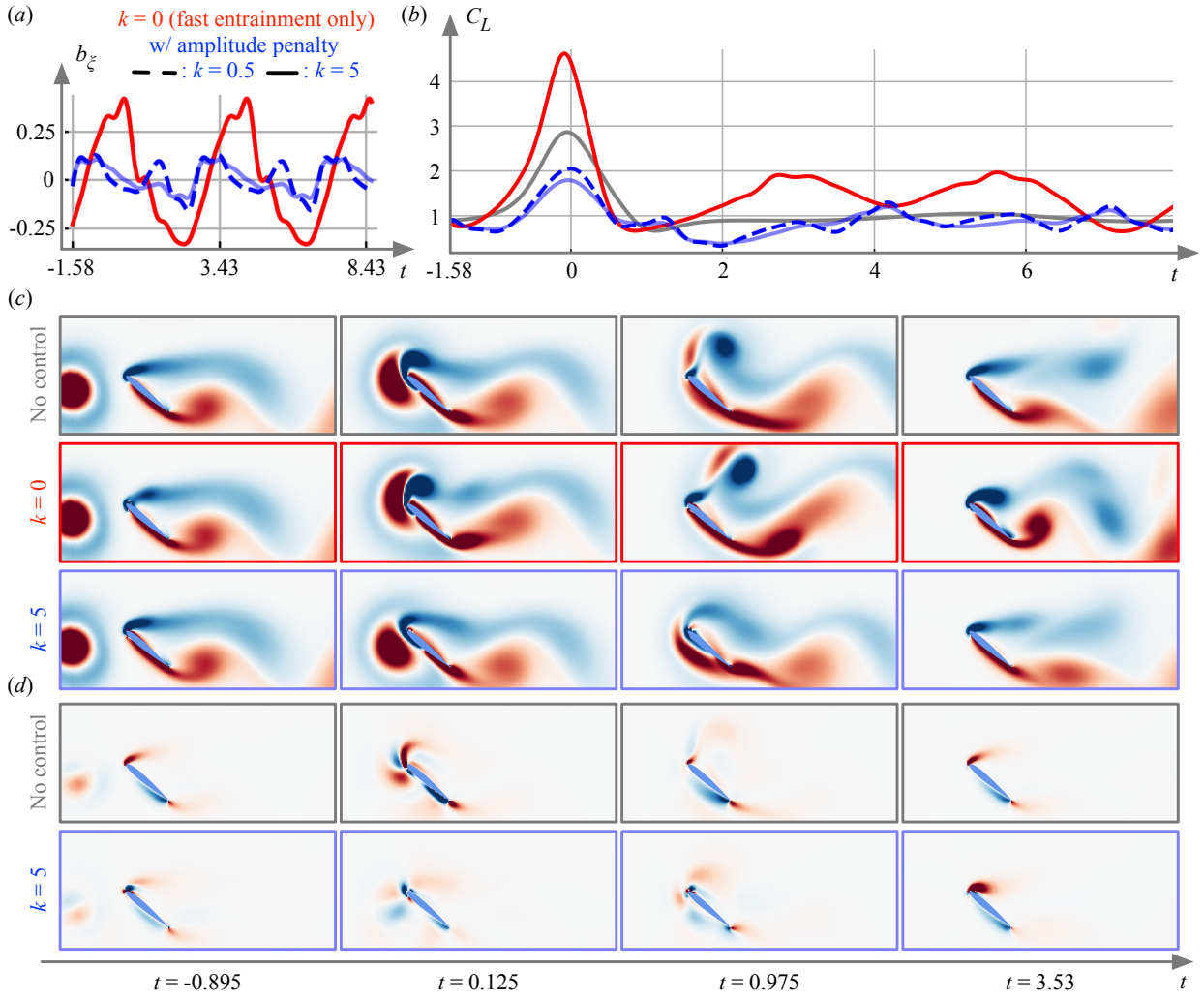

Figure 7.11: Phase-amplitude-based control of an extreme aerodynamic flow of $(\alpha, G, D, Y) = (40°, 2.8, 0.5, -0.3)$. (a) Optimal waveform b_ξ with $k = 0$, 0.5, and 5. (b) Lift coefficient C_L of the uncontrolled and controlled cases with $k = 0$, 0.5, and 5. (c) Vorticity fields and (d) lift force elements of the uncontrolled and controlled cases with $k = 0$ and 5.

The optimal waveform for the case of $(\alpha, G, D, Y) = (40°, 2.8, 0.5, -0.3)$ is shown in figure 7.11(a). To examine the effect of amplitude penalty constrained via equation 7.20, we consider three different weights, namely $k = 0, 0.5$, and 5. The waveform with amplitude penalty provides a more deformed pattern compared to that with $k = 0$ designed for purely fast synchronization only, analogous to the observation with several low-dimensional ODE models in (TKN21).

This wave pattern with amplitude penalty provides enhanced suppression of the transient lift fluctuation. The time series of the lift coefficient for each case is presented in figure 7.11(b). While the lift coefficient with the waveform with $k = 0$ is more amplified, the actuation with the amplitude-constrained optimal waveform can successfully suppress the lift fluctuation, achieving $\eta = -0.357$. We emphasize that the present optimal flow modification strategy is designed with minimal computational cost since all procedures expressed in section 7.3 are performed in a three-dimensional latent space. This suggests that the present method exhibits the potential to significantly and quickly reduce the impact of the extreme vortex gust on a wing in real time.

Let us further examine the control effect with vorticity snapshots, as summarized in figure 7.11(c). While the actuation at the leading edge can be seen at $t = -0.895$, the effect on the vortex gust is clearly observed at $t = 0.125$. For $k = 0$, the vortex core is shifted up due to the actuation, resulting in massive separation at $t = 0.975$. Although this largely contributes to the amplification of lift response, we note that a vorticity field at $t = 3.53$ apparently presents a faster vortex shedding form. This suggests that the fast synchronization-focused optimal waveform can quickly modify the flow states to be a target frequency (GKT23).

In contrast, the amplitude-constrained optimal actuation with $k = 5$ can shift the vortex core downward and the gust slips on the pressure side of the airfoil. Because of this modification of vortex-core position, what would happen at $t = 0.975$ is that the strong vortex gust naturally merges with the trailing-edge vortex. The wake behavior then eventually returns to the baseline natural vortex shedding. In other words, the control strategy developed in a low-order space to suppress the amplitude modulation of latent vector while quickly modifying the low-order dynamics is now elegantly translated to the high-dimensional aerodynamic behavior.

To further analyze the aforementioned control effect with the vortex-core move on the lift response, we also perform force element analysis (Cha92) which identifies responsible vortical structures for lift generation. For an auxiliary potential function ϕ_L satisfying the Laplace equation $\nabla^2\phi_L = 0$ with the boundary condition $-\boldsymbol{n}\cdot\nabla\phi_L = \boldsymbol{n}\cdot\boldsymbol{e}_y$ on the wing surface, where $\boldsymbol{e}_y$ is the unit vector in the lift direction, the lift force F_L can be expressed as

$$F_L = \int_{\mathcal{D}} \boldsymbol{\omega}\times\boldsymbol{u}\cdot\nabla\phi_L dD + \frac{1}{Re}\int_{\partial D}\boldsymbol{\omega}\times\boldsymbol{n}\cdot(\nabla\phi_L + \boldsymbol{e}_y)dl, \tag{7.28}$$

where the first and second terms correspond to the surface integral and the line integral on the wing surface, respectively. The first term is called the lift element L_E, which has often been used to infer the source of lift generation in vortical flows (MSJ21; ZSB22; RYZ22; MKM22).

Lift element fields over extreme vortex-airfoil interaction are shown in figure 7.11(d). For the uncontrolled case, the impingement of the vortex gust at $t = -0.045$ greatly contributes to the large lift force increment. It is also observed that the interaction between the vortex gust and the separated leading edge vortex causes positive contribution to lift, which is difficult to assess from vorticity fields only.

The mechanism of fluctuation suppression with the present control can be understood with the lift element analysis. As shown, the downward shift of vortex core at $t = -0.045$ significantly reduces the positive contribution to the lift force. In addition, at $t = 1.15$, the positive vorticity structure generated due to the merging of the vortex gust and the trailing-edge vortex near the pressure side of the airfoil exhibits a negative effect on the lift force. These suggest that the shift of the vortex gust with the present control can indeed reduce the lift force over the complex interaction dynamics.

Let us also apply the present control to the case of $(\alpha, G, D, Y) = (40°, -4, 0.5, 0.1)$, experiencing a negative vortex disturbance. In contrast to the case with positive vortex gusts, the lift force first drops and then increases, which is similar to the representative cases at $\alpha = 40°$ and $50°$ in figure 7.3. The ratio between the target and natural frequencies is set to be $H = 1.3$ following our preliminary analysis.

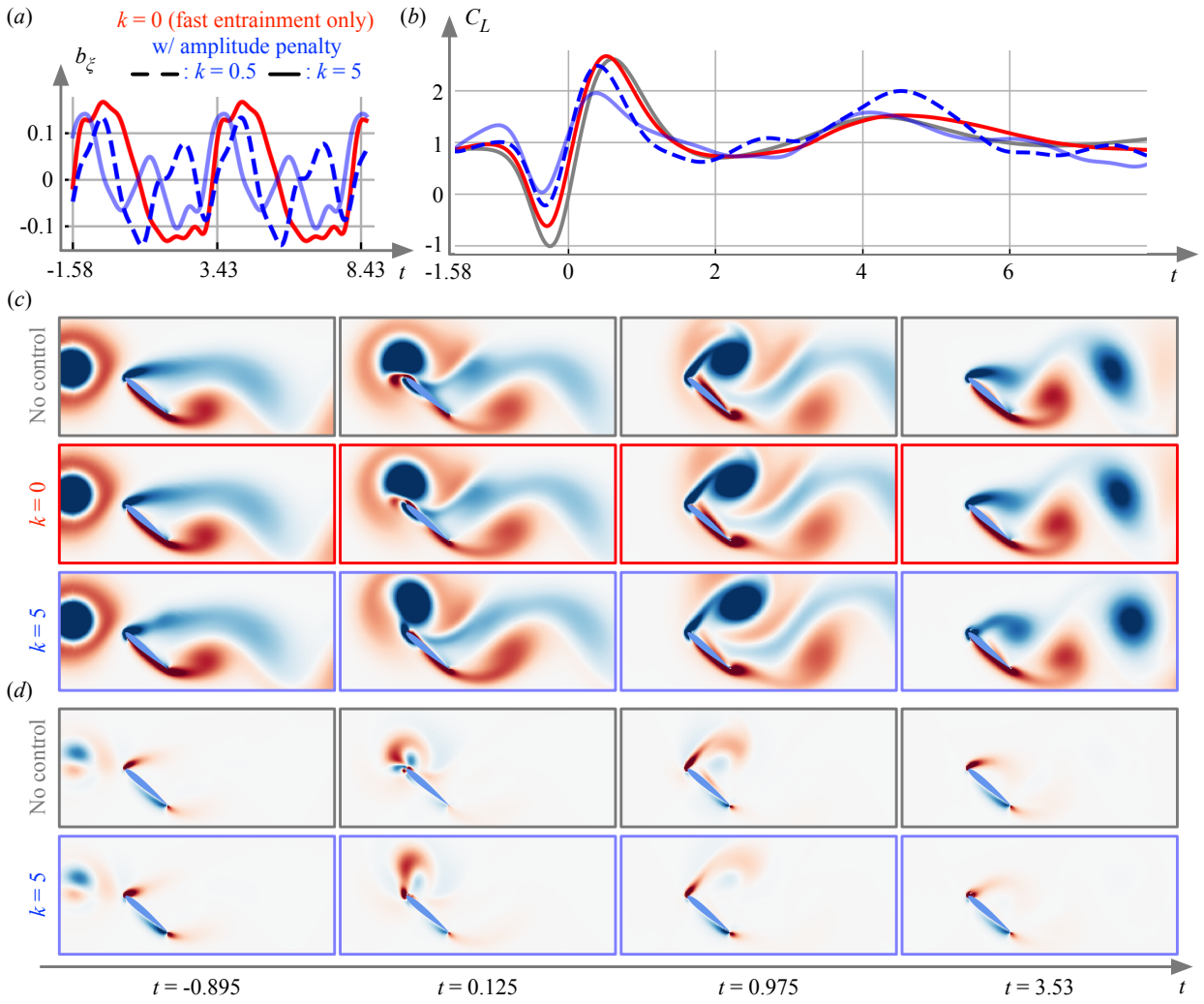

Figure 7.12: Phase-amplitude-based control of an extreme aerodynamic flow of $(\alpha, G, D, Y) = (40°, -4, 0.5, 0.1)$. (a) Optimal waveform b_ξ with $k = 0$, 0.5, and 5. (b) Lift coefficient C_L of the uncontrolled and controlled cases with $k = 0$, 0.5, and 5. (c) Vorticity fields and (d) lift force elements of the uncontrolled case and the controlled cases with $k = 0$ and 5.

The optimal waveform $\boldsymbol{b}_{\xi}$, the corresponding lift response, and vorticity fields are shown in figures 7.12(a)–(c). The actuation with $k = 0$ focusing on the fast entrainment only less modifies the vorticity fields and the lift dynamics compared to the case with positive gust in figure 7.11, due to a larger gust ratio. By introducing the amplitude penalty, the lift fluctuation can be greatly suppressed, reporting $\eta = -0.410$.

Interestingly, the lift force with the amplitude penalty is increased by the actuation around $t = -0.8$ so that the first drop of the lift force around $t = -0.3$ can be mitigated. This mitigation of lift fluctuation can also be evident from the shift up of vortex core occurring around the leading edge in a vorticity field at $t = 0.125$. Due to this vortex-core shift, the positive contribution to lift is enhanced at the leading edge, as shown in the lift force element field of figure 7.12(d). Hence, the positive lift generation here can contribute to suppressing the reduction of lift force by a strong vortex gust. While the mechanism for controlling the flows would be different depending on vortex-gust parameters, these observations suggest the possibility of quick flow modification under extreme aerodynamic conditions in real time.

The present approach can provide the optimal actuation based on phase and amplitude sensitivity functions derived from a low-order dynamical model with undisturbed baseline flow data. Although the current technique relies on the phase and amplitude information defined on a low-dimensional manifold that may be common even for extreme aerodynamic cases to some extent as illustrated in figure 7.7, the actuation pattern is provided in a feedforward manner. In other words, the process does not account for any information on vortex gust parameters. Furthermore, the methods used in the present study involve some linear assumptions, implying that there should exist cases in which the present control is no longer valid. To clarify conditions that can/cannot be handled with the current technique, let us lastly examine the controllability with the present method for extreme aerodynamic flows.

The concept of phase-amplitude reduction could be leveraged for extreme aerodynamic cases that are mapped in the vicinity of the baseline limit cycle (similar to a case in figure 7.7), while cases whose latent vector largely deviates from the undisturbed dynamics may be out of the controllable

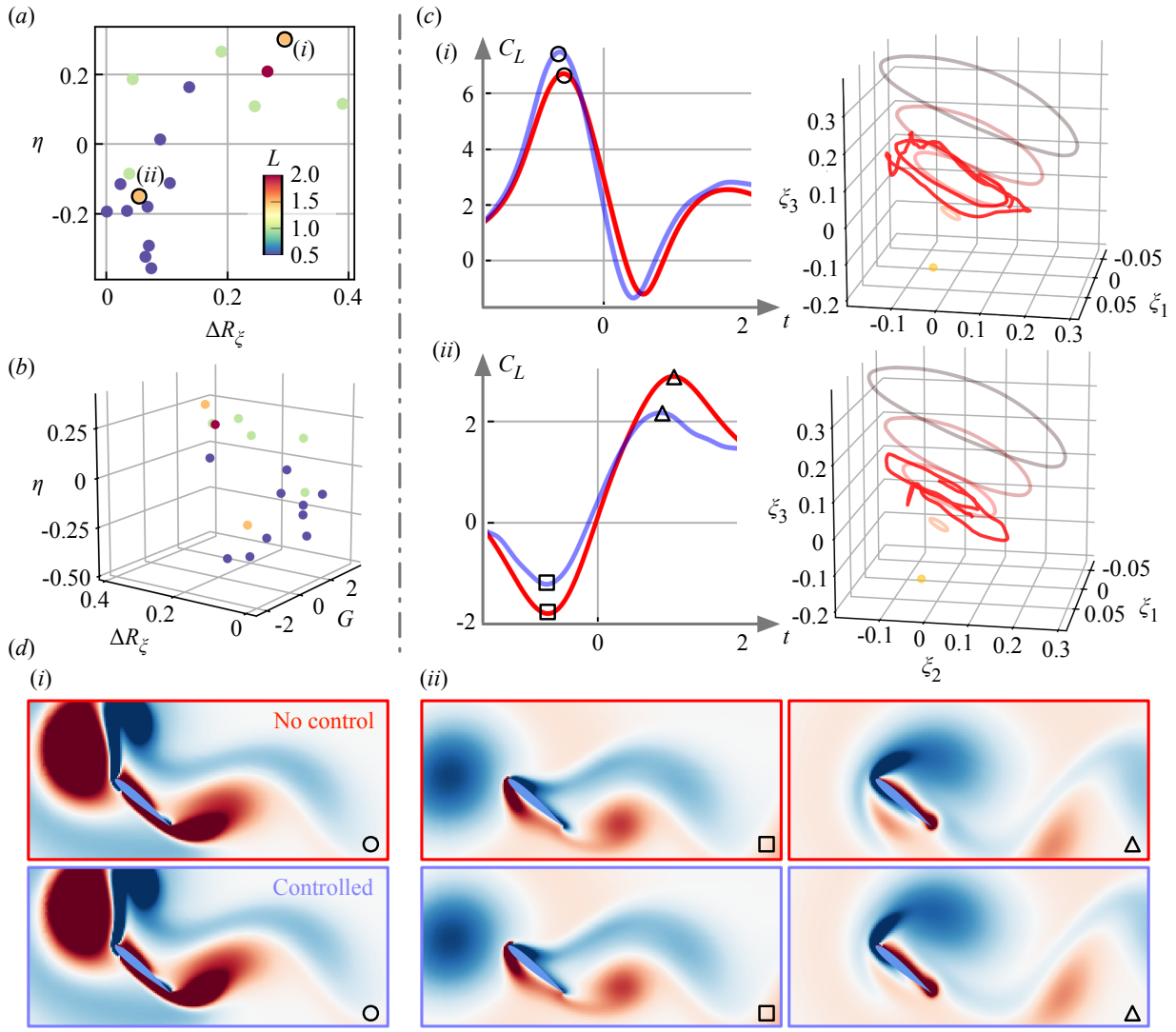

Figure 7.13: Assessments of controllability of the present approach for extreme aerodynamic flows. (a) The relationship between the control effect η and the deviation of the latent vector from the undisturbed baseline state $\Delta R_{\boldsymbol{\xi}}$ colored by the vortex gust size L. (b) The gust ratio G is added as to a two-dimensional view in (a) as a third axis. (c) Lift coefficient C_L, the latent vector $\boldsymbol{\xi}$, and (d) vorticity field ω for cases (i) $(G, D, Y) = (3.6, 1, 0.1)$ and (ii) $(-1.4, 1.5, 0)$ are shown.

cloud in the parameter space. To quantify the deviation from the undisturbed dynamics, we consider the averaged distance ΔR_ξ in a three-dimensional latent space,

$$\Delta R_\xi = ([R_{\xi,\mathrm{dist}}]_t - [R_{\xi,\mathrm{base}}]_t)/[R_{\xi,\mathrm{base}}]_t, \tag{7.29}$$

where

$$R^2_{\xi,\mathrm{base}}(t_i) = \sum_j^3 (\xi_{j,\mathrm{base}}(t_i) - [\xi_{j,\mathrm{base}}]_t)^2, \quad R^2_{\xi,\mathrm{dist}}(t_i) = \sum_j^3 (\xi_{j,\mathrm{dist}}(t_i) - [\xi_{j,\mathrm{base}}]_t)^2, \tag{7.30}$$

with the time-averaging operation $[\cdot]_t$. Hence, R_ξ here can measure how much data deviates from the baseline orbit in the latent space.

The relationship between the control effect η and the distance ΔR_ξ is shown in figure 7.13(a). The plots are colored by the size of the vortex disturbance L. Here, we set the ratio between the natural and target frequencies to be $H = 1.5$. There is a clear trend — smaller ΔR_ξ, better control performance (a negative η). As expected, the present control is valid for cases that reside near the undisturbed baseline orbit in the latent space. Since the dynamical behavior of the extreme aerodynamic trajectories on the manifold is generally affected by the vortex size more than the gust ratio (FT23), cases with a smaller gust size can be relatively controlled well, as observed in figures 7.13(a) and (b).

Since the effects from vortex size and gust ratio are nonlinearly correlated with each other, there are also cases in which the lift fluctuation can be mitigated even with a large vortex gust. We provide a lift curve, the latent vector, and vorticity fields for two extreme aerodynamic cases with the parameters of (i) $(G, D, Y) = (3.6, 1, 0.1)$ and (ii) $(-1.4, 1.5, 0)$ in figures 7.13(c) and (d). While the flow fields and lift response of case (i) do not show significant differences after the actuation due to large G and D, case (ii) with a larger gust size of $D = 1.5$ achieves 15% reduction of the lift fluctuation. This is simply because the absolute gust ratio of case (ii) is smaller than that of case (i); however, we should note that the gust ratio of $G = -1.4$ here already belongs to the condition traditionally thought of as unflyable. These observations suggest that the present feedforward control strategy developed in a three-dimensional space becomes a significant step toward flying under extreme aerodynamic conditions.

7.5 Concluding remarks

We presented a data-driven control to mitigate the impact of vortex gusts for flows around an airfoil. In particular, our consideration lies in the conditions of gust ratio $G > 1$ that are challenging to sustain stable flights, referred to as extreme aerodynamics. The present control strategy was developed in a low-dimensional manifold discovered by a nonlinear autoencoder. Once a collection of extreme aerodynamic data is compressed into a three-dimensional latent variable, we modeled the dynamics of the latent variables using a sparsity-promoting regression. The identified dynamics as a form of ODE was applied to phase-amplitude reduction, providing the phase and amplitude sensitivity functions. These functions tell us how the system is sensitive with respect to the phase shift and amplitude modulation against a given forcing. To quickly suppress the lift fluctuation of extreme vortex gust-airfoil interaction, the control actuation was derived through the amplitude-constrained optimal waveform analysis with the derived phase and amplitude sensitivity functions. We found that the present control technique can suppress the lift fluctuation occurring due to a strong vortex disturbance within a very short time duration for a wide variety of scenarios. Furthermore, the successful impact mitigation with a localized forcing implies the possibility of gust control without necessitating drastic pitching motion of the wing.

The present observations suggest the importance of physically-tractable data compression and preparation of appropriate coordinates to represent complex aerodynamic fluid flow data. The significant data compression into a three-dimensional latent vector can call for a variety of mathematical tools in understanding and controlling fluid flows. In fact, this compression allows us to use the SINDy to model the high-dimensional dynamics in a low-order manner. As the present coherent low-order expression provides a connection between extreme aerodynamic flows and phase-amplitude reduction, preparing a handleable low-dimensional form of high-dimensional data would be a key for analyzing seemingly complex fluid flow data sets.

There are some conceivable extensions of the present study. One can consider the use of feedback formulation in designing the optimal control actuation in either the SINDy-based model

space (BN15; NBT18) or waveform construction (TKN21). This could extend the control bound of the present formulation for high gust ratio and large vortex gusts. In addition, the present formulation can be combined with data-driven sparse reconstruction techniques as demonstrated with decoder-type neural-network-based efforts (EMY20; FMR21; FFT23). Estimating low-dimensional extreme aerodynamic latent vectors from pressure sensors allows for performing the proposed analysis from sensor-based information in a real-time manner. Since the proposed control can be performed in a three-dimensional latent space with minimal costs, the present idea of preparing optimal control actuation in a low-order space can support real-time stable flight operation of modern small-scale aircraft under extreme aerodynamic conditions.

CHAPTER 8

Concluding Remarks

In this thesis, we developed data-driven methods to reconstruct, model, and control unsteady fluid flows based on sparse sensor measurements. The approach is based on super-resolution analysis for flow field reconstruction which estimates high-resolution flow fields from low-resolution data. As sparse reconstruction can be seen as a generalized super resolution idea, we first covered a range of machine-learning-based super-resolution reconstructions in fluid mechanics though a survey study. We also performed supervised machine-learning-based reconstruction of turbulent vortical flows in an industrial setting. Furthermore, a Voronoi tessellation-assisted convolutional neural network was proposed to address scenarios with moving sparse sensor data. Moreover, we supplemented the critical distinction between interpolatory and extrapolatory conditions in turbulent flows, performing the Buckingham Pi theorem-assisted nonlinear scaling. This can facilitate the identification of scale-invariant structures, enabling the quantitative assessment of seen and unseen turbulent physics across available data sets.

Considering flow control based on knowledge gained through the present data-driven techniques, we performed nonlinear autoencoder-based compression, identifying a low-dimensional manifold space. The present autoencoder referred to as observable-augmented autoencoder can translate fluid flow data into a compact, low-dimensional representation while preserving essential dynamic information. For vortex-gust airfoil interactions, we also showed that a physically-explainable latent expression discovered by the present autoencoder can be leveraged for devising control strategies in tandem with phase-amplitude reduction. The developed control strategies in a low-order space achieved swift modification to reduce the impact of vortex gusts.

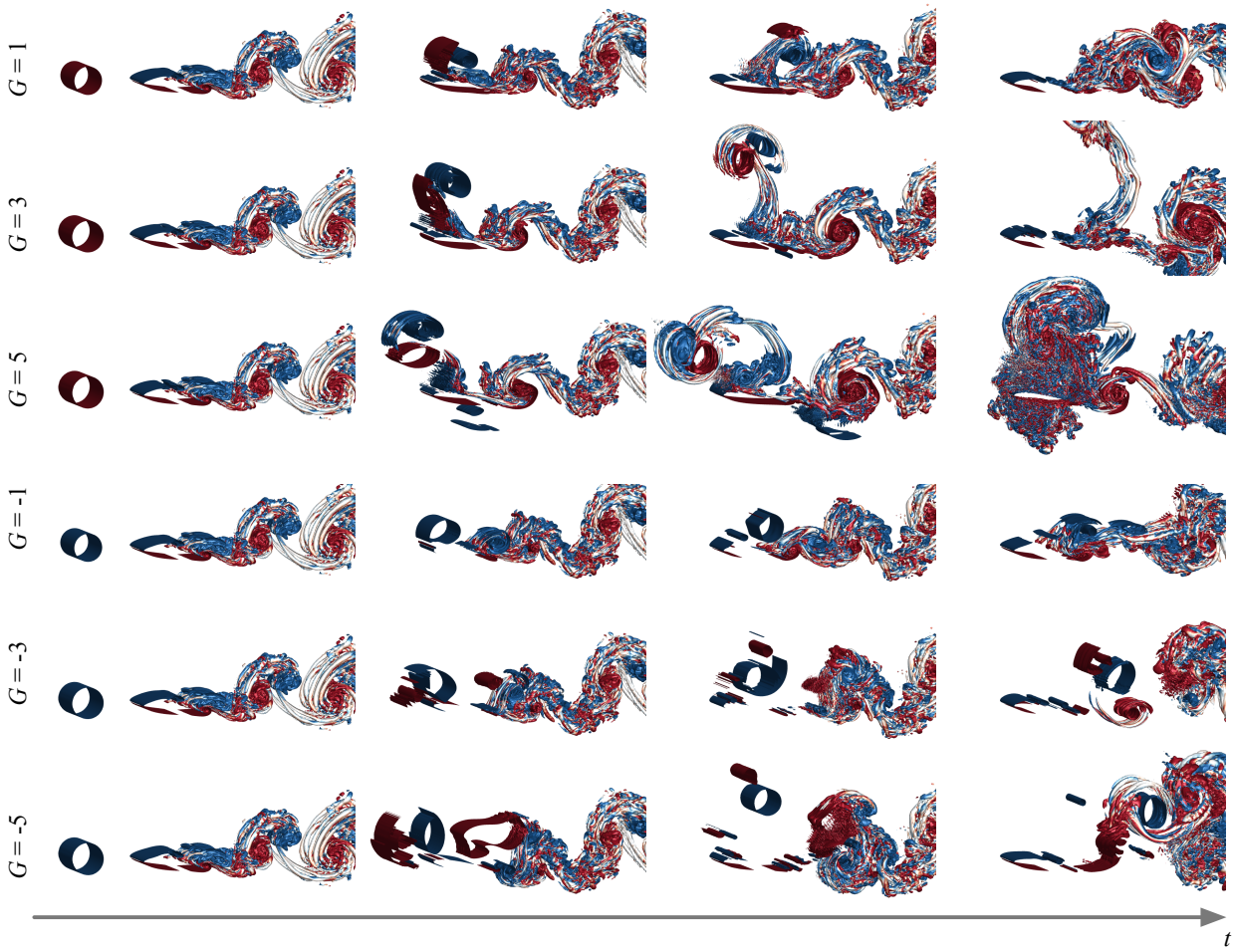

Figure 8.1: Three-dimensional turbulent extreme vortex-airfoil interactions. Flow fields with $G = (\pm 1, 3, 5)$ are visualized using Q criteria (isosurface of $Q = 5$) colored by spanwise vorticity ω_z.

There are a range of conceivable future avenues from the present data-driven studies. From the aspect of global field reconstruction, it is important to find optimal sensor placements to gain situational awareness with minimal costs (MBK18; MOV23). Since the present Voronoi-based model can handle various numbers of sensors and placements at once, a combination with such optimal sensing methods can improve the reconstruction accuracy. In addition, the reconstruction technique proposed in this thesis does not incorporate dynamical information such as time series of sensor measurements. Taking advantage of either sensor dynamics (ZFA23) or some advanced machine-learning techniques that can consider history effects such as recurrent networks (SGA19)

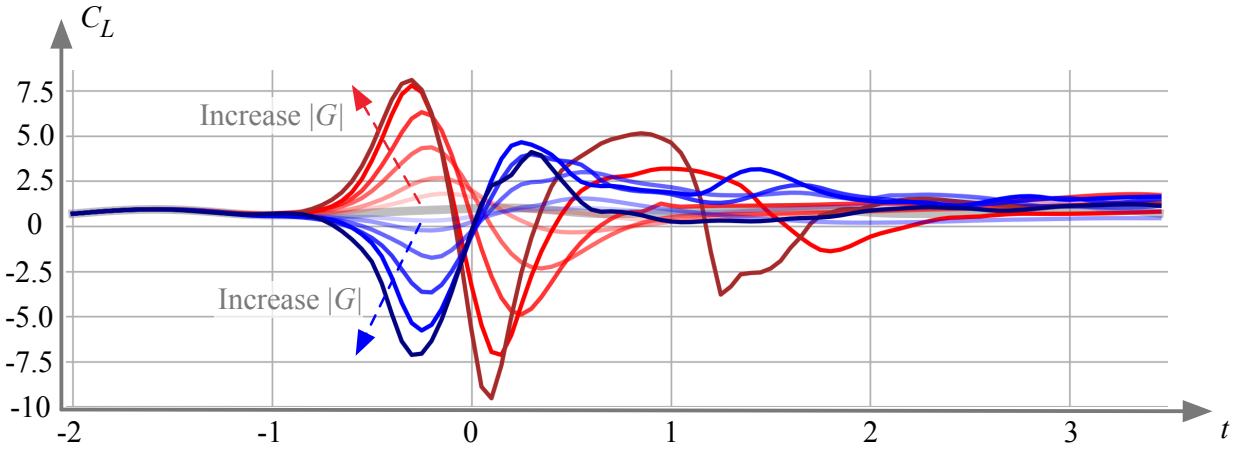

Figure 8.2: Lift coefficients of three-dimensional turbulent extreme vortex-airfoil interactions. Cases with $|G| \in [1, 5]$ are shown. Positive and negative gust cases are respectively colored in red and blue.

can be considered in the future.

Regarding the identification of low-dimensional manifold, the present thesis considered an example of extreme vortex airfoil interactions of two-dimensional laminar separated wakes. It can be anticipated that we may observe a similar manifold expression even with a three-dimensional flow at a higher Reynolds number to some extent due to the commonality of wake shedding and the primary interaction between large vortex gusts and a wing. However, the validation at a three-dimensional high Reynolds number flow is needed.

We have recently started to investigate this aspect with a three-dimensional (spanwise periodic) turbulent separated flow around a NACA0012 airfoil at $Re_c = 5000$ with $\alpha = 14°$, as depicted in figures 8.1 and 8.2. Here, large-eddy simulations are performed with a vortex gust of $0 < |G| < 5$. Extremely fine scales appear due to the impingement of strong vortex gusts once the gust ratio exceeds $|G| \approx 4$, which is not observed in the laminar case. The effect of these complex interactions can also be seen from the lift dynamics in figure 8.2. Before the vortex impinges the airfoil, the increase or decrease of the lift force with the gust ratio is monotonic. Once the vortex gust interacts with turbulent separated wake, the lift trajectories of positive and negative gusts are no longer symmetric. How we can leverage data-driven techniques for such extremely complex aerodynamic

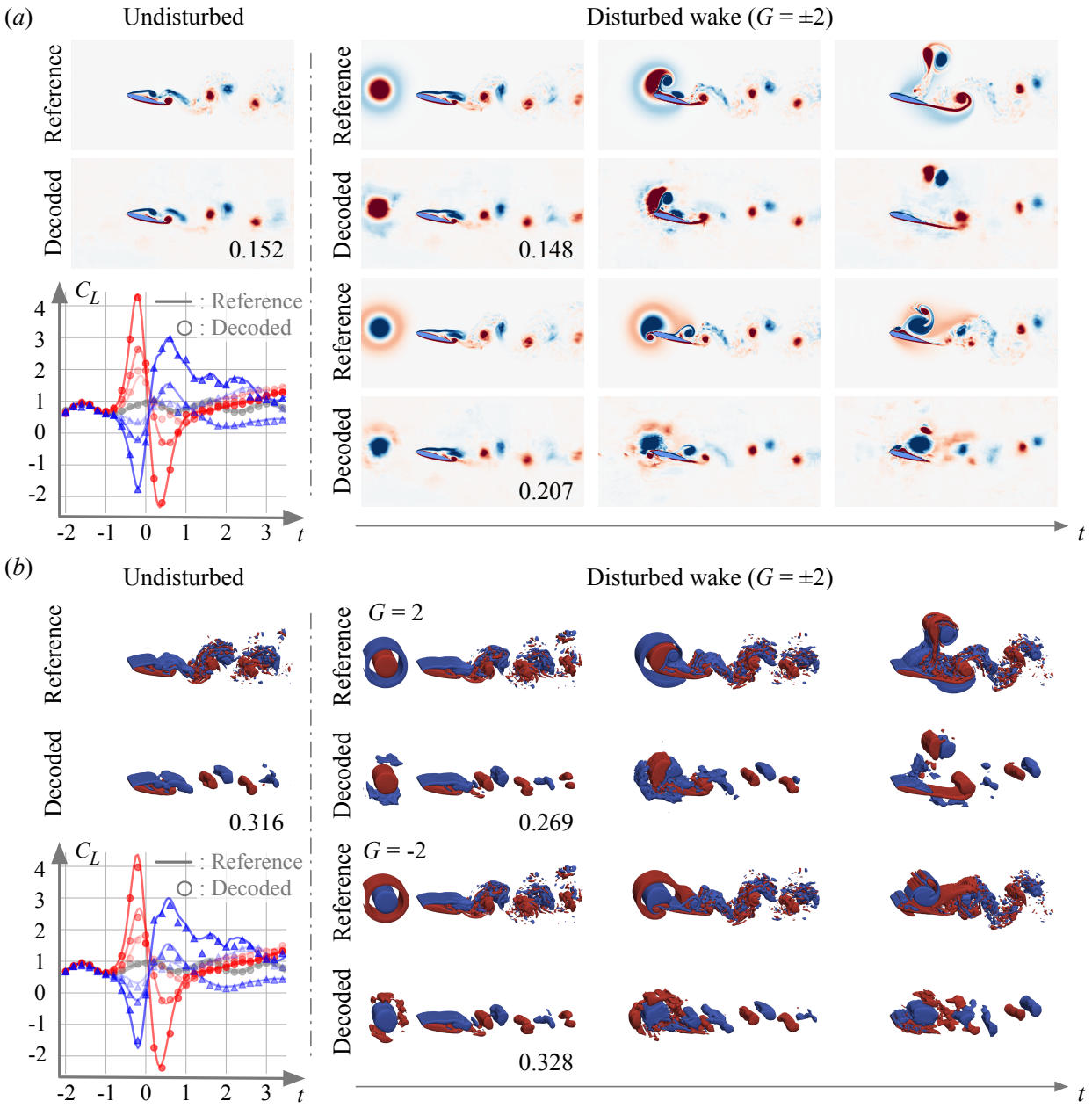

Figure 8.3: The decoded spanwise vorticity field ω_z and lift coefficient C_L of three-dimensional turbulent extreme vortex-airfoil interactions. (a) Spanwise-averaged and (b) three-dimensional field cases are respectively shown. The value underneath each figure reports the L_2 reconstruction error norm.

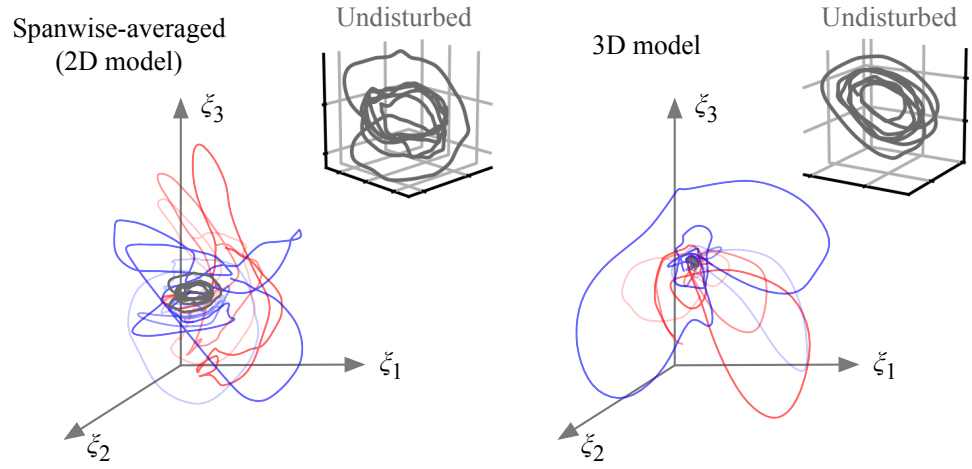

Figure 8.4: Machine-learned latent space of three-dimensional turbulent extreme vortex-airfoil interactions. Spanwise-averaged and three-dimensional field cases are shown.

situations would be of interest.

We also perform data-driven analysis using an observable-augmented autoencoder with multi-scale convolutional filters (FT23; HFM20b) to compress turbulent wake data into three latent variables. We consider spanwise vorticity field ω_z with two different data setups; namely, 1. spanwise-averaged data and 2. three-dimensional field. Two- and three-dimensional convolutional models are employed for each case, respectively. The gust ratio for this preliminary analysis is set to be $0 < |G| < 2$. As presented in figure 8.3, the flow fields are qualitatively reconstructed, capturing the dominant interaction between vortex cores and a wing although finer scales appearing in the spanwise direction are filtered. As well as the laminar case, the lift force can be accurately estimated from the compressed three variables.

Furthermore, the extreme aerodynamic trajectories shown in figure 8.4 appear around the undisturbed one. In other words, the effect of extreme vortex gusts can be expressed about the baseline dynamics in a low-order manner, similar to the extreme aerodynamic manifold in the laminar case. Although these are ongoing studies, these results suggest the applicability of the present work to more challenging, unsteady aerodynamic conditions.

In this thesis, we performed a feedforward control on the identified manifold with the assistance

of phase-amplitude reduction. While the present method can provide the optimal actuation pattern from the aspect of synchronization, one can consider deriving control strategies in a low-order space with other techniques such as model predictive control (BN15; DBN17), reinforcement learning (KLM96; LZG23), and contraction theory (TCS21). We note that preparing appropriate low-order coordinates that capture the essential dynamics of unsteady flows in a tractable manner is a key to combine with such advanced techniques.

Based on the findings in the present thesis, it is important to keep a couple of key considerations in mind. The reliability of given fluid flow data from both computational fluid dynamics (CFD) and experiments should always be ensured. For this reason, checking robustness and uncertainties of machine-learning models against noise is always critical.

Successful performance of data-driven techniques in fluid mechanics suggests that the intrinsic physics within fluid flow data can be extracted with appropriate nonlinear techniques. Such nonlinear machine learning methods often catch coherent and inherent physics of fluid flows, beyond what has been possible with conventional techniques. To correctly understand what nonlinear data-driven techniques extract from fluid flow data, it is essential to carefully design models while incorporating knowledge of fluid mechanics. Furthermore, the preparation of an appropriate optimization setup aligning with the inherent nature of fluid flows is also required. With appropriate data curation, model design, and optimization setup following our engineering knowledge, data-driven techniques can support a range of studies in fluid mechanics.

Bibliography

[AAA19] K. Akiyama, A. Alberdi, W. Alef, K. Asada, R. Azulay, A.-K. Baczko, D. Ball, M. Baloković, J. Barrett, D. Bintley, et al. "First M87 event horizon telescope results. III. Data processing and calibration." *The Astrophysical Journal Letters*, **875**(1):L3, 2019.

[Adr05] R. J. Adrian. "Twenty years of particle image velocimetry." *Exp. Fluids*, **39**(2):159–169, 2005.

[ALM10] M. T. Alonso, P. López-Dekker, and J. J. Mallorquí. "A novel strategy for radar imaging based on compressive sensing." *IEEE Transactions on Geoscience and Remote Sensing*, **48**(12):4285–4295, 2010.

[ALN19] B. An, Q. Liu, M. Nohmi, M. Obuchi, and K. Taira. "Dynamic mode analysis and control of vortical flows in pump sumps." In *APS Division of Fluid Dynamics Meeting Abstracts*, pp. Q27–006, 2019.

[ALT18] B. An, Q. Liu, K. Taira, M. Nohmi, and M. Obuchi. "A research outlook on turbulent vortex control in pump sump." *Ebara Tech. Rev.*, **255**:31–37, 2018.

[AM88] R. J. Adrian and P. Moin. "Stochastic estimation of organized turbulent structure: homogeneous shear flow." *J. Fluid Mech.*, **190**:531–559, 1988.

[And91] J. D. Anderson. *Fundamentals of Aerodynamics, McGraw-Hill*. New York, 1991.

[AS22] R. Arora and A. Shrivastava. "Spatio-Temporal Super-Resolution of Dynamical Systems using Physics-Informed Deep-Learning." *AAAI 2023: Workshop on AI to Accelerate Science and Engineering (AI2ASE)*, 2022.

[ASR21] S. E. Ahmed, O. San, A. Rasheed, and T. Iliescu. "Nonlinear proper orthogonal decomposition for convection-dominated flows." *Phys. Fluids*, **33**(12), 2021.

[Aur91] F. Aurenhammer. "Voronoi diagrams—a survey of a fundamental geometric data structure." *ACM Computing Surveys (CSUR)*, **23**(3):345–405, 1991.

[AW21] S. A. Araujo-Estrada and S. P. Windsor. "Aerodynamic state and loads estimation using bioinspired distributed sensing." *J. Aircr.*, **58**(4):704–716, 2021.

[Ban09] V. Bannore. *Iterative-interpolation super-resolution image reconstruction: a computationally efficient technique*, volume 195. Springer Science & Business Media, 2009.

[BBD21] M. Buzzicotti, F. Bonaccorso, P. C. Di Leoni, and L. Biferale. "Reconstruction of turbulent data with deep generative models for semantic inpainting from TURB-Rot database." *Phys. Rev. Fluids*, **6**(5):050503, 2021.

[BC20] S. Beetham and J. Capecelatro. "Formulating turbulence closures using sparse regression with embedded form invariance." *Phys. Rev. Fluids*, **5**(8):084611, 2020.

[BCB22] J. Bakarji, J. Callaham, S. L. Brunton, and J. N. Kutz. "Dimensionally Consistent Learning with Buckingham Pi." *Nat. Comput. Sci.*, **2**:834–844, 2022.

[BD11] J. Boisson and B. Dubrulle. "Three-dimensional magnetic field reconstruction in the VKS experiment through Galerkin transforms." *New J. Phys.*, **13**(2):023037, 2011.

[BDW04] T. Bui-Thanh, M. Damodaran, and K. Willcox. "Aerodynamic Data Reconstruction and Inverse Design Using Proper Orthogonal Decomposition." *AIAA J.*, **42**(8):1505–1516, 2004.

[BEF19] M. P. Brenner, J. D. Eldredge, and J. B. Freund. "Perspective on machine learning for advancing fluid mechanics." *Phys. Rev. Fluids*, **4**:(100501), 2019.

[BGK19] M. Bode, M. Gauding, K. Kleinheinz, and H. Pitsch. "Deep learning at scale for subgrid modeling in turbulent flows: regression and reconstruction." In *International Conference on High Performance Computing*, pp. 541–560. Springer, 2019.

[BGL21] M. Bode, M. Gauding, Z. Lian, D. Denker, M. Davidovic, K. Kleinheinz, J. Jitsev, and H. Pitsch. "Using physics-informed enhanced super-resolution generative adversarial networks for subfilter modeling in turbulent reactive flows." *Proc. Combust. Inst.*, **38**(2):2617–2625, 2021.

[BHL93] G. Berkooz, P. Holmes, and J. L. Lumley. "The proper orthogonal decomposition in the analysis of turbulent flows." *Annu. Rev. Fluid Mech.*, **25**(1):539–575, 1993.

[BHT20] S. L. Brunton, M. S. Hemati, and K. Taira. "Special issue on machine learning and data-driven methods in fluid dynamics." *Theor. Comput. Fluid Dyn.*, **34**:333–337, 2020.

[BHY23] Y. Bin, G. Huang, and X. I. A. Yang. "Data-enabled recalibration of the Spalart–Allmaras model." *AIAA J.*, **61**(11):4852–4863, 2023.

[BHZ22] A. Burtsev, W. He, K. Zhang, V. Theofilis, K. Taira, and M. Amitay. "Linear modal instabilities around post-stall swept finite wings at low Reynolds numbers." *J. Fluid Mech.*, **944**:A6, 2022.

[BK02] S. Baker and T. Kanade. "Limits on super-resolution and how to break them." *IEEE Trans. Pattern Anal. Mach. Intell.*, **24**(9):1167–1183, 2002.

[BK22] H. J. Bae and P. Koumoutsakos. "Scientific multi-agent reinforcement learning for wall-models of turbulent flows." *Nat. Commun.*, **13**(1):1–9, 2022.

[BMT01] T. R. Bewley, P. Moin, and R. Temam. "DNS-based predictive control of turbulence: an optimal benchmark for feedback algorithms." *J. Fluid Mech.*, **447**:179–225, 2001.

[BN15] S. L. Brunton and B. R. Noack. "Closed-loop turbulence control: Progress and challenges." *Appl. Mech. Rev.*, **67**(5):050801, 2015.

[BNK20] S. L. Brunton, B. R. Noack, and P. Koumoutsakos. "Machine learning for fluid mechanincs." *Annu. Rev. Fluid Mech.*, **52**:477–508, 2020.

[BP04] T. R. Bewley and B. Protas. "Skin friction and pressure: the "footprints" of turbulence." *Phys. D*, **196**(1-2):28–44, 2004.

[BPB20] K. Bieker, S. Peitz, S. L. Brunton, J. N. Kutz, and M. Dellnitz. "Deep model predictive flow control with limited sensor data and online learning." *Theor. Comput. Fluid Dyn.*, **34**(4):577–591, 2020.

[BPK16a] S. L. Brunton, J. L. Proctor, and J. N. Kutz. "Discovering governing equations from data by sparse identification of nonlinear dynamical systems." *Proc. Natl. Acad. Sci. U.S.A.*, **113**(15):3932–3937, 2016.

[BPK16b] S. L. Brunton, J. L. Proctor, and J. N. Kutz. "Sparse identification of nonlinear dynamics with control." *IFAC NOLCOS*, **49**(18):710–715, 2016.

[Bre05] C. E. Brennen. *Fundamentals of multiphase flow*. Cambridge University Press, 2005.

[Bre11] C. E. Brennen. *Hydrodynamics of pumps*. Cambridge University Press, 2011.

[BRG12] M. Bevilacqua, A. Roumy, C. Guillemot, and M.-L. A. Morel. "Low-Complexity Single-Image Super-Resolution based on Nonnegative Neighbor Embedding." In *British Machine Vision Conference (BMVC)*, 2012.

[BSJ21] H. Biler, G. Sedky, A. R. Jones, M. Saritas, and O. Cetiner. "Experimental investigation of transverse and vortex gust encounters at low Reynolds numbers." *AIAA J.*, **59**(3):786–799, 2021.

[Buc14] E. Buckingham. "On physically similar systems; illustrations of the use of dimensional equations." *Phys. Rev.*, **4**(4):345, 1914.

[Buz23] M. Buzzicotti. "Data reconstruction for complex flows using AI: recent progress, obstacles, and perspectives." *EPL*, 2023.

[CCB11] C. H. Colburn, J. B. Cessna, and T. R. Bewley. "State estimation in wall-bounded flow systems. Part 3. The ensemble Kalman filter." *J. Fluid Mech.*, **682**:289–303, 2011.

[CDG22] S. Cuomo, V. S. Di Cola, F. Giampaolo, G. Rozza, M. Raissi, and F. Piccialli. "Scientific machine learning through physics–informed neural networks: Where we are and what's next." *J. Sci. Comput.*, **92**(3):88, 2022.

[CDS14] G. Cai, J. Dias, and L. Seneviratne. "A survey of small-scale unmanned aerial vehicles: Recent advances and future development trends." *Unmanned Syst.*, **2**(02):175–199, 2014.

[CDS21] D. W. Carter, F. De Voogt, R. Soares, and B. Ganapathisubramani. "Data-driven sparse reconstruction of flow over a stalled aerofoil using experimental data." *Data-Centric Eng.*, **2**, 2021.

[CGF23] P. Conti, G. Gobat, S. Fresca, A. Manzoni, and A. Frangi. "Reduced order modeling of parametrized systems through autoencoders and SINDy approach: continuation of periodic solutions." *CComput. Methods Appl. Mech. Engrg.*, **411**:116072, 2023.

[CGL20] X. Chai, H. Gu, F. Li, H. Duan, X. Hu, and K. Lin. "Deep learning for irregularly and regularly missing data reconstruction." *Sci. Rep.*, **10**(1):1–18, 2020.

[Cha92] C.-C. Chang. "Potential flow and forces for incompressible viscous flow." *Proc. Roy. Soc. A*, **437**(1901):517–525, 1992.

[CHB06] M. Chevalier, J. Hœpffner, T. R. Bewley, and D. S. Henningson. "State estimation in wall-bounded flow systems. Part 2. Turbulent flows." *J. Fluid Mech.*, **552**:167–187, 2006.

[Chu08] S. G Chumakov. "A priori study of subgrid-scale flux of a passive scalar in isotropic homogeneous turbulence." *Phys. Rev. E*, **78**(3):036313, 2008.

[CJK19] K. T. Carlberg, A. Jameson, M. J. Kochenderfer, J. Morton, L. Peng, and F. D. Witherden. "Recovering missing CFD data for high-order discretizations using deep neural networks and dynamics learning." *J. Comput. Phys.*, **395**:105 – 124, 2019.

[CKH24] D. Chen, F. Kaiser, J. C. Hu, D. E. Rival, K. Fukami, and K. Taira. "Sparse pressure-based machine learning approach for aerodynamic loads estimation during gust encounters." *AIAA J.*, **62**(1):275–290, 2024.

[CMB19] J. L. Callaham, K. Maeda, and S. L. Brunton. "Robust flow reconstruction from limited measurements via sparse representation." *Phys. Rev. Fluids*, **4**(10):103907, 2019.

[CMK94] H. Choi, P. Moin, and J. Kim. "Active turbulence control for drag reduction in wall-bounded flows." *J. Fluid Mech.*, **262**:75–110, 1994.

[CMW22] S. Cai, Z. Mao, Z. Wang, M. Yin, and G. E. Karniadakis. "Physics-informed neural networks (PINNs) for fluid mechanics: A review." *Acta Mech. Sin.*, pp. 1–12, 2022.

[CPC90] M. S Chong, A. E Perry, and B. J Cantwell. "A general classification of three-dimensional flow fields." *Phys. Fluids A: Fluid Dynamics*, **2**(5):765–777, 1990.

[CPL23] X. Chu, S. Pandey, Y. Liu, and B. Weigand. "Modeling of Coupled Turbulent Channel Porous Media Flow through a Deep Autoencoder Echo State Network Framework." *arXiv:2312.00850*, 2023.

[CRL22] J. L. Callaham, G. Rigas, J.-C. Loiseau, and S. L. Brunton. "An empirical mean-field model of symmetry-breaking in a turbulent wake." *Sci. Adv.*, **8**(19):eabm4786, 2022.

[CT08] T. Colonius and K. Taira. "A fast immersed boundary method using a nullspace approach and multi-domain far-field boundary conditions." *Comput. Methods Appl. Mech. Eng.*, **197**:2131–2146, 2008.

[CWF21] S. Cai, Z. Wang, F. Fuest, Y. J. Jeon, C. Gray, and G. Em. Karniadakis. "Flow over an espresso cup: inferring 3-D velocity and pressure fields from tomographic background oriented Schlieren via physics-informed neural networks." *J. Fluid Mech.*, **915**:A102, 2021.

[CYX04] H. Chang, D.-Y. Yeung, and Y. Xiong. "Super-resolution through neighbor embedding." In *IEEE Computer Society Conference on Computer Vision and Pattern Recognition*, volume 1, pp. I–I. IEEE, 2004.

[CZX19] S. Cai, S. Zhou, C. Xu, and Q. Gao. "Dense motion estimation of particle images via a convolutional neural network." *Exp. Fluids*, **60**:60–73, 2019.

[Dav15] P. A. Davidson. *Turbulence: an introduction for scientists and engineers*. Oxford university press, 2015.

[DBN17] T. Duriez, S. L. Brunton, and B. R. Noack. *Machine learning control-taming nonlinear dynamics and turbulence*, volume 116. Springer, 2017.

[DCU18] G. Di Ilio, D. Chiappini, S. Ubertini, G. Bella, and S. Succi. "Fluid flow around NACA 0012 airfoil at low-Reynolds numbers with hybrid lattice Boltzmann method." *Comput. Fluids*, **166**:200–208, 2018.

[DDD22] G. C. De Croon, J. J. Dupeyroux, C. De Wagter, A. Chatterjee, D. A. Olejnik, and F. Ruffier. "Accommodating unobservability to control flight attitude with optic flow." *Nature*, **610**(7932):485–490, 2022.

[DFS19] A. Dosovitskiy, P. Fischer, J. T. Springenberg, M. Riedmiller, and T. Brox. "Discriminative unsupervised feature learning with exemplar convolutional neural networks." *IEEE Trans. Pattern Anal. Mach. Intell.*, **38**, 2019.

[DG23] C. E. P. De Jesús and M. D. Graham. "Data-driven low-dimensional dynamic model of Kolmogorov flow." *Phys. Rev. Fluids*, **8**(4):044402, 2023.

[DGP22] P. Dubois, T. Gomez, L. Planckaert, and L. Perret. "Machine learning for fluid flow reconstruction from limited measurements." *J. Comput. Phys.*, **448**:110733, 2022.

[DHL19] Z. Deng, C. He, Y. Liu, and K. C. Kim. "Super-resolution reconstruction of turbulent velocity fields using a generative adversarial network-based artificial intelligence framework." *Phys. Fluids*, **31**:125111, 2019.

[DHW16] S. T. M. Dawson, M. S. Hemati, M. O. Williams, and C. W. Rowley. "Characterizing and correcting for the effect of sensor noise in the dynamic mode decomposition." *Exp. Fluids*, **57**:1–19, 2016.

[DIX19] K. Duraisamy, G. Iaccarino, and H. Xiao. "Turbulence modeling in the age of data." *Annu. Rev. Fluid. Mech.*, **51**:357–377, 2019.

[DL23] S. Discetti and Y. Liu. "Machine learning for flow field measurements: a perspective." *Meas. Sci. Technol.*, **34**:021001, 2023.

[DLH14] C. Dong, C. C. Loy, K. He, and X. Tang. "Learning a deep convolutional network for image super-resolution." In *European conference on computer vision*, pp. 184–199. Springer, 2014.

[DLH15] C. Dong, C. C. Loy, K. He, and X. Tang. "Image super-resolution using deep convolutional networks." *IEEE Trans. Pattern Anal. Mach. Intell.*, **38**(2):295–307, 2015.

[DLT16] C. Dong, C. C. Loy, and X. Tang. "Accelerating the super-resolution convolutional neural network." In *European conference on computer vision*, pp. 391–407. Springer, 2016.

[DMB18] P. C. Di Leoni, A. Mazzino, and L. Biferale. "Inferring flow parameters and turbulent configuration with physics-informed data assimilation and spectral nudging." *Phys. Rev. Fluids*, **3**(10):104604, 2018.

[DMB20] P. C. Di Leoni, A. Mazzino, and L. Biferale. "Synchronization to big data: Nudging the Navier-Stokes equations for data assimilation of turbulent flows." *Phys. Rev. X*, **10**(1):011023, 2020.

[DMS20] M. Di Luca, S. Mintchev, Y. Su, E. Shaw, and K. Breuer. "A bioinspired Separated Flow wing provides turbulence resilience and aerodynamic efficiency for miniature drones." *Sci. Robot.*, **5**(38):eaay8533, 2020.

[Dom12] P. Domingos. "A few useful things to know about machine learning." *Commun. ACM*, **55**(10):78–87, 2012.

[DQH18] X. Du, X. Qu, Y. He, and D. Guo. "Single image super-resolution based on multi-scale competitive convolutional neural network." *Sensors*, **789**(18):1–17, 2018.

[Dur21] K. Duraisamy. "Perspectives on machine learning-augmented Reynolds-averaged and large eddy simulation models of turbulence." *Phys. Rev. Fluids*, **6**:050504, 2021.

[DWZ23] Y. Du, M. Wang, and T. A. Zaki. "State estimation in minimal turbulent channel flow: A comparative study of 4DVar and PINN." *Int. J. Heat Fluid Flow*, **99**:109073, 2023.

[DZ21] Y. Du and T. A. Zaki. "Evolutional deep neural network." *Phys. Rev. E.*, **104**:045303, 2021.

[EAK20] S. Esmaeilzadeh, K. Azizzadenesheli, K. Kashinath, M. Mustafa, H. A. Tchelepi, P. Marcus, M. Prabhat, Anandkumar., et al. "MeshfreeFlowNet: A physics-constrained deep continuous space-time super-resolution framework." In *SC20: International Conference for High Performance Computing, Networking, Storage and Analysis*, pp. 1–15. IEEE, 2020.

[ELH22] H. Eivazi, S. Le Clainche, S. Hoyas, and R. Vinuesa. "Towards extraction of orthogonal and parsimonious non-linear modes from turbulent flows." *Expert Syst. Appl.*, **202**:117038, 2022.

[EMY20] N. B. Erichson, L. Mathelin, Z. Yao, S. L. Brunton, M. W. Mahoney, and J. N. Kutz. "Shallow neural networks for fluid flow reconstruction with limited sensors." *Proc. Roy. Soc. A*, **476**(2238):20200097, 2020.

[ES95] R. Everson and L. Sirovich. "Karhunen–Loeve procedure for gappy data." *J. Opt. Soc. Am.*, **12**(8):1657–1664, 1995.

[FAN22] K. Fukami, B. An, M. Nohmi, M. Obuchi, and K. Taira. "Machine-learning-based reconstruction of turbulent vortices from sparse pressure sensors in a pump sump." *J. Fluids Eng.*, **144**(12):121501, 2022.

[FF11] G. Freedman and R. Fattal. "Image and video upscaling from local self-examples." *ACM Trans. Graph.*, **30**(2):1–11, 2011.

[FFT19a] K. Fukami, K. Fukagata, and K. Taira. "Super-resolution analysis with machine learning for low-resolution flow data." In *11th International Symposium on Turbulence and Shear Flow Phenomena (TSFP11), Southampton, UK*, number 208, 2019.

[FFT19b] K. Fukami, K. Fukagata, and K. Taira. "Super-resolution reconstruction of turbulent flows with machine learning." *J. Fluid Mech.*, **870**:106–120, 2019.

[FFT20] K. Fukami, K. Fukagata, and K. Taira. "Assessment of supervised machine learning for fluid flows." *Theor. Comput. Fluid Dyn.*, **34**(4):497–519, 2020.

[FFT21] K. Fukami, K. Fukagata, and K. Taira. "Machine-learning-based spatio-temporal super resolution reconstruction of turbulent flows." *J. Fluid Mech.*, **909**(A9), 2021.

[FFT23] K. Fukami, K. Fukagata, and K. Taira. "Super-resolution analysis via machine learning: a survey for fluid flows." *Theor. Comput. Fluid Dyn.*, **37**:421–444, 2023.

[FGD21] H. J. S. Fernando, I. Gultepe, C. Dorman, E. Pardyjak, Q. Wang, S. W. Hoch, D. Richter, E. Creegan, S. Gaberšek, T. Bullock, et al. "C-FOG: life of coastal fog." *Bull. Am. Meteorol. Soc.*, **102**(2):E244–E272, 2021.

[FGT23] K. Fukami, S. Goto, and K. Taira. "Data-driven nonlinear turbulent flow scaling with Buckingham Pi variables." In review, 2023.

[FHN21] K. Fukami, K. Hasegawa, T. Nakamura, M. Morimoto, and K. Fukagata. "Model order reduction with neural networks: Application to laminar and turbulent flows." *SN Comput. Sci.*, **2**:467, 2021.

[FID23] E. Farzamnik, A. Ianiro, S. Discetti, N. Deng, K. Oberleithner, B. R. Noack, and V. Guerrero. "From snapshots to manifolds–a tale of shear flows." *J. Fluid Mech.*, **955**:A34, 2023.

[FJP02] W. T. Freeman, T. R. Jones, and E. C. Pasztor. "Example-based super-resolution." *IEEE Comput. Graph. Appl.*, **22**(2):56–65, 2002.

[FK20] S. Franchini and S. Krevor. "Cut, overlap and locate: a deep learning approach for the 3D localization of particles in astigmatic optical setups." *Exp. Fluids*, **61**:1–15, 2020.

[FKK06] K. Fukagata, N. Kasagi, and P. Koumoutsakos. "A theoretical prediction of friction drag reduction in turbulent flow by superhydrophobic surfaces." *Phys. Fluids*, **18**:051703, 2006.

[FMR21] K. Fukami, R. Maulik, N. Ramachandra, K. Fukagata, and K. Taira. "Global field reconstruction from sparse sensors with Voronoi tessellation-assisted deep learning." *Nat. Mach. Intell.*, **3**(11):945–951, 2021.

[FMT88] C. Foias, O. Manley, and R. Temam. "Modelling of the interaction of small and large eddies in two dimensional turbulent flows." *ESAIM: Math. Model. Numer. Anal.*, **22**(1):93–118, 1988.

[FMZ21] K. Fukami, T. Murata, K. Zhang, and K. Fukagata. "Sparse identification of nonlinear dynamics with low-dimensionalized flow representations." *J. Fluid Mech.*, **926**:A10, 2021.

[FNF20] K. Fukami, T. Nakamura, and K. Fukagata. "Convolutional neural network based

hierarchical autoencoder for nonlinear mode decomposition of fluid field data." *Phys. Fluids*, **32**:095110, 2020.

[FNK19] K. Fukami, Y. Nabae, K. Kawai, and K. Fukagata. "Synthetic turbulent inflow generator using machine learning." *Phys. Rev. Fluids*, **4**:064603, 2019.

[FNT23] K. Fukami, H. Nakao, and K. Taira. "Controlling extreme vortex-impingement aerodynamics on a machine-learned manifold." to be submitted, 2023.

[FPB20] M. F. Fathi, I. Perez-Raya, A. Baghaie, P. Berg, G. Janiga, A. Arzani, and R. M. D'Souza. "Super-resolution and denoising of 4D-flow MRI using physics-informed deep neural nets." *Comput. Methods Programs Biomed.*, **197**:105729, 2020.

[FPC00] W. T. Freeman, E. C. Pasztor, and O. T. Carmichael. "Learning low-level vision." *Int. J. Comput. Vis.*, **40**(1):25–47, 2000.

[Fri01] J. H. Friedman. "Greedy function approximation: a gradient boosting machine." *Ann. Stat.*, pp. 1189–1232, 2001.

[FT22] K. Fukami and K. Taira. "Learning the nonlinear manifold of extreme aerodynamics." *NeurIPS2022*, 2022.

[FT23] K. Fukami and K. Taira. "Grasping extreme aerodynamics on a low-dimensional manifold." *Nat. Commun.*, **14**:6480, 2023.

[FW15] D. Floreano and R. J. Wood. "Science, technology and the future of small autonomous drones." *Nature*, **521**(7553):460–466, 2015.

[GA20] A. Giannopoulos and J.-L. Aider. "Data-driven order reduction and velocity field reconstruction using neural networks: The case of a turbulent boundary layer." *Phys. Fluids*, **32**(9):095117, 2020.

[GBI09] D. Glasner, S. Bagon, and M. Irani. "Super-resolution from a single image." In *IEEE 12th international conference on computer vision*, pp. 349–356. IEEE, 2009.

[GCS22] Y. Guan, A. Chattopadhyay, A. Subel, and P. Hassanzadeh. "Stable a posteriori LES of 2D turbulence using convolutional neural networks: Backscattering analysis and generalization to higher Re via transfer learning." *J. Comput. Phys.*, **458**:111090, 2022.

[GDI21] A. Güemes, S. Discetti, A. Ianiro, B. Sirmacek, H. Azizpour, and R. Vinuesa. "From coarse wall measurements to turbulent velocity fields through deep learning." *Phys. Fluids*, **33**(7):075121, 2021.

[GGI21] L. Guastoni, A. Güemes, A. Ianiro, S. Discetti, P. Schlatter, H. Azizpour, and R. Vinuesa. "Convolutional-network models to predict wall-bounded turbulence from wall quantities." *J. Fluid Mech.*, **928**:A27, 2021.

[GGJ22] A. Gruber, M. Gunzburger, L. Ju, and Z. Wang. "A comparison of neural network architectures for data-driven reduced-order modeling." *Comput. Methods Appl. Mech. Eng.*, **393**:114764, 2022.

[GGL21] L. A. Garrow, B. J. German, and C. E. Leonard. "Urban air mobility: A comprehensive review and comparative analysis with autonomous and electric ground transportation for informing future research." *Transp. Res. Part C Emerg. Technol.*, **132**:103377, 2021.

[GH17] M. Gamahara and Y. Hattori. "Searching for turbulence models by artificial neural network." *Phys. Rev. Fluids*, **2**(5):054604, 2017.

[GHF21] M. Gao, C. H. Hugenholtz, T. A. Fox, M. Kucharczyk, T. E. Barchyn, and P. R. Nesbit. "Weather constraints on global drone flyability." *Sci. Rep.*, **11**(1):12092, 2021.

[GKS20] A. Glaws, R. King, and M. Sprague. "Deep learning for in situ data compression of large turbulent flow simulations." *Phys. Rev. Fluids*, **5**(11):114602, 2020.

[GKT23] V. Godavarthi, Y. Kawamura, and K. Taira. "Optimal waveform for fast synchronization of airfoil wakes." *J. Fluid Mech.*, **976**:R1, 2023.

[GMM18] N. Gavrilovic, A. Mohamed, M. Marino, S. Watkins, J.-M. Moschetta, and E. Bénard. "Avian-inspired energy-harvesting from atmospheric phenomena for small UAVs." *Bioinspir. Biomim.*, **14**(1):016006, 2018.

[GN20] A. V. Grayver and J. Noir. "Particle streak velocimetry using ensemble convolutional neural networks." *Exp. Fluids*, **61**(2):38, 2020.

[Gol69] S. Goldstein. "Fluid mechanics in the first half of this century." *Annu. Rev. Fluid Mech.*, **1**(1):1–29, 1969.

[GPM20] I. Goodfellow, J. Pouget-Abadie, M. Mirza, B. Xu, D. Warde-Farley, S. Ozair, A. Courville, and Y. Bengio. "Generative adversarial networks." *Commun. ACM*, **63**(11):139–144, 2020.

[Gro14] G. Gross. "On the estimation of wind comfort in a building environment by micro-scale simulation." *Meteorol. Z.*, **23**(1):51–62, 2014.

[GSC23] Y. Guan, A. Subel, A. Chattopadhyay, and P. Hassanzadeh. "Learning physics-constrained subgrid-scale closures in the small-data regime for stable and accurate LES." *Phys. D*, **443**:133568, 2023.

[GSW20] H. Gao, L. Sun, and J.-X. Wang. "PhyGeoNet: Physics-informed geometry-adaptive convolutional neural networks for solving Parameterized Steady-State PDEs on irregular domain." *J. Comput. Phys.*, p. 110079, 2020.

[GSW21] H. Gao, L. Sun, and J.-X. Wang. "Super-resolution and denoising of fluid flow using physics-informed convolutional neural networks without high-resolution labels." *Phys. Fluids*, **33**(7):073603, 2021.

[GT21] M. Gopalakrishnan Meena and K. Taira. "Identifying vortical network connectors for turbulent flow modification." *J. Fluid Mech.*, **915**:A10, 2021.

[GV16] S. Goto and J. C. Vassilicos. "Local equilibrium hypothesis and Taylor's dissipation law." *Fluid Dyn. Res.*, **48**(2):021402, 2016.

[GVD22] A. Güemes, C. S. Vila, and S. Discetti. "Super-resolution generative adversarial networks of randomly-seeded fields." *Nat. Mach. Intell.*, **4**:1165–1173, 2022.

[GVL21] H. Ghraieb, J. Viquerat, A. Larcher, P. Meliga, and E. Hachem. "Single-step deep reinforcement learning for open-loop control of laminar and turbulent flows." *Phys. Rev. Fluids*, **6**(5):053902, 2021.

[GW22] D. Greenblatt and D. R. Williams. "Flow control for unmanned air vehicles." *Annu. Rev. Fluid Mech.*, **54**:383–412, 2022.

[HBP22] B. Herrmann, S. L. Brunton, J. E. Pohl, and R. Semaan. "Gust mitigation through closed-loop control. II. Feedforward and feedback control." *Phys. Rev. Fluids*, **7**(2):024706, 2022.

[HES14] M. S. Hemati, J. D. Eldredge, and J. L. Speyer. "Wake sensing for aircraft formation flight." *J. Guid. Control Dyn.*, **37**(2):513–524, 2014.

[HFM20a] K. Hasegawa, K. Fukami, T. Murata, and K. Fukagata. "CNN-LSTM based reduced order modeling of two-dimensional unsteady flows around a circular cylinder at different Reynolds numbers." *Fluid Dyn. Res.*, **52**(6):065501, 2020.

[HFM20b] K. Hasegawa, K. Fukami, T. Murata, and K. Fukagata. "Machine-learning-based reduced-order modeling for unsteady flows around bluff bodies of various shapes." *Theor. Comp. Fluid Dyn.*, **34**(4):367–388, 2020.

[HGS22] M. Hassanaly, A. Glaws, K. Stengel, and R. N. King. "Adversarial sampling of unknown and high-dimensional conditional distributions." *J. Comput. Phys.*, **450**:110853, 2022.

[HI97] F. C. Hoppensteadt and E. M. Izhikevich. *Weakly connected neural networks*. Springer Science & Business Media, 1997.

[HI04] F. Ham and G. Iaccarino. "Energy conservation in collocated discretization schemes on unstructured meshes." In *Annual Research Briefs*, pp. 3–14. Center for Turbulence Research, 2004.

[HJ11] P. J. Hardin and R. R. Jensen. "Small-scale unmanned aerial vehicles in environmental remote sensing: Challenges and opportunities." *GIScience Remote Sens.*, **48**(1):99–111, 2011.

[HKK14] S. Hatano, D. Kang, S. Kagawa, M. Nohmi, and K. Yokota. "Study of cavitation instabilities in double-suction centrifugal pump." *Int. J. Fluid Mach. Syst.*, **7**(3):94–100, 2014.

[HLB12] P. Holmes, J.L. Lumley, G. Berkooz, and C. W. Rowley. *Turbulence, Coherent Structures, Dynamical Systems and Symmetry*. Cambridge Univ. Press, 2nd edition, 2012.

[HLL15] A. E. Holton, S. Lawson, and C. Love. "Unmanned Aerial Vehicles: Opportunities, barriers, and the future of "drone journalism"." *Journal. Pract.*, **9**(5):634–650, 2015.

[HMI06] F. Ham, K. Mattsson, and G. Iaccarino. "Accurate and stable finite volume operators for unstructured flow solvers." In *Annual Research Briefs*, pp. 243–261. Center for Turbulence Research, 2006.

[HO93] P. C. Hansen and D. P. O'Leary. "The use of the L-curve in the regularization of discrete ill-posed problems." *SIAM J. Sci. Comput.*, **14**(6):1487–1503, 1993.

[Hob88] F. M. Hoblit. *Gust loads on aircraft: concepts and applications*. AIAA, 1988.

[HS97] S. Hochreiter and J. Schmidhuber. "Long short-term memory." *Neural Comput.*, **9**:1735–1780, 1997.

[HS06] G. E. Hinton and R. R. Salakhutdinov. "Reducing the dimensionality of data with neural networks." *Science*, **313**(5786):504–507, 2006.

[HSS18] J. Hu, L. Shen, and G. Sun. "Squeeze-and-excitation networks." In *Proceedings of the IEEE conference on computer vision and pattern recognition*, pp. 7132–7141, 2018.

[HTH10] T. Harada, H. Tanaka, M. J. Hankins, and I. Z. Kiss. "Optimal waveform for the entrainment of a weakly forced oscillator." *Phys. Rev. Lett.*, **105**(8):088301, 2010.

[HWM88] J. C. R. Hunt, A. A. Wray, and P. Moin. "Eddies, streams, and convergence zones in turbulent flows." *Studying Turbulence Using Numerical Simulation Databases, 2. Proceedings of the 1988 Summer Program*, 1988.

[HZR16] K. He, X. Zhang, S. Ren, and J. Sun. "Deep residual learning for image recognition." In *Proceedings of the IEEE conference on computer vision and pattern recognition*, pp. 770–778, 2016.

[HZW24] C. He, X. Zeng, P. Wang, X. Wen, and Y. Liu. "Four-dimensional variational data assimilation of a turbulent jet for super-temporal-resolution reconstruction." *J. Fluid Mech.*, **978**:A14, 2024.

[IG20] M. Inubushi and S. Goto. "Transfer learning for nonlinear dynamics and its application to fluid turbulence." *Phys. Rev. E*, **102**(4):043301, 2020.

[Iim19] M. Iima. "Jacobian-free algorithm to calculate the phase sensitivity function in the phase reduction theory and its applications to Kármán's vortex street." *Phys. Rev. E*, **99**(6):062203, 2019.

[Iim21] M. Iima. "Phase reduction technique on a target region." *Phys. Rev. E*, **103**(5):053303, 2021.

[Iim23] M. Iima. "Optimal external forces of the lock-in phenomena for the flow past inclined plate in a uniform flow." arXiv:2311.00977, 2023.

[IP91] M. Irani and S. Peleg. "Improving resolution by image registration." *CVGIP: Graphical models and image processing*, **53**(3):231–239, 1991.

[IR08] M. Ilak and C. W. Rowley. "Modeling of transitional channel flow using balanced proper orthogonal decomposition." *Phys. Fluids*, **20**(3), 2008.

[IS15] S. Ioffe and C. Szegedy. "Batch normalization: Accelerating deep network training by reducing internal covariate shift." In *International conference on machine learning*, pp. 448–456, 2015.

[JC21] A. R. Jones and O. Cetiner. "Overview of Unsteady Aerodynamic Response of Rigid Wings in Gust Encounters." *AIAA J.*, **59**(2):716–721, 2021.

[JCL21] X. Jin, S. Cai, H. Li, and G. Em. Karniadakis. "NSFnets (Navier–Stokes flow nets): Physics-informed neural networks for the incompressible Navier–Stokes equations." *J. Comput. Phys.*, **426**:109951, 2021.

[JCS22] A. R. Jones, O. Cetiner, and M. J. Smith. "Physics and modeling of large flow disturbances: Discrete gust encounters for modern air vehicles." *Annu. Rev. Fluid Mech.*, **54**:469–493, 2022.

[JH95] J. Jeong and F. Hussain. "On the identification of a vortex." *J. Fluid Mech.*, **285**:69–94, 1995.

[JIS20] B. Jin, S. J. Illingworth, and R. D. Sandberg. "Feedback control of vortex shedding using a resolvent-based modelling approach." *J. Fluid Mech.*, **897**:A26, 2020.

[JKR09] K. Jarrett, K. Kavukcuoglu, M. Ranzato, and Y. LeCun. "What is the best multi-stage architecture for object recognition?" In *2009 IEEE 12th international conference on computer vision*, pp. 2146–2153. IEEE, 2009.

[JM15] M. I. Jordan and T. M. Mitchell. "Machine learning: Trends, perspectives, and prospects." *Science*, **349**(6245):255–260, 2015.

[Jol02] I. T. Jolliffe. *Principal component analysis*. Springer, 2002.

[JSK08] N. Joshi, R. Szeliski, and D. J. Kriegman. "PSF estimation using sharp edge prediction." In *IEEE Conference on Computer Vision and Pattern Recognition*, pp. 1–8. IEEE, 2008.

[KB14] D. P. Kingma and J. Ba. "Adam: A method for stochastic optimization." *arXiv:1412.6980*, 2014.

[KCL20] C. Kong, J.-T. Chang, Y.-F. Li, and R.-Y. Chen. "Deep learning methods for super-resolution reconstruction of temperature fields in a supersonic combustor." *AIP Adv.*, **10**(11):115021, 2020.

[Key81] R. Keys. "Cubic convolution interpolation for digital image processing." *IEEE Trans. Acoust. Speech Signal Process.*, **29**(6):1153–1160, 1981.

[KGB17] B. Kramer, P. Grover, P. Boufounos, S. Nabi, and M. Benosman. "Sparse sensing and DMD-based identification of flow regimes and bifurcations in complex flows." *SIAM J. Appl. Dyn. Sys.*, **16**(2):1164–1196, 2017.

[KGT22] Y. Kawamura, V. Godavarthi, and K. Taira. "Adjoint-based phase reduction analysis of incompressible periodic flows." *Phys. Rev. Fluids*, **7**(10):104401, 2022.

[KKB18] E. Kaiser, J. N. Kutz, and S. L. Brunton. "Sparse identification of nonlinear dynamics for model predictive control in the low-data limit." *Proc. Roy. Soc. A*, **474**(2219):20180335, 2018.

[KKL21] G. E. Karniadakis, I. G. Kevrekidis, L. Lu, P. Perdikaris, S. Wang, and L. Yang. "Physics-informed machine learning." *Nat. Rev. Phys.*, **3**(6):422–440, 2021.

[KKL23] H. Kim, J. Kim, and C. Lee. "Interpretable deep learning for prediction of Prandtl number effect in turbulent heat transfer." *J. Fluid Mech.*, **955**:A14, 2023.

[KKT21] M. A. Khodkar, J. T. Klamo, and K. Taira. "Phase-locking of laminar wake to periodic vibrations of a circular cylinder." *Phys. Rev. Fluids*, **6**(3):034401, 2021.

[KKW21] H. Kim, J. Kim, S. Won, and C. Lee. "Unsupervised deep learning for super-resolution reconstruction of turbulence." *J. Fluid Mech.*, **910**:A29, 2021.

[KL51] S. Kullback and R. A. Leibler. "On information and sufficiency." *Ann. Math. Stat.*, **22**(1):79–86, 1951.

[KL20] J. Kim and C. Lee. "Prediction of turbulent heat transfer using convolutional neural networks." *J. Fluid Mech.*, **882**:A18, 2020.

[KL24] J. Kim and A. Leonard. "The Early Days and Rise of Turbulence Simulation." *Annu. Rev. Fluid Mech.*, **56**, 2024.

[KLM96] L. P. Kaelbling, M. L. Littman, and A. W. Moore. "Reinforcement learning: A survey." *J. Artif. Intell. Res.*, **4**:237–285, 1996.

[KNL19] A. Kawagoe, S. Nakashima, M. Luhar, and K. Fukagata. "Proposal of control laws for turbulent skin friction reduction based on resolvent analysis." *J. Fluid Mech.*, **866**:810–840, 2019.

[KOS20] K. Kotani, Y. Ogawa, S. Shirasaka, A. Akao, Y. Jimbo, and H. Nakao. "Nonlinear phase-amplitude reduction of delay-induced oscillations." *Phys. Rev. Res.*, **2**(3):033106, 2020.

[KP01] J. Katz and A. Plotkin. *Low-speed aerodynamics*, volume 13. Cambridge university press, 2001.

[KRG21] A. Kashefi, D. Rempe, and L. J. Guibas. "A point-cloud deep learning framework for prediction of fluid flow fields on irregular geometries." *Phys. Fluids*, **33**(2):027104, 2021.

[KSA21] D. Kochkov, J. A. Smith, A. Alieva, Q. Wang, M. P. Brenner, and S. Hoyer. "Machine learning–accelerated computational fluid dynamics." *Proc. Nat. Aca. Sci.*, **118**(21), 2021.

[KSN13] W. Kurebayashi, S. Shirasaka, and H. Nakao. "Phase reduction method for strongly perturbed limit cycle oscillators." *Phys. Rev. Lett.*, **111**(21):214101, 2013.

[KT16] T. Kajishima and K. Taira. *Computational fluid dynamics: incompressible turbulent flows*. Springer, 2016.

[KT20] M. A. Khodkar and K. Taira. "Phase-synchronization properties of laminar cylinder wake for periodic external forcings." *J. Fluid Mech.*, **904**:R1, 2020.

[Kug19] L. Kugler. "Real-world applications for drones." *Commun. ACM*, **62**(11):19–21, 2019.

[Kur84] Y. Kuramoto. *Chemical oscillations, waves, and turbulence*. Springer, 1984.

[Kur15] D. F. Kurtulus. "On the unsteady behavior of the flow around NACA 0012 airfoil with steady external conditions at $Re = 1000$." *Int. J. Micro Air Veh.*, **7**(3):301–326, 2015.

[KYK19] D. Kang, S. Yamazaki, S. Kagawa, B. An, M. Nohmi, and K. Yokota. "Flow Characteristics in a V-shaped Region of a Suction Performance Curve in a Double-suction Centrifugal Pump." *Int. J. Fluid Mach. Syst.*, **12**(1):89–98, 2019.

[LAD21] "Los Angeles Department of Transportation: URBAN AIR MOBILITY Policy Framework Considerations." https://ladot.lacity.org/sites/default/files/documents/ladot-uam-policy-framework-considerations.pdf, 2021. Accessed on 20-April-2023.

[LAN18a] Q. Liu, B. An, M. Nohmi, M. Obuchi, and K. Taira. "Core-pressure alleviation for a wall-normal vortex by active flow control." *J. Fluid Mech.*, **853**:R1, 2018.

[LAN18b] Q. Liu, B. An, M. Nohmi, M. Obuchi, and K. Taira. "Core-pressure alleviation for a wall-normal vortex by active flow control." *J. Fluid Mech.*, **853**:R1, 2018.

[LAN20] Q. Liu, B. An, M. Nohmi, M. Obuchi, and K. Taira. "Active flow control of a pump-induced wall-normal vortex with steady blowing." *J. Fluids Eng.*, **142**(8):081202, 2020.

[LB23] A. Lozano-Durán and H. J. Bae. "Machine learning building-block-flow wall model for large-eddy simulation." *J. Fluid Mech.*, **963**:A35, 2023.

[LBB98] Y. LeCun, L. Bottou, Y. Bengio, and P. Haffner. "Gradient-based learning applied to document recognition." *Proc. IEEE*, **86**(11):2278–2324, 1998.

[LBB23] T. Li, M. Buzzicotti, L. Biferale, F. Bonaccorso, S. Chen, and M. Wan. "Multi-scale reconstruction of turbulent rotating flows with proper orthogonal decomposition and generative adversarial networks." *J. Fluid Mech.*, **971**:A3, 2023.

[LBH15] Y. LeCun, Y. Bengio, and G. Hinton. "Deep learning." *Nature*, **521**:436–444, 2015.

[LBR06] H. Lee, A. Battle, R. Raina, and A. Y. Ng. "Efficient sparse coding algorithms." In *Proceedings of the 19th International Conference on Neural Information Processing Systems*, pp. 801–808, 2006.

[LE21] M. Le Provost and J. D. Eldredge. "Ensemble Kalman filter for vortex models of disturbed aerodynamic flows." *Phys. Rev. Fluids*, **6**(5):050506, 2021.

[Lei06] G. J. Leishman. *Principles of helicopter aerodynamics*. Cambridge university press, 2006.

[LG20] A. J. Linot and M. D. Graham. "Deep learning to discover and predict dynamics on an inertial manifold." *Phys. Rev. E*, **101**(6):062209, 2020.

[LG23] A. J. Linot and M. D. Graham. "Dynamics of a data-driven low-dimensional model of turbulent minimal Couette flow." *J. Fluid Mech.*, **973**:A42, 2023.

[LK81] B. D. Lucas and T. Kanade. "An iterative image registration technique with an application to stereo vision." *Proceedings of the DARPA Image Understanding Workshop*, **81**:674–679, 1981.

[LK21] M. Leer and A. Kempf. "Fast Flow Field Estimation for Various Applications with A Universally Applicable Machine Learning Concept." *Flow, Turbul. Comb.*, **107**(1):175–200, 2021.

[LKB97] C. Lee, J. Kim, D. Babcock, and R. Goodman. "Application of neural networks to turbulence control for drag reduction." *Phys. Fluids*, **9**(6):1740–1747, 1997.

[LKC98] C. Lee, J. Kim, and H. Choi. "Suboptimal control of turbulent channel flow for drag reduction." *J. Fluid Mech.*, **358**:245–258, 1998.

[LKL19] S. Li, E. Kaiser, S. Laima, H. Li, S. L. Brunton, and J. N. Kutz. "Discovering time-varying aerodynamics of a prototype bridge by sparse identification of nonlinear dynamical systems." *Phys. Rev. E*, **100**(2):022220, 2019.

[LKL23] T. Lee, J. Kim, and C. Lee. "Turbulence control for drag reduction through deep reinforcement learning." *Phys. Rev. Fluids*, **8**(2):024604, 2023.

[LKT16] J. Ling, A. Kurzawski, and J Templeton. "Reynolds averaged turbulence modelling using deep neural networks with embedded invariance." *J. Fluid Mech.*, **807**:155–166, 2016.

[LLF98] I. E. Lagaris, A. Likas, and D. I. Fotiadis. "Artificial neural networks for solving ordinary and partial differential equations." *IEEE Trans. Neural Netw.*, **9**(5):987–1000, 1998.

[LLN22] S. Li, W. Li, and B. R. Noack. "Machine-learned control-oriented flow estimation for multi-actuator multi-sensor systems exemplified for the fluidic pinball." *J. Fluid Mech.*, **952**:A36, 2022.

[LLZ12] Y. Liu, K. Li, J. Zhang, H. Wang, and L. Liu. "Numerical bifurcation analysis of static stall of airfoil and dynamic stall under unsteady perturbation." *Commun. Nonlinear Sci. Numer. Simul.*, **17**(8):3427–3434, 2012.

[LNJ21] I. A. Loe, H. Nakao, Y. Jimbo, and K. Kotani. "Phase-reduction for synchronization of oscillating flow by perturbation on surrounding structure." *J. Fluid Mech.*, **911**:R2, 2021.

[LPB22] Y. Liu, C. Ponce, S. L. Brunton, and J. N. Kutz. "Multiresolution convolutional autoencoders." *J. Comput. Phys.*, p. 111801, 2022.

[LPW08] Y. Li, E. Perlman, M. Wan, Y. Yang, C. Meneveau, R. Burns, S. Chen, A. Szalay, and G. Eyink. "A public turbulence database cluster and applications to study Lagrangian evolution of velocity increments in turbulence." *J. Turb*, (9):N31, 2008.

[LRT19] Y. Li, D. Roblek, and M. Tagliasacchi. "From here to there: Video inbetweening using 3D convolutions." *arXiv:1905.10240* 2019.

[LSM14] M. Luhar, A. S. Sharma, and B. J. McKeon. "Opposition control within the resolvent analysis framework." *J. Fluid Mech.*, **749**:597–626, 2014.

[LTH17] C. Ledig, L. Theis, F. Huszár, J. Caballero, A. Cunningham, A. Acosta, A. Aitken, A. Tejani, J. Totz, Z. Wang, and W. Shi. "Photo-realistic single image super-resolution using a generative adversarial network." In *Proceedings of the IEEE conference on computer vision and pattern recognition*, pp. 4681–4690, 2017.

[LTH20] B. Liu, J. Tang, H. Huang, and X.-Y. Lu. "Deep learning methods for super-resolution reconstruction of turbulent flows." *Phys. Fluids*, **32**(2):025105, 2020.

[LTT23] C.-T. Lin, M.-L. Tsai, and H.-C. Tsai. "Flow control of a plunging cylinder based on resolvent analysis." *J. Fluid Mech.*, **967**:A41, 2023.

[LU22] S. Li and L. Ukeiley. "Pressure-informed velocity estimation in a subsonic jet." *Phys. Rev. Fluids*, **7**(1):014601, 2022.

[Lum67] J. L. Lumley. "The structure of inhomogeneous turbulent flows." In A. M. Yaglom and V. I. Tatarski, editors, *Atmospheric turbulence and radio wave propagation*. Nauka, 1967.

[LW19] H. F. S. Lui and W. R. Wolf. "Construction of reduced-order models for fluid flows using deep feedforward neural networks." *J. Fluid Mech.*, **872**:963–994, 2019.

[LY19] S. Lee and D. You. "Data-driven prediction of unsteady flow over a circular cylinder using deep learning." *J. Fluid Mech.*, **879**:217–254, 2019.

[LY21] S. Lee and D. You. "Analysis of a convolutional neural network for predicting unsteady volume wake flow fields." *Phys. Fluids*, **33**(3):035152, 2021.

[LYF22] S. Lee, J. Yang, P. Forooghi, A. Stroh, and S. Bagheri. "Predicting drag on rough surfaces by transfer learning of empirical correlations." *J. Fluid Mech.*, **933**:A18, 2022.

[LYH22] B. Liu, H. Yu, H. Huang, N. Liu, and X. Lu. "Investigation of nonlocal data-driven methods for subgrid-scale stress modeling in large eddy simulation." *AIP Adv.*, **12**(6), 2022.

[LYY12] X. Lu, H. Yuan, P. Yan, Y. Yuan, and X. Li. "Geometry constrained sparse coding for single image super-resolution." In *IEEE Conference on Computer Vision and Pattern Recognition*, pp. 1648–1655. IEEE, 2012.

[LZ22] J. Li and M. Zhang. "Reinforcement-learning-based control of confined cylinder wakes with stability analyses." *J. Fluid Mech.*, **932**:A44, 2022.

[LZG23] A. J. Linot, K. Zeng, and M. D. Graham. "Turbulence control in plane Couette flow using low-dimensional neural ODE-based models and deep reinforcement learning." *Int. J. Heat Fluid Flow*, **101**:109139, 2023.

[LZJ22] Q. Liu, W. Zhu, X. Jia, F. Ma, and Y. Gao. "Fluid Simulation System Based on Graph Neural Network." *arXiv:2202.12619*, 2022.

[LZK23] I. A. Loe, T. Zheng, K. Kotani, and Y. Jimbo. "Controlling fluidic oscillator flow dynamics by elastic structure vibration." *Sci. Rep.*, **13**(1):8852, 2023.

[Mar18] Gary Marcus. "Deep learning: A critical appraisal." arXiv:1801.00631, 2018.

[MAW16] A. Mohamed, M. Abdulrahim, S. Watkins, and R. Clothier. "Development and flight testing of a turbulence mitigation system for micro air vehicles." *J. Field Robot.*, **33**(5):639–660, 2016.

[MBK18] K. Manohar, B. W. Brunton, J. N. Kutz, and S. L. Brunton. "Data-driven sparse sensor placement for reconstruction: Demonstrating the benefits of exploiting known patterns." *IEEE Control Syst.*, **38**(3):63–86, 2018.

[MBR21a] T. Mallick, P. Balaprakash, E. Rask, and J. Macfarlane. "Transfer learning with graph neural networks for short-term highway traffic forecasting." In *2020 25th International Conference on Pattern Recognition (ICPR)*, pp. 10367–10374. IEEE, 2021.

[MBR21b] R. Maulik, T. Botsas, N. Ramachandra, L. R. Mason, and I. Pan. "Latent-space time evolution of non-intrusive reduced-order models using Gaussian process emulation." *Phys. D*, **416**:132797, 2021.

[MFF20] T. Murata, K. Fukami, and K. Fukagata. "Nonlinear mode decomposition with convolutional neural networks for fluid dynamics." *J. Fluid Mech.*, **882**:A13, 2020.

[MFF21] M. Morimoto, K. Fukami, and K. Fukagata. "Experimental velocity data estimation for imperfect particle images using machine learning." *Phys. Fluids*, **33**(8):087121, 2021.

[MFM22] M. Morimoto, K. Fukami, R. Maulik, R. Vinuesa, and K. Fukagata. "Assessments of epistemic uncertainty using Gaussian stochastic weight averaging for fluid-flow regression." *Phys. D: Nonlinear Phenom.*, **440**:133454, 2022.

[MFN24] M. Matsuo, K. Fukami, T. Nakamura, M. Morimoto, and K. Fukagata. "Reconstructing three-dimensional bluff body wake from sectional flow fields with convolutional neural networks." *SN Comput. Sci.,* accepted, 2024.

[MFR20] R. Maulik, K. Fukami, N. Ramachandra, K. Fukagata, and K. Taira. "Probabilistic neural networks for fluid flow surrogate modeling and data recovery." *Phys. Rev. Fluids*, **5**:104401, 2020.

[MFZ21] M. Morimoto, K. Fukami, K. Zhang, A. G. Nair, and K. Fukagata. "Convolutional neural networks for fluid flow analysis: toward effective metamodeling and low-dimensionalization." *Theor. Comput. Fluid Dyn.*, **35**(5):633–658, 2021.

[MFZ22] M. Morimoto, K. Fukami, K. Zhang, and K. Fukagata. "Generalization techniques of neural networks for fluid flow estimation." *Neural Comput. App.*, **34**(5):3647–3669, 2022.

[MHC19] N. Machicoane, P. D. Huck, A. Clark, A. Aliseda, R. Volk, and M. Bourgoin. "Recent Developments in Particle Tracking Diagnostics for Turbulence Research." In *Flowing Matter*, pp. 177–209. Springer, Cham, 2019.

[MI13] T. Michaeli and M. Irani. "Nonparametric blind super-resolution." In *Proceedings of the IEEE International Conference on Computer Vision*, pp. 945–952, 2013.

[MJC22] E. Martini, J. Jung, A. V. G. Cavalieri, P. Jordan, and A. Towne. "Resolvent-based tools for optimal estimation and control via the Wiener–Hopf formalism." *J. Fluid Mech.*, **937**:A19, 2022.

[MJW23] Q. Meng, Z. Jiang, and J. Wang. "Artificial neural network-based subgrid-scale models for LES of compressible turbulent channel flow." *Theor. Appl. Mech.*, **13**(1):100399, 2023.

[MK02] M. Milano and P. Koumoutsakos. "Neural network modeling for near wall turbulent flow." *J. Comput. Phys.*, **182**:1–26, 2002.

[MKK14] K. V. Mishra, A. Kruger, and W. F. Krajewski. "Compressed sensing applied to weather radar." In *2014 IEEE Geoscience and Remote Sensing Symposium*, pp. 1832–1835. IEEE, 2014.

[MKM22] K. Menon, S. Kumar, and R. Mittal. "Contribution of spanwise and cross-span vortices to the lift generation of low-aspect-ratio wings: Insights from force partitioning." *Phys. Rev. Fluids*, **7**(11):114102, 2022.

[MLB21] R. Maulik, B. Lusch, and P. Balaprakash. "Reduced-order modeling of advection-dominated systems with recurrent neural networks and convolutional autoencoders." *Phys. Fluids*, **33**(3), 2021.

[MLC23] A. T. Mohan, N. Lubbers, M. Chertkov, and D. Livescu. "Embedding hard physical constraints in neural network coarse-graining of three-dimensional turbulence." *Phys. Rev. Fluids*, **8**(1):014604, 2023.

[MLE21] P. M. Milani, J. Ling, and J. K Eaton. "Turbulent scalar flux in inclined jets in crossflow: counter gradient transport and deep learning modelling." *J. Fluid Mech.*, **906**:A27, 2021.

[MM98] P. Moin and K. Mahesh. "Direct numerical simulation: a tool in turbulence research." *Annu. Rev. Fluid Mech.*, **30**(1):539–578, 1998.

[MM18] A. Mauroy and I. Mezić. "Global computation of phase-amplitude reduction for limit-cycle dynamics." *Chaos*, **28**(7), 2018.

[MMM13] A. Mauroy, I. Mezić, and J. Moehlis. "Isostables, isochrons, and Koopman spectrum for the action–angle representation of stable fixed point dynamics." *Phys. D: Nonlinear Phenom.*, **261**:19–30, 2013.

[MMW23] A. Mohamed, M. Marino, S. Watkins, J. Jaworski, and A. Jones. "Gusts Encountered by Flying Vehicles in Proximity to Buildings." *Drones*, **7**(1):22, 2023.

[MMZ22] K. H. Manohar, C. Morton, and P. Ziadé. "Sparse sensor-based cylinder flow estimation using artificial neural networks." *Phys. Rev. Fluids*, **7**(2):024707, 2022.

[MOV23] A. Marcato, D. O'Malley, H. Viswanathan, E. Guiltinan, and J. E. Santos. "Reconstruction of Fields from Sparse Sensing: Differentiable Sensor Placement Enhances Generalization." *arXiv:2312.09176*, 2023.

[MS10] B. J. McKeon and A. S. Sharma. "A critical-layer framework for turbulent pipe flow." *J. Fluid Mech.*, **658**:336–382, 2010.

[MS17] R. Maulik and O. San. "A neural network approach for the blind deconvolution of turbulent flows." *J. Fluid Mech.*, **831**:151–181, 2017.

[MSF21] J. F. MacArt, J. Sirignano, and J. B. Freund. "Embedded training of neural-network subgrid-scale turbulence models." *Phys. Rev. Fluids*, **6**(5):050502, 2021.

[MSJ19a] R. Maulik, O. San, J. D. Jacob, and C. Crick. "Sub-grid scale model classification and blending through deep learning." *J. Fluid Mech.*, **870**:784–812, 2019.

[MSJ19b] R. Maulik, O. San, J. D. Jacob, and C. Crick. "Sub-grid scale model classification and blending through deep learning." *J. Fluid Mech.*, **870**:784–812, 2019.

[MSJ21] M. Moriche, G. Sedky, A. R. Jones, O. Flores, and M. García-Villalba. "Characterization of aerodynamic forces on wings in plunge maneuvers." *AIAA J.*, **59**(2):751–762, 2021.

[MSR19] R. Maulik, O. San, A. Rasheed, and P. Vedula. "Subgrid modelling for two-dimensional turbulence using neural networks." *J. Fluid Mech.*, **858**:122–144, 2019.

[MTK23] S. Maejima, K. Tanino, and S. Kawai. "Unsupervised machine-learning-based sub-grid scale modeling for coarse-grid LES." In review, 2023.

[MU07] N. E. Murray and L. S. Ukeiley. "An application of Gappy POD." *Exp. Fluids*, **42**(1):79–91, 2007.

[MWG23] R. Mojgani, D. Waelchli, Y. Guan, P. Koumoutsakos, and P. Hassanzadeh. "Extreme Event Prediction with Multi-agent Reinforcement Learning-based Parametrization of Atmospheric and Oceanic Turbulence." *arXiv:2312.00907*, 2023.

[MWK20] W. Majewski, R. Wei, and V. Kumar. "Developing particle image velocimetry software based on a deep neural network." *J. Flow Vis. Image Process.*, **27**(4), 2020.

[MWM23] K. H. Manohar, O. Williams, R. J. Martinuzzi, and C. Morton. "Temporal super-resolution using smart sensors for turbulent separated flows." *Exp. Fluids*, **64**(5):101, 2023.

[MZN23] P. Mircheski, J. Zhu, and H. Nakao. "Phase-Amplitude Reduction and Optimal Phase Locking of Collectively Oscillating Networks." *Chaos*, **33**:103111, 2023.

[Nak16] H. Nakao. "Phase reduction approach to synchronisation of nonlinear oscillators." *Contemp. Phys.*, **57**(2):188–214, 2016.

[Nak21] H. Nakao. "Phase and amplitude description of complex oscillatory patterns in reaction-diffusion systems." In *Physics of Biological Oscillators: New Insights into Non-Equilibrium and Non-Autonomous Systems*, pp. 11–27. Springer, 2021.

[NAM03] B. R. Noack, K. Afanasiev, M. Morzynski, G. Tadmor, and F. Thiele. "A Hierarchy of Low-Dimensional Models for the Transient and Post-Transient Cylinder Wake." *J. Fluid Mech.*, **497**:335–363, 2003.

[NBT18] A. G. Nair, S. L. Brunton, and K. Taira. "Networked-oscillator-based modeling and control of unsteady wake flows." *Phys. Rev. E*, **97**(6):063107, 2018.

[ND99] F. Nicoud and F. Ducros. "Subgrid-scale stress modelling based on the square of the velocity gradient tensor." *Flow Turbul. Combust.*, **62**(3):183–200, 1999.

[NE94] B. R. Noack and H. Eckelmann. "A global stability analysis of the steady and periodic cylinder wake." *J. Fluid Mech.*, **270**:297–330, 1994.

[NF22] T. Nakamura and K. Fukagata. "Robust training approach of neural networks for fluid flow state estimations." *Int. J. Heat Fluid Flow*, **96**:108997, 2022.

[NFF22] T. Nakamura, K. Fukami, and K. Fukagata. "Identifying key differences between linear stochastic estimation and neural networks for fluid flow regressions." *Sci. Rep.*, **12**(3726), 2022.

[NG20] N. J. Nair and A. Goza. "Leveraging reduced-order models for state estimation using deep learning." *J. Fluid Mech.*, **897**:R1, 2020.

[NG23] N. J. Nair and A. Goza. "Bio-inspired variable-stiffness flaps for hybrid flow control, tuned via reinforcement learning." *J. Fluid Mech.*, **956**:R4, 2023.

[NH10] V. Nair and G. E. Hinton. "Rectified linear units improve restricted Boltzmann machines." *In Proc. 27th International Conference on Machine Learning*, 2010.

[NLK21] G. Novati, H. L. de Laroussilhe, and P. Koumoutsakos. "Automating turbulence modelling by multi-agent reinforcement learning." *Nat. Mach. Intell.*, **3**(1):87–96, 2021.

[NMM21] P. A. S. Nogueira, P. Morra, E. Martini, A. V. G. Cavalieri, and D. S. Henningson. "Forcing statistics in resolvent analysis: application in minimal turbulent Couette flow." *J. Fluid Mech.*, **908**:A32, 2021.

[NTB21] A. G. Nair, K. Taira, B. W. Brunton, and S. L. Brunton. "Phase-based control of periodic flows." *J. Fluid Mech.*, **927**:A30, 2021.

[OLS22] S. Oh, S. Lee, M. Son, J. Kim, and H. Ki. "Accurate prediction of the particle image velocimetry flow field and rotor thrust using deep learning." *J. Fluid Mech.*, **939**:A2, 2022.

[OMS99] A. Ooi, J. Martin, J. Soria, and M. S. Chong. "A study of the evolution and characteristics of the invariants of the velocity-gradient tensor in isotropic turbulence." *J. Fluid Mech.*, **381**:141–174, 1999.

[OPD21] C. Ott, C. Pivot, P. Dubois, Q. Gallas, J. Delva, M. Lippert, and L. Keirsbulck. "Pulsed jet phase-averaged flow field estimation based on neural network approach." *Exp. Fluids*, **62**:1–16, 2021.

[OS19] N. Omata and S. Shirayama. "A novel method of low-dimensional representation for temporal behavior of flow fields using deep autoencoder." *AIP Adv.*, **9**(1):015006, 2019.

[OSM19] R. Onishi, D. Sugiyama, and K. Matsuda. "Super-resolution simulation for real-time prediction of urban micrometeorology." *SOLA*, **15**:178–182, 2019.

[OVM21] O. Obiols-Sales, A. Vishnu, N. P. Malaya, and A. Chandramowlishwaran. "SURFNet: Super-resolution of Turbulent Flows with Transfer Learning using Small Datasets." In *IEEE 30th International Conference on Parallel Architectures and Compilation Techniques (PACT)*, pp. 331–344. IEEE, 2021.

[PB06] D. J. Pines and F. Bohorquez. "Challenges Facing Future Micro-Air-Vehicle Development." *J. Aircraft*, **43**(2):290–305, 2006.

[PBD21] R. Paris, S. Beneddine, and J. Dandois. "Robust flow control and optimal sensor placement using deep reinforcement learning." *J. Fluid Mech.*, **913**:A25, 2021.

[PBK21] J. Page, M. P. Brenner, and R. R. Kerswell. "Revealing the state space of turbulence using machine learning." *Phys. Rev. Fluids*, **6**(3):034402, 2021.

[PC20] J. Park and H. Choi. "Machine-learning-based feedback control for drag reduction in a turbulent channel flow." *J. Fluid Mech.*, **904**:A24, 2020.

[PD23] A. Pradhan and K. Duraisamy. "Variational multiscale super-resolution: A data-driven approach for reconstruction and predictive modeling of unresolved physics." *Int. J. Numer. Methods Eng.*, **124**(19):4339–4370, 2023.

[PF20] P. Pant and A. B. Farimani. "Deep learning for efficient reconstruction of high-resolution turbulent DNS data." *arXiv:2010.11348*, 2020.

[PFM18] S. Prudden, A. Fisher, M. Marino, A. Mohamed, S. Watkins, and G. Wild. "Measuring wind with small unmanned aircraft systems." *J. Wind. Eng. Ind. Aerodyn.*, **176**:197–210, 2018.

[PKK22] A. F. Psaros, K. Kawaguchi, and G. E. Karniadakis. "Meta-learning PINN loss functions." *J. Comput. Phys.*, **458**:111121, 2022.

[PNS21] G. D. Portwood, B. T. Nadiga, J. A. Saenz, and D. Livescu. "Interpreting neural network models of residual scalar flux." *J. Fluid Mech.*, **907**:A23, 2021.

[PPK03] S. C. Park, M. K. Park, and M. G. Kang. "Super-resolution image reconstruction: a technical overview." *IEEE Signal Process. Mag.*, **20**(3):21–36, 2003.

[Pre98] L. Prechelt. "Automatic early stopping using cross validation: quantifying the criteria." *Neural Netw.*, **11**(4):761–767, 1998.

[PSR20] S. Pawar, O. San, A. Rasheed, and P. Vedula. "A priori analysis on deep learning of subgrid-scale parameterizations for Kraichnan turbulence." *Theor. Comput. Fluid Dyn.*, **34**:429–455, 2020.

[PSR23a] S. Pawar, O. San, A. Rasheed, and P. Vedula. "Frame invariant neural network closures for Kraichnan turbulence." *Phys. A*, **609**:128327, 2023.

[PSR23b] F. Pino, L. Schena, J. Rabault, and M. A. Mendez. "Comparative analysis of machine learning methods for active flow control." *J. Fluid Mech.*, **958**:A39, 2023.

[PSS20] N. Parashar, B. Srinivasan, and S. S. Sinha. "Modeling the pressure-Hessian tensor using deep neural networks." *Phys. Rev. Fluids*, **5**(11):114604, 2020.

[PY09] S. J. Pan and Q. Yang. "A survey on transfer learning." *IEEE Trans. Knowl. Data Eng.*, **22**(10):1345–1359, 2009.

[QSM17] C. R. Qi, H. Su, K. Mo, and L. J. Guibas. "PointNet: Deep learning on point sets for 3D classification and segmentation." In *Proceedings of the IEEE conference on computer vision and pattern recognition*, pp. 652–660, 2017.

[QWG23] Y. Qian, Z. Wang, and I. Gursul. "Lift alleviation in travelling vortical gusts." *Aeronaut. J.*, pp. 1–22, 2023.

[RD17] C. W. Rowley and S. T. M. Dawson. "Model reduction for flow analysis and control." *Annu. Rev. Fluid. Mech.*, **49**:387–417, 2017.

[RDM23] A. Racca, N. A. K. Doan, and L. Magri. "Predicting turbulent dynamics with the convolutional autoencoder echo state network." *J. Fluid Mech.*, **975**:A2, 2023.

[RHW86] D. E. Rumelhart, G. E. Hinton, and R. J. Williams. "Learning representations by back-propagation errors." *Nature*, **322**:533—536, 1986.

[RIM16] Y. Romano, J. Isidoro, and P. Milanfar. "RAISR: rapid and accurate image super resolution." *IEEE Trans. Comput. Imaging*, **3**(1):110–125, 2016.

[RJF22] L. V. Rolandi, T. Jardin, J. Fontane, J. Gressier, and L. Joly. "Stability of the low Reynolds number compressible flow past a NACA0012 airfoil." *AIAA J.*, **60**(2):1052–1066, 2022.

[RKJ19] J. Rabault, M. Kuchta, A. Jensen, U. Réglade, and N. Cerardi. "Artificial neural networks trained through deep reinforcement learning discover control strategies for active flow control." *J. Fluid Mech,*, **865**:281–302, 2019.

[RMW14] D. J. Rezende, S. Mohamed, and D. Wierstra. "Stochastic backpropagation and approximate inference in deep generative models." In *International conference on machine learning*, pp. 1278–1286. PMLR, 2014.

[RPK19] M. Raissi, P. Perdikaris, and G. E. Karniadakis. "Physics-informed neural networks: A deep learning framework for solving forward and inverse problems involving nonlinear partial differential equations." *J. Comput. Phys.*, **378**:686–707, 2019.

[RRL22] P. Ren, C. Rao, Y. Liu, Z. Ma, Q. Wang, J.-X. Wang, and H. Sun. "Physics-informed Deep Super-resolution for Spatiotemporal Data." *arXiv:2208.01462*, 2022.

[RS00] S. T. Roweis and L. K. Saul. "Nonlinear dimensionality reduction by locally linear embedding." *Science*, **290**(5500):2323–2326, 2000.

[RW17] J. H. M. Ribeiro and W. R. Wolf. "Identification of coherent structures in the flow past a NACA0012 airfoil via proper orthogonal decomposition." *Phys. Fluids*, **29**(8), 2017.

[RYK20] M. Raissi, A. Yazdani, and G. E. Karniadakis. "Hidden fluid mechanics: Learning velocity and pressure fields from flow visualizations." *Science*, **367**(6481):1026–1030, 2020.

[RYZ22] J. H. M. Ribeiro, C.-A. Yeh, K. Zhang, and K. Taira. "Wing sweep effects on laminar separated flows." *J. Fluid Mech.*, **950**:A23, 2022.

[RZ85] D. E. Rumelhart and D. Zipser. "Feature discovery by competitive learning." *Cogn. Sci.*, **9**(1):75–112, 1985.

[SAK01] S. Stolz, N. A. Adams, and L. Kleiser. "An approximate deconvolution model for large-eddy simulation with application to incompressible wall-bounded flows." *Phys. Fluids*, **13**(4):997–1015, 2001.

[Sal16] J. Salvador. *Example-Based super resolution*. Academic Press, 2016.

[SCC22] A. T. Sage, M. Cypel, M. Cardinal, J. Qiu, A. Humar, and S. Keshavjee. "Testing the delivery of human organ transportation with drones in the real world." *Sci. Robot.*, **7**(73):eadf5798, 2022.

[Sch10] P. J. Schmid. "Dynamic mode decomposition of numerical and experimental data." *J. Fluid Mech.*, **656**:5–28, 2010.

[Sch11] P. J. Schmid. "Application of the dynamic mode decomposition to experimental data." *Experiments in fluids*, **50(4)**:1123–1130, 2011.

[Sch22] P. J. Schmid. "Dynamic mode decomposition and its variants." *Annu. Rev. Fluid Mech.*, **54**:225–254, 2022.

[SFI11] O Shahar, A Faktor, and M Irani. "Space-time super-resolution from a single video." In *CVPR 2011*, pp. 3353–3360. IEEE Computer Society, 2011.

[SFS23] L. Smith, K. Fukami, G. Sedky, A. Jones, and K. Taira. "A cyclic perspective on transient gust encounters through the lens of persistent homology." *arXiv:2306.15829*, 2023.

[SGA19] P. A. Srinivasan, L. Guastoni, H. Azizpour, P. Schlatter, and R Vinuesa. "Predictions of turbulent shear flows using deep neural networks." *Phys. Rev. Fluids*, **4**:054603, 2019.

[SGD24] Á. M. Soto, A. Güemes, and S. Discetti. "Complete flow characterization from snapshot PIV, fast probes and physics-informed neural networks." *Comput. Methods Appl. Mech Eng.*, **419**:116652, 2024.

[SGH20] K. Stengel, A. Glaws, D. Hettinger, and R. N. King. "Adversarial super-resolution of climatological wind and solar data." *Proc. Natl. Acad. Sci. U.S.A.*, **117**(29):16805–16815, 2020.

[SGL23] G. Sedky, A. Gementzopoulos, F. D. Lagor, and A. R. Jones. "Experimental mitigation of large-amplitude transverse gusts via closed-loop pitch control." *Phys. Rev. Fluids*, **8**(6):064701, 2023.

[SH01] P. J. Schmid and D. S. Henningson. "Stability and Transition in Shear Flows." *Applied Mathematical Sciences*, 2001.

[SH06] T. Suzuki and Y. Hasegawa. "Estimation of turbulent channel flow at $\mathrm{Re}_\tau = 100$ based on the wall measurement using a simple sequential approach." *J. Fluid Mech.*, **830**:760–796, 2006.

[SHB23] C. M. Stutz, J. T. Hrynuk, and D. G. Bohl. "Dimensional analysis of a transverse gust encounter." *Aerosp. Sci. Technol.*, **137**:108285, 2023.

[SHP22] J. Shin, M. Hansinger, M. Pfitzner, and M. Klein. "A priori analysis on deep learning of filtered reaction rate." *Flow Turbul. Combust.*, **109**(2):383–409, 2022.

[SIM07] S.-B. Shim, M. Imboden, and P. Mohanty. "Synchronized oscillation in coupled nanomechanical oscillators." *Science*, **316**(5821):95–99, 2007.

[SJL20] G. Sedky, A. R. Jones, and F. D. Lagor. "Lift regulation during transverse gust encounters using a modified Goman–Khrabrov model." *AIAA J.*, **58**(9):3788–3798, 2020.

[SKN17] S. Shirasaka, W. Kurebayashi, and H. Nakao. "Phase-amplitude reduction of transient dynamics far from attractors for limit-cycling systems." *Chaos*, **27**(2), 2017.

[SL07] D. Sipp and A. Lebedev. "Global stability of base and mean flows: a general approach and its applications to cylinder and open cavity flows." *J. Fluid Mech.*, **593**:333–358, 2007.

[SLI23] T. Sonoda, Z. Liu, T. Itoh, and Y. Hasegawa. "Reinforcement learning of control strategies for reducing skin friction drag in a fully developed turbulent channel flow." *J. Fluid Mech.*, **960**:A30, 2023.

[SM18] O. San and R. Maulik. "Neural network closures for nonlinear model order reduction." *Adv. Comput. Math.*, **44**(6):1717–1750, 2018.

[SMD17] A. P. Singh, S. Medida, and K. Duraisamy. "Machine-learning-augmented predictive modeling of turbulent separated flows over airfoils." *AIAA J.*, **55**(7):2215–2227, 2017.

[SNS21] Z. Shadram, T. M. Nguyen, A. Sideris, and W. A. Sirignano. "Neural network flame closure for a turbulent combustor with unsteady pressure." *AIAA J.*, **59**(2):621–635, 2021.

[Spa23] P. Spalart. "An old-fashioned framework for machine learning in turbulence modeling." *arXiv:2308.00837*, 2023.

[SPM22] V. Shankar, G. D. Portwood, A. T. Mohan, P. P. Mitra, D. Krishnamurthy, C. Rackauckas, L. A. Wilson, D. P. Schmidt, and V. Viswanathan. "Validation and parameterization of a novel physics-constrained neural dynamics model applied to turbulent fluid flow." *Phys. Fluids*, **34**(11), 2022.

[SR23] L. Sliwinski and G. Rigas. "Mean flow reconstruction of unsteady flows using physics-informed neural networks." *Data-Centric Eng.*, **4**:e4, 2023.

[SS04] A. J. Smola and B. Schölkopf. "A tutorial on support vector regression." *Stat. Comput.*, **14**(3):199–222, 2004.

[SSM19] S. Symon, D. Sipp, and B. J. McKeon. "A tale of two airfoils: resolvent-based modelling of an oscillator versus an amplifier from an experimental mean." *J. Fluid Mech.*, **881**:51–83, 2019.

[SSS20] I. Scherl, B. Strom, J. K. Shang, O. Williams, B. L. Polagye, and S. L. Brunton. "Robust principal component analysis for modal decomposition of corrupt fluid flows." *Phys. Rev. Fluids*, **5**:054401, 2020.

[STM21] T. Saitoh, Y. Takahashi, H. Minami, Y. Nakashima, S. Aramaki, Y. Mihara, T. Iwakura, K. Odagiri, Y. Maekawa, and A. Yoshino. "Real-time breath recognition by movies from a small drone landing on victim's bodies." *Sci. Rep.*, **11**(1):5042, 2021.

[SW20] L. Sun and J.-X. Wang. "Physics-constrained Bayesian neural network for fluid flow reconstruction with sparse and noisy data." *Theor. Appl. Mech. Lett.*, **10**(3):161–169, 2020.

[SYS22] C. S. Skene, C.-A. Yeh, P. J. Schmid, and K. Taira. "Sparsifying the resolvent forcing mode via gradient-based optimisation." *J. Fluid Mech.*, **944**:A52, 2022.

[Tay18] G. I. Taylor. "On the dissipation of eddies." *Meteorology, Oceanography and Turbulent Flow*, pp. 96–101, 1918.

[TBD17] K. Taira, S. L. Brunton, S. T. M. Dawson, C. W. Rowley, T. Colonius, B. J. McKeon, O. T. Schmidt, S. Gordeyev, V. Theofilis, and L. S. Ukeiley. "Modal analysis of fluid flows: An overview." *AIAA J.*, **55**(12):4013–4041, 2017.

[TC07] K. Taira and T. Colonius. "The immersed boundary method: A projection approach." *J. Comput. Phys.*, **225**(2):2118–2137, 2007.

[TCS21] H. Tsukamoto, S.-J. Chung, and J.-J. E. Slotine. "Contraction theory for nonlinear stability analysis and learning-based control: A tutorial overview." *Annu. Rev. Control*, **52**:135–169, 2021.

[TDB23] A. Towne, S. Dawson, G. A. Brès, A. Lozano-Durán, T. Saxton-Fox, A. Parthasarathy, A. R. Jones, H. Biler, C.-A. Yeh, H. D. Patel, and K. Taira. "A database for reduced-complexity modeling of fluid flows." *AIAA J.*, **61**(7):2867–2892, 2023.

[Tem89] R. Temam. "Do inertial manifolds apply to turbulence?" *Phys. D: Nonlinear Phenom.*, **37**(1-3):146–152, 1989.

[TH23] G. Tabe Jamaat and Y. Hattori. "A priori assessment of nonlocal data-driven wall modeling in large eddy simulation." *Phys. Fluids*, **35**(5), 2023.

[THB20a] K. Taira, M. S. Hemati, S. L. Brunton, Y. Sun, K. Duraisamy, S. Bagheri, S. Dawson, and C-A. Yeh. "Modal Analysis of Fluid Flows: Applications and Outlook." *AIAA J.*, **58**(3):998–1022, 2020.

[THB20b] K. Taira, M. S. Hemati, S. L. Brunton, Y. Sun, K. Duraisamy, S. Bagheri, S. Dawson, and C.-A. Yeh. "Modal Analysis of Fluid Flows: Applications and Outlook." *AIAA J.*, **58**(3):998–1022, 2020.

[The11] V. Theofilis. "Global linear instability." *Annu. Rev. Fluid Mech.*, **43**:319–352, 2011.

[TIK23] N. Takeda, H. Ito, and H. Kitahata. "Two-dimensional hydrodynamic simulation for synchronization in coupled density oscillators." *Phys. Rev. E*, **107**(3):034201, 2023.

[TKN21] S. Takata, Y. Kato, and H. Nakao. "Fast optimal entrainment of limit-cycle oscillators by strong periodic inputs via phase-amplitude reduction and Floquet theory." *Chaos*, **31**(9), 2021.

[TN18] K. Taira and H. Nakao. "Phase-response analysis of synchronization for periodic flows." *J. Fluid Mech.*, **846**, 2018.

[TNB16] K. Taira, A. G. Nair, and S. L. Brunton. "Network structure of two-dimensional decaying isotropic turbulence." *J. Fluid Mech.*, **795**:R2, 2016.

[TWW23] H. Tang, Y. Wang, T. Wang, L. Tian, and Y. Qian. "Data-driven Reynolds-averaged turbulence modeling with generalizable non-linear correction and uncertainty quantification using Bayesian deep learning." *Phys. Fluids*, **35**(5), 2023.

[Vas15] J. C. Vassilicos. "Dissipation in turbulent flows." *Annu. Rev. Fluid Mech.*, **47**:95–114, 2015.

[Vor08] G. Voronoi. "New applications of continuous parameters to the theory of quadratic forms. First thesis. On some properties of perfect positive quadratic forms." *Journal fur die Reine und angewandte Mathematik*, **133**:97–178, 1908.

[VP17] N. Van Noord and E. Postma. "Learning scale-variant and scale-invariant features for deep image classification." *Pattern Recognit.*, **61**:583–592, 2017.

[VS09] A. Vlasenko and C. Schnörr. "Superresolution and denoising of 3D fluid flow estimates." In *Joint Pattern Recognition Symposium*, pp. 482–491. Springer, 2009.

[VSV06] P. Vandewalle, S. Süsstrunk, and M. Vetterli. "A frequency domain approach to registration of aliased images with application to super-resolution." *EURASIP J. Adv. Signal Process.*, **2006**:1–14, 2006.

[VYA23] A. Vadrot, X. I. A. Yang, and M. Abkar. "Survey of machine-learning wall models for large-eddy simulation." *Phys. Rev. Fluids*, **8**(6):064603, 2023.

[WBM20] S. Watkins, J. Burry, A. Mohamed, M. Marino, S. Prudden, A. Fisher, N. Kloet, T. Jakobi, and R. Clothier. "Ten questions concerning the use of drones in urban environments." *Build. Environ.*, **167**:106458, 2020.

[WBS04] Z. Wang, A. C. Bovik, H. R. Sheikh, and E. P. Simoncelli. "Image quality assessment: from error visibility to structural similarity." *IEEE Trans. Image Process.*, **13**(4):600–612, 2004.

[WEA13] J. Westerweel, G. E. Elsinga, and R. J. Adrian. "Particle image velocimetry for complex and turbulent flows." *Annu. Rev. Fluid Mech.*, **45**:409–436, 2013.

[WFJ23] Z. Wang, D. Fan, X. Jiang, M. S. Triantafyllou, and G. Em. Karniadakis. "Deep reinforcement transfer learning of active control for bluff body flows at high Reynolds number." *J. Fluid Mech.*, **973**:A32, 2023.

[WGS22] S. W. Wurster, H. Guo, H.-W. Shen, T. Peterka, and J. Xu. "Deep Hierarchical Super Resolution for Scientific Data." *IEEE Trans. Vis. Comput. Graph.*, 2022.

[Wil06] K. Willcox. "Unsteady flow sensing and estimation via the gappy proper orthogonal decomposition." *Comput. Fluids*, **35**(2):208–226, 2006.

[WLT13] K. C. A. Wedgwood, K. K. Lin, R. Thul, and S. Coombes. "Phase-amplitude descriptions of neural oscillator models." *J. Math. Neurosci.*, **3**:1–22, 2013.

[WM08] X. Wu and P. Moin. "A direct numerical simulation study on the mean velocity characteristics in turbulent pipe flow." *J. Fluid Mech.*, **608**:81–112, 2008.

[WM16] D. Wilson and J. Moehlis. "Isostable reduction of periodic orbits." *Phys. Rev. E*, **94**(5):052213, 2016.

[WMZ07] J.-Z. Wu, H.-Y. Ma, and M.-D. Zhou. *Vorticity and vortex dynamics*. Springer Science & Business Media, 2007.

[WPC20] Z. Wu, S. Pan, F. Chen, G. Long, C. Zhang, and S. Y. Philip. "A comprehensive survey on graph neural networks." *IEEE Transactions on Neural Networks and Learning Systems*, 2020.

[WSG21] S. W. Wurster, H.-W. Shen, H. Guo, T. Peterka, M. Raj, and J. Xu. "Deep hierarchical super-resolution for scientific data reduction and visualization." *arXiv:2107.00462*, 2021.

[WSV24] Y. Wang, A. Solera-Rico, C. S. Vila, and R. Vinuesa. "Towards optimal β-variational autoencoders combined with transformers for reduced-order modelling of turbulent flows." *Int. J. Heat Fluid Flow*, **105**:109254, 2024.

[WTJ98] H. G. Weller, G. Tabor, H. Jasak, and C. Fureby. "A tensorial approach to computational continuum mechanics using object-oriented techniques." *Comput. Phys.*, **12**(6):620–631, 1998.

[WYL20] H. Wang, Z. Yang, B. Li, and S. Wang. "Predicting the near-wall velocity of wall turbulence using a neural network for particle image velocimetry." *Phys. Fluids*, **32**(11):115105, 2020.

[WYW18] X. Wang, K. Yu, S. Wu, J. Gu, Y. Liu, C. Dong, Y. Qiao, and C. Change L. "ESRGAN: Enhanced super-resolution generative adversarial networks." In *Proceedings of the European conference on computer vision (ECCV) workshops*, pp. 63–79, 2018.

[WZG22] X. Wang, S. Zhu, Y. Guo, P. Han, Y. Wang, Z. Wei, and X. Jin. "TransFlowNet: A physics-constrained Transformer framework for spatio-temporal super-resolution of flow simulations." *J. Comput. Sci.*, **65**(101906), 2022.

[WZK22] J. Williams, O. Zahn, and J. N. Kutz. "Data-driven sensor placement with shallow decoder networks." *arXiv:2202.05330*, 2022.

[XD20] J. Xu and K. Duraisamy. "Multi-level convolutional autoencoder networks for parametric prediction of spatio-temporal dynamics." *Comput. Methods Appl. Mech. Eng.*, **372**:113379, 2020.

[XFC18] Y. Xie, E. Franz, M. Chu, and N. Thuerey. "tempogan: A temporally coherent, volumetric GAN for super-resolution fluid flow." *ACM Trans. Graph.*, **37**(4):1–15, 2018.

[XLW20] W. Xu, W. Luo, Y. Wang, and Y. You. "Data-driven three-dimensional super-resolution imaging of a turbulent jet flame using a generative adversarial network." *Appl. Opt.*, **59**(19):5729–5736, 2020.

[XS23] A. Xuan and L. Shen. "Reconstruction of three-dimensional turbulent flow structures using surface measurements for free-surface flows based on a convolutional neural network." *J. Fluid Mech.*, **959**:A34, 2023.

[XSG22] X. Xie, A. Samaei, J. Guo, W. K. Liu, and Z. Gan. "Data-driven discovery of dimensionless numbers and governing laws from scarce measurements." *Nat. Commun.*, **13**(7562), 2022.

[XWY23] D. Xu, J. Wang, C. Yu, and S. Chen. "Artificial-neural-network-based nonlinear algebraic models for large-eddy simulation of compressible wall-bounded turbulence." *J. Fluid Mech.*, **960**:A4, 2023.

[Yan17] H. Q. Yang. "A computational fluid dynamics study of swirling flow reduction by using anti-vortex baffle." In *AIAA paper* 2017-1707, 2017.

[YBF23] C. Yu, X. Bi, and Y. Fan. "Deep learning for fluid velocity field estimation: A review." *Ocean Eng.*, **271**:113693, 2023.

[YH19] J. Yu and J. S. Hesthaven. "Flowfield reconstruction method using artificial neural network." *AIAA J.*, **57**(2):482–498, 2019.

[YHJ19] D. Yang, S. Hong, Y. Jang, T. Zhao, and H. Lee. "Diversity-sensitive conditional generative adversarial networks." In *7th International Conference on Learning Representations, ICLR 2019*. International Conference on Learning Representations, ICLR, 2019.

[YLC13] J. Yang, Z. Lin, and S. Cohen. "Fast image super-resolution based on in-place example

regression." In *Proceedings of the IEEE conference on computer vision and pattern recognition*, pp. 1059–1066, 2013.

[YO22] Y. Yasuda and R. Onishi. "Spatio-temporal Super-Resolution Data Assimilation (SRDA) Utilizing Deep Neural Networks with Domain Generalization Technique Toward Four-Dimensional SRDA." *arXiv:2212.03656*, 2022.

[YOH22] Y. Yasuda, R. Onishi, Y. Hirokawa, D. Kolomenskiy, and D. Sugiyama. "Super-resolution of near-surface temperature utilizing physical quantities for real-time prediction of urban micrometeorology." *Build. Environ.*, **209**:108597, 2022.

[YT19] C.-A. Yeh and K. Taira. "Resolvent-analysis-based design of airfoil separation control." *J. Fluid Mech.*, **867**:572–610, 2019.

[YW23] X. Yu and T. Wu. "Simulation of unsteady flow around bluff bodies using knowledge-enhanced convolutional neural network." *J. Wind. Eng. Ind. Aerodyn.*, **236**:105405, 2023.

[YWH08] J. Yang, J. Wright, T. Huang, and Y. Ma. "Image super-resolution as sparse representation of raw image patches." In *IEEE conference on computer vision and pattern recognition*, pp. 1–8. IEEE, 2008.

[YWH10] J. Yang, J. Wright, T. S. Huang, and Y. Ma. "Image super-resolution via sparse representation." *IEEE Trans. Image Process.*, **19**(11):2861–2873, 2010.

[YYH22] M. Z. Yousif, L. Yu, S. Hoyas, R. Vinuesa, and H. C. Lim. "A deep-learning approach for reconstructing 3D turbulent flows from 2D observation data." *arXiv:2208.05754*, 2022.

[YYJ18] W. Yoo, E. Yu, and J. Jung. "Drone delivery: Factors affecting the public's attitude and intention to adopt." *Telemat. Inform.*, **35**(6):1687–1700, 2018.

[YYL21] M. Z. Yousif, L. Yu, and H.-C. Lim. "High-fidelity reconstruction of turbulent flow from spatially limited data using enhanced super-resolution generative adversarial network." *Phys. Fluids*, **33**(12):125119, 2021.

[YYL22a] M. Z. Yousif, L. Yu, and H.-C. Lim. "Physics-guided deep learning for generating turbulent inflow conditions." *J. Fluid Mech.*, **936**:A21, 2022.

[YYL22b] M. Z. Yousif, L. Yu, and H.-C. Lim. "Super-resolution reconstruction of turbulent flow fields at various Reynolds numbers based on generative adversarial networks." *Phys. Fluids*, **34**(1):015130, 2022.

[YZC22] C. Yan, Y. Zhang, and H. Chen. "Data augmented turbulence modeling for three-dimensional separation flows." *Phys. Fluids*, **34**(7), 2022.

[YZT19] W. Yang, X. Zhang, Y. Tian, W. Wang, J.-H. Xue, and Q. Liao. "Deep learning for single image super-resolution: A brief review." *IEEE Trans. Multimed.*, **21**(12):3106–3121, 2019.

[YZW19] X. I. A. Yang, S. Zafar, J.-X. Wang, and H. Xiao. "Predictive large-eddy-simulation wall modeling via physics-informed neural networks." *Phys. Rev. Fluids*, **4**(3):034602, 2019.

[YZY23] M. Z. Yousif, M. Zhang, L. Yu, R. Vinuesa, and H. C. Lim. "A transformer-based synthetic-inflow generator for spatially-developing turbulent boundary layers." *Journal of Fluid Mechanics*, **957**:A6, 2023.

[ZCK13] A. Zlotnik, Y. Chen, I. Z. Kiss, H. Tanaka, and J.-S. Li. "Optimal waveform for fast entrainment of weakly forced nonlinear oscillators." *Phys. Rev. Lett.*, **111**(2):024102, 2013.

[ZFA22] Y. Zhong, K. Fukami, B. An, and K. Taira. "Machine-learning-based reconstruction of transient vortex-airfoil wake interaction." AIAA paper, 2022-3244, 2022.

[ZFA23] Y. Zhong, K. Fukami, B. An, and K. Taira. "Sparse sensor reconstruction of vortex-impinged airfoil wake with machine learning." *Theor. Comput. Fluid Dyn.*, **37**:269–287, 2023.

[ZFZ20] Y. Zhou, D. Fan, B. Zhang, R. Li, and B. R. Noack. "Artificial intelligence control of a turbulent jet." *J. Fluid Mech.*, **897**:A27, 2020.

[ZFZ23] B. F. Zhang, D. W. Fan, and Y. Zhou. "Artificial intelligence control of a low-drag Ahmed body using distributed jet arrays." *J. Fluid Mech.*, **963**:A3, 2023.

[ZG09] X. Zhu and A. B. Goldberg. *Introduction to semi-supervised learning*, volume 3. Morgan & Claypool Publishers, 2009.

[ZGT12] K. Zhang, X. Gao, D. Tao, and X. Li. "Single image super-resolution with non-local means and steering kernel regression." *IEEE Trans. Image Process.*, **21**(11):4544–4556, 2012.

[Zha10] L. Zhao. "Visualization of Vortices in Pump Sump." *J. Visualization Soc. Jpn.*, **30**(116):28–33, 2010.

[ZHY21] Z. Zhou, G. He, and X. Yang. "Wall model based on neural networks for LES of turbulent flows over periodic hills." *Phys. Rev. Fluids*, **6**(5):054610, 2021.

[ZK12] C. Zhang and J. M. Kovacs. "The application of small unmanned aerial systems for precision agriculture: a review." *Precis. Agric.*, **13**:693–712, 2012.

[ZLH23] K. Zhou, J. Li, J. Hong, and S. J. Grauer. "Stochastic particle advection velocimetry (SPAV): theory, simulations, and proof-of-concept experiments." *Meas. Sci. Technol.*, **34**(6):065302, 2023.

[ZMI13] M. Zontak, I. Mosseri, and M. Irani. "Separating signal from noise using patch recurrence across scales." In *IEEE conference on computer vision and pattern recognition*, pp. 1195–1202, 2013.

[ZNK16] A. Zlotnik, R. Nagao, I. Z. Kiss, and J.-S. Li. "Phase-selective entrainment of nonlinear oscillator ensembles." *Nat. Commun.*, **7**(1):10788, 2016.

[ZOK22] B. Zhang, R. Ooka, H. Kikumoto, C. Hu, and K. T. Tim. "Towards real-time prediction of velocity field around a building using generative adversarial networks based on the surface pressure from sparse sensor networks." *J. Wind. Eng. Ind.*, **231**:105243, 2022.

[Zou06] H. Zou. "The adaptive lasso and its oracle properties." *J. Am. Stat. Assoc.*, **101**(476):1418–1429, 2006.

[ZPI17] J.-Y. Zhu, T. Park, P. Isola, and A. A. Efros. "Unpaired image-to-image translation using cycle-consistent adversarial networks." In *Proceedings of the IEEE international conference on computer vision*, pp. 2223–2232, 2017.

[ZSB22] K. Zhang, B. Shah, and O. Bilgen. "Low-Reynolds-Number Aerodynamic Characteristics of Airfoils with Piezocomposite Trailing Surfaces." *AIAA J.*, **60**(4):2701–2706, 2022.